Corrosion Product Growth Kinetics/Characteristics and Inhibitor Performance in CO_2 Environments

By

Amir Shamsa

Submitted in accordance with the requirements for the degree of
Doctor of Philosophy

The University of Leeds
Institute of Functional Surfaces
School of Mechanical Engineering

September 2019

Publication Statement

The candidate confirms that the work submitted is his/her own, except where work which has formed part of jointly-authored publications has been included. The contribution of the candidate and the other authors to this work has been explicitly indicated below. The candidate confirms that appropriate credit has been given within the thesis where reference has been made to the work of others.

In all papers listed below, the primary author completed all experimental studies, evaluation of data and preparation of publications. All authors contributed to proof reading of the articles prior to publication.

Papers contributing to this thesis:

- Shamsa, A., Barker, R., Hua, Y., Barmatov, E., Hughes, T.L. and Neville, A., 2019. The role of Ca2+ ions on Ca/Fe carbonate products on X65 carbon steel in CO2 corrosion environments at 80 and 150°C. *Corrosion Science*, *156*, pp.58-70.

Acknowledgements

I would like to thank my primary supervisor, Professor Anne Neville for providing me with this PhD opportunity and for her excellent supervision, advice and encouragement during my PhD. I am extremely grateful for her continuous support and for always providing me with great opportunities. I would also like to thank my co-supervisors Dr Richard Barker and Dr Yong Hua for their daily support and advice about lab work and writing of research papers and thesis. The continuous support and encouragement by all of my supervisors throughout my PhD has made it an even more enjoyable experience.

I would also like to thank my industrial supervisors at Schlumberger, Mr Trevor Hughes and Dr Evgeny Barmatov for their technical guidance and support. I am also extremely grateful for all of the lab support provided by the research technicians in IFS. I am also very happy to have worked with and become friends with all of my colleagues at IFS.

I am tremendously grateful to my parents for always helping me and my brother achieve what we are passionate about in life. This accomplishment would not have been possible without their endless support and encouragement.

Finally, I am extremely grateful to my fiancée for being so supportive and encouraging particularly during the write-up of my thesis.

Abstract

The application of corrosion inhibitors is extremely common in the oil and gas industry as it enables the use of carbon steel thereby reducing project initial capital expenditure. In many cases, once the use of corrosion inhibitors has become requirement, corrosion products have already precipitated onto the pipeline steel surfaces. The presence of Ca^{2+} ions can facilitate precipitation of mixed carbonates such as iron-calcium carbonate ($Fe_xCa_yCO_3$ – where x+y=1). This results in a scale/corrosion product with different chemical and morphological properties to pure $FeCO_3$ which normally forms when CO_2 corrosion occurs in the absence of Ca^{2+} ions. It is therefore of great importance to evaluate any possible antagonistic or synergistic effects associated with the use of corrosion inhibitors in the presence of such corrosion products.

This thesis addresses these issues by evaluating the role of Ca^{2+} ions on the corrosion behaviour of carbon steel in CO_2-corrosion environments at 80ºC and 150ºC using *in-situ* electrochemistry assessment of corrosion in an autoclave. The ability of an imidazoline derivative to provide corrosion protection for X65 carbon steel in CO_2-saturated sodium chloride (NaCl) brines at 80°C was investigated and the role of pre-corrosion on the performance of an imidazoline corrosion inhibitor was evaluated using a two-stage testing procedure with autoclave pre-corrosion and glass cell inhibition testing of X65 carbon steel. The extent of localised/pitting corrosion was assessed using NPFLEX 3D optical non-contact profilometry and was found to be increasing through the addition of Ca^{2+} ions indicating that Ca^{2+} plays a role in promoting localised corrosion. XRD based calculations, along with FIB/EDX-line scans and SEM/EDX-point scans confirmed that $Fe_xCa_yCO_3$ corrosion products had precipitated. A concentration gradient was measured across the depth of the deposited layer.

This thesis demonstrates that the optimum inhibitor concentration required for suppression of uniform corrosion is significantly lower than that for localised corrosion protection. Pre-corrosion of X65 carbon steel was found to cause and in some cases promote severe localised attack especially in the presence of crystalline $FeCO_3$ where the corrosion inhibitor was found to only provide 25-58% of the overall corrosion protection on pre-corroded specimens depending on the characteristics of the corrosion product.

Table of Contents

List of Tables

List of Figures

Chapter 1 Introduction

1.1 Problem Background

There are several types of corrosion that occur in the oil and gas industry, one of which is known as carbon dioxide corrosion or sweet corrosion (1). CO_2 corrosion is known to be one of the most prevalent and predominant types of corrosion in the oil and gas industry, having been first recorded in the United States in the 1940s. CO_2 corrosion failures in the oil and gas industry have existed for many years due to several factors such as insufficient knowledge with regards to CO_2 corrosion and its mechanisms and due to the lack of predictive capability by CO_2 corrosion prediction models (1-4). Studies conducted by several countries including the United Kingdom have all concluded that the worldwide overall estimated cost of corrosion exceeds $1.8 trillion in terms of direct annual costs (5). However, several studies have also concluded that these costs could be reduced by up to 30% if optimum corrosion management is employed. These statistics suggests that corrosion management plays a key role in the effort to reduce the cost of corrosion, environmental disasters and health and safety risks (5). However good management is based on knowledge of the mechanisms that control the corrosion process.

There have been several studies and extensive research focused on CO_2 corrosion, however the understanding of CO_2 corrosion and its mechanisms are still far from complete, particularly at high temperatures. CO_2 gas is usually present as a produced gas either due to its own presence in reservoirs or due to the injection of CO_2 during enhanced oil recovery (EOR). Dry CO_2 gas by itself is not corrosive, however, when CO_2 is dissolved in an aqueous phase it becomes corrosive by promoting electrochemical reactions at the interface between the steel surface and the aqueous phase (1-3).

There are several undeveloped gas reserves such as the Natuna D-Alpha field in Indonesia/south China Sea. There are several reasons for fields as such not being developed, however the main reason being the cost of development due to corrosion caused by the highly CO_2 rich (70 mole% CO_2) reserves. A project as such would only be feasible with oil prices above $100/barrel and with the use

of cheaper materials such as carbon steel (6). Carbon steel is widely used in the oil and gas industry mainly due to its low cost however also because of its availability, weldability and its mechanical properties. Carbon steels have several advantages such as the ones previously mentioned, however they are not very corrosion resistant, unless a highly protective film develops on the material surface (7). The formation of protective surface films such as iron carbonate ($FeCO_3$) are of great importance in the oil and gas industry as they can prolong the lifetime of the materials, such as the ones used in downhole casing/tubing or the mild steels used in the transportation of the hydrocarbons (7). Collected scale samples from the oil and gas industry have shown that calcium carbonate ($CaCO_3$) is the most prevalent type of corrosion product along with iron carbonate (8).

1.1.1 Types of Oil/Gas Reservoir Formations

Rock formations can be classified into three classes based on their formation; sedimentary, metamorphic and igneous (9, 10). Sedimentary rocks form by the accumulation of particles such as sand and pebbles into layers which harden over long periods of time to form sedimentary rocks. Metamorphic rocks form beneath the earth's surface and are extremely dependent upon heat and pressure. Igneous rock formations are formed by the cooling and hardening process of magma which can either occur when magma erupts from volcanos or when it cools inside the earth (9, 10). However most geologists agree that oil and gas generates from sedimentary rocks such as carbonates which consist of limestone and dolomites (11, 12). Limestone's are composed of calcium carbonate ($CaCO_3$) and dolomites are composed of calcium magnesium carbonate ($CaMgCO_3$) (9, 10). As a result of the nature of reservoir rocks which typically host oil and gas, Ca^{2+} ions are widely present in oil and gas formation brines. The total dissolved inorganic content within oil and gas formation brines are commonly in the range of 100-350 g/L where sodium chloride is typically the major inorganic constituent of oilfield brines. However they may also contain 1-30 g/L calcium, 0.1-30 g/L magnesium, 0-3 g/L strontium, 0.1-2 g/L bicarbonate, 0.4 g/L sulphate and up to ≈ 0.1 g/L barium (13). The presence of such inorganic content can have a major influence on the corrosion processes that occur during both upstream and downstream processes due to the different types of corrosion products that can precipitate with different chemical and morphological

properties onto steel surfaces. For example, the level of dissolved calcium within formation brines can influence the type of corrosion product which precipitates. Greater volumes of dissolved calcium within formation brines can lead to precipitation of $CaCO_3$ and $Fe_xCa_yCO_3$ rather than $FeCO_3$ when Fe^{2+} ions are also present in the production fluid (14). The presence of calcium ions or any other dissolved inorganic content within brines may not only originate from reservoir source rocks, they can also become present years after production of a specific oil and gas reserve where enhanced oil recovery (EOR) has been used to extend the lifespan of a reservoir (15-18). Water injection is readily used as a method of EOR in the oil and gas industry in an attempt to increase reservoir pressures to boost oil and gas recovery and to extend the lifespans of oil and gas fields. However the water used for injection is commonly sourced from either seas nearby or aquifers depending on the geographic location of the oilfield. These types of waters are usually not treated and will therefore most likely contain dissolved inorganic content which may have a substantial influence on both upstream and downstream corrosion processes (15-17).

1.1.2 The Transition Towards High Temperature Reservoir Formations

The decline of oil production from conventional reserves and rise in production from unconventional oil reserves has been widely predicted by economists for years (19), however due to the uncertainty in unconventional oil reserve predictions and discoveries of new conventional oil and gas fields, the decline in oil/gas production from conventional reserves has been smaller than expected (20). The production of oil/gas from unconventional reserves has also risen (Figure 1-1) due to several combining factors such as oil price, magnitude of reserves available and new technology which has made it more feasible to produce oil/gas from the more challenging and unconventional oil and gas reserves (20).

Geothermal gradients of oil/gas reserves suggest that reservoir temperatures increase with increasing reservoir depths where the temperature of deep reservoirs may be greater than 370ºC (21). The greater depths of oil and gas reserves are also associated with greater gas contents (6, 21).

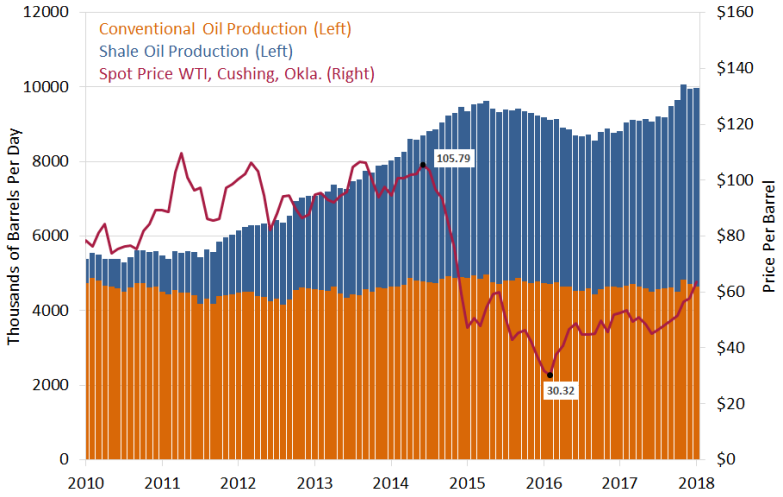

Figure 1-1 Production of conventional oil and unconventional shale oil as a function of time (20)

The combination of high temperatures and high CO_2 contents can have major implications on the corrosion processes which occur in both upstream and downstream oil and gas processes. It has been well documented that oil/gas reservoirs have average geothermal gradients of 25-35 ºC/km depending on their location. Average depths of conventional and unconventional oil wells range between 2-3 km and 3-5 km respectively (22). Using the upper range, temperatures for conventional and unconventional oil/gas wells are on average 80 and 150 ºC respectively (Figure 1-2).

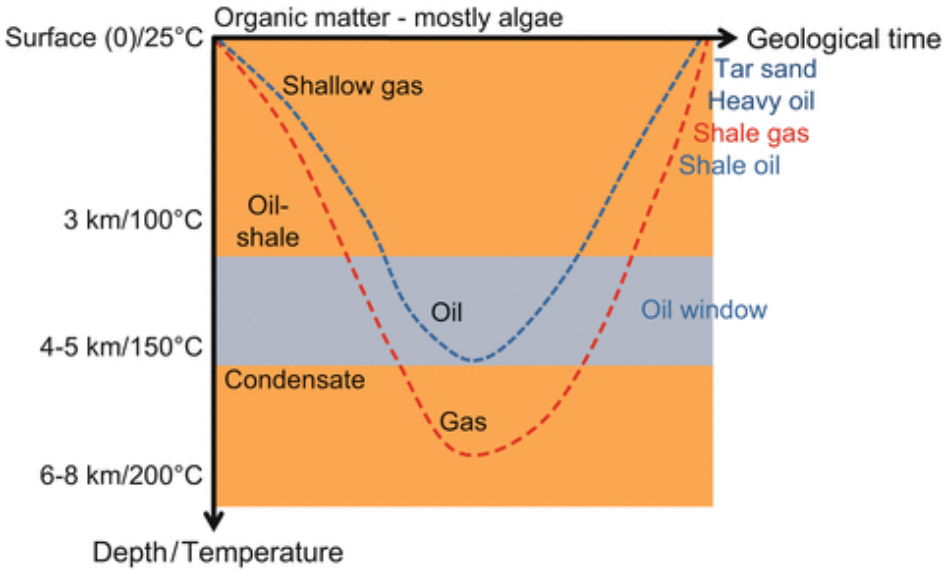

Figure 1-2 Depth and temperature of oil/gas reservoirs as a function of geological time (22)

1.1.3 Corrosion Control Using Corrosion Inhibitors

As previously mentioned the economic losses due to corrosion both directly and indirectly within the oil and gas industry are exceptionally large which makes it paramount to combat corrosion in a cost effective manner. There are several methods that can be used to combat corrosion (Figure 1-3) however mitigation of corrosion using corrosion inhibitors has become extremely common in the oil and gas industry due to the overall economic benefits (23). Corrosion inhibitors can be administered by continuous injection, batch dosing or through squeeze treatments. Most corrosion inhibitors mainly consist of nitrogen containing compounds which operate by forming a protective film onto the steel surface. However, such chemicals have limitations; they may not necessarily have favourable environmental profiles and can bioaccumulate and thereby impose limitations on their use (24).

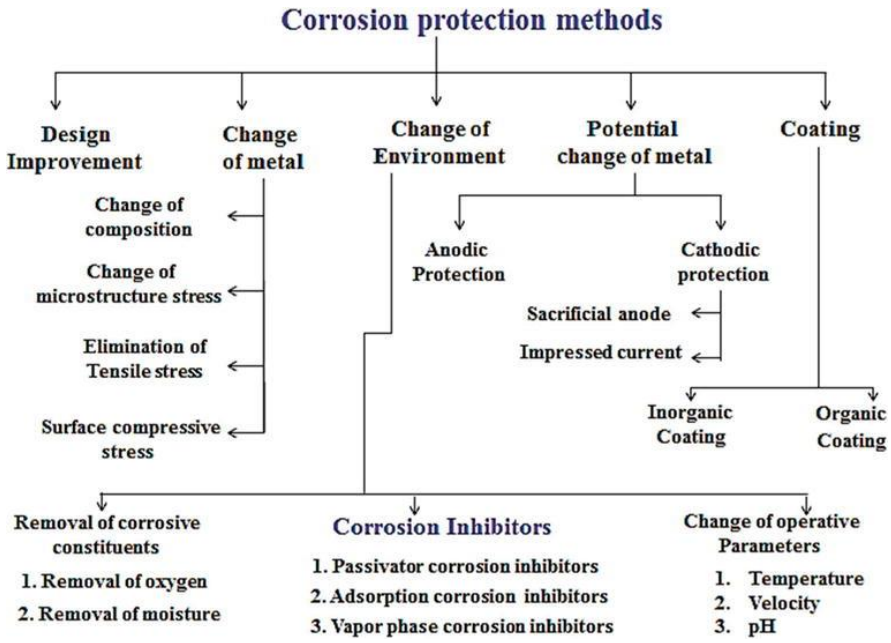

Figure 1-3 Methods available for corrosion mitigation (25)

In order to successfully use corrosion inhibitors in the oil and gas industry, the inhibitors need to be tested thoroughly. This means that all inhibitors need to be tested to ensure compatibility with the environment that it is intended for, provide sufficient protection against corrosion and most importantly not cause side effects such as localised corrosion that cannot be effectively mitigated. In terms of corrosion control only, this requires rigorous corrosion inhibitor testing with respect to both general and localised corrosion behaviours to make sure that by

using a corrosion inhibitor both corrosion mechanisms will be successfully mitigated (26, 27).

Organic corrosion inhibitors with film forming properties are becoming increasingly popular due to environmental requirements. These type of corrosion inhibitors are extremely surface active as they consist of a polar grouping at one end of the molecule and a non-polar hydrocarbon soluble group at the other end, where the polar head group of the molecule attaches to the steel surface and the hydrocarbon soluble non-polar tail of the molecule is oriented away from the steel surface which results in a hydrophobic surface (27). The efficiency of these corrosion inhibitors in terms of corrosion suppression is highly dependent upon the extent of surface coverage of the formed protective film. There is commonly a direct relationship between the inhibitor concentration and the protection offered, where protection against corrosion increases with increasing inhibitor concentration until a maximum protection value is achieved (27). The selection and testing of corrosion inhibitors is commonly dependent on several environmental factors such as flow conditions, temperature, pH and pressure etc. However in many cases it is extremely common for corrosion inhibitors to be used years after oil and gas production has commenced. This is all in an attempt to reduce costs and therefore only mitigate corrosion when necessary (26, 27). The consequence of this is that corrosion inhibitors are in many cases used to protect steel surfaces which have been severely corroded and are therefore covered by corrosion products such iron carbonate ($FeCO_3$). The compatibility of specific corrosion inhibitors with corrosion products as such then become of great relevance and importance from a corrosion mitigation perspective. The interaction between corrosion inhibitors and corrosion products is rarely evaluated. Selection of corrosion inhibitors without evaluation of the steel surface conditions can have severe implications on the overall protection afforded by corrosion inhibitors (28-32).

1.2 Research Contributions

The research conducted and presented within this thesis will contribute to three corrosion related research areas within the existing literature (Figure 1-4). The kinetics and characteristics of corrosion products in the absence/presence of Ca^{2+} is evaluated at 80 and 150 ºC to provide an in depth analysis on the effects

of calcium ions on the overall corrosion behaviour and incorporation of calcium into Iron carbonate ($FeCO_3$) corrosion products. The complexity and heterogeneity of mixed iron-calcium carbonate corrosion products is evaluated using SEM, FIB and XRD analysis along with a derivation of a new equation based on existing data, enabling the molar fractions of iron and calcium to be determined within mixed iron-calcium carbonates ($Fe_xCa_yCO_3$). The development of *in-situ* electrochemical measurements within an autoclave system is presented and validated using mass loss measurements at 80 and 150 ºC in an attempt to gain a better understanding of how temperature and the presence of calcium ions affect the overall corrosion behaviour and the characteristics of corrosion products.

The performance of an imidazoline corrosion inhibitor is evaluated in glass cells and the significance of performance analysis of corrosion inhibitors with respect to both the uniform and localised corrosion behaviours is presented to illustrate the importance of localised corrosion evaluations on the determination of the optimum inhibitor dosage. The performance test of the imidazoline corrosion inhibitor extends beyond typical uniform corrosion evaluations of inhibitors and evaluates the effects of inhibitor dosage, short term pre-corrosion in the absence of corrosion products and inhibitor aging on both uniform and localised corrosion behaviours to demonstrate both beneficial and detrimental attributes related to each aspect.

The research knowledge gathered while evaluating corrosion products and their characteristics at 80 and 150 ºC in the absence/presence of calcium ions along with the performance evaluations of an imidazoline corrosion inhibitor are combined to study the interaction between an imidazoline corrosion inhibitor and different pre-corroded corrosion product covered surfaces. A two stage methodology is developed to enable the performance of the corrosion inhibitor to be examined and compared across different pre-corroded carbon steel surfaces. A detailed analysis of how a corrosion inhibitor can have both synergistic and antagonistic interactions within a pre-corroded environment will be depicted using corrosion and surface wettability studies.

The research presented in this thesis can be categorised into three sections; 1- corrosion product kinetics and characteristics, 2 - evaluation of corrosion inhibitor

performance and 3 - interaction between corrosion products and an imidazoline based corrosion inhibitor (Figure 1-4).

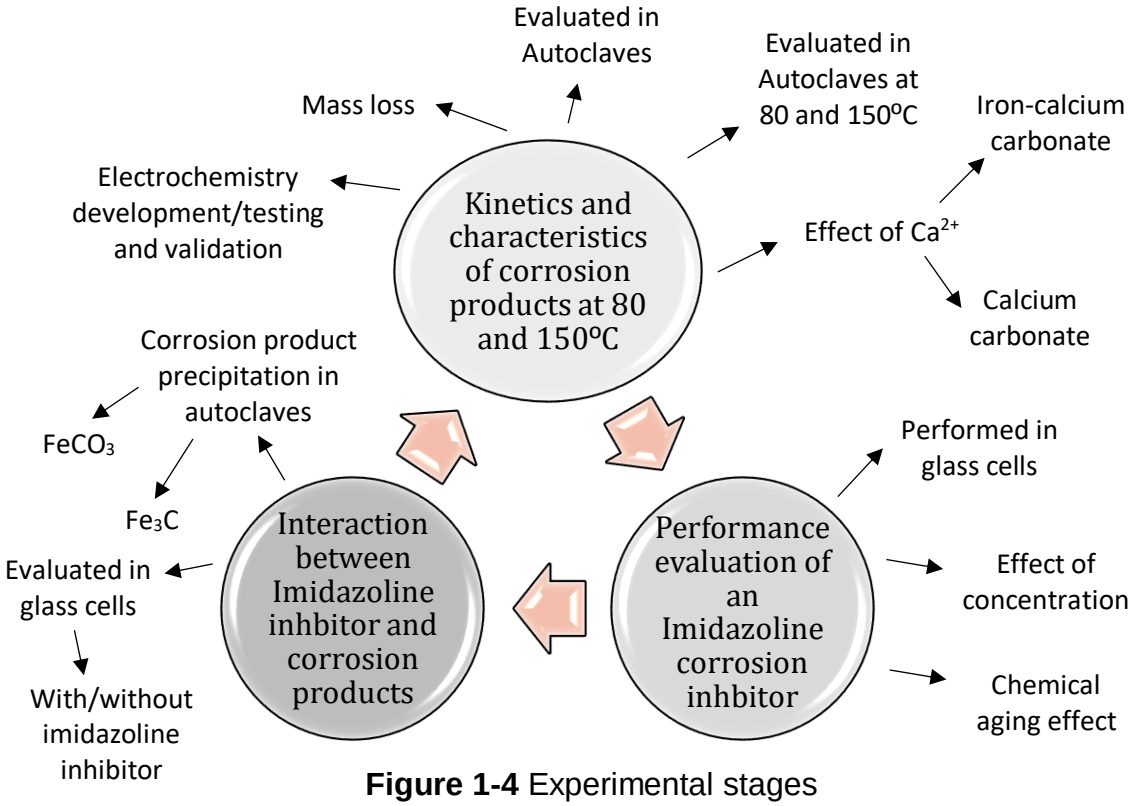

Figure 1-4 Experimental stages

1.3 Research Objectives

The research objectives can be outlined as follows;

1. To determine the kinetics and characteristics of corrosion products that precipitate at 80 and 150 ºC in the absence/presence of 1.83 wt.% $CaCl_2 \cdot 2H_2O$ in CO_2 saturated autoclave environments using mass loss measurements, NPFLEX non-contact surface profilometry, Scanning electron microscopy (SEM) and X-ray diffraction (XRD).
2. Develop and validate an autoclave system capable of performing *in-situ* electrochemical corrosion rate measurements.
3. Evaluate the role of Ca^{2+} concentration within brines on the precipitation and characteristics of mixed iron-calcium carbonates at 80 ºC.
4. Evaluate the performance and effect of dosage on an imidazoline corrosion inhibitor with respect to both uniform and localised corrosion behaviours.

5. Investigate the effects of inhibitor aging at 80 and 120 ºC on its performance and ability to supress uniform and localised corrosion at 80 ºC.
6. Develop a methodology enabling the study of corrosion inhibitor performance on different pre-corroded corrosion product covered surfaces in an initially standardised environment allowing for a performance comparison and separation of individual contributions provided by the inhibitor and corrosion products towards overall protection.
7. Study the synergistic/antagonistic interaction between an imidazoline corrosion inhibitor and different corrosion product covered surfaces using corrosion and wettability studies.

1.4 Outline of Thesis

This thesis contains 8 chapters including the current chapter. The current chapter provides a general overview of corrosion related issues within the oil and gas industry. The objectives and novelty of the work presented within this thesis are also highlighted within the first chapter. Chapter 2 provides an introduction to carbon dioxide (sweet) corrosion and the mechanisms/reactions that are associated with it. An overview of aqueous corrosion thermodynamics/kinetics and monitoring techniques is also provided. The types of corrosion products and factors controlling the CO_2 corrosion process are also discussed along with the types of corrosion inhibitors used in the oil and gas industry. An extensive literature review of relevant research on the evaluation of corrosion products, corrosion inhibitors and the interaction between the two is also provided within chapter 2. Chapter 3 explains the experimental preparation and testing procedures. The development of an autoclave capable of *in-situ* electrochemical measurements and methods used for *ex-situ* surface analysis are also included within Chapter 3. Chapter 4 provides the experimental findings for the evaluation of corrosion product characteristics and growth kinetics at 80 and 150 ºC in the absence and presence of calcium ions gathered by mass loss measurements, X-ray diffraction (XRD), scanning electron microscopy (SEM), Focused ion beam (FIB) and NPFLEX non-contact surface profilometry measurements. Chapter 4 also delivers the findings gathered from a developed autoclave system capable

of *in-situ* electrochemical measurements along with its validation using mass loss measurements. The derivation of an equation for the estimation of molar fractions within mixed carbonate corrosion products are also described in Chapter 4. Chapter 5 presents experimental findings from the performance evaluation of an imidazoline corrosion inhibitor, where the corrosion inhibitor is evaluated in terms of concentration, short term pre-corrosion in the absence of corrosion products and aging time/temperature with respect to both uniform and localised corrosion behaviours. Chapter 6 explains the experimental procedure and findings for the performance of an imidazoline corrosion inhibitor on different pre-corroded corrosion product covered surfaces. Interaction with iron carbide and different iron carbonate covered surfaces is provided using both corrosion and wettability studies. Analysis of the results are provided within each results chapter (Chapter 4, 5 and 6) however an overall discussion for each results chapter is also provided in Chapter 7. Conclusions drawn from the experimental findings are provided at the end of each results chapter, however an overall conclusion is provided in Chapter 8. Recommendations for future research are also provided in Chapter 8.

Chapter 2 Theory of Aqueous CO_2 Corrosion and Review of Literature

2.1 Introduction to CO_2 Corrosion

Corrosion can be defined as the deterioration of a material which is caused by chemical reactions with the surrounding environment. In the case of metals, corrosion is an electron transfer reaction where a neutrally charged metal atom will lose at least one electron to become a charged metal ion, as shown by equation 2.1 (33). Two processes are involved in the electron transfer, an oxidation reaction and a reduction reaction. The oxidation reaction is the loss of electrons from the metal atom and the reduction reaction is the gain in electrons by the surrounding environment (33-35). The anodic and cathodic reactions will be detailed later.

$$M \rightarrow M^{n+} + ne^{-} \tag{2.1}$$

CO_2 corrosion, sometimes referred to as sweet corrosion is known to be one of the most prevalent types of corrosion in the oil gas industry, especially in upstream oil and gas operations (36). CO_2 corrosion has been a major problem for the oil and gas industry having been first documented by the US petroleum industry in the 1940s. CO_2 gas is not corrosive by itself however when dissolved in an aqueous phase it can promote electrochemical reactions (1). The electrochemical reactions can result in either uniform or localised corrosion attack and in some cases a combination of the two (37, 38). The extent of this type of corrosion is dependent upon several environmental and metallurgical factors which will be detailed in Chapter 2.7.

2.2 Aqueous Corrosion Thermodynamics

Corrosion thermodynamics can be used to provide an indication of the tendency of corrosion reactions to occur (39). At constant temperature and pressure a chemical reaction will only occur if there is an overall reduction in the free energy during the reaction within that particular system. It is therefore important to know whether the change in enthalpy or entropy would dictate the direction of a particular reaction. Only a part of the total enthalpy of a system is converted into useful work, this useful work is known as free energy (ΔG) which is expressed in

joules/mole. Free energy can be defined in terms of change in enthalpy (ΔH), change in entropy (ΔS) and temperature which is also known as the second law of thermodynamics (39-41), and can be rearranged and expressed as shown in equation 2.2.

$$\Delta G = \Delta H - T\Delta S \tag{2.2}$$

ΔG is therefore the driving force for a chemical reaction to occur and at constant temperature and pressure a reaction will occur in the direction which will cause a reduction in the free energy (ΔG).

Electrical energy is generated in electrochemical cells due to electrochemical reactions where the available electrical energy can be expressed as follows (39);

$$Electrical\ energy = E \times I \times t = EQ \tag{2.3}$$

Where E is the electromotive force (emf) in volts, I is the current, t is time and Q is the charge in coulombs which can be defined as follows;

$$Q = nF \tag{2.4}$$

Where n is the number of electrons in the reaction and F is Faraday's constant.

As previously mentioned work can only be performed through a reduction of a cells free energy which results in the following equation;

$$\Delta G = -nFE \tag{2.5}$$

The potential (E) is known and available for different metals at standardized conditions of atmospheric temperature and pressure. The standard redox potential (E^o) can therefore replace E in equation 2.5 to generate equation 2.6.

$$\Delta G^\circ = -nFE^\circ \tag{2.6}$$

As previously mentioned, corrosion reactions are composed of two half-cell reactions, where one half reaction takes place at the anode (oxidation reaction) and the other taking place at the cathode (reduction reaction) (39-41);

$$M_1 \rightarrow M_1^{n+} + ne \quad (oxidation\ reaction) \tag{2.7}$$

$$M_2^{n+} + ne \rightarrow M_2 \quad (reduction\ reaction) \tag{2.8}$$

The Nernst equation can either be applied to the half reactions or to the complete corrosion reaction. The Nernst equation can be applied in order to define the

potentials of metals in aqueous solutions (41). The Nernst equation can be defined as follows;

$$E = E^{\circ} - \frac{RT}{nF} ln \frac{[Products]}{[Reactants]} \quad (2.9)$$

Where R is the ideal gas constant in J/mol.K, T is the temperature in Kelvin and [Products] and [Reactants] are the molar concentrations of the products and the reactants, respectively.

2.3 Aqueous Corrosion Kinetics

As previously mentioned, the tendency of corrosion reactions to occur can be addressed using thermodynamics however corrosion kinetics helps address the rates of those reactions (39, 40). The kinetics of electrochemical reactions can be described using the mixed potential theory and the Butler-Volmer equation. A mixed potential plot also known as an Evans diagram provides a graphical representation of the kinetics of the anodic and cathodic reactions and can be used to show the corrosion potential at equilibrium (E_{corr}) through the shifts in anodic and cathodic reactions by a corrosion current (I_{corr}) (Figure 2-1). However it is important to note that Evans diagrams provide an imaginative illustration and can therefore not be measured experimentally and therefore unable to provide an actual value of the corrosion current (39, 40).

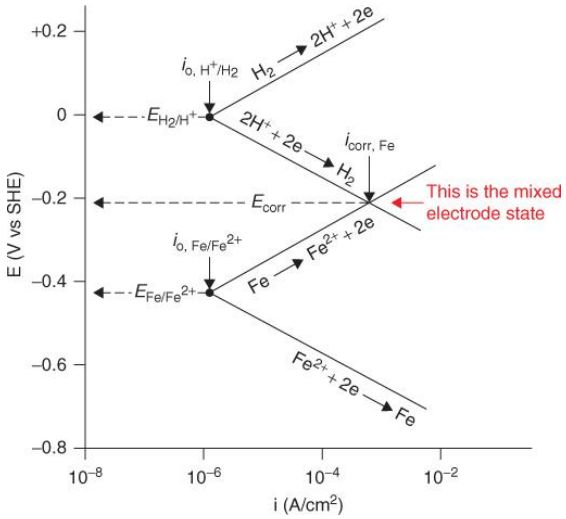

Figure 2-1 Evans diagram of iron corrosion in acid (39)

The Butler-Volmer equation is the fundamental formula which can be used to explain the kinetics of an electrochemical reaction as it can be used in conjunction with the mixed-potential theory (39). The Butler-Volmer equation is defined as follows;

$$i_o = i_{corr}\left[exp^{\left(\frac{(1-\alpha)nF(E-E_{corr})}{RT}\right)} - exp^{\left(\frac{-\alpha nF(E-E_{corr})}{RT}\right)}\right] \quad (2.10)$$

Where i_o is the external current (Amps/cm^2) which flows from or to an electrode because of an applied potential, E is the applied potential (Volts) and α is a coefficient which is typically 0.5.

2.4 Corrosion Monitoring

2.4.1 Weight Loss Method

The weight loss method is one of the oldest and simplest of methods used for corrosion loss estimation. A metal coupon is weighed before exposure to a corrosive environment. After the steel coupon has been exposed to the corrosive environment it is cleaned using inhibited acid to remove any corrosion products and then weighed once more. The weight loss can then be used to determine an averaged corrosion rate for the exposure time (41). The corrosion rate is calculated using equation 2.11.

$$CR = \left(\frac{W}{D \times A \times T}\right) \quad (2.11)$$

Where W is the weight loss in mg, D is the metal density in g/cm^3, A is the area of the steel coupon in cm^2 and T is the exposure time in hours.

2.4.2 Three-Electrode Cell

A three-electrode cell consists of three electrodes; a working electrode, a reference electrode and a counter electrode. It also consists of an electrolyte and a potentiostat. These components make a complete cell which enables the measurement of a potential (39, 42). The working electrode is the steel coupon of interest which is where the corrosion reaction of interest occurs. The potential of the working electrode is controlled and measured against the potential of the reference electrode. As a result of this the drop in solution resistance between the working and reference electrode is generally very small which results in a stable reference potential and compensation for any reduction in the solution

resistance. This enables superior control over the potential of the working electrode. The counter electrode completes the circuit and it therefore passes all of the current required to balance the current at the working electrode (42). The most commonly used reference and counter electrodes are combined reference and counter electrodes such as Ag/AgCl electrodes.

The potentiostat enables the voltage across the working and reference electrodes to be controlled and the current between the working and counter electrodes to be measured, as shown by Figure 2-2 (39).

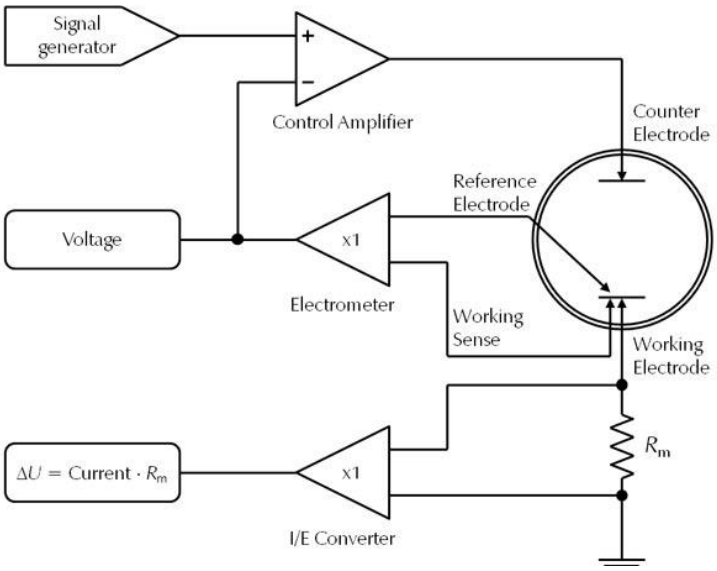

Figure 2-2 Potentiostat schematic diagram (43)

2.4.3 Linear Polarisation Resistance (LPR)

Linear polarisation resistance is an electrochemical corrosion monitoring technique which enables direct corrosion rate measurements in real time. Using a potential (E) versus current density (log i) plot at the corrosion potential (E_{corr}) the rate of corrosion can be measured by measuring the slope to define the polarization resistance (R_p) on a linear polarisation plot. Linear polarisation resistance can therefore be used to investigate the electrochemical response of a corroding steel surface near its open circuit potential (OCP). This is achieved by polarising the working electrode with 30 mV which results in a linear current response. Since only small polarisation is applied to the working electrode, this electrochemical technique does not result in any additional reactions and is therefore a non-destructive technique which does not alter the surface conditions of the working electrode (40, 42).

The correlation between the slope of a linear polarisation resistance plot and the corrosion current (i_{corr}) is known as the Stern and Geary correlation (39, 42);

$$\frac{\Delta E}{\Delta I} = R_p = \frac{1}{2.3 i_{corr}} \left(\frac{\beta_a \beta_c}{\beta_a + \beta_c} \right) = \frac{1}{2.3 i_{corr}} B \qquad (2.12)$$

Where β_a and β_c are anodic and cathodic Tafel slopes respectively and B is the Stern Geary coefficient.

2.4.4 Potentiodynamic Polarisation

Anodic and cathodic potentiodynamic polarisation is generally used for the determination of Tafel slopes to be used in conjunction with linear polarisation resistance (LPR) measurements for improved accuracy of corrosion rate measurements however this method can also be used for the determination of the corrosion rate directly using Faraday's law. Tafel plots are constructed by applying an overpotential several hundreds of mV away from the corrosion potential while monitoring the current (39). The potential is then plotted against the logarithmic current as shown in Figure 2-3.

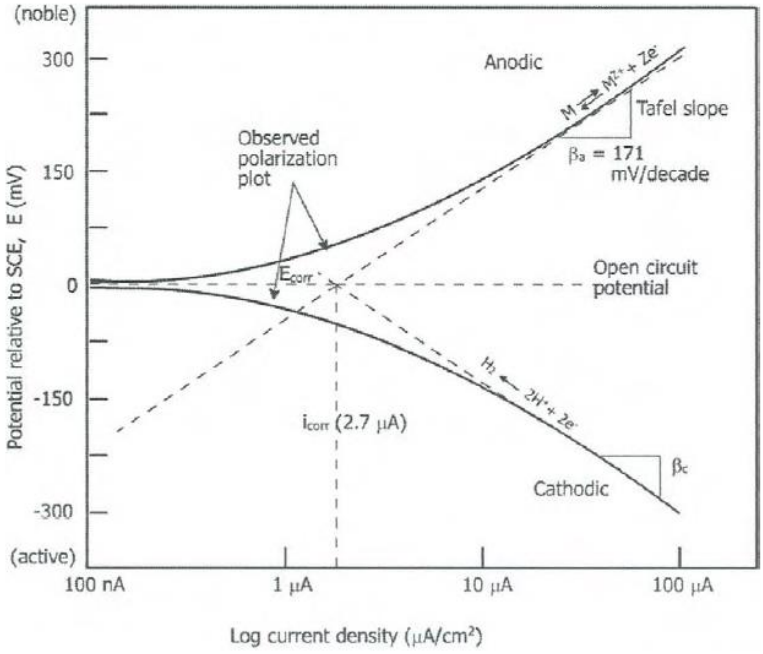

Figure 2-3 Hypothetical Tafel diagram (39)

Using the Tafel plot, E_{corr} and i_{corr} can be obtained by extrapolation of the linear regions which can then be used to determine the corrosion rate using equation 2.13, however it is important to note that Tafel techniques can cause damage to

the working electrode due to the high currents which means that this method will not be feasible for long term corrosion rate monitoring (39, 42).

$$CR\left(\frac{mm}{year}\right) = \frac{Ki_{corr}M_{Fe}}{nF\rho} \quad (2.13)$$

Where K is the unit conversion factor (3.16×10^5), M_{Fe} is the molar mass of iron (55.85 g/mol), n are the equivalents per mole (2), F is the Faraday constant (96,485 C/mol) and ρ is the density of iron (7.86 g/cm^3).

Apart from providing useful information about anodic and cathodic corrosion processes, Tafel plots can also be used to determine the anodic and cathodic Tafel constants (β_a and β_c). These can be obtained by extrapolating ±50 mV away from the corrosion potential (44) and can then be used to improve the accuracy of corrosion rate measurements obtained by linear polarisation resistance.

It is important to note that both weight loss calculations and electrochemical techniques have both advantages and limitations with respect to determining the corrosion rate. The weight loss technique is relatively affordable as only a precision balance is required for its use. However it can be extremely time consuming to determine the corrosion rates for prolonged test periods using this method and its accuracy is highly dependent upon the precision of the balance used and the level of accuracy in determining the exposed surface area of the corroding metal. The corrosion rates calculated by means of weight loss are also typically based on accumulated mass loss of the corroding steel surface which can cause overestimations of the actual corrosion rates (39-41). As previously discussed, linear polarisation resistance can be used to continuously monitor the corrosion behaviour and can therefore be extremely useful for prolonged test durations. However, as explained by equation 2.12 the accuracy of the measured corrosion rates as determined by LPR are dependent upon the accuracy of the measured Tafel constants. The Tafel constants are highly sensitive to surface conditions and are therefore continuously changing during corrosion product precipitation onto the corroding steel surface (40, 41, 44). It can therefore be cumbersome to accurately measure Tafel constants during precipitation which in turn limits the accuracy of the measured corrosion rates. It can therefore be useful to monitor the corrosion behaviour using both weight loss and LPR in order

to obtain a more reflective understanding of the overall corrosion kinetics, especially during corrosion product precipitation and growth.

2.5 Carbon Dioxide (CO_2) Corrosion Mechanisms

2.5.1 Cathodic and Anodic Reactions

It is well known that CO_2 is soluble in water or brine, CO_2 therefore dissolves in water (formation water) which produces carbonic acid (H_2CO_3). Carbonic acid is known to be a weak acid which does not fully dissociate. Carbonic acid is also known to accelerate the cathodic reaction which thereby accelerates the corrosion rate (1, 2, 4, 45). This process can be explained by the following steps (2).

$$CO_{2\,(g)} \rightleftharpoons CO_{2\,(aq)} \tag{2.14}$$

CO_2 gas is dissolved in water, where some of the dissolved carbon dioxide gas hydrates to produce carbonic acid (45);

$$CO_{2\,(aq)} + H_2O_{\,(l)} \rightleftharpoons H_2CO_{3\,(aq)} \tag{2.15}$$

There is much debate in the rate determining step with regards to the cathodic reaction and as a result several mechanisms have been proposed in the past (1, 2, 4). However most of the mechanisms that have been proposed in the past have not been general enough to apply to CO_2 corrosion as such and have therefore not received universal recognition (1). There are perhaps two or three well known mechanisms that have been proposed in the past. The first one is the de Waard and Milliams; who proposed that carbonic acid (H_2CO_3) is directly reduced at the surface of the steel. This is known as the direct reduction mechanism and was proposed in 1975 (1, 4, 45).

Equation 2.16 and 2.17 show that the partial dissociation of carbonic acid produces both hydrogen and bicarbonate ions, where the bicarbonate ions then dissociate to form more hydrogen ions as well as carbonate ions (1, 4).

$$H_2CO_{3\,(aq)} \rightleftharpoons H^+_{(aq)} + HCO^-_{3\,(aq)} \tag{2.16}$$

$$HCO^-_{3\,(aq)} \rightleftharpoons H^+_{(aq)} + CO^{2-}_{3\,(aq)} \tag{2.17}$$

A second mechanism was proposed by Schwenk, who suggested that carbonic acid (H_2CO_3) provides a source of H^+ ions by dissociation which leads to a

cathodic hydrogen evolution reaction, this is known as the buffering effect (1, 4, 45). Equation 2.18 shows the reduction of hydrogen ions which results in the formation of hydrogen gas.

$$2H^{+}_{(aq)} + 2e^{-} \rightarrow H_{2(aq)} \qquad (2.18)$$

However, Crolet proposed that the rate determining step is dependent on the pH. The table produced by Crolet (Figure 2-4) summarizes the anodic dissolution of iron for different pH conditions in a carbon dioxide environment (1).

Reaction No.	Reaction or Equilibrium	pH < 4	4<pH<5	pH> 5
1a	$HCO_3^- \Leftrightarrow (HCO_3^-)_{ads}$	1a	1a	1b
1b	$CO_2+(OH^-)_{ads} \Leftrightarrow (HCO_3^-)_{ads}$			
2	$(HCO_3^-)_{ads} \Rightarrow (HCO_3)_{ads}+e^-$	$\Leftrightarrow$	$\Leftrightarrow$	RDS$\Rightarrow$
3	$(HCO_3)_{ads} \Rightarrow (HCO_3^+)_{ads}+e^-$	$\Leftrightarrow$	RDS[A]$\Rightarrow$	$\Rightarrow$
4	$(HCO_3^+)_{ads}+OH^- \Rightarrow (CO_3)_{ads}+H_2O$	RDS$\Rightarrow$	$\Rightarrow$	$\Rightarrow$
5	$Fe-(CO_3)_{ads}+H_2O \Rightarrow Fe^{++}+HCO_3^-+OH^-$	$\Rightarrow$	$\Rightarrow$	$\Rightarrow$
1 → 5	Tafel slope (mV/log)	60/2 = 30	60/1.5=40	60/0.5= 120
1 → 5	H^+ reaction order	−2	−1	0
1 → 5	CO_2 reaction order	1	1	1

[A] RDS = rate-determining step.

Figure 2-4 Mechanisms proposed by Crolet for the anodic dissolution of iron in a carbon dioxide environment (1)

Due to the clear link between a corrosion reaction, the dissolved CO_2 species and the mass transport of these species to the surface of the steel, it could be argued that the approach to the mechanisms proposed by Crolet are more realistic as compared to the previously mentioned mechanisms. Crolet not only considered the water chemistry but also how the cathodic reaction is influenced by all the dissolved species present. However the cathodic reaction proposed by Schwenk is regarded as the most agreed upon and realistic mechanism for CO_2 corrosion within the corrosion society (1, 2, 4, 38, 45). It is also important to note that even though there may not be complete agreement within the literature as to which of these mechanisms is the most realistic; one thing that all the mechanisms suggest is that the concentrations of the species present (H^+, HCO_3^- and CO_3^{2-}) play a major role in the corrosion process. Factors such as water chemistry and temperature and their effect on the CO_2 corrosion process will be further discussed.

The anodic reaction for carbon dioxide corrosion is known to be the electrochemical dissolution of iron in an aqueous solution (2, 45) as shown by equation 2.19.

$$Fe \rightarrow Fe^{2+} + 2e^{-} \quad (2.19)$$

The anodic reaction for carbon dioxide corrosion has been extensively studied in the past and is regarded as the dominant anodic reaction in CO_2 environments (2, 45).

2.5.2 General and Localised Corrosion

General corrosion sometimes also referred to as uniform corrosion is a type of corrosion which occurs uniformly on a surface without any serious localisation which results in a uniform loss of material across an exposed steel surface (46). It is commonly recognised by a roughened surface and often with corrosion products present on the steel surface (47). Due to the nature of this corrosion attack it is relatively easy to detect and prevent general corrosion unlike other types of corrosion such as localised corrosion. Prevention of this type of corrosion can be made in early design stages by using more expensive corrosion resistant materials and coatings, however mostly depending on the application it is cheaper to use non-corrosion resistant materials in conjunction with corrosion inhibitors (48).

Localised corrosion occurs in discrete locations where there is a very intense attack relative to the rest of the steel surface (49). This type of corrosion attack might occur due to formation of a protective corrosion product or it could be caused by an environmental factor. Due to the nature of this type of corrosion attack it can be quite difficult to detect and therefore also harder to prevent (50). One of the main driving forces for localised corrosion is the smaller anodic surface areas compared to the larger cathodic area. Another driving force could be the corrosive microenvironments which can massively differ from the bulk environment which could influence the initiation and propagation of localised corrosion attacks (49-51). Localised corrosion can be characterised into several types such as crevice corrosion or pitting corrosion. Pitting corrosion is a type of localised corrosion attack which initiates on the free surface of a component. This type of localised attack has been found to be the most serious and dangerous type of attack along with general corrosion (51). Pits can develop in different sizes and shapes depending on the extent of the localised attack (52), as shown by Figure 2-5.

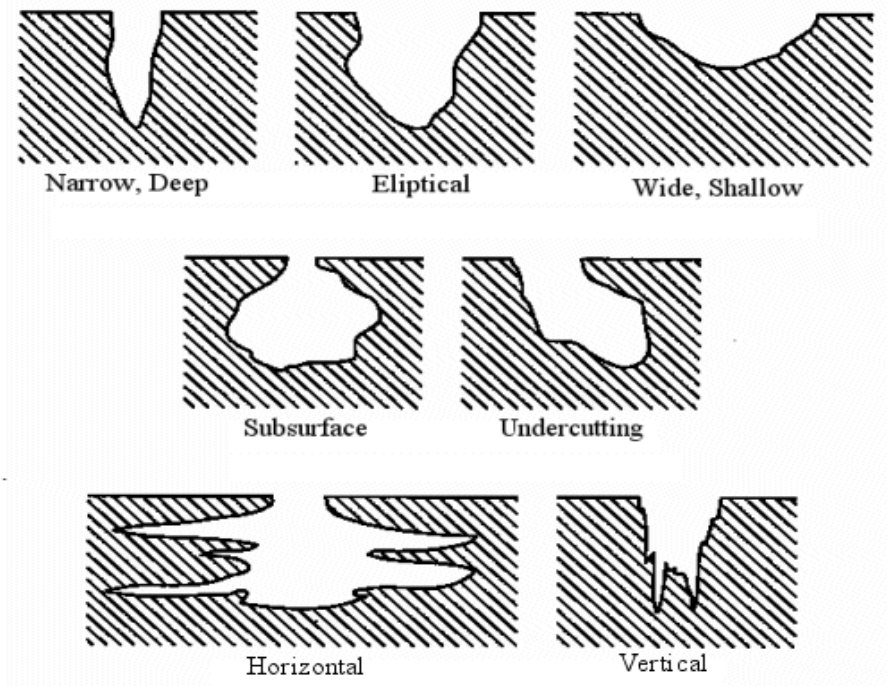

Figure 2-5 ASTM-G46 standard visual rating chart for pitting corrosion (52)

2.6 Corrosion Product Formation in CO_2 Environments

The CO_2 corrosion process of mild steels is greatly influenced by the nature, type, protectiveness and stability of corrosion products (53). The rate of precipitation of corrosion products also plays a major role in the corrosion process. The growth kinetics and morphology of corrosion products are affected by several factors such as brine composition/concentrations, temperature, pH and CO_2 partial pressure. It is therefore possible for the same type of corrosion product to be either protective, semi-protective or in some cases even corrosive (1, 53, 54). It is therefore of great significance to poses knowledge of the different types of corrosion products that occur in CO_2 corrosion processes of mild steels.

2.6.1 Iron Carbide (Fe_3C) Corrosion Products

Iron carbide (Fe_3C) corrosion products, also known as cementite are a common type of non-crystalline corrosion product that can occur in CO_2 environments. Iron carbide corrosion products commonly reveal themselves in the early stages of the corrosion process (1, 55, 56). During the corrosion process of mild steels there is a build-up of dissolved ferrous ions which leaves behind an iron carbide corrosion product film through preferential dissolution of the ferrite phase. Iron carbide films can be extremely adherent to steel substrates however can cause

an acceleration in the corrosion process due to several reasons such as; galvanic coupling, local acidification or by Fe^{2+} enrichment (1). Fe_3C films are also known to be extremely porous and fragile which makes them extremely un-protective however they tend to lead to the precipitation of more protective and crystalline corrosion product layer such as iron carbonate ($FeCO_3$) (1, 56). Images of an iron carbide corrosion product which revealed itself on X65 carbon steel at 80 ºC is provided in Figure 2-6.

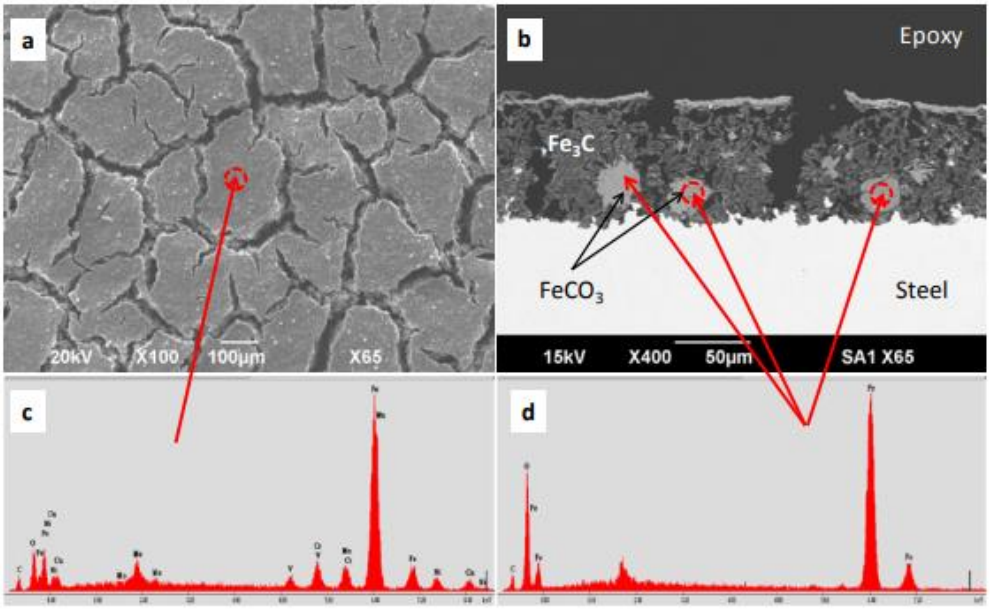

Figure 2-6 Top-view and cross-sectional SEM/EDX of iron carbide corrosion product formed on X65 carbon steel at 80 ºC (56)

2.6.2 Iron Carbonate ($FeCO_3$) Corrosion Products

Iron carbonate ($FeCO_3$) also known as siderite is one of the most commonly occurring and widely studied types of corrosion products in CO_2 environments (1, 4, 54). This type of corrosion product is regarded as one of the most important corrosion products which can precipitate in CO_2 environments due to the protectiveness and stability that it can provide by covering the surface or by acting as a diffusion barrier (57). Formation and growth of $FeCO_3$ is highly dependent upon supersaturation. The precipitation process of $FeCO_3$ consists of two steps; particle nucleation and particle growth. There are several factors that affect the growth and protectiveness of iron carbonate such as temperature, pH, partial pressure of CO_2 (P_{CO2}) and Fe^{2+} concentration (57-59). Increasing temperature can result in larger and more protective iron carbonate crystals to precipitate onto a steel surface. This generally results in a lower film porosity and

improved surface coverage which can result in a greater reduction of the corrosion rate. A greater bulk solution pH can also increase the precipitation rate of $FeCO_3$ by decreasing its solubility (1, 57, 59). An image of a $FeCO_3$ corrosion product precipitated at 80 ºC on X65 carbon steel is provided in Figure 2-7.

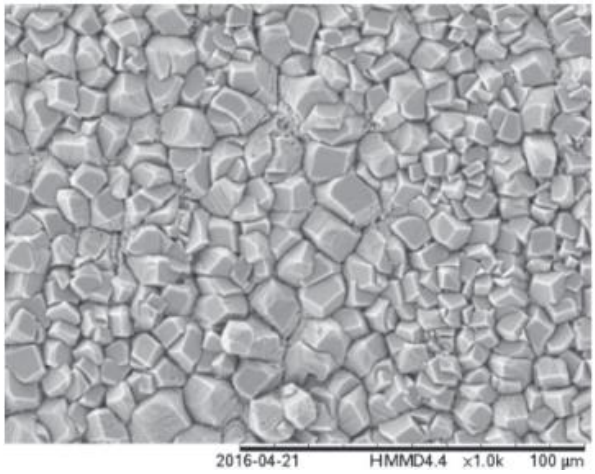

Figure 2-7 Top-view SEM image of iron carbonate corrosion product precipitated on X65 carbon steel at 80 ºC (60)

For $FeCO_3$ to be able to precipitate in a CO_2 environment the product of the Fe^{2+} and CO_3^{2-} concentrations must exceed the solubility product (K_{SP}) (57). The solubility product can be defined as follows;

$$K_{SP} = [Fe^{2+}]_{eq}[CO_3^{2-}]_{eq} \tag{2.20}$$

The solubility product of iron carbonate can be calculated using 3 different correlations; the Greenberg and Tomson (G&T) correlation, Johnson and Tomson (J&T) correlation or using the Sun and Nesic (S&N) correlation (57).

The Greenberg and Tomson (G&T) correlation:

$$log_{10}K_{SP} = -59.2385 - 0.041377(T) - \frac{2.1963}{(T)} + 24.5724log_{10}(T) \tag{2.21}$$

Where T is temperature in Kelvin.

The Johnson and Tomson (J&T) correlation:

$$log_{10}K_{SP} = -0.4343\left(\frac{-30140}{8.314(T + 273.15)} + 36.22\right) \tag{2.22}$$

Where T is temperature in Celsius.

The Sun and Nesic (S&N) correlation:

$$log_{10}K_{SP} = -59.2385 - 0.041377(T) - \frac{2.11963}{(T)} + 24.5724log_{10}(T) + 2.518I^{0.5} - 0.6578I \quad (2.23)$$

Where T is temperature in Kelvin and I is the solution ionic strength.

The solubility product can be used for determining the saturation level (S) which is the driving force for iron carbonate precipitation (57), and is defined as follows;

$$S = \frac{[Fe^{2+}][CO_3^{2-}]}{K_{SP}} \quad (2.24)$$

The saturation level can be used to determine whether a particular system is saturated or under-saturated (57). When the saturation level is < 1 then the system is under-saturated. In a scenario as such, iron carbonate will not precipitate however if iron carbonate is already present on a steel surface then it will start to dissolve as shown by equation 2.25. When S > 1 the system is saturated and iron carbonate will precipitate according to equation 2.26 (57-59).

When S < 1:

$$Fe + 2H_2CO_3 \rightarrow Fe^{2+} + H_2 + 2HCO_3^- \quad (2.25)$$

When S > 1:

$$Fe + H_2CO_3 \rightarrow FeCO_3 + H_2 \quad (2.26)$$

The protectiveness of an iron carbonate corrosion product layer can be estimated using the concept of scaling tendency (ST). The scaling tendency is the ratio of the precipitation rate of iron carbonate to the corrosion rate (57, 61) and is given by equation 2.27.

$$ST = \frac{P_{FeCO3}}{CR} \quad (2.27)$$

A scaling tendency of < 1 suggest that the precipitated corrosion product layer will be porous and un-protective while a scaling tendency > 1 suggests precipitation of a protective corrosion product layer (57, 61).

2.6.3 Iron Oxide (Fe_3O_4) Corrosion Products

Iron oxides such as magnetite (Fe_3O_4) have been found to be in some cases extremely protective corrosion products which can greatly reduce uniform

corrosion rates by precipitating in between iron carbonate crystal boundaries, however they have also been found to lead to severe localised corrosion (62, 63). Iron oxides such as magnetite have generally been found to precipitate on mild steels exposed to high pressure environments. Dissolved oxygen has also been found to prevent the precipitation of protective iron carbonate corrosion products by ferrous ion oxidation to form ferric ions which ultimately results in the precipitation of non-protective iron oxides (62, 63). Other types of iron oxides also exist such as goethite and hematite. These iron oxides have been found to precipitate in brines that are nearly saturated by dissolved oxygen. Goethite and hematite are unstable iron oxides which will eventually transform to a more stable state being magnetite (62-64).

2.6.4 Calcium Carbonate ($CaCO_3$) Corrosion Products

Calcium carbonate ($CaCO_3$) corrosion products can occur in three different mineral forms; Aragonite, Calcite and Vaterite (65). $CaCO_3$ has a higher solubility product compared to $FeCO_3$ and is therefore less stable and less protective than $FeCO_3$. Aragonite and Vaterite are both metastable phases of $CaCO_3$, however Vaterite being the least stable with a greater solubility than both Aragonite and Calcite which means that in an H_2O environment Vaterite will transform into either Aragonite or Calcite depending on the environmental conditions (65, 66). Aragonite is less stable than calcite however only converts into Calcite at extremely high temperatures (67). An SEM image of calcium carbonate corrosion products is provided in Figure 2-8.

Calcium carbonate precipitates onto a steel surface according to equation 2.28.

$$Ca^{2+} + CO_3^{2-} \rightarrow CaCO_3 \qquad (2.28)$$

The solubility product for calcium carbonate can be determined using the following correlation (68);

$$log_{10}K_{SP} = -1228.732 - 0.299444(T) + \frac{35512.75}{(T)} + 485.818\log(T) \qquad (2.29)$$

Where T is temperature in Kelvin.

The solubility product can once again be used for determining the saturation level (S) which is the driving force for calcium carbonate precipitation (68), and is defined as follows;

$$S = \frac{[Ca^{2+}][CO_3^{2-}]}{K_{SP}} \tag{2.30}$$

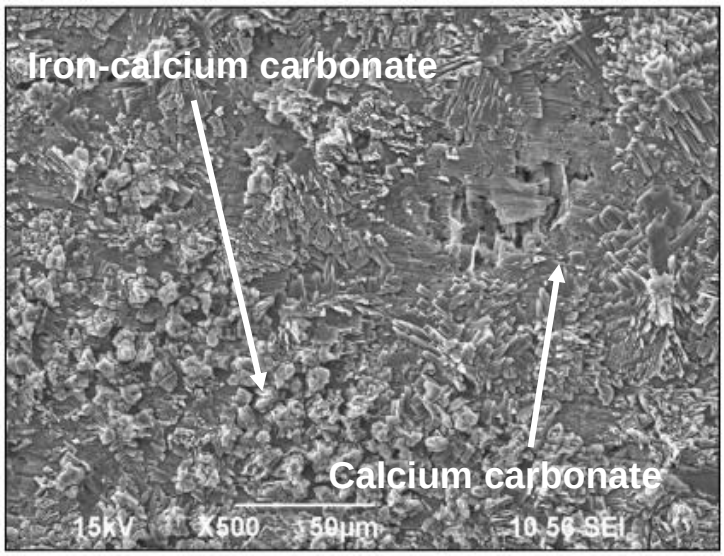

Figure 2-8 Top-View SEM image of iron-calcium carbonate and calcium carbonate corrosion products precipitated at 80 ºC in CO_2 environment (69)

2.6.5 Iron-Calcium Carbonate ($FeCaCO_3$) Corrosion Products

Iron-calcium carbonate is a mixed carbonate corrosion product which forms in CO_2 environments containing calcium ions. Calcium carbonate and iron carbonate are isostructural which means that Ca^{2+} can incorporate into an iron carbonate crystal lattice or Fe^{2+} can incorporate into a calcium carbonate crystal lattice to form a more complex mixed iron-calcium carbonate ($Fe_xCa_yCO_3$) where (x+y=1) (67, 68, 70). The resulting iron-calcium carbonate structure has different chemical and morphological properties compared to both iron carbonate and calcium carbonate. However, the properties and protectiveness of iron-calcium carbonates are not fully understood due to a lack of research and due to their complexities (67, 68, 70). An image of iron-calcium carbonate corrosion products is provided in Figure 2-8.

2.7 Factors Controlling the CO_2 Corrosion Process

There are several factors that can influence CO_2 corrosion processes such as temperature, pH, CO_2 partial pressure (P_{CO2}), flow, water chemistry, surface wettability, presence of corrosion products etc. Some of these parameters are dependent on each other and may therefore have major effects on the overall corrosion behaviour (71).

2.7.1 Effect of Temperature on CO_2 Corrosion

Temperature has a major effect on the CO_2 corrosion behaviour due to its influence on the rates of electrochemical reactions and ultimately on the rate of corrosion product formation (71, 72). Increasing temperature results in an increase in the rates of chemical and electrochemical reactions and on the rate of diffusion of species. It can also increase the rate of reaction of corrosion products which tend to become more protective with increasing temperature and time, resulting in a reduction in the corrosion rate (2, 71). This is related to the corrosion product solubility which decreases with increasing temperature which results in the formation of more protective and adherent corrosion products. Figure 2-9 shows how the corrosion rate tends to initially increase with temperature up to a critical point due to acceleration of electrochemical reactions after which protective or partially protective corrosion products precipitate which results in a reduction in the corrosion rate (2, 71-74).

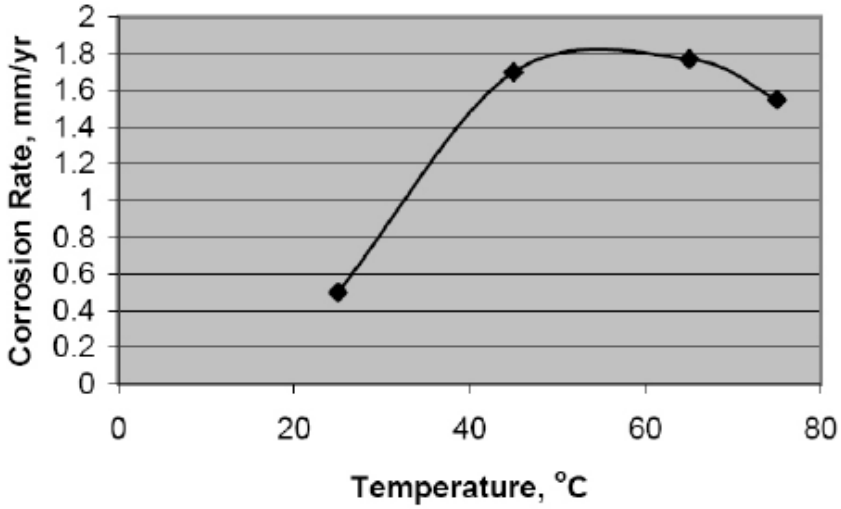

Figure 2-9 Corrosion rate as a function of temperature for X70 steel in CO2 saturated brine (71)

2.7.2 Effect of CO_2 Partial Pressure on CO_2 Corrosion

Carbon dioxide partial pressure has been found to have different effects on CO_2 corrosion behaviours depending on the environment (71). In film-free conditions i.e. when there is no precipitation of corrosion products, increasing CO_2 partial pressure generally results in an increase in the corrosion rate due to a reduction in the bulk solution pH and due to the increasing rate of carbonic acid reduction (71, 75), as shown by Figure 2-10. However, in film forming conditions increasing CO_2 partial pressure can result in a reduction in the corrosion rate due to the precipitation of protective or partially protective corrosion products which result in a reduction in the availability of cathodic sites (75, 76).

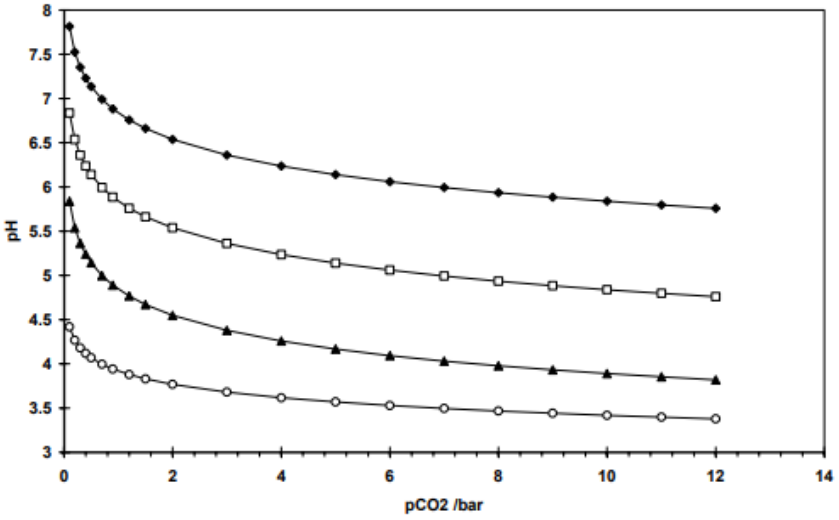

Figure 2-10 Effect of CO_2 partial pressure on bulk solution pH (75)

2.7.3 Effect of Bulk Solution Chemistry/pH on CO_2 Corrosion

As previously discussed the solution chemistry can have a major influence on the types of corrosion products which precipitate onto carbon steel surfaces. For example, the presence of calcium or magnesium cations (Ca^{2+} and Mg^{2+}) in addition to sodium chloride (NaCl) can influence the corrosion product type/morphology which precipitates, which will in turn influence the protectiveness of the corrosion product layer. This can in turn have an influence on the localised corrosion behaviour (67, 68, 70, 71). For example, the addition of calcium chloride ($CaCl_2$) to sodium chloride (NaCl) based brine can promote the precipitation of $Fe_xCa_yCO_3$ and $CaCO_3$ rather than the more common $FeCO_3$ corrosion product. The change in the corrosion product composition could promote more porous and less compact corrosion products to precipitate which

could result in an increase in the general corrosion rate, localised corrosion rate or even both (67, 68, 70). The solubility of corrosion products such as $FeCO_3$ is highly dependent on the bulk solution and surface pH (75) which is why the precipitation of protective corrosion products occurs more readily at higher temperatures. However higher bulk solution pH (low acidity) can cause the reduction of dissolution rates of corrosion products which results in the reduction of corrosion rates (formation of corrosion products) at lower temperatures (2, 71, 75). This is due to the fact that the Fe^{2+} concentration required to reach $FeCO_3$ saturation, decreases with increasing bulk solution pH as shown by Figure 2-11. The bulk pH is also a function of the CO_2 partial pressure, where decreasing CO_2 partial pressure results in an increase in the solution pH which in turn causes a decrease in the corrosion rate due to the precipitation of protective corrosion products (75).

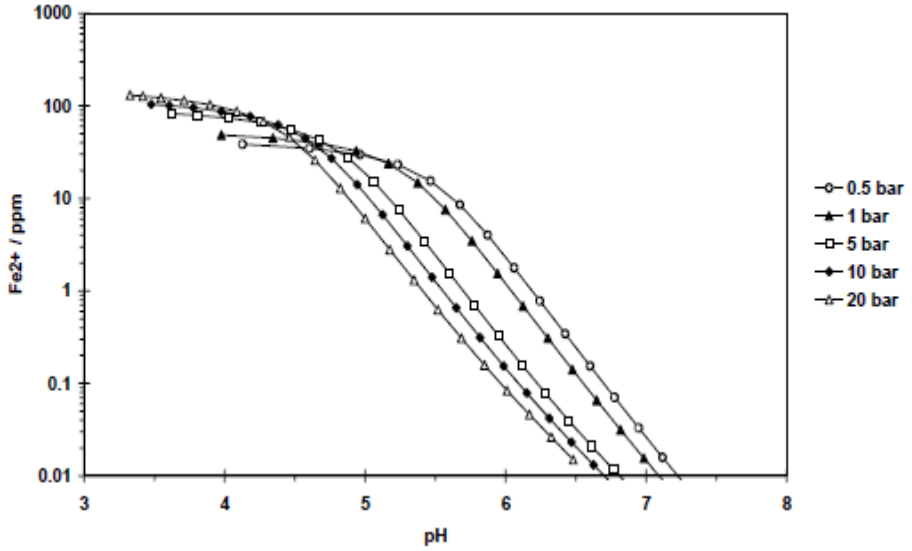

Figure 2-11 Fe^{2+} required to reach iron carbonate saturation as a function of pH for different CO_2 partial pressures (75)

2.7.4 Effect of Fluid Flow on Corrosion Products in CO_2 Environments

Increased flow causes a gradual increase in the corrosion rate until a critical flow intensity is reached, as shown by Figure 2-12. This is caused by a reduction in the supersaturation which causes a reduction in the precipitation rate of corrosion products (71). Once the critical flow intensity is reached the shear stress becomes very high which causes the dissolution/destruction of corrosion products which can also result in the prevention of re-precipitation of corrosion

products onto a steel surface. The near wall turbulence which results in the destruction of corrosion products can also result in an increase in the localised corrosion rate (71, 77, 78).

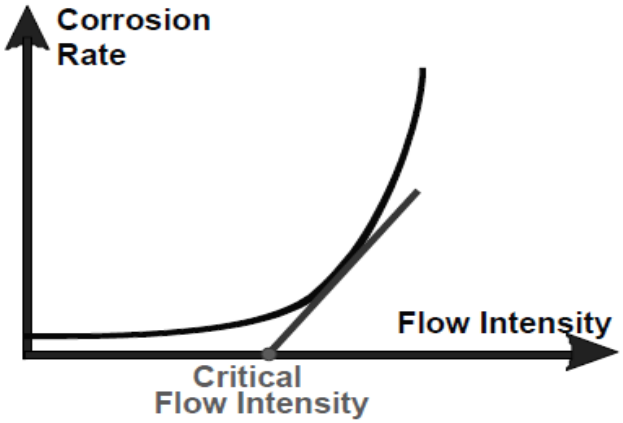

Figure 2-12 Effect of flow intensity of corrosion behaviour (71)

2.8 Application of CO_2 Corrosion Inhibitors

2.8.1 Application of Corrosion Inhibitors in the Oil/Gas Industry

Mitigation of corrosion using corrosion inhibitors is a major solution in dealing with severe corrosion problems within the oil and gas industry (79). This is due to the relative affordability as opposed to using more expensive corrosion resistant materials. Severe corrosion problems encountered during either upstream or downstream oil and gas processes can be mitigated efficiently by continuous injection, batch dosing or through squeeze treatments of relatively small dosages of corrosion inhibitors (24). The effective use of a corrosion inhibitor is dependent upon several factors such as type of flow and flow rates, water to oil ratio, presence of gases (O_2, CO_2 or H_2S), temperature and pre-existing corrosion. Corrosion inhibitors are in essence chemical agents and can therefore also chemically breakdown with time which can also result in a decrease in their efficiency (80, 81). The influence of process parameters on corrosion inhibition along with appropriate measures of action (80, 81) are summarised in Figure 2-13.

Parameter	*Change*	*Action*
Flow rates (oil/water/gas)	+ or -	Alter CI delivery rate to maintain concentration in the water
Water cut	+ or -	May increase or decrease CI delivery depending on its o/w partitioning properties
Temperature	+ -	Increase [CI] Scope to reduce [CI]
pCO_2 and pH_2S in gas	+ -	Increase [CI] Scope to reduce [CI]
pO_2 in gas	+	May need to reselect CI
pH	+ -	Scope to reduce [CI] Increase [CI], may need to reselect
Sand	+	Reselect CI and/or increase [CI], reduce velocity, install downhole sand screen

Figure 2-13 Process parameters that influence corrosion inhibition and their appropriate measure of action (80, 81)

2.8.2 Types of CO_2 Corrosion Inhibitors

As previously mentioned, there are strict regulations especially in European countries as to which type of corrosion inhibitors can be used within the oil and gas industry. As a result, organic corrosion inhibitors are becoming more popular due to the rise of recent environmental standards and regulations (80, 82). Corrosion inhibitors are generally classified based on their chemical nature as either organic or inorganic, as shown in Figure 2-14. Inorganic corrosion inhibitors can be further classified as either anodic or cathodic depending on their mechanism of action. Organic corrosion inhibitors tend to have combined mechanisms of action where they can be both anodic and cathodic, however generally operate by adsorption of a protective film (79, 80, 82, 83).

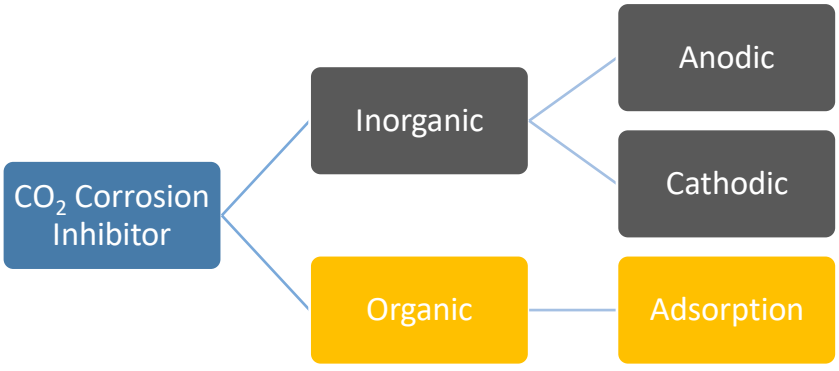

Figure 2-14 Types of corrosion inhibitors for oil and gas applications

2.8.3 Corrosion Inhibitor Mechanisms

Corrosion inhibitors may have more than one mechanism of action which generally includes at least one of the following (82, 83);

- Chemical adsorption (chemisorption) of inhibitor onto steel surface to form a thin protective film.
- Corrosion inhibitor results in the formation of a protective oxide film onto the steel surface.
- Reaction between corrosion inhibitor and corrosive components within a particular system.

Anodic inorganic corrosion inhibitors reduce the anodic reaction by blocking the anodic reaction and by assisting in the natural passivation of a steel surface (82). This type of corrosion inhibitor can also result in the adsorption of a protective film which can react with corrosion products to form an insoluble protective film on the steel surface. The reaction between metallic ions (produced at the anode) with the inhibitor results in hydrolysis of the corrosion inhibitor which results in the formation of hydroxide anions (OH^-) (82, 83), as shown by Figure 2-15(a). The use of anodic inorganic corrosion inhibitors result in a positive shift in the corrosion potential and a reduction in the corrosion current as shown in Figure 2-15(b). The optimum dosage is of extreme importance for anodic inorganic corrosion inhibitors as inappropriate concentrations can result in poor film coverage which can result in localised corrosion (82, 83).

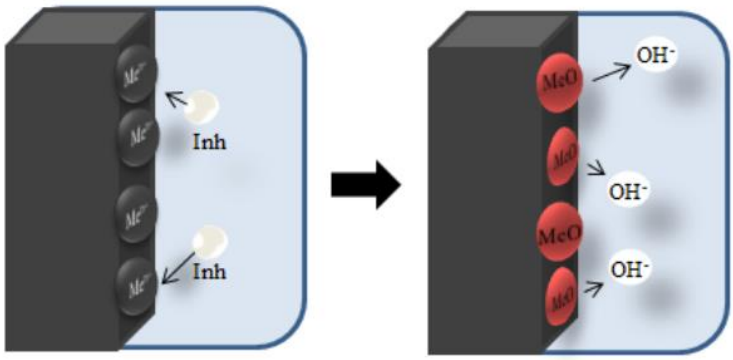

(a)

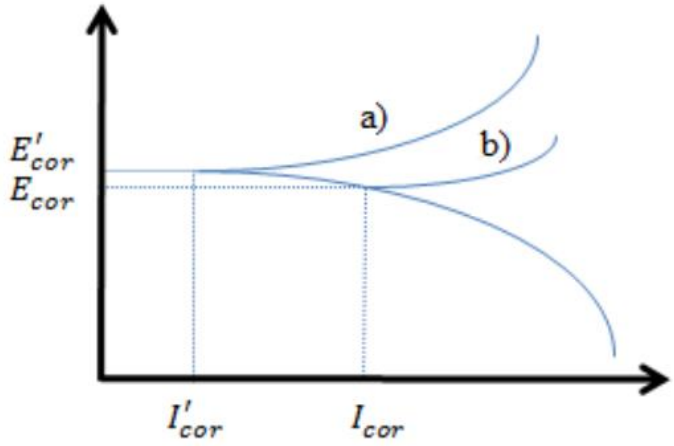

(b)

Figure 2-15 (a) Mechanism of action and (b) electrochemical behaviour for anodic inorganic corrosion inhibitors, where E_{cor} and I_{cor} are the corrosion potential and current respectively in the absence of the inhibitor and E'_{cor} and I'_{cor} are the corrosion potential and current respectively in the presence of the corrosion inhibitor (82)

Cathodic inorganic corrosion inhibitors operate by preventing cathodic reactions at the steel surface. They achieve this by producing insoluble compounds which selectively precipitate onto cathodic sites (83). This results in the deposition of a compact and adherent film onto the steel surface which limits diffusion of species in these areas. The created film acts as a barrier which limits contact between the steel surface and the surrounding environment. As a result of their mechanism, this type of corrosion inhibitor is independent of its concentration which makes them safer to use as compared to anodic inorganic corrosion inhibitors (82, 83). Figure 2-16(a) shows the mechanism of action whereby the ions of the inhibitor, such as magnesium reacts with the hydroxyl present within the water to form insoluble hydroxides such as $Mg(OH)_2$ (82). Cathodic inorganic corrosion inhibitors result in a negative shift in the corrosion potential and corrosion current, as shown by Figure 2-16(b).

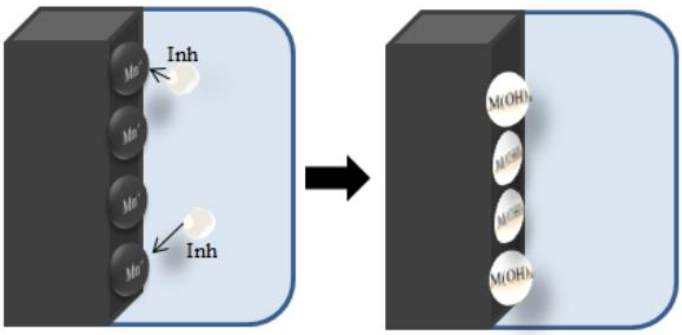

(a)

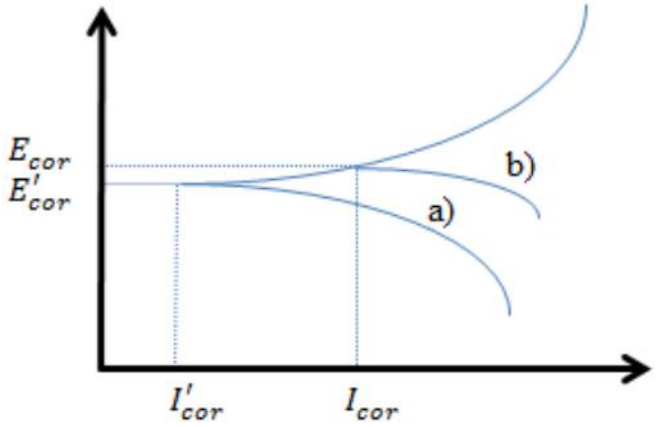

(b)

Figure 2-16 (a) Mechanism of action and (b) electrochemical behaviour for cathodic inorganic corrosion inhibitors, where E_{cor} and I_{cor} are the corrosion potential and current respectively in the absence of the inhibitor and E'_{cor} and I'_{cor} are the corrosion potential and current respectively in the presence of the corrosion inhibitor (82)

As previously mentioned, organic corrosion inhibitors can act as either anodic, cathodic or mixed anodic and cathodic inhibitors however they all operate by adsorption of protective films onto a steel surface (82, 83). Organic corrosion inhibitors have lower environmental and health and safety risks compared to inorganic corrosion inhibitors and are becoming more popular due to the introduction of strict regulations regarding the chemistry of corrosion inhibitors. Organic corrosion inhibitors operate by adsorption of molecules onto steel surfaces to form extremely protective and hydrophobic films as shown by Figure 2-17(a). The hydrophobic film provides a barrier between the steel surface and the corrosive electrolyte (79, 80, 82, 83). Organic corrosion inhibitors cause a reduction in the corrosion current as shown by Figure 2-17(b).

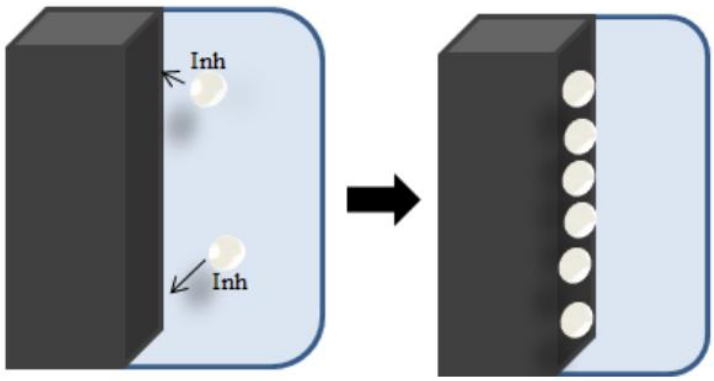

(a)

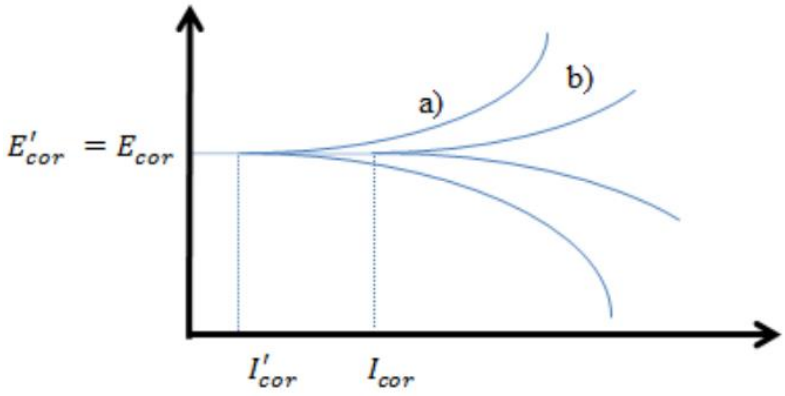

(b)

Figure 2-17 Mechanism of action (a) and electrochemical behaviour (b) for organic corrosion inhibitors, where E_{cor} and I_{cor} are the corrosion potential and current respectively in the absence of the inhibitor and E'_{cor} and I'_{cor} are the corrosion potential and current respectively in the presence of the corrosion inhibitor (82)

2.9 Corrosion Product Characteristics and Growth Kinetics

The growth kinetics and characteristics of corrosion products in CO_2 environments has been documented by several authors (32, 72, 74, 84-91). Factors such as temperature, CO_2 partial pressure and brine chemistry have been widely evaluated with respect to the type and overall protectiveness of corrosion products. These studies are extremely important as environmental conditions can have major effects on precipitation kinetics and characteristics of corrosion products, and as a result a great influence on the overall corrosion behaviour. The knowledge obtained from these studies are not only important in terms of protectiveness of corrosion products but also help set a basis for the

understanding of how corrosion products interact with corrosion inhibitors. The following sub chapters provide an extensive literature review of relevant literature regarding the characteristics and growth kinetics of corrosion products such as $FeCO_3$, $CaCO_3$ and $Fe_xCa_yCO_3$. A summary of the main findings within the existing literature is provided at the end of this chapter.

2.9.1 Iron Carbonate ($FeCO_3$) Corrosion Products

The mechanism of corrosion product precipitation was evaluated by Dugstad *et al* (91) using a methodology which covered a temperature range of 40-120˚C, flow rates between 0.1 and 7 m/s, CO_2 partial pressure's between 1.8 and 2.6 bar for a bulk solution pH between 5.5 and 6. The experiments were conducted using a high pressure one-phase flow loop integrated with *in-situ* electrochemical measurements. Other techniques such as weight loss and scanning electron microscopy were also used to confirm and analyse the corrosion products present on the steel surfaces. Using this methodology, Dugstad *et al* (91) was able to evaluate 4 different types of carbon steels simultaneously. Findings indicated that the rate of precipitation of corrosion products increased with increasing temperature as shown by Figure 2-18, and that the morphology of corrosion products is dependent upon both temperature and steel microstructure.

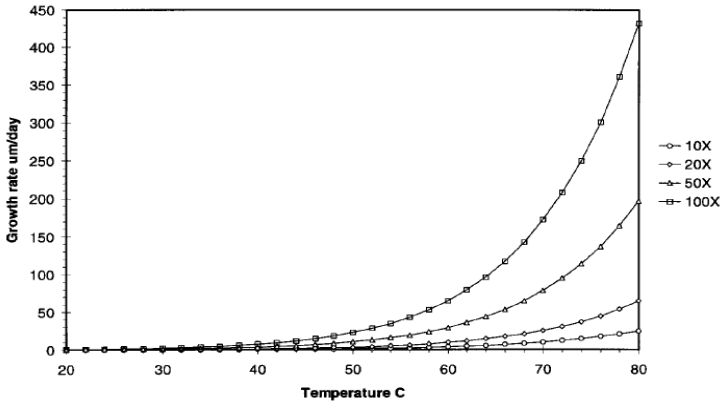

Figure 2-18 Calculated growth rate of iron carbonate as a function of temperature for different supersaturation (91)

Further findings indicated that at temperatures above 60˚C, dense and protective corrosion product layers had precipitated onto the steel surfaces however corrosion products were found to be more protective at 80 ˚C as compared to 120˚C. Further findings indicated that it could take 2-3 days until substantial

precipitation takes place and that corrosion products can be very porous when precipitated at low temperatures (based on visual observations). The porosity was found to be decreasing with increasing experimental temperature (91).

The effect of temperature, CO_2 partial pressure and type of steel on the morphology of corrosion products was investigated by Lin *et al* (90). This was achieved by conducting two different types of experiments; one where temperature was varied at a fixed CO_2 partial pressure between 1.38-2.07 MPa and one where pressure was varied at a constant temperature of 90˚C. The tests were conducted in autoclaves under static conditions for durations of 96 hours using simulated brines with properties similar to oil field brines. Three types of steels were tested during these experiments; N80, P110 and J55 steel. The steel surfaces were evaluated post-test test using SEM, XRD and XPS. The findings gathered by Lin *et al* (90) indicated that the maximum thickness and largest crystal grain sizes of corrosion products had precipitated at 120˚C, whereas the most compact corrosion products with the smallest crystal grain sizes had precipitated at temperatures ranging from 160 ˚C to 180 ˚C (Figure 2-19).

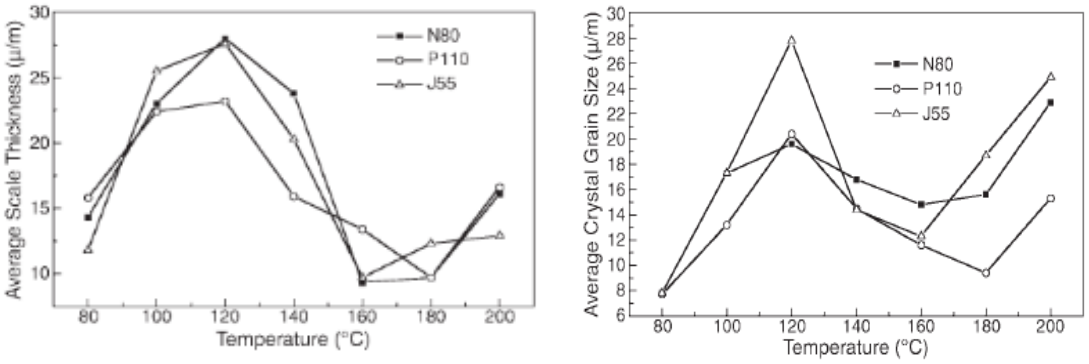

(a) **(b)**

Figure 2-19 (a) Effect of temperature on corrosion product thickness and (b) on crystal grain size for different types of steel (90)

Further findings by Lin *et al* (90) indicated that the corrosion products consisted mainly of iron carbonate ($FeCO_3$) however some $CaCO_3$, Fe_3C and Fe_3O_4 corrosion products were also identified. Duplex structured corrosion products which consisted of a thin inner layer and a thicker outer layer were also identified using SEM. The influence of pressure on corrosion product characteristics and morphology was also evaluated and Lin *et al* (90) reported that at high pressures, the precipitated corrosion product crystal grains are finer, denser and more

irregular which reduces the risk of pitting due to solution passage through interfaces to the substrate (Figure 2-20). It was concluded that both the thickness and crystal grain size increase with temperature up to 120˚C, then decrease up to a temperature of 160˚C and then finally start to increase once again.

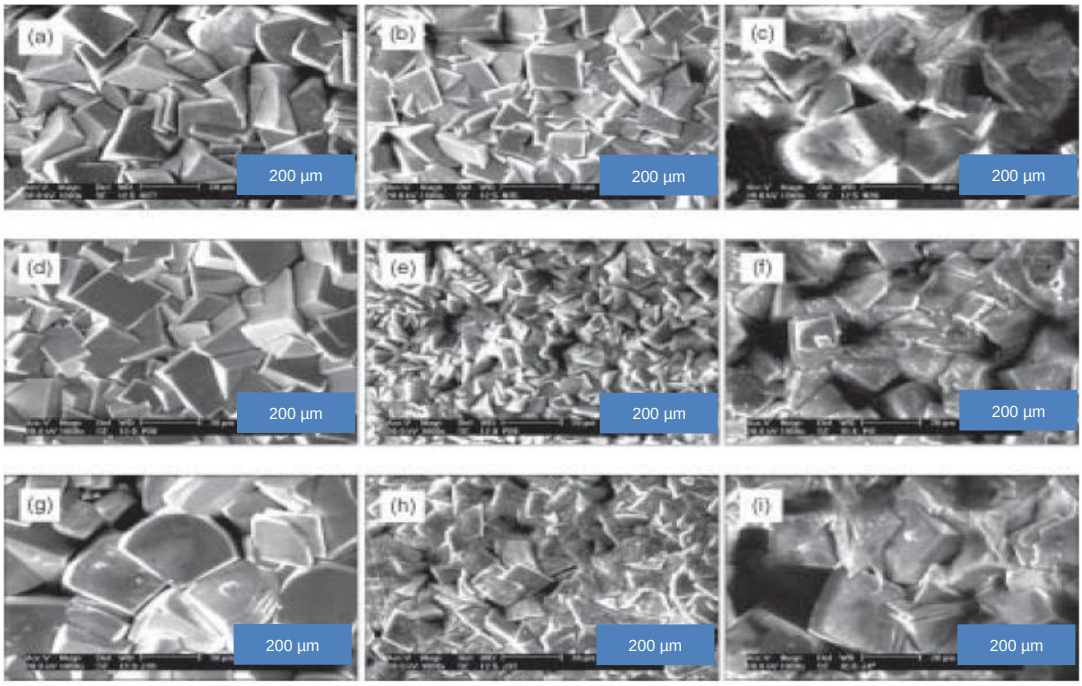

Figure 2-20 Top-view SEM images for N80 steel at (a) 120 ˚C, (b) 160 ˚C and (c) 200 ˚C, for P110 steel at (d) 120 ˚C, (e) 180 ˚C and (f) 200 ˚C, for J55 steel at (g) 120 ˚C, (h) 160 ˚C and (i) 200 ˚C (90)

The kinetics of $FeCO_3$ precipitation on X65 carbon steel in CO_2 saturated environments was investigated by Sun *et al* (89) using a glass cell set-up. The corrosion tests were conducted at a temperature range of 60-90˚C in stagnant conditions using a simple brine consisting of 1 wt.% NaCl in distilled water. A set of experiments was conducted at a specified temperature range for different supersaturations using weight gain/loss and porosity calculations. The results gathered by Sun *et al* (89) at 80 ˚C indicated that the precipitation rate of iron carbonate decreased steadily with time due to decreasing supersaturation as shown by Figure 2-21.

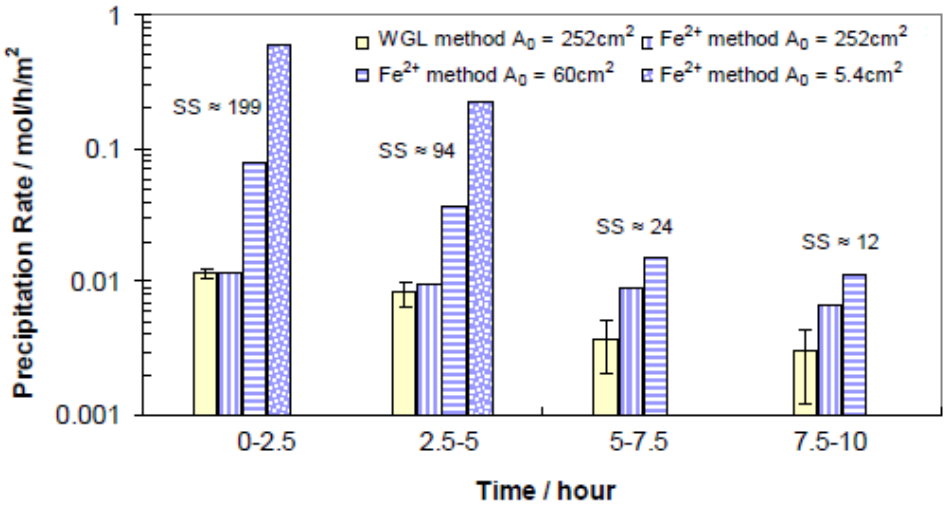

Figure 2-21 Precipitation rate vs time comparison plot using different techniques (89)

Further findings indicated that both the scaling tendency and the surface coverage of corrosion products increased with increasing temperature resulting in the precipitation of more protective corrosion products (89). It was also observed that corrosion products become denser and therefore more protective with increasing exposure periods. These results are consistent with findings by Lin *et al* (90). Sun *et al* (89) concluded that the precipitation rate of corrosion products is a function of both temperature and supersaturation. Sun et al (89) also calculated the porosity of the iron carbonate corrosion products after different exposure periods for the whole temperature range, however did not provide any analysis for these results or mention whether this was an averaged porosity calculation based on visual observations or a more complex 3D porosity of the corrosion product layer. However, the porosity calculations did indicate that the porosity increased with increasing temperature up to 80˚C and then slightly decreased at 90˚C after 5 hours of exposure (89) which is consistent with findings by Dugstad *et al* (91).

Han *et al* (88) examined the chemistry and structure of protective corrosion products using a glass cell experimental set-up containing a simple brine consisting of 1 wt.% NaCl in distilled water. The tests were conducted at 80˚C, pH 8.0 using X65 and C1018 carbon steels. Linear polarization resistance (LPR) was used to monitor the corrosion rate, while scanning transmission electron microscope (STEM), energy dispersive X-ray spectroscopy (EDX), grazing incidence x-ray diffraction (GIXRD) and focused ion beam (FIB) were used post-

test to analyse the morphology and characteristics of corrosion products. Findings by Han *et al* (88) indicated that the corrosion rate had been reduced by 50%, down to 0.5mm/year within the first 3 hours of exposure to the experimental brine, indicating that a protective corrosion product was precipitating onto the steel surface. Using GIXRD it was found that 99.6% of the corrosion product consisted of $FeCO_3$ and the remaining 0.4% consisted of Fe_3O_4 as shown by Figure 2-22. The relatively small amount of iron oxide could not be detected by XRD alone, however it could be confirmed using STEM and EDX. It was found that the Fe_3O_4 was not a continuous corrosion product layer however located at $FeCO_3$ crystal boundaries. It was concluded that the iron oxide layer had passivated the steel surface. These results are not consistent with findings by other authors, however some techniques such as GIXRD and STEM are rarely used by others. It could also be argued that the results provided by GIXRD are not sufficient to prove the presence of Fe_3O_4 as the passive layer. Furthermore, two different types of carbon steel were used for different parts of analysis during these experiments which may have affected the corrosion product type/morphology as observed by Lin *et al* (90), however the reason behind this methodology was not detailed.

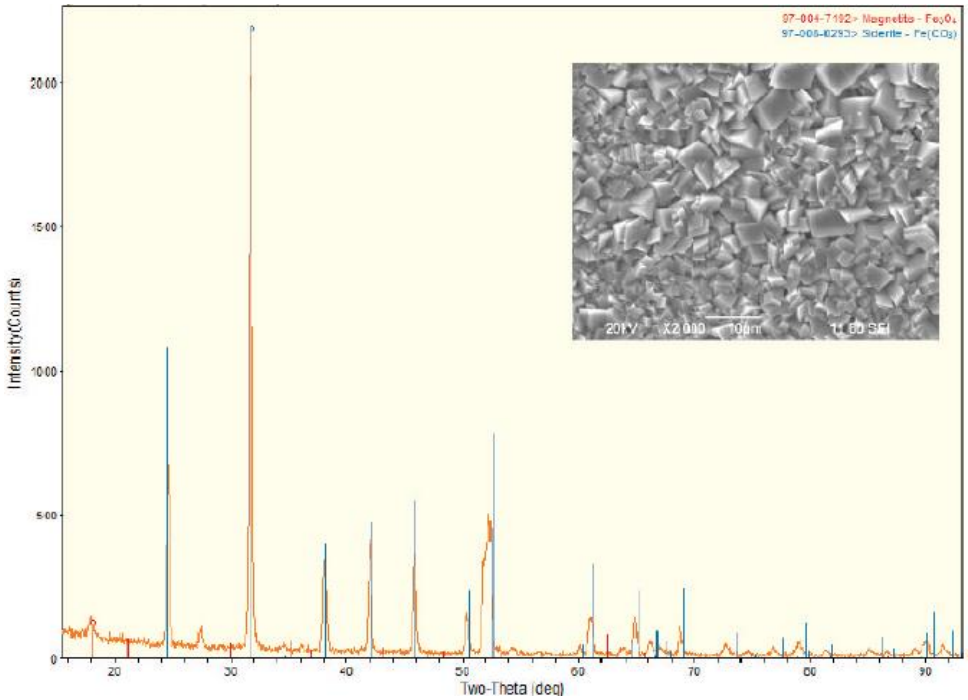

Figure 2-22 GIXRD plot with an SEM image of steel surface covered by corrosion products for an exposure time of 65 hours (88)

Yin *et al* (74) conducted a series of experiments using autoclaves to evaluate the effect of temperature on corrosion product layers. These experiments were conducted on P110 carbon steel at temperatures ranging from 50-180˚C in autoclaves pressurised with carbon dioxide (partial pressure of 4 MPa). The experiments were conducted in static conditions using a complex brine consisting of 165 g/L NaCl, 1.3 g/L $CaCl_2$ and 12.6 g/L $MgCl_2.6H_2O$ in distilled water. The thickness, morphology and structure of the precipitated iron carbonate corrosion products were assessed post-test using weight loss, SEM, XRD, XPS and EDS analysis. It was reported that both thickness and porosity of precipitated corrosion product layers decreased with increasing temperature which resulted in a reduction in the corrosion rate as shown by Figure 2-23. These findings are consistent with findings by both Dugstad *et al* and Lin *et al* (90, 91).

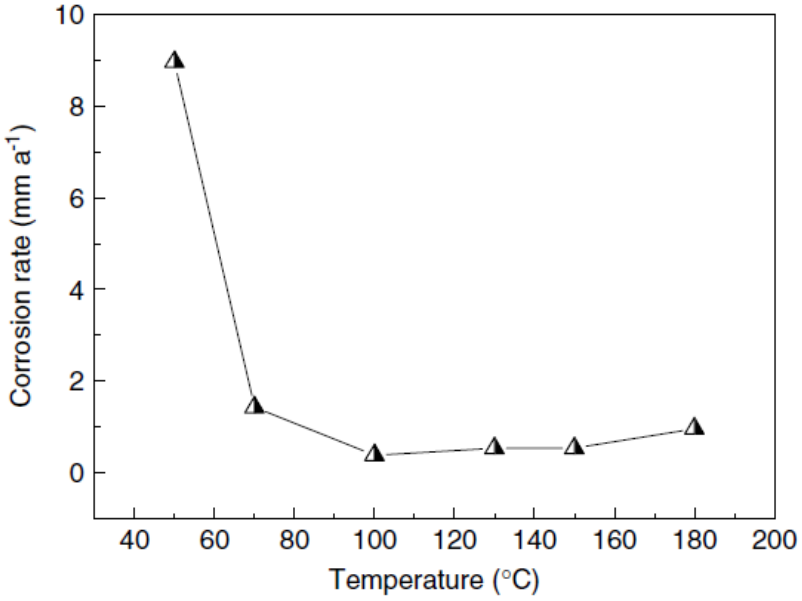

Figure 2-23 Corrosion rate plot gathered by weight loss for different temperatures (74)

Further findings by Yin *et al* (74) indicated that the smallest crystal grain sizes had precipitated at 100˚C whereas the largest crystal grain sizes were observed at 150˚C, as shown by Figure 2-24. These findings are not consistent with results gathered by Lin et al (90), however the autoclave experimental pressure was greater in the experiments conducted by Yin *et al* (74) which may have had an influence on the difference in results obtained by the two authors. It was also reported that at a temperature of 180˚C, the crystals are adherent to each other

with no visual pores in between. Yin *et al* (74) concluded that two types of corrosion products can be observed; thick, porous and non-adherent or thin, dense and adherent. Yin *et al* (74) also indicated that Fe_3C and Fe_3O_4 corrosion products were identified at both low and high temperatures. Although the exact temperatures at which these corrosion products were identified was never mentioned, however these results are consistent with findings by Han *et al* (88).

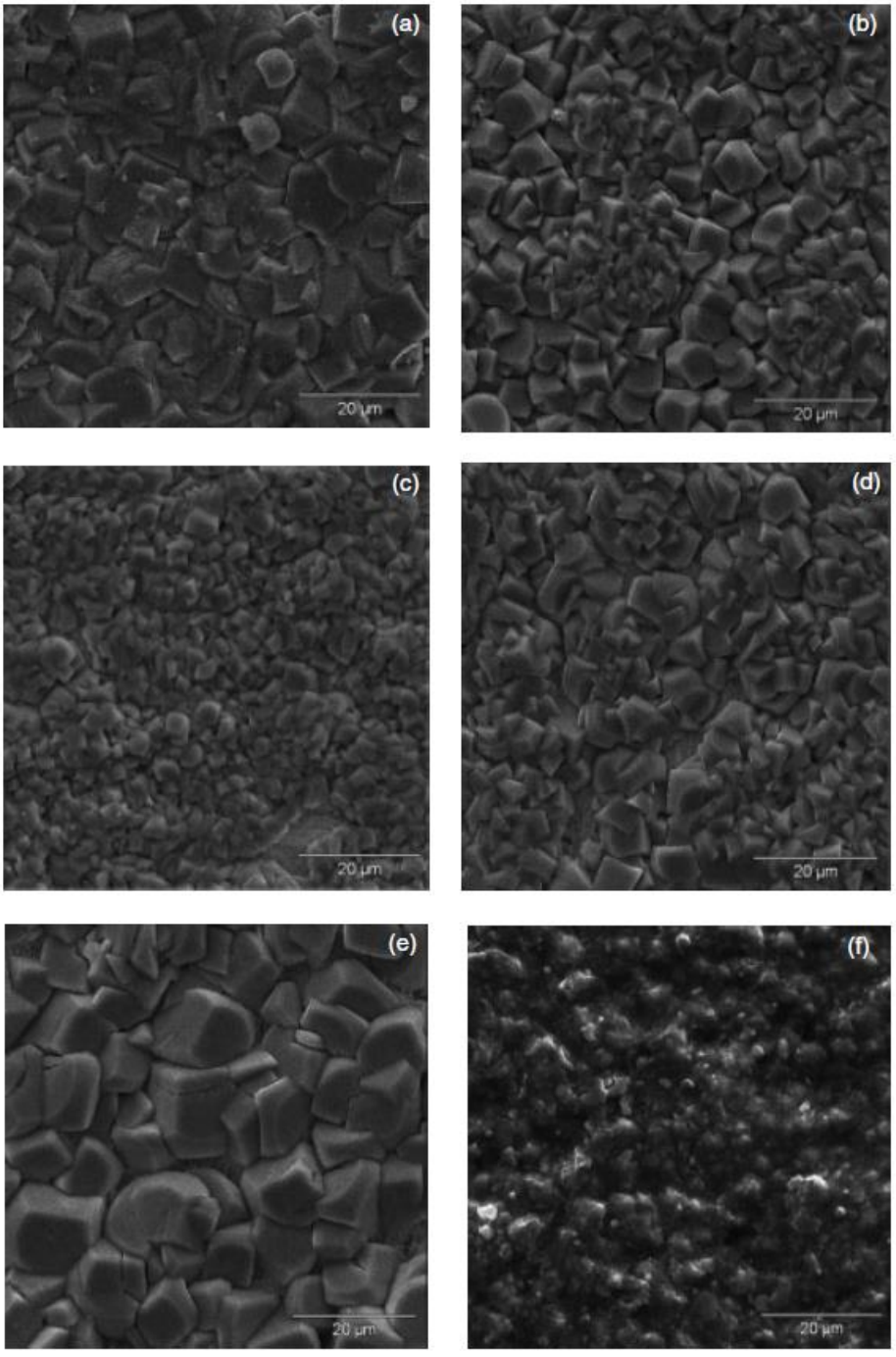

Figure 2-24 Top-view SEM images of corrosion products at (a) 50˚C, (b) 70˚C, (c) 100˚C, (d) 130˚C, (e) 150˚C and (f) 180˚C (74)

The effect of temperature and bulk solution pH on the characteristics and composition of corrosion products was considered by Nazari *et al* (72). Tests were conducted in glass cells containing 3.5 wt.% NaCl in distilled water with CO_2 bubbled into the system at 1bar. The experiments were conducted on X70 steel at temperatures ranging from 55-85˚C at a pH ranging from 5.5-6.5. Corrosion product layers were analysed post-test using XRD and SEM. Findings by Nazari *et al* (72) indicated that the temperature had more of an effect on the precipitation rate compared to the bulk solution pH. Results also showed that the corrosion products became more compact with increasing temperature as shown by Figure 2-25, and the thickness of iron carbonate corrosion product layers was also found to be increasing as a function of both pH and temperature.

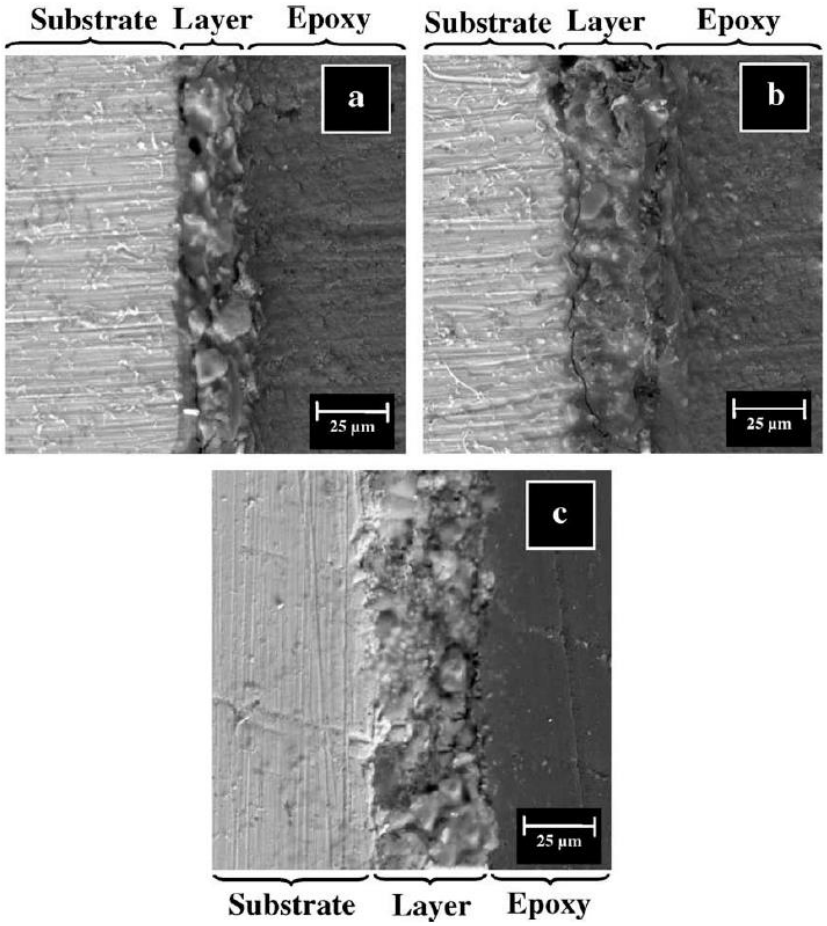

Figure 2-25 Cross-sectional SEM images of iron carbonate precipitated at (a) 65˚C, (b) 75˚C and (c) 85˚C at pH 6.5 for and exposure period of 72 hours (72)

These findings are not consistent with findings by either Lin *et al* or Yin *et al* (74, 90) however the experiments were conducted using different types of steel which is in accordance with findings by Dugstad *et al* (91). Further analysis of images gathered by scanning electron microscopy revealed that the iron carbonate

crystals were rhombohedral and formed a discontinuous and porous layer on the steel surface. Nazari *et al* (72) concluded that the temperature of 85˚C and pH 6.5 were the optimum conditions for precipitation of thick and dense corrosion product layers and also showed that the growth of $FeCO_3$ is caused by the interaction between corrosion on the steel surface and precipitation of $FeCO_3$ onto the steel surface. Although some of these findings are consistent with other authors (90), they were not consistent with findings by Yin *et al* (74) who emphasised that corrosion products can be categorised into two types; thick, porous and non-adherent or thin, dense and adherent, whereas Nazari *et al* (72) concluded that 85˚C and pH 6.5 were the optimum conditions for formation of both thick and dense corrosion product layers.

Gao *et al* (87) investigated the growth mechanism of corrosion products on X65 carbon steel under static CO_2 conditions using autoclaves. The tests were conducted in brines which simulated water found in the Bo-Hai Sea in China. Tests were conducted at 75 and 90˚C at pH 6.5 with a constant CO_2 partial pressure of 10bar. The growth and structure of the corrosion products were investigated using LPR, EIS, and *ex-situ* SEM. UV spectrophotometry and gas adsorption were also used for ferrous ion concentration and porosity measurements respectively. The results obtained by Gao *et al* (87) revealed the precipitation of duplex structured corrosion product layers at both of the tested temperatures, with thick inner layers and thin outer layers as shown by Figure 2-26.

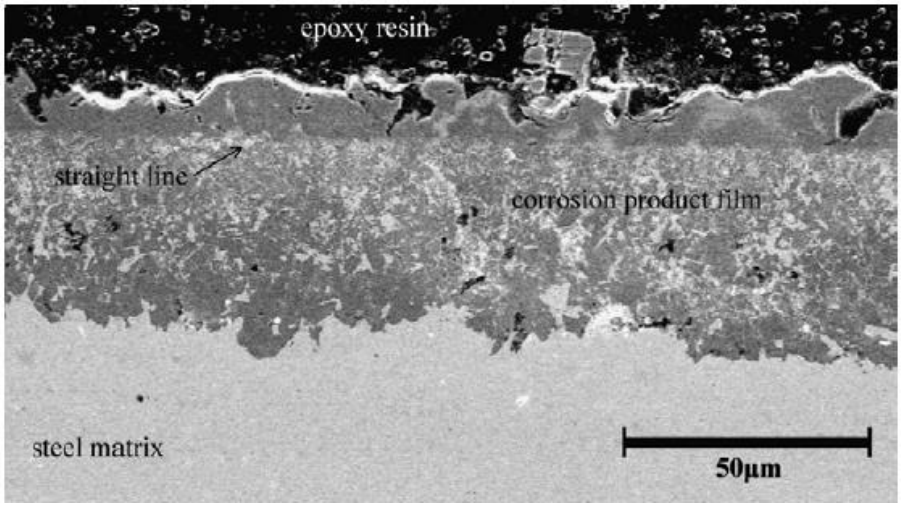

Figure 2-26 Cross-sectional SEM image of duplex layered corrosion product precipitated at 75˚C, 10 bar Pco_2, pH 6.5 after 240 hours of exposure (87)

The thicknesses of these layers increased with increasing exposure time. However using EIS, it was determined that the inner layer of the corrosion product was more protective than the outer layer which would suggest that the structure of the inner layer is different from the structure of the outer layer. The duplex layered corrosion products were found to have precipitated onto steel surfaces after an exposure time of 144 hours at 75˚C, however it was also found that they developed faster and more protective at 90˚C. These findings are consistent with findings by Lin *et al* (90) however unlike Lin *et al* (90) who observed a thin and protective inner layer and a thicker outer layer, Gao *et al* (87) observed a thicker inner layer which becomes more protective with time. The difference in results between the two authors could be explained by the difference in CO_2 partial pressures and brine compositions used by the two authors. Gao *et al* (87) also gathered that the porosity of the corrosion products decreased with increasing exposure time and temperature which is consistent with findings by Dugstad *et al* (91). It was concluded that there is a critical point at which the second corrosion product layer forms; when this happens the porosity of the inner layer (initially single and only layer) decreases and thereby causes a further reduction in the corrosion rate. It was also highlighted that apart from $FeCO_3$, Fe_3C and $CaCO_3$ may have been present on the steel surfaces however these findings were not confirmed.

The surface wettability of wet-ground and pre-corroded X65 carbon steel was considered by Tang *et al* (92). The contact angle on initially oil and water wetted steel was examined on carbon steel surfaces of different surface roughness's and pre-corrosion periods. Carbon steel was polished using grit 400 and 36, and by machine scratching to then be characterised using infinite focus microscopy (IFM) to achieve steel roughness's of 1.5, 6 and 40 µm. Pre-corrosion of carbon steel at 80ºC, pH 6.6 for 24 hours resulted in the precipitation of an $FeCO_3$ layer which was also examined in the wettability study. The wettability of the 4 surfaces were conducted under CO_2 saturation using a 1 wt.% NaCl brine as the water phase and LVT 200 model oil as the oil phase. On initially oil wetted surfaces, Tang *et al* (92) observed a change of contact angles with time until equilibrium was reached between the steel surface and the water droplets. The contact angle was found to be increasing with increasing surface roughness however, the iron carbonate covered surface was found to be more hydrophilic than bare steel of

40 µm surface roughness. On initially water wetted steel the contact angle was not time dependant and remained constant for all of the surfaces including the pre-corroded $FeCO_3$ surface as shown by Figure 2-27 (92).

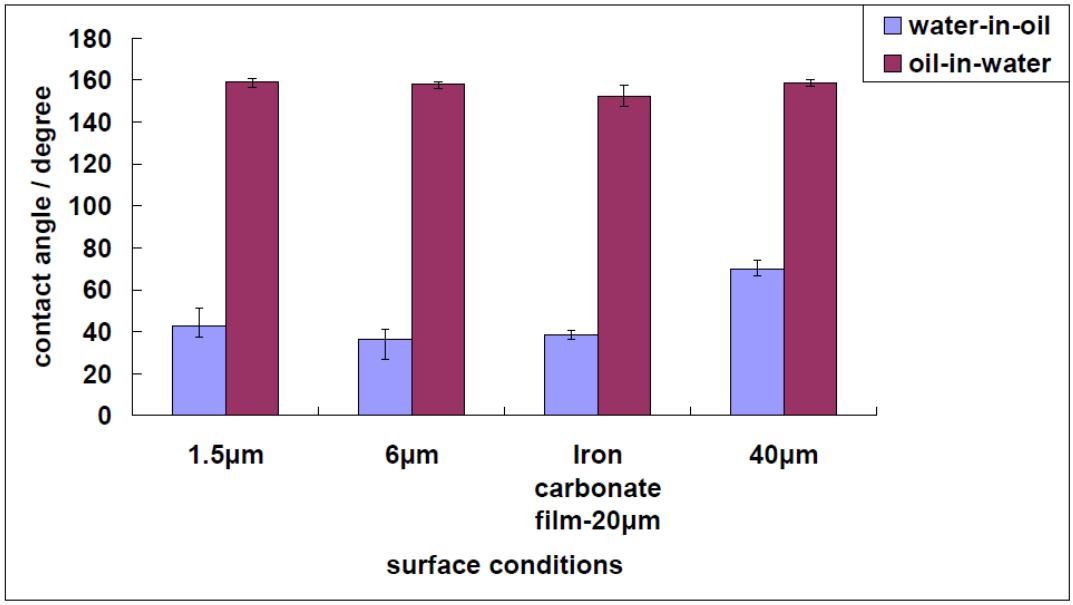

Figure 2-27 Contact angle on initially water and oil wetted surfaces at equilibrium (92)

2.9.2 Iron Calcium Carbonate ($FeCaCO_3$) and Calcium Carbonate ($CaCO_3$) Corrosion Products

The influence of calcium carbonate ($CaCO_3$) on the type/morphology of corrosion products as well as on the corrosion rate of carbon steel was evaluated by Tavares *et al* (86). Corrosion tests were conducted in 1L autoclaves containing CO_2 saturated NaCl brines, in the absence and presence of $CaCO_3$. The tests were conducted at 80°C at a pressure of 15 MPa and lasted for durations of up to 672 hours. Tavares *et al* (86) monitored the corrosion rate using the weight loss method and analysed the corrosion product type/morphology using SEM, EDS and XRD post-test analysis. The weight loss measurements gathered by Tavares *et al* (86) indicated that the corrosion rate decreased with increasing exposure time for both brines (with and without $CaCO_3$) which indicated that corrosion products had precipitated onto the steel surfaces and were providing protection against corrosion in both conditions. The weight loss results provided further indications that after a total exposure period of 672 hours, the corrosion rate was lower in brines containing $CaCO_3$ (0.5mm/year) compared to 1.5 mm/year in the absence of $CaCO_3$ as shown by Figure 2-28(a).

Post-test analysis of the corrosion product layers using XRD and EDS indicated that the corrosion products which had precipitated in the absence and presence of $CaCO_3$ consisted of $FeCO_3$ and $Fe_xCa_yCO_3$ respectively, as shown by Figure 2-29. Results gathered by SEM cross-sectional analysis indicated that corrosion products which had precipitated in the presence of $CaCO_3$ were thinner (~20 µm) compared to an approximate thickness of 30 µm. Tavares *et al* (86) concluded that mixed carbonate corrosion products are more susceptible to Cl^- permeation due to their greater porosity compared to iron carbonate corrosion products (based on visual observations), which makes the mild steel surface exposed to $CaCO_3$ brines more susceptible to localised corrosion, as shown by Figure 2-28(b).

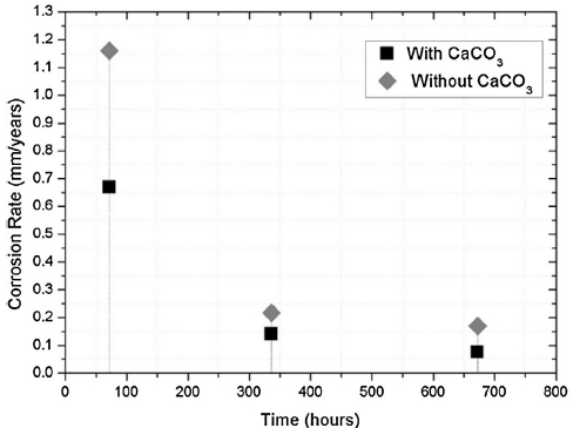

(a)

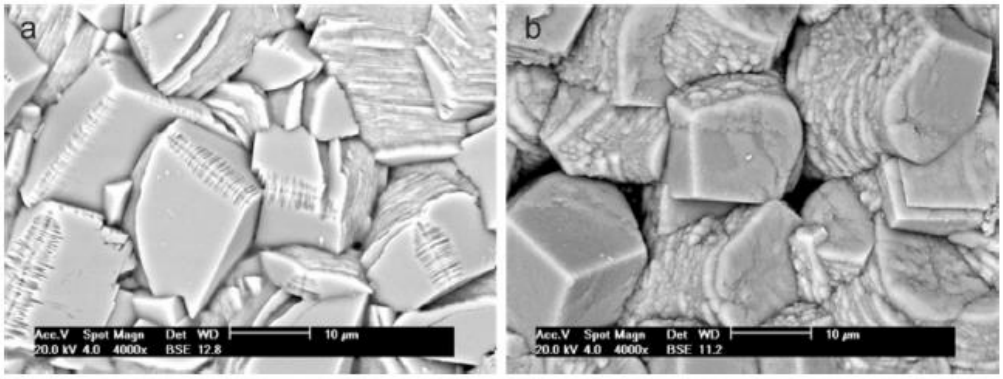

(b)

Figure 2-28 (a) Corrosion rate gathered by weight loss as a function of time, with and without $CaCO_3$ and (b) SEM images of corrosion products precipitated after 672 hours of exposure, without $CaCO_3$ (left) and with $CaCO_3$ (right) (86)

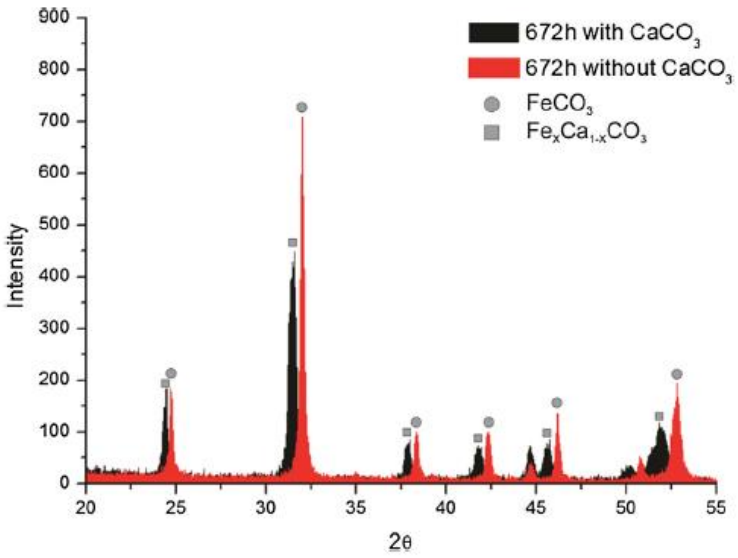

Figure 2-29 XRD of steel surfaces after 672 hours of exposure, in the absence/presence of $CaCO_3$ (86)

The influence of calcium ions on the precipitation of crystalline corrosion products in CO_2 environments was evaluated by Esmaeely *et al* (68). Tests were conducted on mild steel in glass cells using a three electrode configuration. The tests were conducted using CO_2 saturated 1 wt.% NaCl brines at 80ºC and pH 6.6 in stagnant conditions. The iron ion (Fe^{2+}) concentration was fixed while the calcium ion (Ca^{2+}) concentration was varied using calcium concentrations ranging from 0 to 10,000 ppm. The overall corrosion behaviour was monitored during the tests using linear polarisation resistance (LPR) while IFM analysis was performed post-test to evaluate the localised corrosion behaviour. SEM/EDS and XRD were also used post-test for corrosion product characterisation. Findings by Esmaeely *et al* (68) indicated precipitation of iron carbonate ($FeCO_3$) in tests conducted in the absence of calcium ions and a combination of iron carbonate and mixed iron-calcium carbonate ($Fe_xCa_yCO_3$) corrosion products in tests conducted at low Ca^{2+} concentrations (10 and 100ppm) as shown by Figure 2-30. The characteristics of corrosion products also remained relatively unaltered in experiments conducted under low concentrations of Ca^{2+}. These corrosion products were found to be relatively protective which resulted in a decline in the uniform corrosion rates. However in tests conducted in brines with high Ca^{2+} concentrations (1000 and 10,000ppm) no such decline was observed due to the precipitation of non-protective calcium carbonate ($CaCO_3$) corrosion products as shown by Figure 2-31.

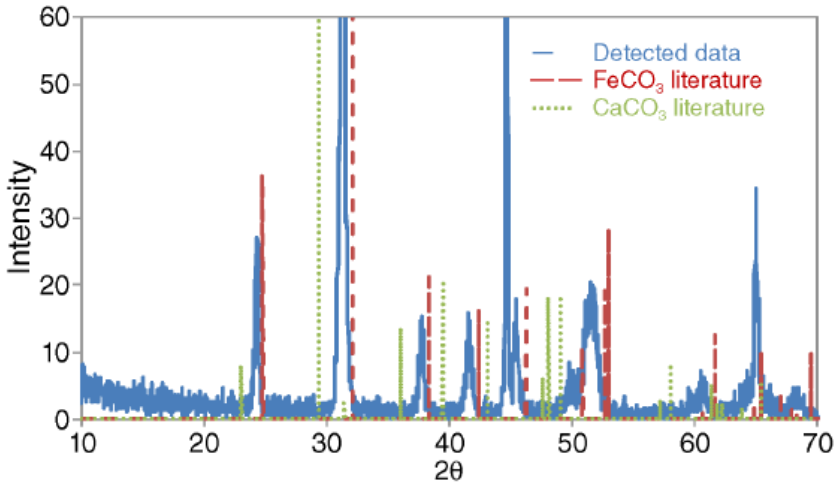

Figure 2-30 XRD pattern for mild steel after exposure to a brine containing 100 ppm of Ca^{2+} at 80ºC (68)

The non-protective corrosion products which had precipitated at 10,000 ppm of Ca^{2+} resulted in localised corrosion in the form of pits. At a Ca^{2+} concentration of 1000 ppm cross-sectional SEM/EDS analysis revealed duplex layered corrosion products which may have consisted of a $CaCO_3$ inner layer and an outer layer of $FeCO_3$. However due to the nature of these results, it is difficult to confirm whether or not this was the case and it was therefore concluded that the presence of high Ca^{2+} concentration within brines can have a negative influence on the corrosion behaviour of mild steel (68).

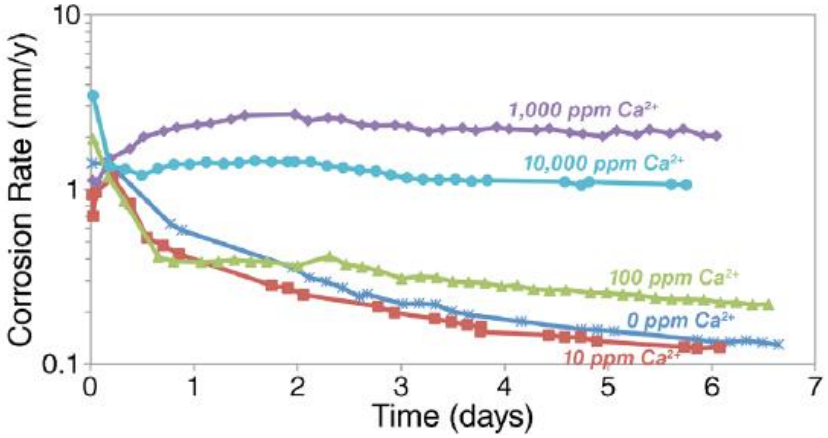

Figure 2-31 Corrosion rate as a function of time for experiments conducted at 80ºC in brines with varied Ca^{2+} concentrations (68)

Esmaeely *et al* (85) further evaluated the effect of calcium ions on the precipitation of iron-calcium carbonate corrosion products and its influence on the extent of localised corrosion using three-electrode glass cell tests. The

experiments were conducted in CO_2 saturated brines, in the absence and presence of 10,000 ppm of $CaCl_2$. Esmaeely *et al* (85) maintained the chloride content throughout the corrosion tests to solely determine the effect of Ca^{2+} ions. Linear polarisation resistance (LPR) was used to determine the corrosion rate during the experiments. Post-test analysis using SEM, XRD and EDS was performed to determine the composition/morphology of corrosion products. The effect of flow on corrosion product precipitation was also evaluated using a magnetic stirrer. They also used Bragg's law together with equations relating inter-planar spacings to unit cell parameters and XRD data to determine the mole fractions of calcium and iron within the mixed iron-calcium carbonate corrosion products, as shown by Figure 2-32.

XRD results indicated that a mixed layer of $Fe_xCa_yCO_3$ had precipitated onto the carbon steel surface. Further findings by Esmaeely *et al* (85) also indicated that the presence of Ca^{2+} ions resulted in an increase in the localised corrosion rate which is consistent with finding by Tavares *et al* (86). Results also showed that higher flow rates resulted in a more agitated solution which lead to the precipitation of a less protective layer consisting of iron-calcium carbonate. Calculated Ca/Fe mole fractions indicated that higher Ca mole fractions corresponded to less protective corrosion product layers which could potentially result in more severe localised corrosion rates, as shown by Figure 2-32.

Flow Condition	Initial Ca^{2+}/ppm	Weight Loss Corrosion mm/yr	Localized Corrosion mm/yr	Calculated *x from EDS Spectra*	Calculated *x from XRD Data using "c"*	Calculated *x from XRD Data using "V"*	$Ca_xFe_yCO_3$ $(x+y=1)$
Previous Study							
Stagnant	10	0.6	-	0.045	0.05	0.05	$Ca_{0.05}Fe_{0.95}CO_3$
	100	NA	-	0.22	0.22	0.22	$Ca_{0.22}Fe_{0.78}CO_3$
	1,000	1.3	-	†	0.25	0.21	$Ca_{0.25}Fe_{0.75}CO_3$
				†	0.94	0.90	$Ca_{0.94}Fe_{0.06}CO_3$
	10,000	0.7	6.0	0.91	0.94	0.91	$Ca_{0.94}Fe_{0.06}CO_3$
Current Study							
Stagnant	10,000	0.8	8.5	0.96	0.91	0.91	$Ca_{0.91}Fe_{0.09}CO_3$
300 rpm	10,000	0.5	6.2	0.94	0.88	0.87	$Ca_{0.88}Fe_{0.12}CO_3$
600 rpm	10,000	1.2	-	0.91	0.88	0.87	$Ca_{0.88}Fe_{0.12}CO_3$

Figure 2-32 Calculated molar compositions of Fe and Ca in Iron calcium carbonates using Bragg's law, XRD and EDS data (85)

The influence of Cl^-, Ca^{2+} and Mg^{2+} on the protectiveness and characteristics of corrosion products in high pressure CO_2 environments was considered by Hua *et al* (93). Corrosion tests were conducted on X65 carbon steel in autoclaves

using a surface area to volume ratio of 93 cm^2/l. The tests were conducted in static conditions at 60ºC and 100 bar of CO_2 partial pressure. The influence of calcium ions on the protectiveness and characteristics of corrosion products was evaluated by varying the calcium concentrations within the brine using calcium chloride dehydrate. The calcium concentration was varied at concentrations of 0, 1000 and 10,000 ppm at a maintained chloride content of 35,249 ppm, which enabled the sole effect of calcium ions to be evaluated. Mass loss measurements were conducted at exposure periods of 6, 24, 48 and 96 hours to monitor the uniform corrosion behaviour. Corrosion product characteristics were evaluated using a combination of post-test analysis methods such as SEM/EDX, XRD and focused ion beam (FIB). The localised corrosion behaviour was evaluated using non-contact surface profilometry measurements.

Findings obtained by Hua *et al* (93) indicated that the introduction of 1000 ppm calcium chloride dehydrate had resulted in a reduction in the uniform corrosion rate which was further amplified at 10,000 ppm. XRD analysis of the corrosion products revealed that $FeCO_3$ had precipitated onto the steel surface in the absence of calcium ions. However in the presence of calcium ions, a mixed iron-calcium carbonate corrosion product had precipitated onto the steel surface. Using XRD based calculations similar to the calculations conducted by Esmaeely *et al* (85), the mole fraction of calcium within the mixed carbonate ($Fe_xCa_yCO_3$) was found to be increasing with increasing calcium concentrations within the brine solution. However unlike the finding by Esmaeely *et al* (85), the mixed iron-calcium carbonate corrosion products were becoming more protective with increasing mole fractions of calcium which could be attributed to the higher CO_2 partial pressure used by Hua *et al* (93). Further analysis of the mixed iron-calcium carbonate corrosion products revealed regions within the mixed carbonate which were either rich in iron or calcium, as shown by Figure 2-33.

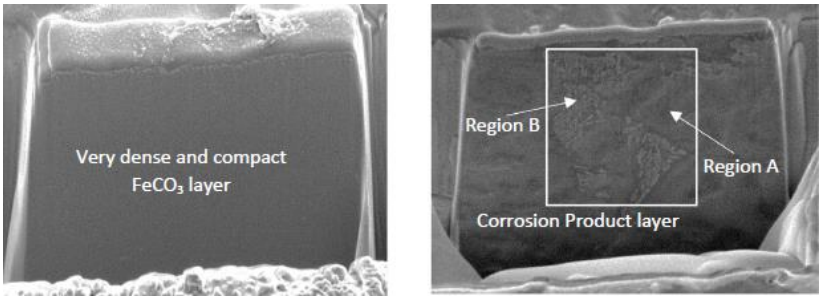

(a) **(b)**

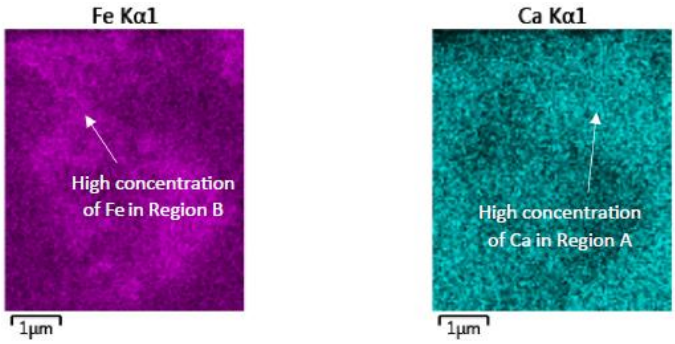

(c) **(d)**

Figure 2-33 FIB images of (a) iron carbonate, (b) iron-calcium carbonate and (c) EDX map of iron, (d) EDX map of calcium within the mixed iron-calcium carbonate corrosion product (93)

However similar to other authors (68, 85, 86), the introduction of calcium ions within the brine was found to have a negative effect on the localised corrosion behaviour. This effect was found to diminish with increasing exposure periods (93). The morphology of corrosion products only changed significantly at high concentrations of calcium chloride (10,000 ppm) which was associated with slower precipitation rates within the initial experimental hours. However after four days of exposure to the calcium containing brine, surface coverage was similar to carbon steel specimens exposed to brines in the absence of calcium ions as shown by Figure 2-34. It was concluded by Hua *et al* (93) that further studies are required to improve our understanding of the accelerated localised corrosion behaviour in the presence of calcium ions.

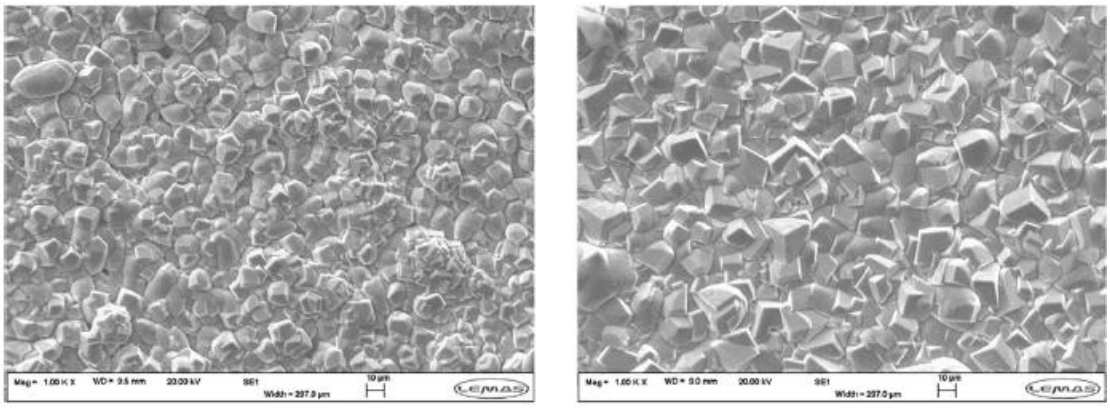

(a) **(b)**

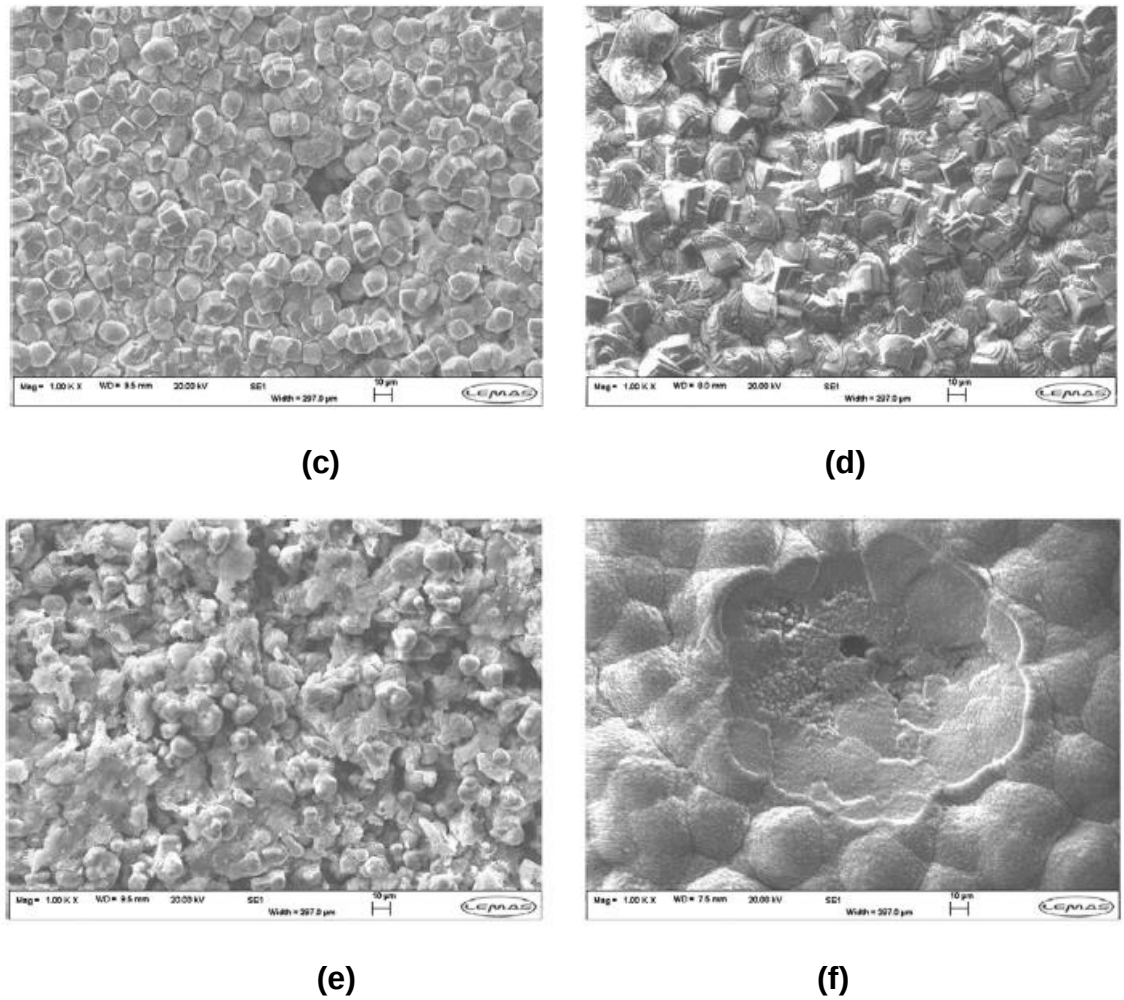

(c) **(d)**

(e) **(f)**

Figure 2-34 SEM images of corrosion products after exposure for (a) 24 h in NaCl brine, (b) 96 h in NaCl brine, (c) 24 h in 1000 ppm $CaCl_2$, (d) 96 h in 1000 ppm $CaCl_2$, (e) 24 h in 10,000 ppm $CaCl_2$ and (f) 96 h in 10,000 ppm $CaCl_2$ (93)

The influence of calcium ions on the localised corrosion behaviour in CO_2 environments was considered by Jiang *et al* (94), who conducted a series of corrosion tests on N80 steel in stagnant and dynamic conditions with and without pre-corrosion. The corrosion tests were conducted in brines in the absence/presence of 1.5 wt.% $CaCl_2$ at a maintained chloride content to solely evaluate the effect of calcium ions on the localised corrosion behaviour. The tests were conducted under CO_2 saturation at 57 ºC. EIS was used in conjunction with LPR to monitor the overall corrosion behaviour. SEM imaging was used for post-test analysis of steel surfaces.

Findings by Jiang *et al* (94) indicated that in the absence calcium ions, iron carbide and iron carbonate corrosion products had precipitated onto the steel

surface where as in tests with $CaCl_2$, iron carbide, iron carbonate and calcium carbonate corrosion products precipitated onto the N80 steel surface. These findings are not consistent with findings by others (68, 85, 86, 93), however this may have been caused by the relatively low concentration of Ca^{2+} ions within the bulk solution. The extent of localised corrosion was not detailed in the study conducted by Jiang *et al* (94) however it was explained using electrochemical measurements that the initiation period for pit development was delayed by the addition of calcium ions within brine. It was concluded that the increase in the initiation period of localised pits was caused by the thicker and visibly more porous corrosion products, as shown by Figure 2-35 (94).

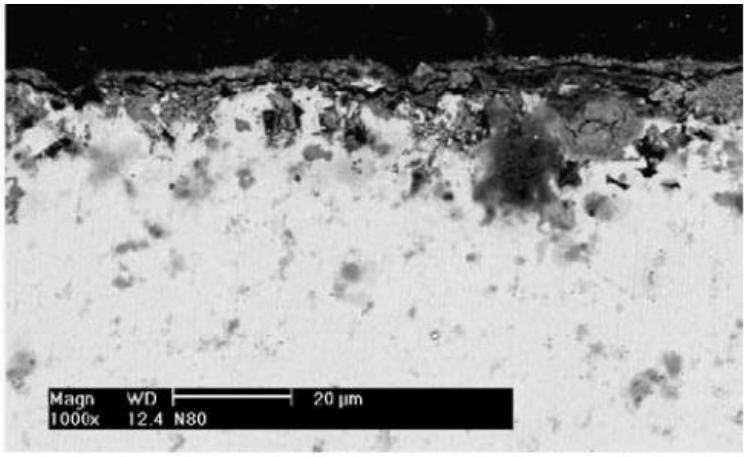

Figure 2-35 Cross-sectional SEM image of N80 steel after exposure to calcium containing brine after 96h at 57ºC (94)

The mechanical properties of corrosion products and their influence on the CO_2 corrosion behaviour was evaluated by Gao *et al* (95). Corrosion tests were conducted on X65 carbon steel specimens in autoclaves at 65ºC. The test duration was 240 hours in complex brines containing $CaCl_2$, Na_2SO_4, NaCl, $MgCl_2.6H_2O$ and $NaHCO_3$. The flow rate and CO_2 partial pressure were varied between 0-1 m/s and 0-1 MPa respectively. The composition and morphology of corrosion products were analysed post-test using XRD and SEM/EDX. The mechanical properties of the corrosion products were evaluated using Nano-indentation, Vicker's indentation and tensile tests.

Results gathered by Gao *et al* (95) under static conditions indicated that at the lower CO_2 partial pressure of 0.1 MPa, a combination of $FeCO_3$, $CaCO_3$ and $MgCO_3$ corrosion products had precipitated onto the steel surface whereas at

0.3 and 1 MPa, $FeCaMgCO_3$ and $Fe_xCa_yCO_3$ corrosion products were present on steel surfaces respectively. However under dynamic conditions only $Fe_xCa_yCO_3$ was found to be precipitating onto the carbon steel surfaces. Increasing experimental flow rates were found to have reduced the nucleation of $FeCO_3$ crystals due to mass transport. The increase in flow rate and CO_2 partial pressure also resulted in more severe localised corrosion. Due to the nature of the complex brine used by Gao *et al* (95), it is difficult to compare these findings with results gathered by others. However the presence of mixed carbonates was found to have a negative influence on the localised corrosion behaviour which is consistent with others (68, 85, 86, 93, 94). Gao *et al* (95) indicated that corrosion products with high interfacial fracture toughness (Figure 2-36) resulted in low uniform and localised corrosion rates and therefore concluded that the interfacial fracture toughness is the best mechanical parameter to be used for the evaluation of corrosion product protectiveness in corrosive environments.

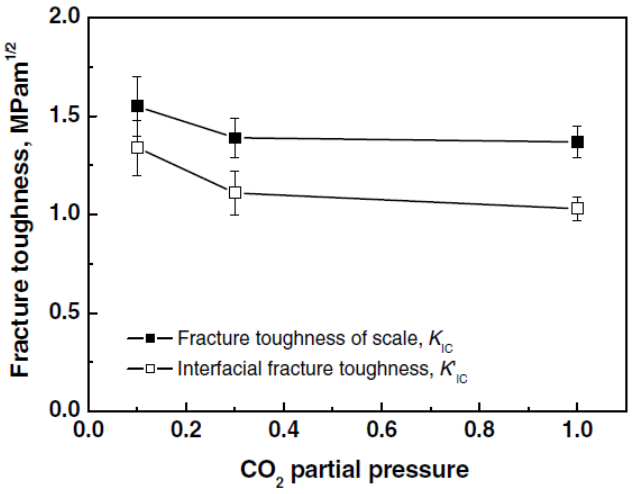

Figure 2-36 Fracture toughness of corrosion products as a function of CO_2 partial pressure (95)

2.10 Performance Evaluation of CO_2 Corrosion Inhibitors

Palmer *et al* (96) examined the performance of three different corrosion inhibitors with respect to the localised corrosion behaviour using an artificial pit technique shown in Figure 2-37. Zero resistance ammetry (ZRA) was used to measure the current between the carbon steel artificial pit and a carbon steel counter electrode which had a considerably greater surface area. The measured current was used to examine the ability of each corrosion inhibitor in combating localised

corrosion. This technique was used in conjunction with polarisation resistance measurements of the de-coupled electrodes which was used to provide the individual corrosion rates of each of the two electrodes.

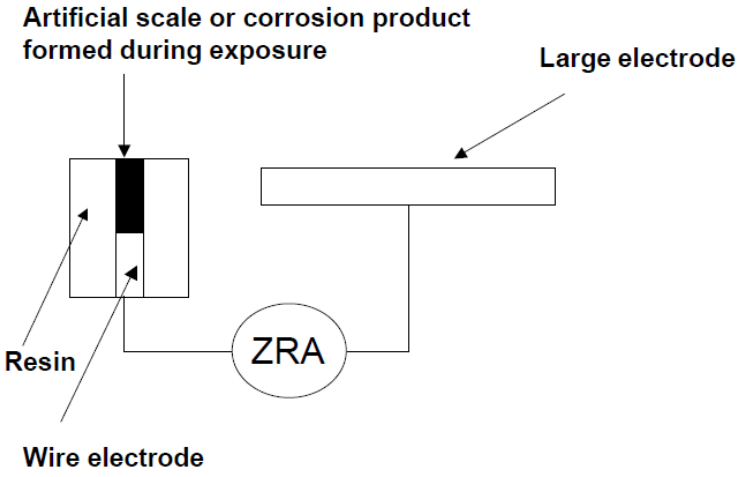

Figure 2-37 Schematic of artificial pit technique (96)

The tests were carried out at ambient temperature conditions in 3 wt.% NaCl saturated with 1 wt.% H_2S in CO_2 to achieve slightly sour experimental conditions. The three corrosion inhibitors examined by Palmer *et al* (96) were; oleic imidazoline, benzyl coco dimethyl ammonium chloride and 6.5 molar generic phosphate ester and were tested at concentrations of 25 ppm. The results obtained by Palmer *et al* (96) indicated that the amine and imidazoline corrosion inhibitors were extremely effective in combating uniform corrosion, however only the amine corrosion inhibitor was effective in reducing the corrosion rate within the artificial pit. It was also determined that once a pit has developed, extremely high inhibitor dosages are required to reduce pit growth. Palmer *et al* (96) concluded that performance testing of corrosion inhibitors with respect to the localised corrosion behaviour should be an integral part of any inhibitor selection programme and that corrosion inhibitors which are effective in reducing uniform corrosion rates may not be as effective with respect to the localised corrosion behaviour.

Jenkins (81) developed and performance tested three environmentally friendly modified quaternary amine corrosion inhibitors for use in high temperature environments. Three modified compounds were evaluated using kettle tests, rotating cylinder electrode (RCE) tests and high temperature autoclave tests. The experimental conditions and brine's used for the tests replicated a UK North

Sea gas/condensate field. A brine to kerosene ratio of 7:3 was used for all experiments. Kettle tests were performed at 90ºC, rotating cylinder electrode tests were conducted at 2000 rpm and autoclave tests were CO_2 saturated at 100 and 120 ºC. The kettle tests were conducted by Jenkins (81) in order to evaluate the effect of 24 hour aging of the three compounds. The corrosion tests indicated that all three corrosion inhibitors provided excellent corrosion protection at 90 ºC and ambient pressure. Further examination using rotating cylinder electrode tests proved that all three inhibitors were also effective in the presence of moderate wall shear stress (5 Pa). At 100 and 120 ºC, 35 and 50 ppm respectively was required in order to achieve over 97% efficiency as shown in Figure 2-38. Jenkins (81) concluded that there were no signs of localised corrosion during either of the corrosion tests.

Product	Temperature (°C)	Dose (ppm/vol)	Corrosion Rate (mm/yr)	% Protection
Blank	100	N/A	3.387	N/A
Inhibitor A	100	20	0.352	89.61
Inhibitor A	100	35	0.087	97.43
Inhibitor B	100	20	0.376	88.90
Inhibitor B	100	35	0.144	95.75
Inhibitor B	100	50	0.096	97.17
Inhibitor C	100	20	0.149	95.60
Inhibitor C	100	35	0.091	97.31
Blank	120	N/A	2.31	N/A
Inhibitor A	120	50	0.268	88.40
Inhibitor A	120	100	0.097	95.80
Inhibitor B	120	50	0.316	86.32
Inhibitor B	120	100	0.144	93.77
Inhibitor C	120	50	0.04	98.27

Figure 2-38 Uninhibited and inhibited corrosion rates at 100 and 120 ºC (81)

The performance of an imidazoline corrosion inhibitor was assessed by Wang *et al* (97) using electrochemical impedance spectroscopy (EIS), atomic force microscopy (AFM) and X-ray photoelectron spectroscopy (XPS). Tests were conducted on X235 steel at ambient temperature in CO_2 saturated 2 wt.% NaCl brines. The tests were conducted for 72 hour periods using a three electrode configuration. Using XPS and AFM, Wang *et al* (97) reported that the imidazoline based corrosion inhibitor was able to efficiently reduce the corrosion rate by the formation of a chemisorbed film onto the steel surface. AFM force curves were used to quantify the adhesive force between the solid surface and the adsorbed inhibitor film as shown by Figure 2-39. The adhesive force was found to be more

than 2 times greater in the presence of the corrosion inhibitor which confirmed that a hydrophobic film had adsorbed onto the steel surface after soaking the steel specimen in the imidazoline corrosion inhibitor.

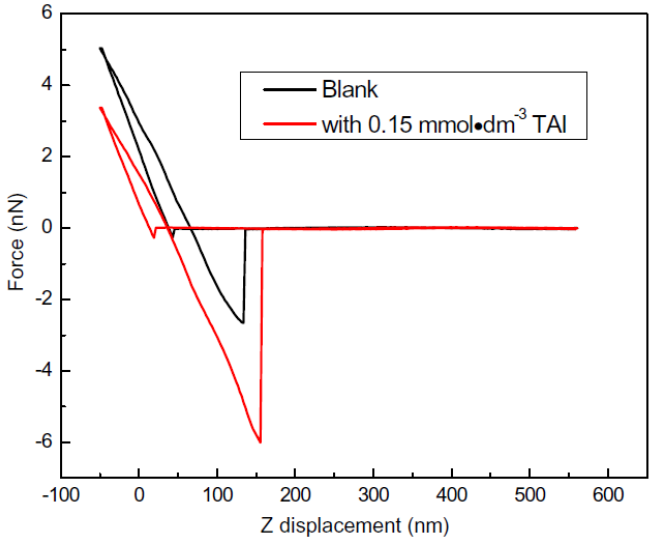

Figure 2-39 Force-distance curves for blank and inhibited experiments (97)

Wang *et al* (97) confirmed these findings using XPS as shown by Figure 2-40, which indicated peaks for carbon and nitrogen which make up the basis of the Imidazoline based corrosion inhibitor.

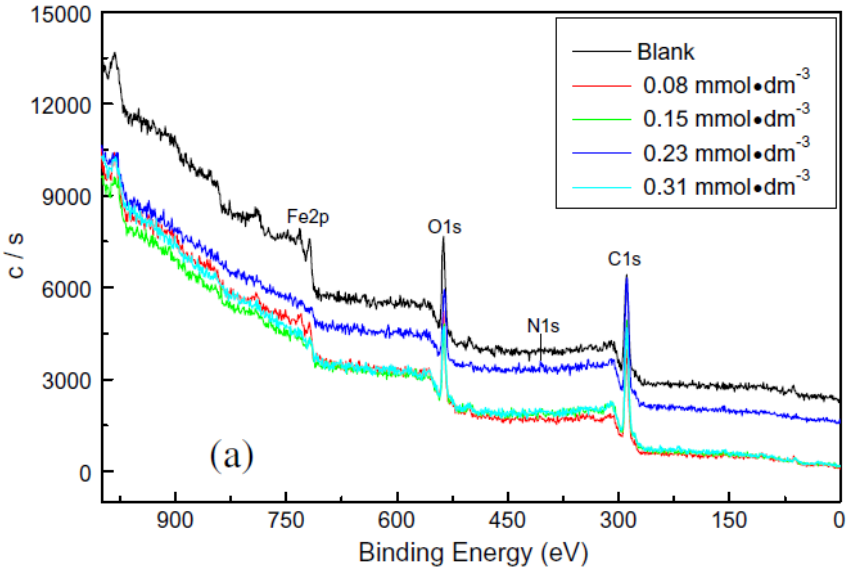

Figure 2-40 XPS spectra for uninhibited and inhibited Q235 steel (97)

The influence of autoclave heat up and cooling periods on the evaluation of corrosion inhibitor performance testing was considered by Ding *et al* (98). Tests were performed and compared across two autoclave systems; a single autoclave system and a modified twin autoclave system, shown in Figure 2-41. The twin

autoclave system was developed in an attempt to reduce effects caused by long heating and cooling periods of experimental brines within autoclaves. The tests were conducted on X65 carbon steel specimens under CO_2 saturated 1 wt.% NaCl brines at 120 and 150ºC. Linear polarisation resistance (LPR) was used to monitor the uniform corrosion behaviour and surface analysis of the carbon steel surfaces was performed using SEM, EDS and XRD.

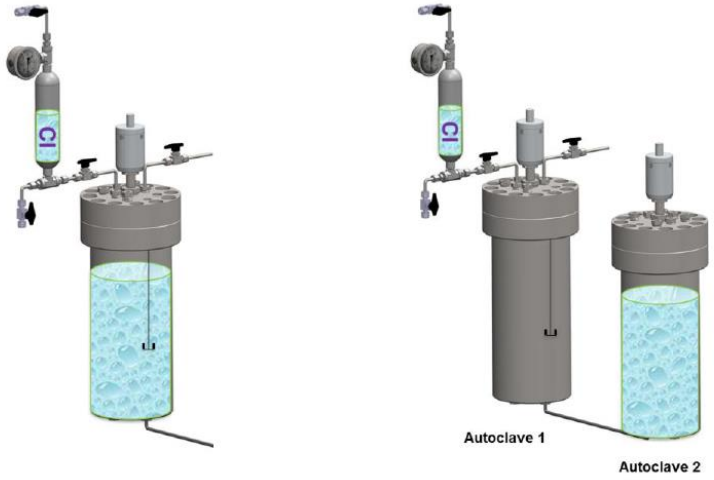

(a) **(b)**

Figure 2-41 (a) Single and (b) twin autoclave systems used and compared by Ding *et al* (98)

In the single autoclave system, $FeCO_3$ and Fe_3O_4 corrosion products were found to have precipitated onto steel surfaces at 120 and 150ºC respectively in uninhibited conditions. The precipitation of $FeCO_3$ at 120ºC was reduced in the twin-autoclave system however at 150ºC, the formation of Fe_3O_4 was not affected indicating that the heat up and cooling periods have more of an influential effect at 120ºC. Ding *et al* (98) further reported that the imidazoline based corrosion inhibitor was able to provide 61% efficiency at 120ºC, however was unable to operate at 150ºC. The precipitation of corrosion products at both temperatures was also found to have been reduced in the presence of the imidazoline corrosion inhibitor, as shown by Figure 2-42. It was concluded that the imidazoline corrosion inhibitor had been degrading into its amide precursor, where 40-50% of the inhibitor was lost due to hydrolysis which partly caused the poor inhibition performance.

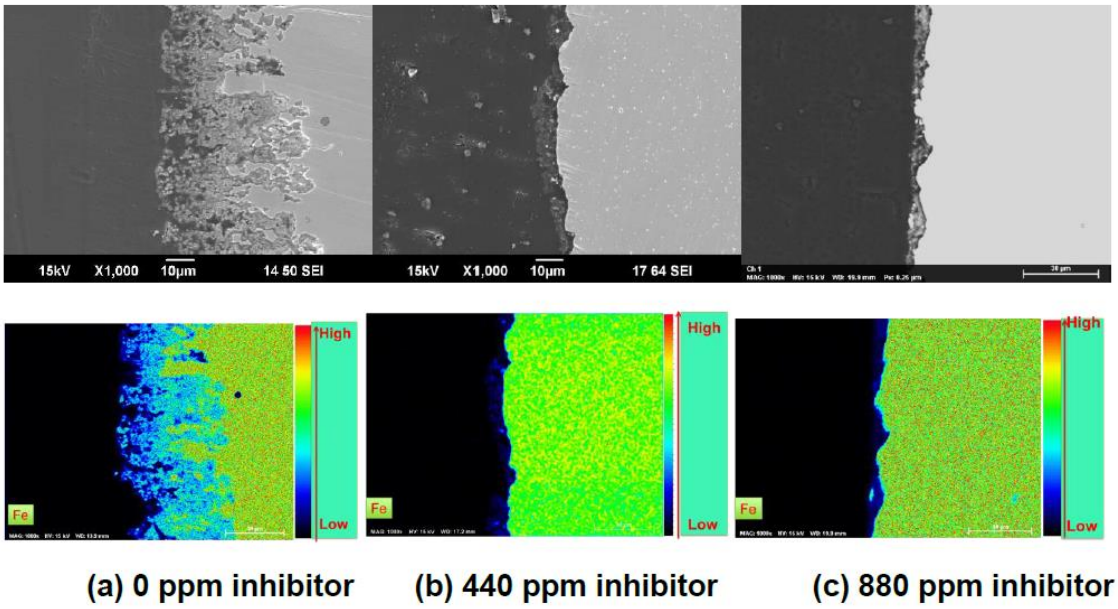

Figure 2-42 Cross-sectional SEM and EDS mapping at 150ºC without/with imidazoline corrosion inhibitor (98)

The performance of corrosion inhibitors before and after chemical aging was evaluated by Liu *et al* (99) in order to determine the thermal stability of three classes of corrosion inhibitors; imidazolines, phosphate esters and quaternary amine compounds. Their thermal degradation kinetics was also evaluated in order to determine their compatibility in high temperature environments. Several corrosion inhibitors were aged at temperatures ranging from 150-230ºC for 7 days at 1000 psi of nitrogen before their corrosion inhibitor performance was assessed using kettle tests. Corrosion inhibitors which were found to be stable at temperatures of up to 180ºC underwent further testing at 80 and 150ºC. Kettle test evaluations were conducted using linear polarisation resistance (LPR) at 80ºC in 9:1 brine to oil mixtures under CO_2 saturation using low carbon steels as working electrodes. Liu *et al* (99) reported that the efficiency of corrosion inhibitors generally decreases with increasing ageing temperature as shown by Figure 2-43. However it was also found that at considerably higher inhibitor dosages (X10), some inhibitor compounds were able to maintain high efficiencies even after chemical ageing at 230ºC for 7 days. It was concluded that in some cases synergistic effects can be achieved by combining two or more inhibitor intermediates together.

Ageing Temp.	None		300°F		350°F		400°F		450°F		Thermal Stability Limit
Dosage, ppm	10	100	10	100	10	100	10	100	10	100	
CI ID	% protection		% protection		% protection		% protection		% protection		
1	99.2	92.7	37.6	99.2	21.2	99.9	94.1	98.7	32.7	92.6	450
2	93.7	96.1	81.3	99.0	95.5	99.4	97.9	96.6	-2.8	64.4	400
3	91.2	91.9	91.6	91.3			90.4	96.9	96.4	89.7	>450
4	12.2	47.3	10.8	60.8			12.1	96.6	-0.3	95.9	450
5	69.9	91.4	54.3	86.8			94.1	98.7	9.0	97.9	450
6	51.2	94.1	-23.0	19.9	1.6	8.2					<300
7	26.0	26.1	26.0*	34.0*	26.7	12.8					350
8	38.6	32.6	-13.0	-11.4	10.1	11.6	5.9	5.7			<300
9	45.2	68.3	41.3	75.9	48.9	77.9	12.1	96.6	11.8	4.9	400
10	83.3	92.2	82.2	97.1	76.8	94.5	97.9	96.6	8.7	37.1	400
14	100	99.4	26.3	100							<300
15	99.7	99.8	27.0	99.9							<300
16	18.0	76.0	2.9	12.4							<300
17	28.2	71.9	18.6	75.3			-22	96	69.3	76.7	>450
18	7.2	96.6	-1.8	13.7	10.1	8.3	0.3	7.3			<300
19	16.7	83.2	14.5	85.3	11.3	67.1	10.4	28.9			350
20	9.6	27.8	4.8	2.7	41^	97^	-1.4	9.6			350
21	91.3	95.4	-6.3	-6.4	0.7	-4.9					<300

Figure 2-43 Inhibitor efficiency and thermal stability as a function of chemical ageing temperature for several inhibitor compounds (99)

The high temperature/pressure inhibitor performance of an imidazoline based corrosion inhibitor was assessed by Hong *et al* (100). High temperature and pressure experimental inhibition tests were achieved using a large diameter flow loop capable of flow rates of up to 100 m^3/hour, shown in Figure 2-44. Tests were conducted on carbon steel in two phase salt water brine and oil (8:2) at 90ºC and 3000 psi. The corrosion behaviour was monitored using electrochemical impedance spectroscopy (EIS). Hong *et al* (100) reported that at concentrations above 50 ppm, there were no apparent performance improvements by the imidazoline corrosion inhibitor which led to the conclusion that 50 ppm was the optimum inhibitor dosage.

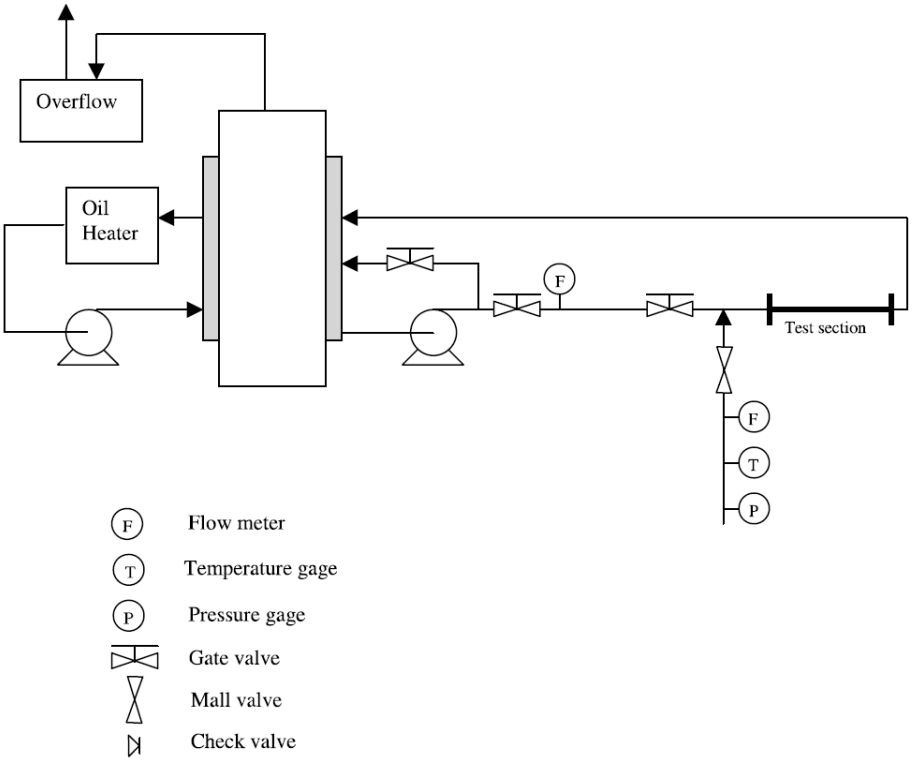

Figure 2-44 Schematic diagram of high temperature/pressure flow loop (100)

It was also observed that inhibitor injection led to an increase in charge transfer resistance which resulted in a reduction in the corrosion rate. The Warburg impedance coefficient was found to be changing with exposure time within the first 8 hours. Based on these findings it was concluded that an inhibitor film had formed onto the steel surface which became more compact and more protective with time within the first 8 hours of exposure. The Warburg impedance coefficient as a function of time is provided in Figure 2-45 (100).

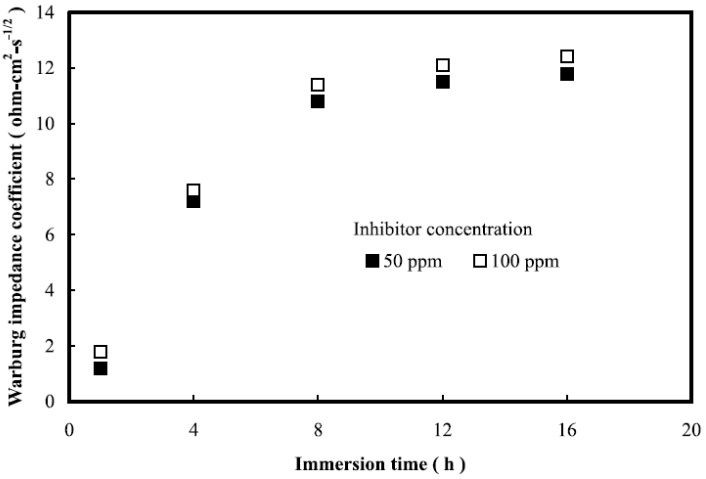

Figure 2-45 Warburg impedance coefficient as a function of exposure time (100)

High temperature/pressure corrosion inhibitor testing for use in deep wells was investigated by Ramachandran *et al* (101). Corrosion inhibition tests were conducted in high speed autoclaves with rotating cages. The tests were conducted at 188ºC, 10.3 MPa CO_2 partial pressure and at 232ºC, 2.88 MPa CO_2 partial pressure on mild steel specimens rotating at 2000 rpm. The tests were conducted in 80:20 brine-Isopar mixtures containing 12 ppm H_2S. Four oil soluble corrosion inhibitors were tested; cyclic amine, amido-imidazoline, quaternary amine imidazoline and an imidazoline surfactant based corrosion inhibitor. Ramachandran *et al* (101) reported that corrosion rates decreased in the absence of a corrosion inhibitor due to precipitation of porous and non-protective iron carbonate corrosion products. It was also determined that both the quaternary amine and imidazoline surfactant corrosion inhibitors performed well at 188ºC however only the cyclic amine performed well at 232ºC. The imidazoline surfactant corrosion inhibitor was able to reduce the corrosion rate from 5 mm/year to less than 0.2 mm/year at 188ºC at a concentration of 1000 ppm, shown in Figure 2-46.

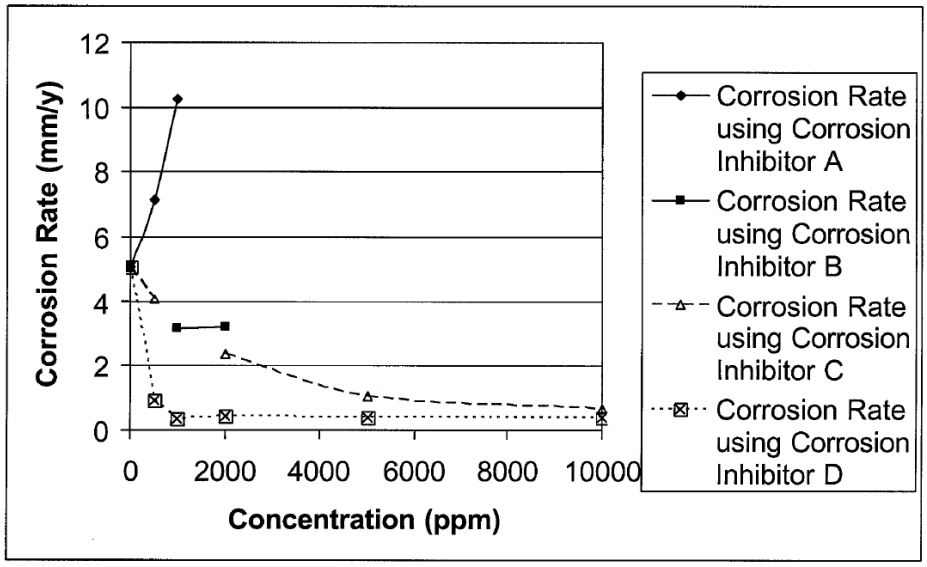

Figure 2-46 Corrosion rates at 188ºC, 10.3 MPa CO_2 partial pressure as a function of inhibitor concentration, where inhibitor A, B, C and D correspond to cyclic amine, amido-imidazoline, quaternary amine imidazoline and imidazoline surfactant based corrosion inhibitors respectively (101)

It was concluded that the transport and incorporation of corrosion inhibitors with corrosion products is extremely important in determining the true performance of corrosion inhibitors in high temperature/pressure environments and as a result,

testing corrosion inhibitors using field conditions can lead to an improved choice of corrosion inhibitors.

Palencsar *et al* (26) investigated the performance of corrosion inhibitors at high temperatures using jet impingement loops which were built around titanium autoclaves, capable of temperatures of up to 150ºC. Two corrosion inhibitors; oleic imidazoline and coco alkyl quat were tested at a temperature range of 100-150ºC in CO_2 saturated 3 wt.% NaCl brines at pH 4. Performance of the corrosion inhibitors was evaluated using electrochemical linear polarisation resistance (LPR) measurements. Kerosene was used in some experiments to simulate brine-oil two phase flow. The corrosion experiments were conducted on carbon steel at a flow velocity of 2 m/s using 200 ppm inhibitor dosages. In order to supress precipitation of iron carbonate, the iron ion (Fe^{2+}) concentration was kept bellow its saturation. This was done in order to solely investigate the performance of the corrosion inhibitors. Palencsar *et al* (26) reported that the performance of the corrosion inhibitors reduced with increasing temperature however there were no signs of inhibitor degradation as shown by Figure 2-47.

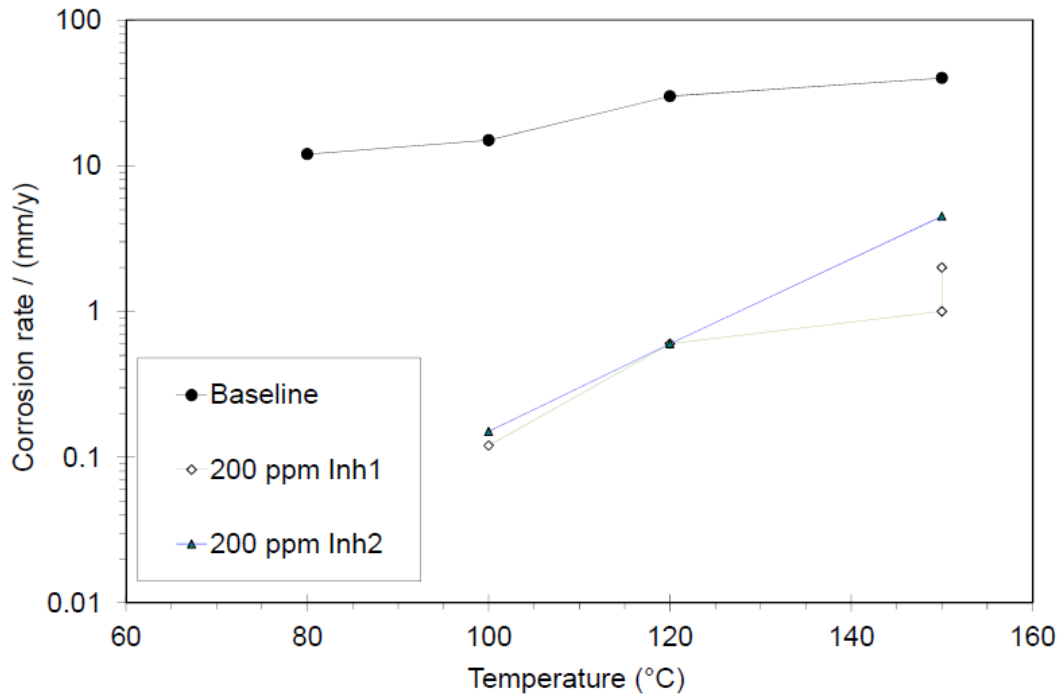

Figure 2-47 Corrosion rate Vs temperature for uninhibited and inhibited brines, where Inh1 and 2 correspond to an oleic imidazoline and a coco alkyl quat respectively (26)

The performance of the corrosion inhibitors also increased in brine-oil two phase flow due to improved inhibitor film properties. This synergy was observed to be reducing with increasing exposure periods at 150ºC. It was concluded that inhibitor performance studies in brine-oil two phase flow can lead to an improved understanding of the performance of corrosion inhibitors at high temperatures.

The high temperature and pressure performance of imidazoline and amide corrosion inhibitors was further evaluated by Chen *et al* (102). The evaluations were conducted at 65 and 150ºC at 3000 psig using wheel tests in CO_2 saturated 5 wt.% NaCl based brines with kerosene as the oil phase. The wheel tests were conducted at 30 rpm on mild steel coupons. Chen *et al* (102) reported that both the imidazoline and amide corrosion inhibitors provided excellent corrosion protection at 65ºC (>95% efficiency), however their performance reduced with increasing temperature. As a result the efficiency was reduced at 150ºC to 38 and 72% for the imidazoline and amide corrosion inhibitors respectively. Chen *et al* (102) reported that the relatively greater performance of the amide inhibitor also indicated greater thermal stability, as shown by Figure 2-48.

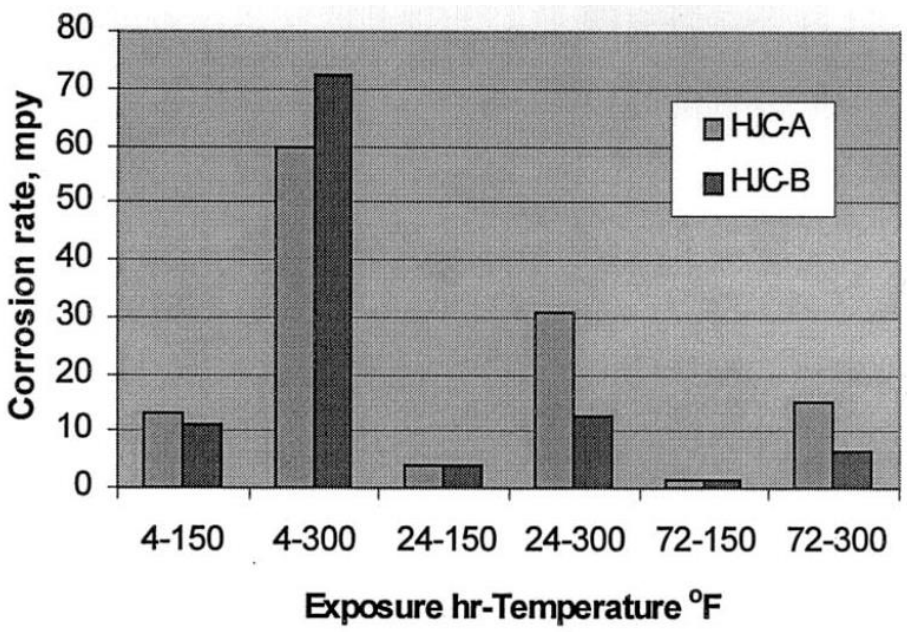

Figure 2-48 Corrosion rate as a function of exposure time and temperature for (HJC-A) imidazoline and (HJC-B) amide corrosion inhibitor (102)

The reduction in inhibitor performance with increasing temperature was overcome by using higher inhibitor dosages (1000 ppm) which resulted in improved inhibitor efficiencies, 90 and 89% for imidazoline and amide inhibitors respectively. However Chen *et al* (102) noted that extremely high inhibitor

dosages can influence downstream processes such as oil-water separation and ultimately the quality of water which may be used for the purpose of water injection (Enhanced oil recovery). It was concluded that 40 times greater inhibitor dosages are required at 150ºC as compared to 65ºC.

2.11 Interaction between Corrosion Products and Corrosion Inhibitors

The effect of flow on corrosion inhibition was evaluated by Kvarekval *et al* (32) using flow loops. Tests were conducted in simple brines at temperatures ranging from 60 to 150˚C at flow rates of 1-9 m/s. The experiments were conducted on wet-ground and pre-corroded X65 carbon steel specimens using three corrosion inhibitors to evaluate the interaction between inhibitors and corrosion products. Three corrosion inhibitors were tested; an amine inhibitor, a surfactant and a phosphate ester. The pre-corroded carbon steel surface had a 10 µm thick layer of iron oxide (Fe_3O_4), shown in Figure 2-49. The overall corrosion behaviour was assessed using linear polarisation resistance (LPR) measurements and the carbon steel coupons were later analysed post-test using scanning electron microscopy (SEM). Results gathered using Electrochemistry and SEM indicated that the flow velocity had a negligible effect on the performance of corrosion inhibitors (32).

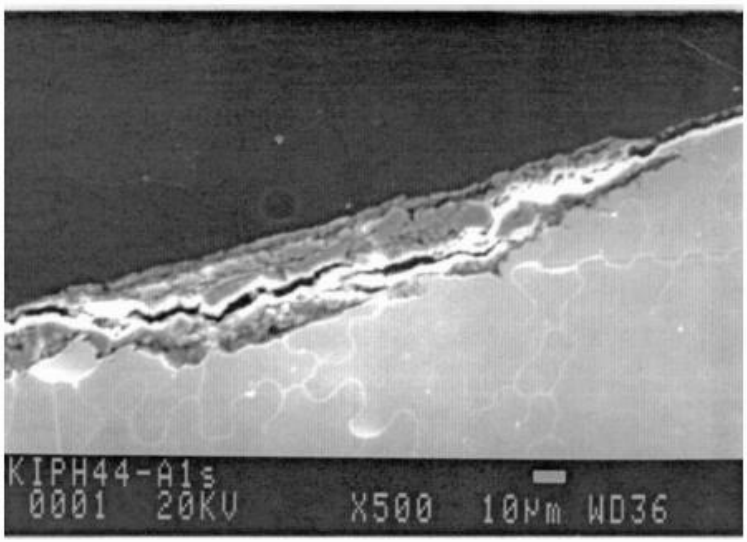

Figure 2-49 Cross-section SEM image of pre-corroded X65 carbon steel with an Fe_3O_4 corrosion product layer (32)

Further findings indicated that the inhibitors worked together with the corrosion product to protect the X65 carbon steel surfaces, where the corrosion inhibitors did not prevent corrosion products from precipitating onto the steel surfaces. Kvarekval *et al* (32) also indicated that the effect of temperature is dependent on the inhibitor formulation. It was concluded that the inhibitors may have adsorbed onto the surface which led to strengthening of corrosion products, however as no baseline measurements were recorded, it is difficult to separate the individual contribution of the inhibitors and the corrosion products towards the overall protection afforded by the two.

The interaction between an imidazoline corrosion inhibitor and iron carbonate corrosion products was evaluated by Sun *et al* (84) to determine the effect of corrosion inhibition on precipitation and growth of iron carbonate. Glass cell experiments were conducted at 80˚C in CO_2 saturated brines containing 1 wt. % NaCl. Electrochemistry and weigh loss was used to determine the interaction between the inhibitor and the corrosion product. Post-test SEM analysis was conducted to confirm the influence of the inhibitor on the precipitation and growth of iron carbonate. To determine the individual contributions by the inhibitor and the corrosion product, Sun *et al* (84) conducted three sets of experimental tests. The first experiment was conducted without an inhibitor while corrosion products were precipitating onto the steel surface, the second was conducted with an imidazoline inhibitor added before any corrosion products had precipitated and the third experiment was conducted with the imidazoline inhibitor added while the iron carbonate corrosion products were precipitating. This methodology enabled the determination of individual contributions provided by the inhibitor and the corrosion product towards the overall corrosion protection afforded by the two components. Findings obtained by Sun *et al* (84) indicated that in the absence of the imidazoline corrosion inhibitor, the corrosion rate decreased from 1 to 0.08 mm/year after 70 hours of exposure due to the formation of an iron carbonate corrosion product layer. However, when 25 ppm of the imidazoline corrosion inhibitor was added after 2 hours of exposure, the corrosion rate decreased from 1 mm/year to 0.1 mm/year within 5 hours of exposure. With the inhibitor added in non-scaling conditions the corrosion rate also managed to decrease to 0.1 mm/year however it took 20 hours, as indicated in Figure 2-50.

These results indicated that the imidazoline corrosion inhibitor was more efficient in the presence of corrosion products.

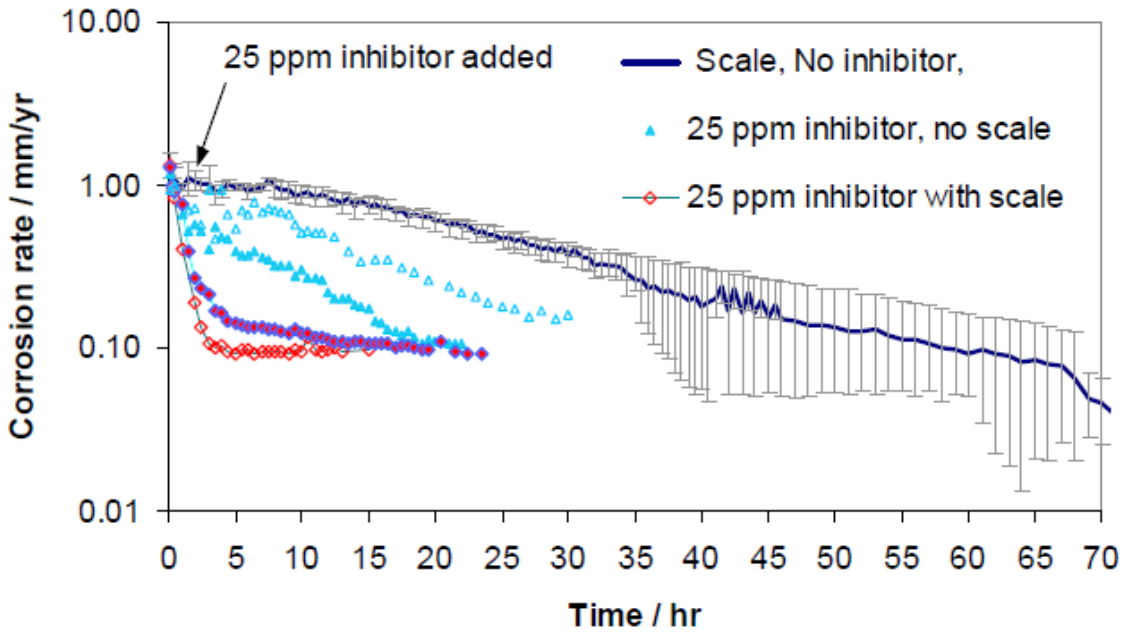

Figure 2-50 Influence of imidazoline inhibitor on corrosion rate in scaling and non-scaling conditions at 80˚C, pH 6.6, with inhibitor addition after 2 hours of exposure (84)

To further evaluate this, Sun *et al* (84) conducted another experiment where the inhibitor was added after 40 hours of exposure. This was done in order to determine whether or not the imidazoline corrosion inhibitor would be more effective in the presence of a more protective iron carbonate corrosion product layer. The obtained results indicated that the corrosion rate decreased from 1 mm/year to 0.05 mm/year, proving that the inhibitor was more efficient when injected in the presence of protective corrosion products. SEM analysis showed that the imidazoline corrosion inhibitor retarded the growth of iron carbonate on the steel surface when dosed 5 hours after the experiment had started, as shown by Figure 2-51.

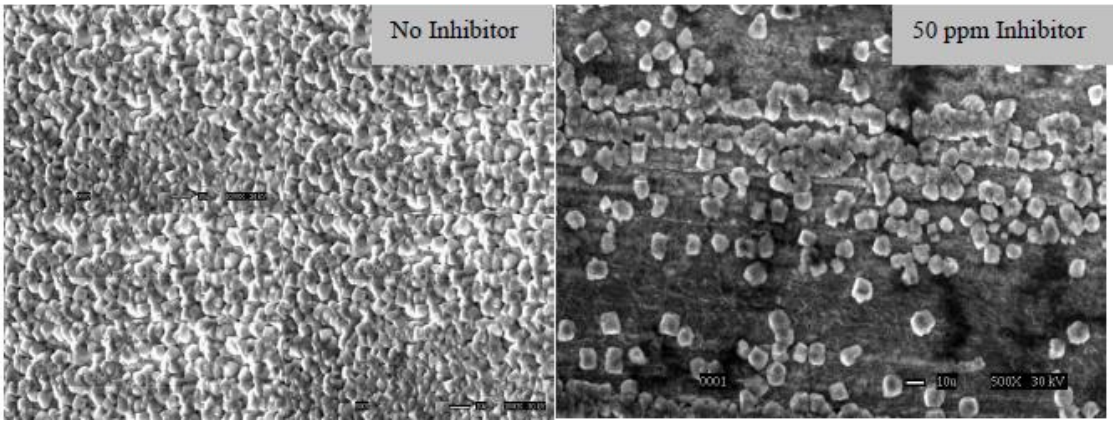

Figure 2-51 Top-view SEM images of experiments with no inhibitor (left) and with 50ppm of an imidazoline inhibitor (right), injected after 5 hours of exposure at pH 6.6 and 80˚C (84)

The interaction between corrosion inhibitors and corrosion products was evaluated by Gulbrandsen *et al* (31) using a combination of glass cell tests and contact angle experiments. Contact angle experiments were conducted on initially oil and water wetted surfaces to determine whether inhibitors have an influence on the wettability of steel surfaces covered with partially protective layers of iron carbonate corrosion products. Tests were conducted at ambient temperature with 1 bar of CO_2. Three inhibitors were tested; a cetyl trimethyl ammonium bromide (CTAB), an oleic imidazoline salt and a phosphate ester corrosion inhibitor. Findings indicated that on initially oil wetted surfaces, all inhibitors changed the wettability of the iron carbonate covered surfaces, resulting in hydrophobic states at concentrations as low as 10 ppm except the CTAB inhibitor which caused the surface to become more hydrophilic at all concentrations, as indicated by Figure 2-52. However, on initially water wetted surfaces, none of the inhibitors changed the contact angles at any inhibitor concentration which meant that the surfaces remained hydrophilic.

Electrochemical experiments were also conducted using glass cells containing 3 wt.% NaCl brines at 60˚C. The obtained results indicated that the presence of oil had enhanced corrosion inhibitor performance which may be explained by the change in wettability observed on initially oil wetted iron carbonate surfaces. However the nature of electrochemical tests conducted by Gulbrandsen *et al* (31); almost simultaneous addition of oil and inhibitor and change in temperature during experiments makes it difficult to relate the results from the two sets of experiments. Not only were the two sets of experiments conducted at different

temperatures but no baseline measurements were gathered during the glass cell experiments which makes it difficult to establish whether the observed effects of the inhibitors would be similar in the two different environmental conditions.

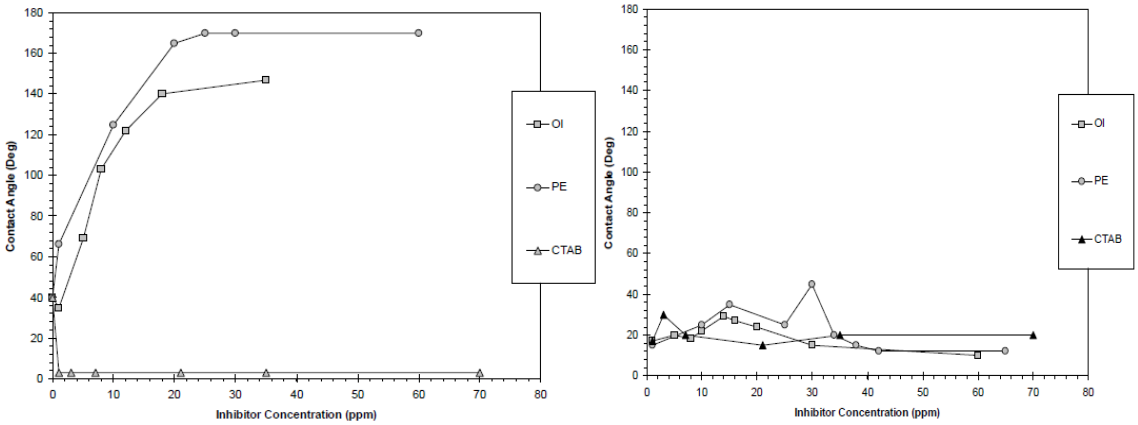

Figure 2-52 Contact angle as a function of inhibitor concentration for water in oil experiments on iron carbonate (left) and oil in water experiments on iron carbonate (right) at 1 bar CO_2, 3 wt.% NaCl at ambient temperature (31)

Foss *et al* (103) evaluated the influence of corrosion inhibitors on wettability alteration and found that both oleic imidazoline salt and phosphate ester corrosion inhibitors cause a complete hydrophilic to hydrophobic transition at 35 and 95 ppm respectively. These results are not consistent with results gathered by Gulbrandsen *et al* (31), although this could have been caused by the difference in pre-corrosion time/conditions which might have influenced the steel surface conditions.

Foss *et al* (104) further studied the effect of corrosion inhibitors on pre-corroded surfaces and used zeta potentials to determine whether inhibitors adsorb onto iron carbonate using iron carbonate particles. Tests were conducted in 0.1 wt.% NaCl brines at 1 bar CO_2 and 22˚C. Three corrosion inhibitors were tested; a cetyl trimethyl ammonium bromide (CTAB), an oleic imidazoline salt and a phosphate ester. The experiments were conducted in the absence of oil and in the presence of 2 vol.% oil. Results gathered by Foss *et al* (104) indicated that all three inhibitors had adsorbed onto the iron carbonate surfaces at both pH 4 and 6, as shown by Figure 2-53. The results also indicated that the addition of oil had no effect on the zeta potential which indicates that the adsorption of inhibitors onto iron carbonate is not affected by the presence or absence of oil. Calculations conducted by Foss *et al* (104) indicated that 0.1 ppm of the inhibitor

would be consumed due to adsorption and although several assumptions had to be made for this calculation, it was never mentioned whether the total inhibitor consumption due to adsorption would vary across different inhibitors. The Zeta potential tests conducted by Foss *et al* (104) were conducted on an iron carbonate suspension and not on a steel specimen with iron carbonate however the methodology is very unique which makes it extremely difficult to comprehend how realistic these findings are.

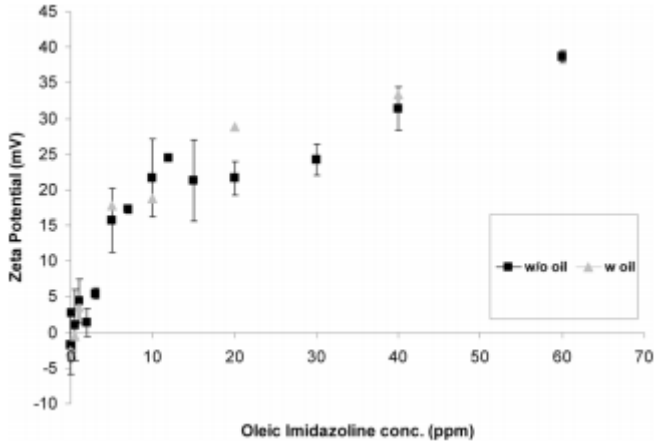

Figure 2-53 Zeta potential of $FeCO_3$ as a function of inhibitor concentration (104)

The interaction between a quaternized amine corrosion inhibitor and iron carbonate corrosion products was evaluated by Wong *et al* (105). Glass cell tests were set up at 80˚C in CO_2 saturated brines with varied Cl^- contents ranging from 1000 to 10,000 ppm. LPR was conducted in order to determine the corrosion rates. SEM/EDS and XRD were used for post-test analysis to examine the corrosion products present on the steel surfaces. Baseline measurements were conducted while corrosion products were precipitating onto the steel surface in absence of the quaternized amine inhibitor. This was tests conducted in the presence of 50 ppm of the corrosion inhibitor while corrosion products were precipitating onto the steel surface. These experiments were repeated with and without flow using a rotating cylinder electrode (RCE). Results obtained by Wong *et al* (105) indicated that there was a synergistic relationship between the quaternized amine corrosion inhibitor and the $FeCO_3$ corrosion products which had precipitated or were precipitating onto the surface. Electrochemistry data together with ex-situ analytical techniques indicated that the quaternized amine corrosion inhibitor increased the precipitation rate of iron carbonate and therefore

caused it to become more compact and resistant, as shown by Figure 2-54. These findings are consistent with results obtained by Kvarekval *et al* (32).

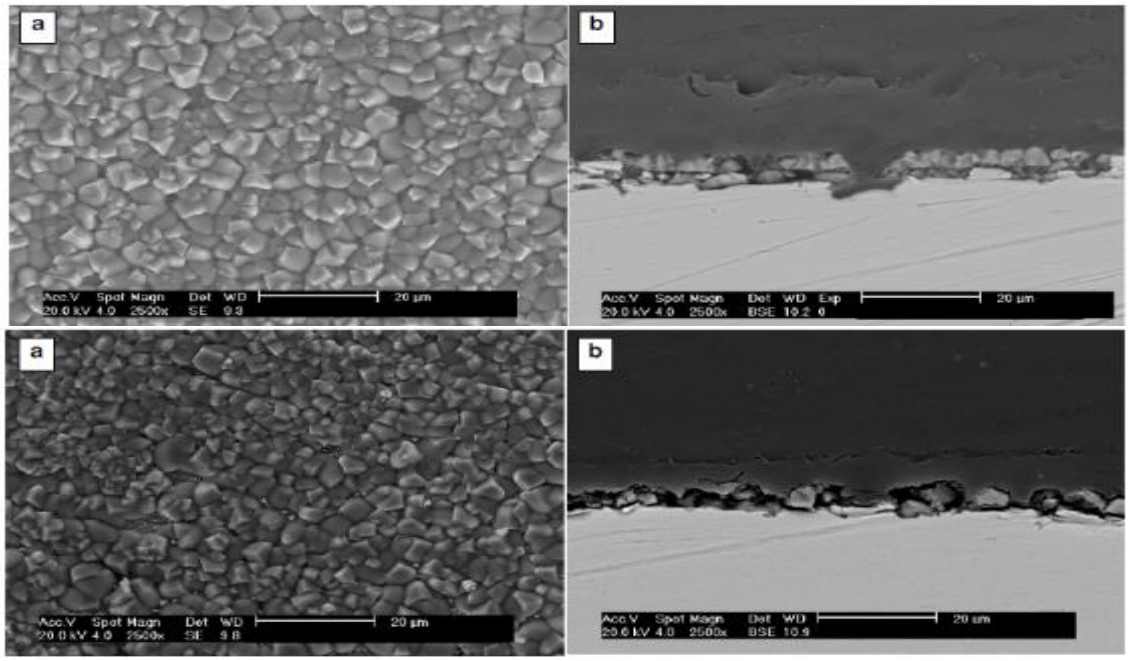

Figure 2-54 SEM images of experiments at 80˚C, pH 6.5 at 1000rpm, without inhibitor (top), with quat inhibitor (bottom), Top-view (left) and cross-section (right) (105)

LPR measurements indicated that in the absence of the corrosion inhibitor the corrosion rate decreased from 4 to 0.3 mm/year within 6 hours of exposure. However, with the inhibitor injected into the system at the beginning of the test, the corrosion rate stabilised at 0.15 mm/year after 8 hours indicating a synergistic relationship between the inhibitor and the corrosion product. Results gathered by Wong *et al* (105) indicated that there was a synergistic relationship between a quaternized amine inhibitor and iron carbonate, however the inhibitor was only tested at the beginning of the experiment before any iron carbonate had precipitated onto the steel surface which raises the question of whether the inhibitor would have the same synergistic effect when used on an already precipitated, partially or fully protective layer of $FeCO_3$.

Wong *et al* (106) conducted a further study on the interaction between corrosion inhibitors and corrosion products. Further tests were conducted using the same conditions as the ones previously mentioned, however this time using an imidazoline corrosion inhibitor and a phosphate ester inhibitor. EDS was used to identify the corrosion products on the steel surface and impedance

measurements were used in conjunction with SEM to determine whether the inhibitors had adsorbed onto the steel surfaces. Results obtained by Wong *et al* (106) indicated that the imidazoline corrosion inhibitor had prevented the growth of iron carbonate crystals when concentrations of 25 ppm or more were used. These results are consistent with findings by others such as Sun *et al* (84), however Wong *et al* (106) also found that the imidazoline inhibitor and the iron carbonate corrosion product were complementary when 10ppm or less was used. Wong *et al* (106) indicated that the phosphate ester inhibitor prevented the growth of iron carbonate, and it was therefore assumed that the inhibitor had been adsorbed onto the steel surface. It was concluded that both of the corrosion inhibitors had provided similar results in terms of protection however by different mechanisms of action.

The performance of an imidazoline corrosion inhibitor in CO_2 environments was investigated as a function of pre-corrosion time by Paolinelli *et al* (28). Tests were conducted at 40ºC in CO_2 saturated 5 wt.% NaCl brines at pH 6. Carbon steel was pre-corroded for 24 and 72 hours which resulted in the precipitation of iron carbide corrosion products. The 24 and 72 hour pre-corroded carbon steel surfaces were then exposed to 72 hour exposures in brines containing the imidazoline corrosion inhibitor. The obtained results were compared to tests conducted in the absence of the corrosion inhibitor, as shown by Figure 2-55.

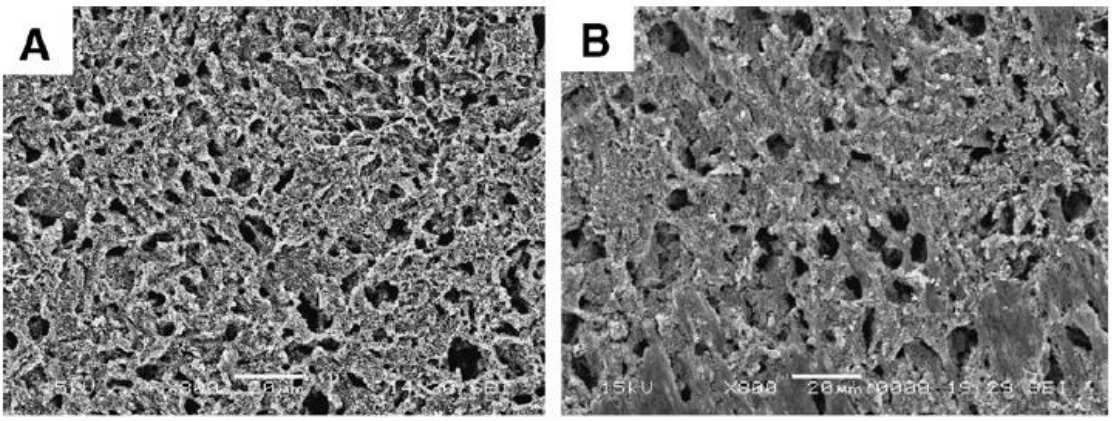

Figure 2-55 Top-view SEM after 72 hour pre-corrosion (a) before inhibitor addition and (b) after exposure to the inhibitor (28)

50ppm of the corrosion inhibitor was injected and its behaviour was monitored using electrochemical measurements. The injection of the imidazoline corrosion inhibitor resulted in the formation of iron carbide corrosion products for both pre-

corrosion periods which appeared to have been modified morphologically after exposure to the imidazoline corrosion inhibitor. Paolinelli *et al* (28) concluded that the addition of the corrosion inhibitor had led to formation of a protective film however this was not confirmed.

Gulbrandsen *et al* (29) also examined the effects of pre-corrosion on the performance of corrosion inhibitors in CO_2 environments. However unlike the studies conducted by Paolinelli *et al* (28), Gulbrandsen *et al* (29) evaluated the effects of long term pre-corrosion. Carbon steel was pre-corroded for durations of up to 18 days before exposure to the corrosion inhibitor. The pre-corroded carbon steel surfaces were tested using four corrosion inhibitors; two imidazoline corrosion inhibitors and two amine corrosion inhibitors. Experiments were conducted in CO_2 saturated 1-3 wt.% NaCl, pH 5 at 20 and 50ºC. The tests were conducted in glass cells and in glass loops in order to evaluate the effects of flow. The corrosion behaviour was monitored using linear polarisation resistance (LPR) and using the mass loss technique. Further information regarding the overall corrosion behaviour was gathered using slow potentiodynamic polarisation sweeps. The iron content was kept at a minimum during all tests in order to avoid precipitation of iron carbonate and as a result the pre-corrosion periods only led to the formation of iron carbide corrosion products. Gulbrandsen *et al* (29) observed a reduction in the performance of all four corrosion inhibitors with increasing experimental temperature and pre-corrosion time as shown by Figure 2-56.

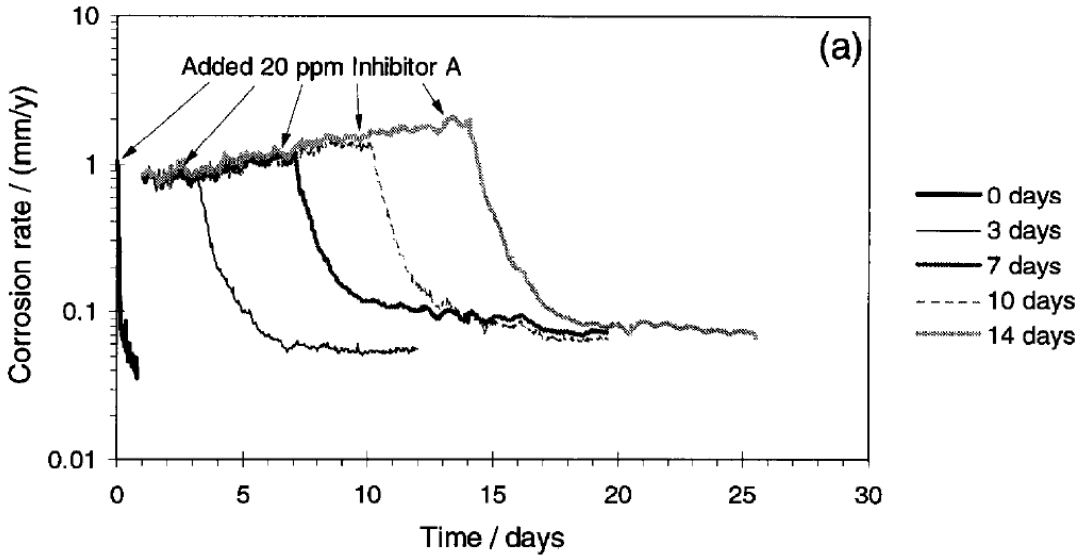

Figure 2-56 Effect of pre-corrosion time on corrosion inhibition (29)

The reduction in inhibitor performance was found to be associated with localised corrosion in the form of deep pits. The localised corrosion attacks were attributed to the iron carbide corrosion products which had formed on the steel surfaces. It was concluded that the influence of pre-corrosion on corrosion inhibition should be given more attention during corrosion inhibitor evaluation, as the side effects associated with inhibition on pre-corroded steel surfaces can then be overcome by careful inhibitor selection (29).

The impact of pre-corrosion on the inhibition process of low alloy steel was considered by Zhang *et al* (30). Tests were conducted using 3 wt.% NaCl brines at 60ºC and 1 MPa CO_2 partial pressure for pre-corrosion periods of 2, 24 and 48 hours. The effect of pre-corrosion on inhibition was evaluated using an imidazoline corrosion inhibitor. The weight loss method was used in conjunction with electrochemical measurements for corrosion rate monitoring and for inhibitor efficiency calculations. Steel surfaces were analysed using SEM, EDS and XRD for the purpose of characterisation. The 2, 24 and 48 hour pre-corrosion periods resulted in a roughened surface, an iron carbide covered surface and precipitation of a porous and non-protective iron carbonate layer respectively, as shown by Figure 2-57.

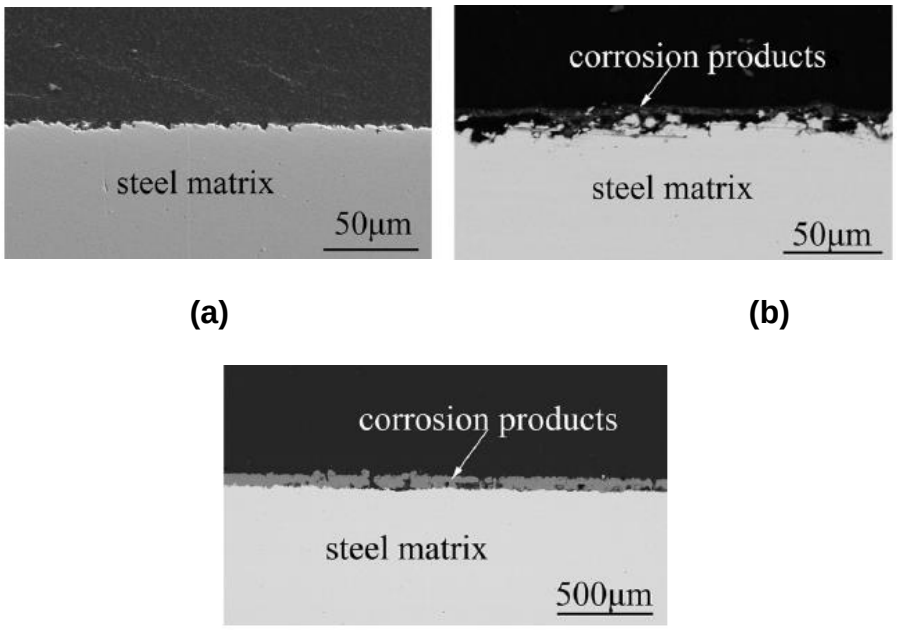

Figure 2-57 Low alloy steel pre-corroded for (a) 2, (b) 24 and (c) 48 hours at 60ºC resulting in a roughened surface, an iron carbide layer and porous iron carbonate respectively (30)

Zhang *et al* (30) observed a reduction in the efficiency of the imidazoline corrosion inhibitor after exposure to the pre-corroded surfaces, where the efficiency reduced by 26.8, 93.9 and 79.6% for 2, 48 and 48 hours of pre-corrosion respectively. These findings are consistent with results obtained by Gulbrandsen *et al* (29). The reduction in inhibition efficiency with pre-corrosion also resulted in localised corrosion, as indicated by Figure 2-58 which was attributed to corrosion product precipitation and increase in steel surface area. However the localised corrosion rate in the absence of the corrosion inhibitor was not provided which makes it difficult to determine the extent of localised corrosion. However at a doubled inhibitor dosage, the reduction in inhibitor efficiency caused by pre-corrosion was found to be greatly reduced where the efficiencies where then only 2.3, 17.2 and 13.9% less than the inhibitor efficiency obtained on wet-ground steel (98.7%).

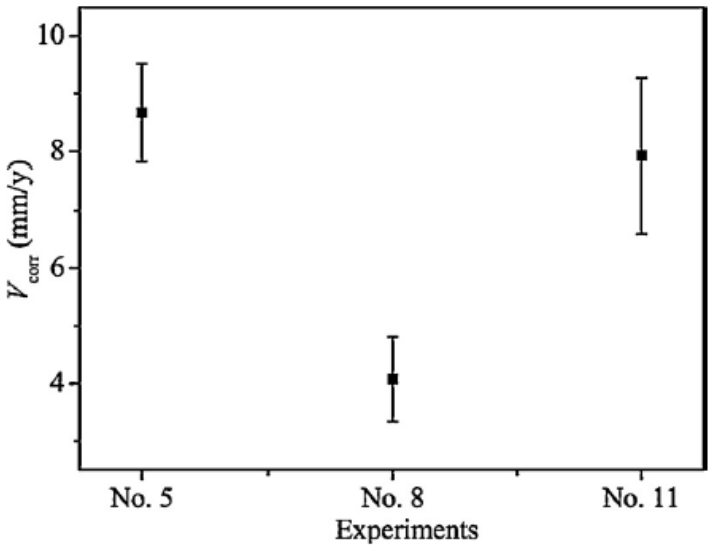

Figure 2-58 Localised corrosion rates of inhibited surfaces pre-corroded for 2 (No. 5), 24 (No. 8) and 48 hours (No. 11) (30)

2.12 Summary and Knowledge Gap

The kinetics and characteristics of $FeCO_3$ corrosion products have been widely studied in CO_2 environments (54, 56, 57, 59, 61, 62, 71-76). The review of literature conducted in this research area has indicated that the kinetics and characteristics of $FeCO_3$ corrosion products is extremely dependant on environmental conditions such as temperature and CO_2 partial pressure. The influence of cations such as Ca^{2+} ions on the kinetics and characteristics of

corrosion products and precipitation of mixed carbonates has been far less documented within the existing literature (67, 68, 70). However the following can be concluded from the review of corrosion products in CO_2 environments;

1. Iron carbonate ($FeCO_3$) corrosion products generally become more protective with increasing exposure time and temperature due to the establishment of more compact corrosion products with improved surface coverage.
2. The rate of precipitation and morphology of iron carbonate is extremely dependant on temperature, pH and exposure time.
3. The porosity of corrosion products tends to decrease with increasing exposure time and temperature resulting in improved protection against uniform corrosion.
4. Crystal grain sizes of iron carbonate increase with increasing temperature which is also associated with more compact corrosion products resulting in improved protection against uniform corrosion.
5. Duplex layered iron carbonate corrosion products with protective and non-protective layers can precipitate in CO_2 environments.
6. The presence of $CaCO_3$ or $CaCl_2$ within test brines can result in the precipitation of mixed iron-calcium carbonates ($Fe_xCa_yCO_3$).
7. $Fe_xCa_yCO_3$ is generally more porous and less protective than $FeCO_3$ which tends to result in more severe localised corrosion attacks.
8. Greater incorporation of Ca^{2+} into $FeCO_3$ crystal lattice can results in a less protective $Fe_xCa_yCO_3$ layer.

Several corrosion inhibitors have been tested and evaluated in the past for both low and high temperature application in CO_2 environments (99-102, 107), however only a few were found to have assessed their performance on the localised corrosion behaviour (86, 96). The performance of corrosion inhibitors is not only dependent on the type of compound but is also highly dependent on the specific formulation which makes it extremely difficult to compare findings across different studies. However the following conclusions could the drawn from the review of corrosion inhibitor evaluation in CO_2 environments;

1. Imidazoline based corrosion inhibitors are believed to protect steel surfaces by adsorption of a hydrophobic film.

2. The performance of corrosion inhibitors tends to decrease with increasing temperature which is believed to be partly due to degradation caused by hydrolysis of corrosion inhibitors at elevated temperatures.
3. The presence of oil can influence the performance of corrosion inhibitors and usually results in improved performance due to improved inhibitor film properties.
4. Up to 50 times greater inhibitor concentrations may be required to achieve sufficient corrosion protection at temperatures above 120 ºC using corrosion inhibitors however this is highly dependent upon the chemical formulation.
5. Once pits develop on steel surfaces, extremely high inhibitor concentrations may be required to reduce or prevent pit growth.

Numerous publications which have focused on the evaluation of corrosion inhibitor performance have concluded that testing inhibitors in the presence of corrosion products (pre-corroded surfaces) can help improve our knowledge of how inhibitors operate, interact, transport and incorporate with/within corrosion products, however existing literature within this area of study is extremely restricted (29-32, 84, 97, 103-106). However a review of the existing literature has led to the following conclusions;

1. Both Synergistic and antagonistic relationships between corrosion inhibitors and corrosion products have been reported within the existing literature demonstrating the dependency of inhibitor formulation on their performance on pre-corroded steel.
2. In some cases corrosion inhibitors have been observed to result in strengthened and improved protectiveness of corrosion products resulting in a faster rate of reduction in corrosion rate (Synergistic effect).
3. Some have reported a reduced efficiency of corrosion inhibitors when used in the presence of corrosion products (Antagonistic effect).
4. Some corrosion inhibitors may able to prevent the precipitation of corrosion products at specific concentration thresholds illustrating the importance of evaluating corrosion inhibitors across a range of concentrations
5. Corrosion inhibition on pre-existing corrosion product covered surfaces may result in modification of the corrosion products.

6. The performance of corrosion inhibitors generally decreases in the presence of increasingly protective corrosion product layers.
7. The use of corrosion inhibitors in the presence of corrosion products may result in severe localised corrosion attacks.
8. Corrosion inhibitors can change the wettability of pre-corroded surfaces.

Based on these findings the following knowledge gaps can be summarised;

1. The influence of calcium ions on the overall corrosion behaviour has not been evaluated at high temperatures (above 80ºC).
2. The optimum inhibitor dosage has never been evaluated for any type of corrosion inhibitor using a systematic testing procedure taking into consideration both the uniform and the localised corrosion behaviour.
3. The influence of aged inhibitor compounds on localised/pitting corrosion has not been evaluated in the past.
4. The performance/interaction of corrosion inhibitors with corrosion products has never been evaluated in standardised conditions which enable comparison of inhibitor performance on different corrosion product covered surfaces.
5. The individual contributions provided by inhibitor and corrosion products towards corrosion protection have never been de-coupled in an attempt to understand the true synergistic/antagonistic interaction between a corrosion inhibitor and a corrosion product.

Chapter 3 Experimental Methodology

3.1 Material Preparation

X65 carbon steel specimens were used as working electrodes for all corrosion tests presented throughout this thesis. However the preparation procedure varied depending on the nature of the experiment. In addition to the X65 carbon steel specimens, platinum specimens were prepared and used as counter electrodes for electrochemical testing within autoclaves. The preparation procedure for these electrodes will be detailed.

3.1.1 Specimens Used for Mass Loss Evaluation

X65 carbon steel specimens were machined into discs with diameters of 25 mm and thicknesses of 6 mm. A 3 mm diameter hole was drilled into in the edge of each specimen to enable attachment onto the autoclave specimen holder. The carbon steel specimen is shown in Figure 3-1. The specimens were prepared no more than 30 minutes prior to each experiment. The preparation procedure consisted of wet-grinding each coupon successively with P120, P320 and P600 silicon carbide (SiC) paper, followed by rinsing with distilled water and acetone before gently drying with compressed air. Two specimens (total surface area of ~29 cm^2) were prepared for each experiment and were weighed after they had been wet-ground and degreased to enable corrosion rates to be determined via gravimetric analysis. The X65 carbon steel specimens were weighed using an electronic balance to within an accuracy of 0.01 mg. The manufacturer's elemental composition of X65 carbon steel is provided in Table 3-1, with the material possessing a ferritic-pearlitic microstructure, shown in Figure 3-2.

Figure 3-1 X65 carbon steel mass loss specimen

Table 3-1 Elemental composition of X65 steel (wt.%)

C	Si	Mn	P	S	Cr	Mo	Ni
0.12	0.18	1.27	0.008	0.002	0.11	0.17	0.07
Cu	**Sn**	**Al**	**B**	**Nb**	**Ti**	**V**	**Fe**
0.12	0.008	0.022	0.0005	0.054	0.001	0.057	Balance

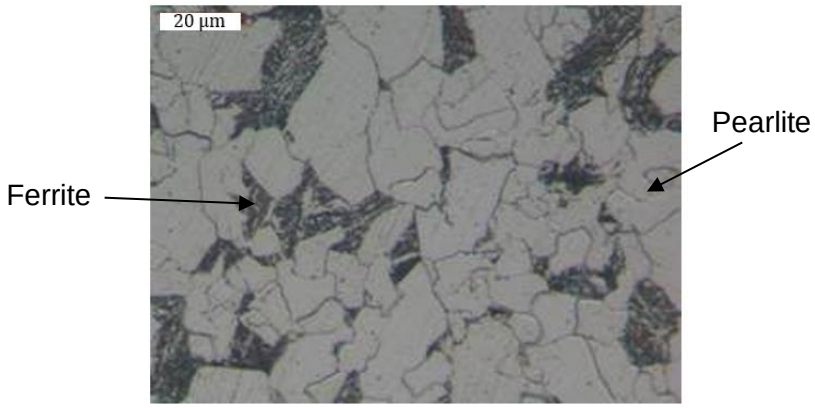

Figure 3-2 X65 carbon steel microstructure

3.1.2 Specimens Used for Electrochemical Measurements

3.1.2.1 Autoclave Testing

X65 carbon steel specimens were machined into discs with diameters of 25 mm and thicknesses of 6 mm. The steel specimens were then wet-grinded with 120 silicon carbide (SiC) grit paper, followed by rinsing with acetone and distilled water before drying gently with compressed air. A single high temperature resistant Kapton insulated wire was then attached to each carbon steel specimen using a two-component conductive glue and was left to set for 24 hours. Once the conductive glue had set, a layer of high temperature resistant silicone was applied onto the carbon steel disc face containing the Kapton insulated wire. The purpose of the silicone was to seal the entire surface area of the disc shaped sample where the Kapton insulated wire had been attached with conductive glue. The total exposed carbon steel surface area for each specimen was 9.6 cm^2. The X65 specimen was then wet-grinded no more than 30 minutes prior to an experiment successively with 120, 320 and 600 silicon carbide (SiC) grit paper, followed by rinsing with acetone and distilled water before gently drying with

compressed air. One specimen was used for each test in conjunction with a mass loss specimen for the purpose of maintaining a surface area to volume ratio of 38.4 cm^2/L. Platinum specimens were used as counter electrodes during autoclave electrochemical tests. The platinum counter electrode was square shaped with dimensions of 10×10×5 mm and was prepared using the same procedure as for the X65 carbon steel working electrode. Figure 3-3 shows a prepared autoclave electrochemistry specimen.

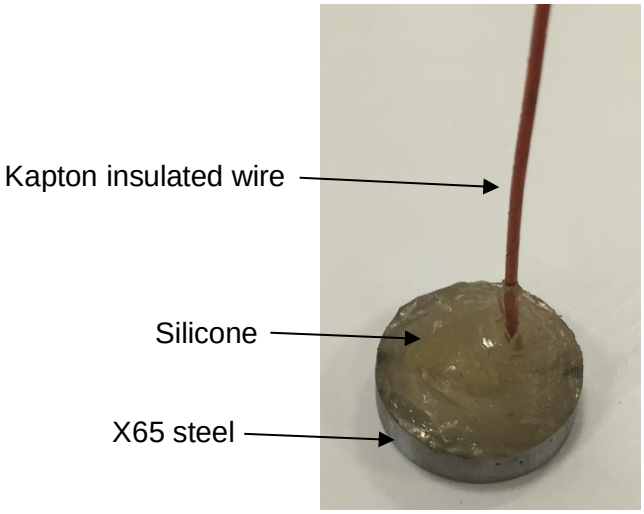

Figure 3-3 X65 carbon steel specimen used for electrochemical evaluation within autoclaves

3.1.2.2 Glass Cell Testing

X65 carbon steel discs with diameters of 25 mm and thicknesses of 6 mm were machined and embedded within a resin to expose a total surface of 4.9cm^2. Insulated wires were soldered to the steel specimens prior to the steel being embedded within a two component commercially available resin. The preparation procedure prior to each experiment consisted of wet-grinding each specimen successively with 120, 320 and 600 silicon carbide (SiC) grit paper. Specimens were then rinsed with acetone and distilled water before being dried using compressed air. Figure 3-4 shows a prepared X65 carbon steel specimen used for electrochemical evaluation within glass cells.

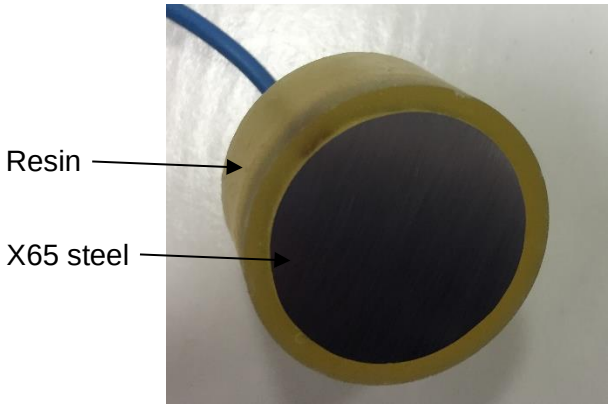

Figure 3-4 X65 carbon steel specimen used for electrochemical evaluation within glass cell tests

3.2 Brine Preparation Procedure

Corrosion tests were conducted in brines free of calcium ions and in brines which included varying concentrations of calcium ions, as demonstrated by Table 3-2. For experiments performed in the absence of Ca^{2+}, a 3 wt.% NaCl solution was used. In experiments containing Ca^{2+}, the required concentration of the divalent cation was achieved through the addition of calcium chloride di-hydrate ($CaCl_2 \cdot 2H_2O$) salt to distilled water, with the appropriate amount of NaCl added to the solution to maintain a consistent chloride concentration at 18197 ppm. A maximum concentration of 5000 ppm Ca^{2+} was used in tests in order to evaluate its influence under realistic brine compositions. Each solution was prepared at least 24 hours in advance with CO_2 bubbled into the solution to ensure saturation before every experiment. The full list of solution chemistries and temperatures considered within this thesis is provided in the experimental test matrix in Table 3-2.

Table 3-2 Experimental brine compositions

Test condition	NaCl content (wt.%)	Total Cl^- (ppm)	Ca^{2+} (ppm) ($CaCl_2 \cdot 2H_2O$ in wt.%)
1	3	18197	0
2	1.54		5000 (1.83)
3	2.98		50 (0.018)
4	2.97		100 (0.037)
5	2.93		250 (0.092)
6	2.85		500 (0.18)
7	2.71		1000 (0.37)
8	2.27		2500 (0.92)

3.3 Autoclave Development and Testing Procedures

3.3.1 Mass Loss Testing Procedure

A full schematic representation of the autoclave setup is shown in Figure 3-5. Two X65 carbon steel specimens were attached to the non-conducting autoclave sample holder using screws manufactured from a high temperature resistant polymer. The specimens were placed away from the autoclave walls and other components to prevent any galvanic effects during the experiments. 750 ml of the prepared deaerated brine solution was then pumped into the autoclave through CO_2 purged lines to avoid oxygen ingress before sealing the fluid entry system. The specimen surface area to brine volume ratio within the autoclave system was 38.4 cm^2/L. Inlet and outlet lines to and from the autoclave were then sparged with CO_2 for an hour to remove any potential residual traces of oxygen from the system. The autoclave was then heated to 25˚C whilst being continuously purged at atmospheric pressure with CO_2, allowing the gas to vent through one exit fitting. Once the solution reached 25ºC, CO_2 pressurisation was ceased and the autoclave system was shut in at room pressure. The autoclave

was then heated to the desired experimental temperature (either 80 or 150ºC). The starting point of the experiment was taken from the point at which the required operating temperature was reached. Once the experiment had finished, the autoclave was cooled down to 80˚C and depressurised. The specimens were then removed from the autoclave, rinsed with distilled water and dried with compressed air. One specimen was preserved in a desiccator to allow for further analysis of the corrosion product, while the other specimen was used for mass loss/gain measurements. For mass loss/gain calculations, all the specimens were weighed before the experiment, after the experiment with the corrosion products on the surface and after the experiment in the absence of corrosion product. For the final mass measurement, the corrosion product was removed with the aid of Clarke's solution (20 g antimony trioxide + 50 g tin (II) chloride + 1000 ml hydrochloric acid) in accordance with ASTM Standard G1-03 (108). The mass measurements were then used to determine the corrosion product mass and the integrated corrosion rate over the duration of the experiment in units of mm/year (based on the specimen surface area exposed to the test solution). The CO_2 partial pressures and total pressures for all experimental conditions are illustrated in Table 3-3.

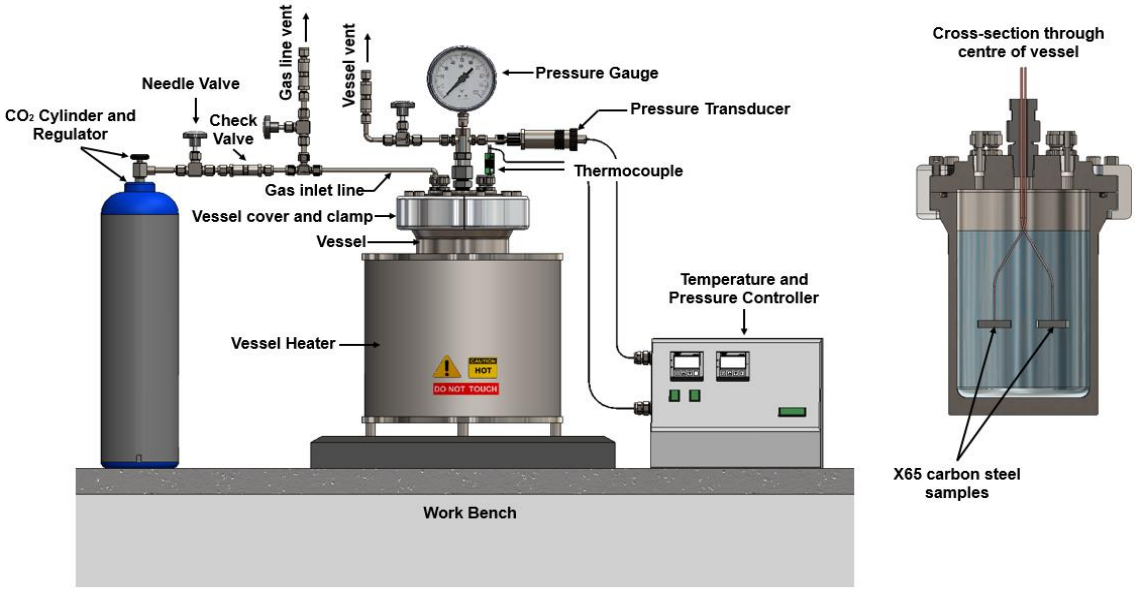

Figure 3-5 Schematic of autoclave set-up for evaluation of X65 carbon steel corrosion in CO_2-containing environments at elevated temperatures

Table 3-3 Measured total and calculated partial pressures in autoclave experiments at 80 and 150 ºC

Test Condition	p_{CO2} at 25˚C (bar)	p_{CO2} at 80˚C (bar)	P_{Total} at 80˚C (bar)	p_{CO2} at 150˚C (bar)	P_{Total} at 150˚C (bar)
1 - 2	1	1.4	1.9	1.5	6.2
3 - 8	1	1.4	1.9	Na	Na

3.3.2 Autoclave *in-situ* Electrochemistry Development

The design and development of an autoclave system capable of electrochemical measurements at high temperatures included the following criteria;

1. Contamination free system.
2. Sealed wires that can be changed before/after each test.
3. Wires capable of electrochemical measurements within liquids at temperatures of up to 150ºC.
4. Specimens capable of operation in pressurised high temperature environments without connection issues.
5. Reference probe capable of electrochemical measurements in pressurised high temperature environment.
6. Ability to de-pressurize autoclave instantly without damaging reference probe.

The listed criteria cover three main aspects of design; Specimen and wiring, connection seal and the reference probe for electrochemical measurements.

3.3.2.1 Connection Seal

The purpose of the connection seal is to establish a perfect seal between wires exiting the autoclave system. To enable the capability of conducting electrochemical measurements within a closed autoclave environment, wires attached to working and counter electrodes within the autoclave require a sealed point of exist. As a result a seal is required to enable high temperature/pressure tests to be conducted while performing electrochemical measurements. The sealed wires are also required to be able to be removed and interchanged in an efficient manner in order to be able to insert and remove steel coupons before

and after electrochemical testing. A Conax Model PL gland was selected and used for its capability to meet the previously mentioned criteria. The Conax gland uses soft sealant technology (Teflon seal) with the capability of providing seals against liquids and gases. The gland is capable of operating temperatures and pressures of up to 232ºC and 690 bar respectively. The gland was connected to the autoclave system using an NPT thread mount and contained feedthroughs for 2 wires. The Conax gland is shown in Figure 3-6.

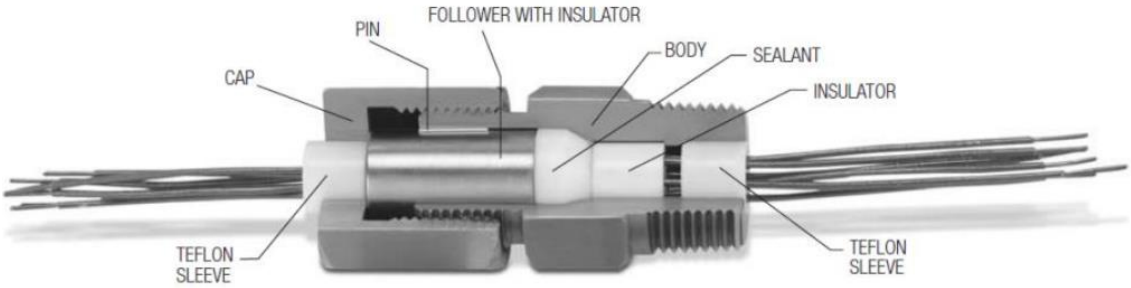

Figure 3-6 Conax model PL gland (109)

3.3.2.2 Wiring

X65 carbon steel and platinum specimens used as working and counter electrodes respectively, for electrochemical measurements within the autoclave system had to be modified in order to eliminate connection and contamination issues. X65 carbon steel specimens were machined into 25 mm discs with thicknesses of 6 mm and were prepared using the procedure detailed in Chapter 3.1.2. The wires used for electrochemical measurements were Kapton insulated wires. This type of wire was selected in order to eliminate brine contamination caused by copper wiring and due to its capability to perform for long exposure durations in high temperature/pressure environments without any connection problems. The wires used for testing were used once and then disposed of to eliminate them as a source of contamination.

3.3.2.3 Reference Probe

A CorrInstruments UltraDeg high temperature/pressure saturated Ag/AgCl reference electrode was fitted to the autoclave system to enable electrochemical measurements. The probe is specifically designed for electrochemical measurements within closed systems and is made of 316L stainless steel and has the capability of performing continuously at temperatures and pressures ranging from 0 to 305 ºC and 0 to 206 bar respectively. The probe was fitted to

the autoclave using a NPT fitting. A schematic diagram of the reference probe is illustrated in Figure 3-7.

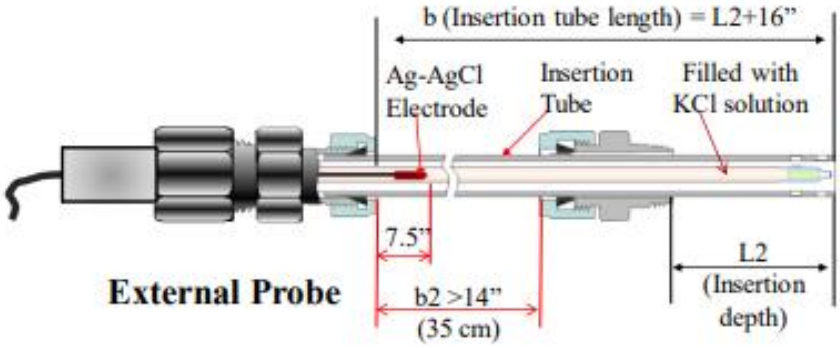

Figure 3-7 Schematic of Ag/AgCl reference probe (110)

3.3.3 Autoclave Electrochemical Testing Procedure

One X65 carbon steel specimen (working electrode) and one platinum specimen (counter electrode) were inserted into the autoclave using the Conax gland to feed their respective wires out of the autoclave lid. Both specimens were placed in the middle of the autoclave avoiding contact with each other or with the autoclave walls to prevent any galvanic effects during testing. Due to the addition of components fitted to the autoclave system to enable electrochemical measurements, the liquid capacity of the autoclave had reduced to 800 ml. However the surface area to volume ratio was once again maintained at 38.4 cm^2/l to allow for comparison with results gathered by mass loss evaluation. This was achieved by reducing the brine volume to 625 ml and by using an additional X65 carbon steel specimen (mass loss specimen). The combined X65 carbon steel surface area was therefore 24 cm^2. The mass loss carbon steel specimen was attached to a non-conducting autoclave sample holder using a high temperature resistant polymer screw, similar to the one used for mass loss testing. This carbon steel specimen was also placed away from the autoclave walls and any other components to prevent any galvanic effects during the experiments. Once the specimens had been inserted into the autoclave, it was purged with CO_2 for 2 hours to remove any potential residual traces of oxygen from the system. The desired volume of a pre-prepared and CO_2 saturated brine was then pumped into the autoclave system using an inlet fitting. The autoclave system was then shut in at room pressure and sparged with CO_2 for an additional hour before it was heated to the desired experimental temperature (either 80 or

150 ºC). The starting point of the experiment was taken from the point at which the required operating temperature was reached.

An Ivium CompactStat potentiostat was used to polarise the working electrode at ±15 mV about the open circuit potential (OCP) at a scan rate of 0.25 mV/s with a time interval of 15 minutes between measurements. Once the experiment had finished, the autoclave was cooled down to 80˚C and depressurised. The specimens were then removed from the autoclave, rinsed with distilled water, dried with compressed air and stored under vacuum until used for further analysis.

Anodic and cathodic potentiodynamic polarisation was conducted at 80 and 150 ºC in order to determine the anodic and cathodic Tafel constants. Potentials of ±300 mV away from the corrosion potential were applied at a scan rate of 0.5 mV/s. The recorded potentials was then plotted against the currents on a logarithmic scale which was then used to determine the anodic and cathodic Tafel constants. The Tafel constants were determined by extrapolating the anodic and cathodic polarization branches at potentials ±50 mV away from the corrosion potential in accordance with ASTM standards (111).

3.4 Glass Cell Testing Procedure

Glass cell experiments were conducted in 1 litre beakers containing pre-prepared 3 wt.% NaCl brines (prepared according to the procedure detailed in Chapter 3.2). One litre of the brine solution was poured into the glass cell. The brine solution was then bubbled with CO_2 for an additional two hours to eliminate any residual traces of oxygen. The brine temperature was regulated using a temperature probe and a hot plate. A single X65 carbon steel specimen (working electrode) along with a combined counter and reference Ag/AgCl probe were then inserted into the glass beaker after the 2 hour CO_2 saturation and heat-up period using holes within the beaker lid. The electrochemical measurement commenced as soon as the working electrode had been inserted into the glass cell system. The working electrode was polarised using an ACM Gill 8 potentiostat at ±15 mV about the open circuit potential (OCP) at a scan rate of 0.25 mV/s with a time interval of 15 minutes between measurements. Once the experiment had finished the working electrode was removed from the glass cell, rinsed with distilled water, dried with compressed air and stored under vacuum

for further analysis. A schematic illustration of the glass cell experimental set-up is shown in Figure 3-8.

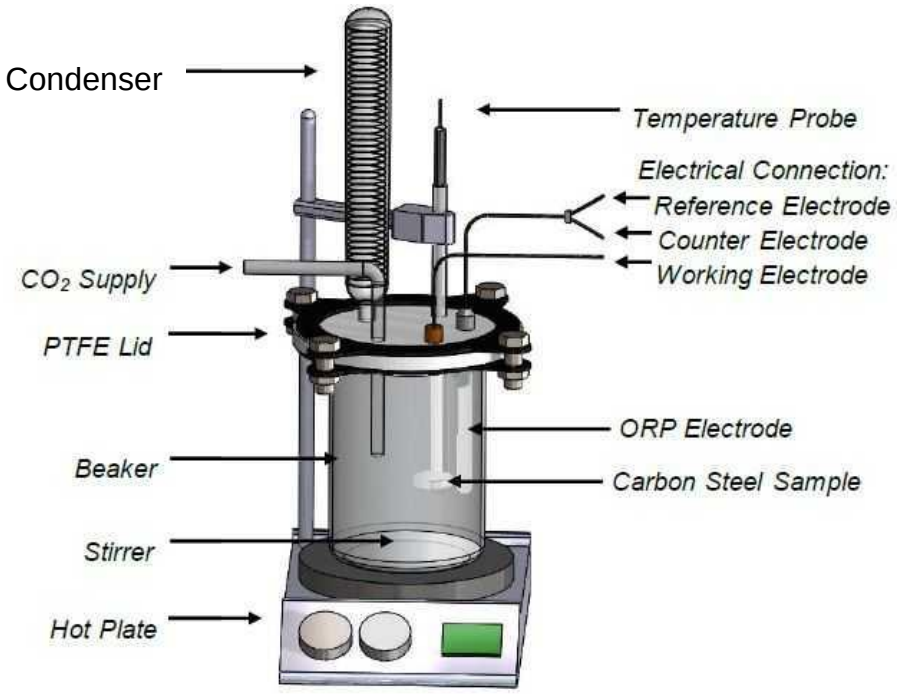

Figure 3-8 Schematic diagram of glass cell experimental set-up

3.5 Surface Analysis Methods

3.5.1 Scanning Electron Microscopy (SEM) and Energy Dispersive X-Ray spectroscopy (EDX)

3.5.1.1 Methodology

A Carl Zeiss EVO MA15 VP-SEM scanning electron microscope (SEM) integrated with an Oxford instruments AZtecEnergy energy dispersive X-ray (EDX) system with an 80mm X-max SDD detector was used for *ex-situ* surface analysis. The system provided secondary and backscattered imaging, EDX elemental mapping and point/line scans. The secondary electron function was generally used for the top-view SEM imaging. This function was selected for top-view images as it provides a higher resolution due to it being more surface sensitive (112). However in some cases the backscattered electron function was used as the backscattered electrons are more sensitive to the atomic mass of the nuclei which provides a greater contrast between the elements in a backscattered electron image (112). This results in improved imaging on surfaces where surface charging is a matter of concern. For surface analysis of

cross-sectional specimens, the backscattered electron function was used. This was due to the presence of a resin which could result in induced surface charging. A working distance of 8 mm and an accelerating voltage of 20 kV were used to collect images.

3.5.1.2 Preparation Procedure

Two types of specimens were used for analysis; top view specimens and cross-section specimens. The resin was left to completely set for at least 24 hours before the specimen was cut in half within the resin. The specimen was then polished along its face successively using P600 and P1200 SiC paper. It was then rinsed with distilled water and dried with using an air gun. The resin surrounding the steel cross-section was then carbon coated. The specimens were carbon coated beforehand along the height of their circumference to eliminate any surface charging effect. The entire face of the specimen was then iridium coated to reduce any surface charging effect. Figure 3-9 shows a prepared cross-sectioned specimen.

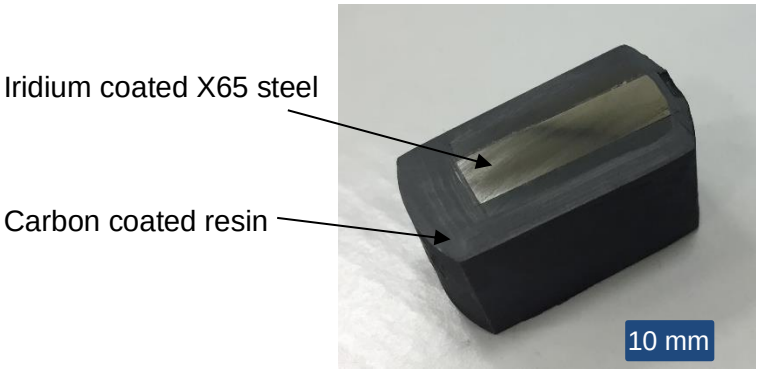

Figure 3-9 Prepared cross-sectional specimen

3.5.2 Bruker NPFLEX 3D Optical Non-Contact Profiler

NPFLEX 3D surface profilometry was used for localised corrosion analysis of steel specimens. The specimens used for NPFLEX analysis were cleaned beforehand using Clarke's solution to remove any corrosion product on the steel surface. This was done according to the procedure detailed in chapter 3.1. This was necessary for identification of pits on the steel surfaces as localised areas of pitting corrosion may have been filled with corrosion products during the experiments. Two random 3*3 mm regions were targeted on each specimen (Two for each experimental condition). A 2.5X objective was used with a working distance of approximately 3.5 mm. The results gathered were then analysed

using Vision64 on a PC. The top 10 deepest pits were selected for both regions and an average was determined. This was done for two samples of which the results were once again averaged according to ASTM standard G46-94 (52).

3.5.3 Focused Ion Beam (FIB)

A FEI Nova200 dual beam FIB/SEM was used to provide SEM images with EDX linescans of cross-sections. Samples were prepared by coating the corrosion product layer with a platinum coating before a trench was cut in the corrosion product layer for scanning electron microscopy imaging. A voltage range of 5-30 kV was used along with a current range of 0.1-5 nA.

3.5.4 Contact Angle Measurements

A KSV CAM200 goniometer was used for optical contact angle measurements. The system provides contact angles on liquid droplets using curve fittings based on Young's and Laplace equations. Contact angle measurements were conducted on X65 carbon steel surfaces in the absence and presence of a corrosion inhibitor. The contact angle measurements were conducted in oil (droplet of water in oil) and in water (inverted droplet of oil in water) to analyse the hydrophobicity of steel surfaces. Contact angles were determined at room temperature where 3 wt.% NaCl was used as the water phase and Kerosene was used as the oil phase. Both phases including the measurement chamber were purged with CO_2 prior to testing to ensure saturation and eliminate any form of contamination on the steel surfaces. The goniometer was calibrated using a 4 mm calibration ball prior to the start of an experiment. Contact angle measurements were repeated at different inhibitor concentrations ranging from 0-100 ppm to determine the effect of inhibitor concentration. A straight syringe was used for water in oil contact angle measurements. However for oil in water measurements, a J-shaped syringe was used to suspend a droplet of oil on an inverted steel surface. The two syringes used for suspending liquid droplets are shown in Figure 3-10. Experiments were repeated of which an average contact angle was determined and to enable the experimental error to be determined and expressed as error bars.

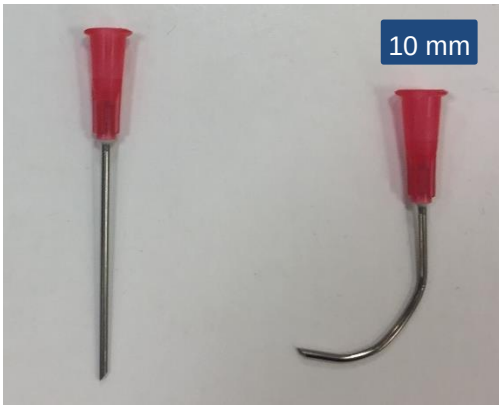

Figure 3-10 Syringes used for water in oil and oil in water contact angle measurements

3.5.5 X-ray Powder Diffraction (XRD)

A Bruker D8 X-ray diffractometer was used for *ex-situ* phase identification. The X65 carbon steel specimens required no preparation prior to testing and could therefore simply be inserted onto a sample holder and analysed using the Bruker D8 system. The Bruker D8 system employs Cu Ka radiation covering a 10*10 mm active area. XRD scans were conducted over a 2theta range of 20-70º over a total scan time of approximately 51 minutes. Phase identification of crystalline corrosion products were obtained according to Bragg's law of diffraction (Equation 3.1).

$$n\lambda = 2dsin\theta \qquad (3.1)$$

Where d is the d-spacing and θ is the angle of incident.

3.6 Corrosion Inhibitor and Application

An imidazoline based corrosion inhibitor was performance tested in various conditions with results presented within Chapter 5 and 6. The imidazoline corrosion inhibitor is a compound prepared by the reaction of tall oil fatty acid (TOFA) with diethylenediamine (DETA). The inhibitor has a critical micelle concentration (CMC) of 10 ppm. The corrosion inhibitor was injected into the experimental brine either before or during the corrosion test (depending on type of test) using a calibrated 10-100 µL pipette.

Chapter 4 Role of Ca^{2+} on Corrosion Product Growth Kinetics and Characteristics at 80 and 150ºC

4.1 Introduction

This chapter focuses on the kinetics and characteristics of corrosion products precipitated in the absence and presence of Ca^{2+} ions at 80 and 150ºC on X65 carbon steel. The results provided within this chapter were gathered from autoclave mass loss and electrochemical experiments. The experimental test conditions which were used to obtain the results presented within this chapter are illustrated in Table 4-1. The experimental methodologies are described in Chapter 3.3.

Table 4-1 Experimental test matrix used to evaluate the role of Ca^{2+} ions on corrosion product formation and corrosion behaviour of X65 carbon steel

Test Condition	NaCl content (wt.%)	Total Cl^- (wt.%)	Ca^{2+} (wt.%)	Temperature (˚C)	P_{CO2} (bar)	Time (h)
1	3	1.82	0	80 and 150	1.4 at 80ºC	6, 24, 48 and 96
2	1.54	1.82	1.830		1.5 at 150ºC	
3	2.98	1.82	0.018	80	1.4 at 80ºC	48
4	2.97	1.82	0.037			
5	2.93	1.82	0.092			
6	2.85	1.82	0.118			
7	2.71	1.82	0.370			
8	2.27	1.82	0.920			

4.2 3 wt.% NaCl brine

4.2.1 Corrosion Rate and Corrosion Product Precipitation Analysis Based on Mass Loss Data

The corrosion rates as gathered by mass loss measurements decreased with increasing exposure periods at both 80 and 150 ºC. Figure 4-1 shows a greater rate of reduction at 150 ºC which resulted in a lower overall mass loss after 96 hours of exposure.

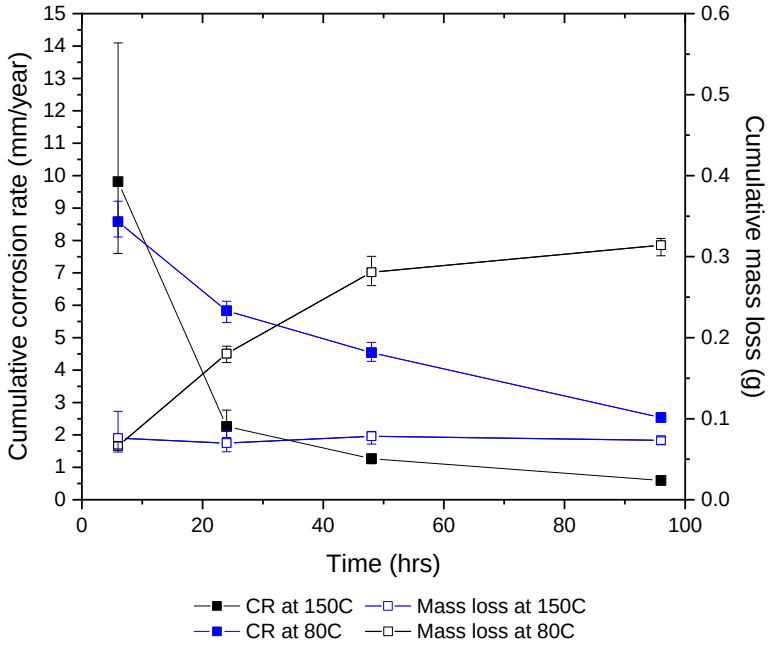

Figure 4-1 Corrosion rate and mass loss of X65 carbon steel as a function of exposure time gathered by mass loss measurements at 80 and 150 ºC in 3 wt.% NaCl

The relatively higher corrosion rates throughout the 96 hour corrosion tests at 80 ºC resulted in the precipitation of corrosion products with a greater corrosion product mass (0.24 grams) as compared to the corrosion product mass of 0.11 grams at 150 ºC as indicated by Figure 4-2, where most of the corrosion product mass at 150 ºC had accumulated onto the steel surface within the first 6 hours of the 96 hour test.

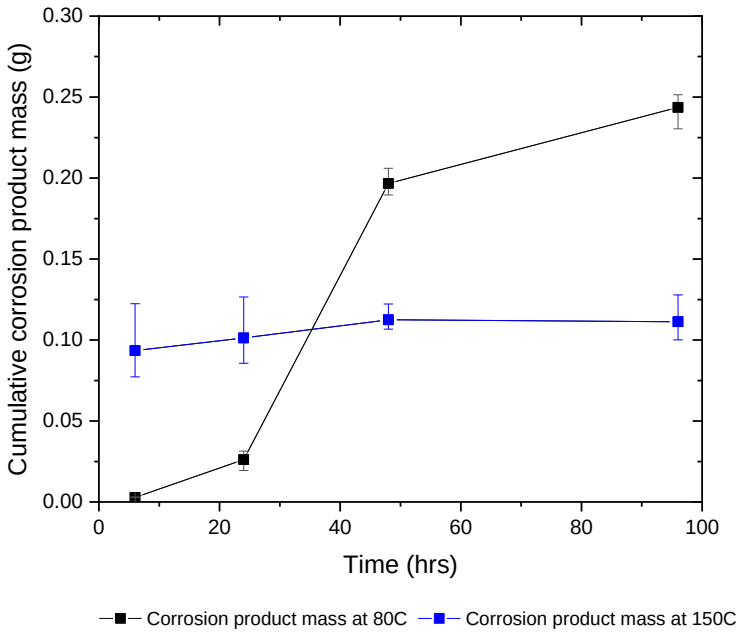

Figure 4-2 Corrosion product mass on X65 carbon steel as a function of exposure time gathered by mass loss measurements at 80 and 150 ºC in 3 wt.% NaCl

4.2.2 Corrosion Rate Obtained by Electrochemical Measurements and Validation against Weight Loss Measurements

Anodic and cathodic potentiodynamic polarisation was conducted in order to construct Tafel plots at 80 and 150ºC, as shown by Figure 4-3 and Figure 4-4 respectively. Potentiodynamic polarisation was conducted in order to improve the accuracy of corrosion rates determined by LPR measurements by considering the influence of oxidation and reduction reactions prior to corrosion product precipitation. The Tafel constants (β_a and β_c) at both temperatures were estimated by extrapolation of the anodic and cathodic sites according to the experimental procedure detailed in Chapter 3.3.

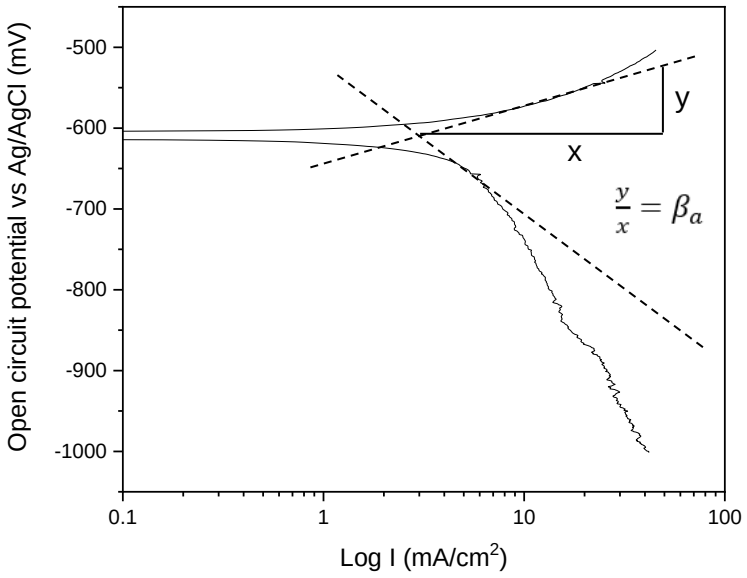

Figure 4-3 Anodic and Cathodic potentiodynamic polarisation of X65 carbon steel at 80 ºC in 3 wt.% NaCl

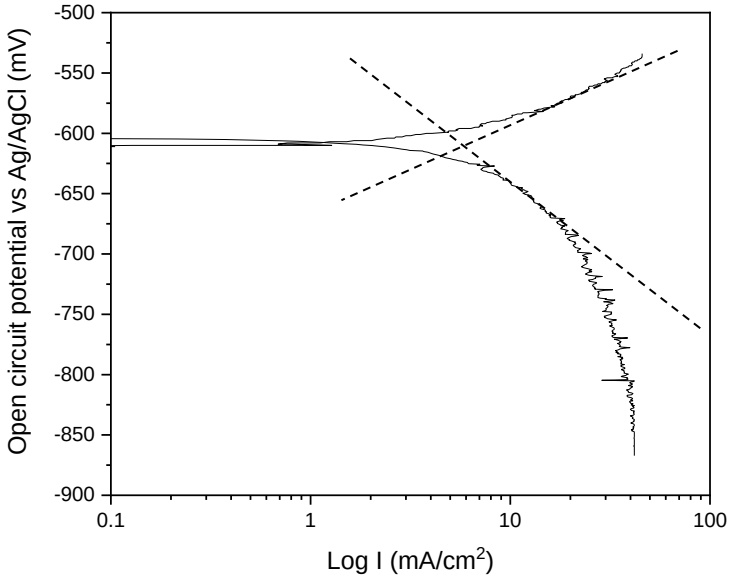

Figure 4-4 Anodic and Cathodic potentiodynamic polarisation of X65 carbon steel at 150 ºC in 3 wt.% NaCl

The Tafel constants and their associated Stern-Geary coefficients which were experimentally determined before corrosion product precipitation at 80 and 150ºC are summarised in Table 4-2.

Table 4-2 Tafel constants and their associated Stern-Geary coefficients at 80 and 150 ºC obtained before precipitation of corrosion products

	80ºC	**150ºC**
β_a (mV/decade)	91.32	65.49
β_c (mV/decade)	160.77	95.15
Stern-Geary	25.32	16.86

The corrosion rate data obtained by Linear Polarisation Resistance (LPR) shown in Figure 4-5 is calculated based on the Tafel constants obtained by potentiodynamic polarisation. The corrosion rate data obtained by LPR measurements confirmed that the corrosion rates decreased with time at both temperatures however with a greater rate of reduction at 150 ºC. The corrosion rates obtained by LPR measurements were lower in comparison to corrosion rates obtained by the mass loss method. Tests were conducted for 24 hours of exposure at 150 ºC to avoid any damage to the reference probe due to prolonged exposure at high temperature.

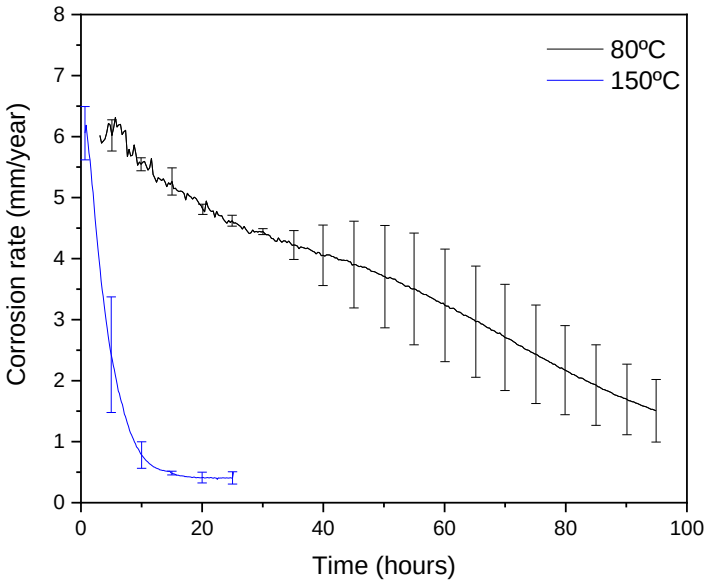

Figure 4-5 Corrosion rate of X65 carbon steel as a function of exposure time obtained by linear polarisation resistance measurements at 80 and 150 ºC in 3 wt.% NaCl

The open circuit potential was higher at the start of the corrosion tests at 150 ºC as shown by Figure 4-6. The open circuit potential increased at a greater rate at

150 ºC and stabilised at approximately -610 mV as compared to -685 mV at 80 ºC after 96 hours of exposure.

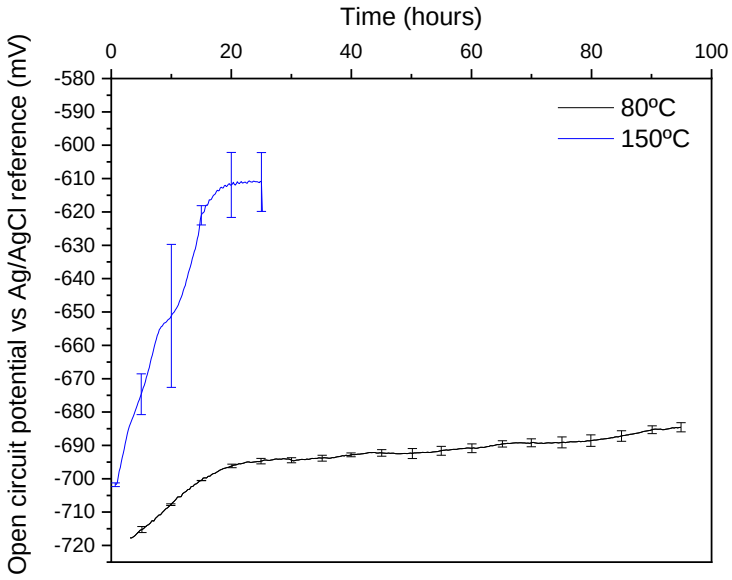

Figure 4-6 Open circuit potential of X65 carbon steel as a function of exposure time obtained by linear polarisation resistance measurements at 80 and 150 ºC in 3 wt.% NaCl

Corrosion rate measurements determined by linear polarisation resistance were validated by determining the accumulative mass loss and comparing against the mass loss gathered by the weight loss technique. Mass loss comparisons at 80 and 150 ºC are shown in Figure 4-7 and Figure 4-8 respectively. Figure 4-7 shows that at 80 ºC the mass loss is almost identical within the first 50 hours of the corrosion tests, however after 50 hours the mass loss gathered by electrochemical measurements deviates positively away from the mass loss results.

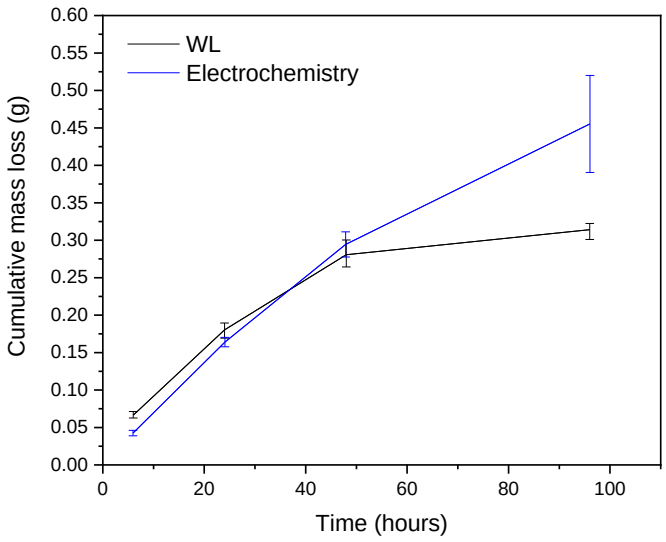

Figure 4-7 Mass loss comparison as gathered by weight loss and electrochemical techniques at 80 ºC in 3 wt.% NaCl

Figure 4-7 shows a comparison at 150 ºC, where the mass loss obtained by the weight loss technique was greater throughout the 24 hour test period. There was a larger deviation at the beginning of the test

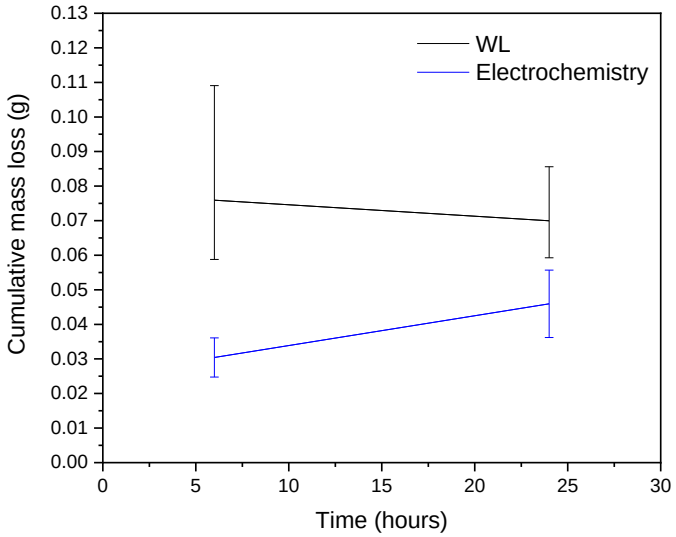

Figure 4-8 Mass loss comparison as gathered by weight loss and electrochemical techniques at 150 ºC in 3 wt.% NaCl

4.2.3 Corrosion Product Morphology and Characteristics

Top-view SEM images at 80 ºC after 6, 24, 48 and 96 hours of exposure are provided in Figure 4-9. Figure 4-9a indicates that after 6 hours of exposure, the steel surface was covered by an iron carbide layer. After 24 hours of exposure iron carbonate had precipitated onto the steel surface with the surface coverage and crystal grain size increasing with time, as shown by Figure 4-9b, c and d).

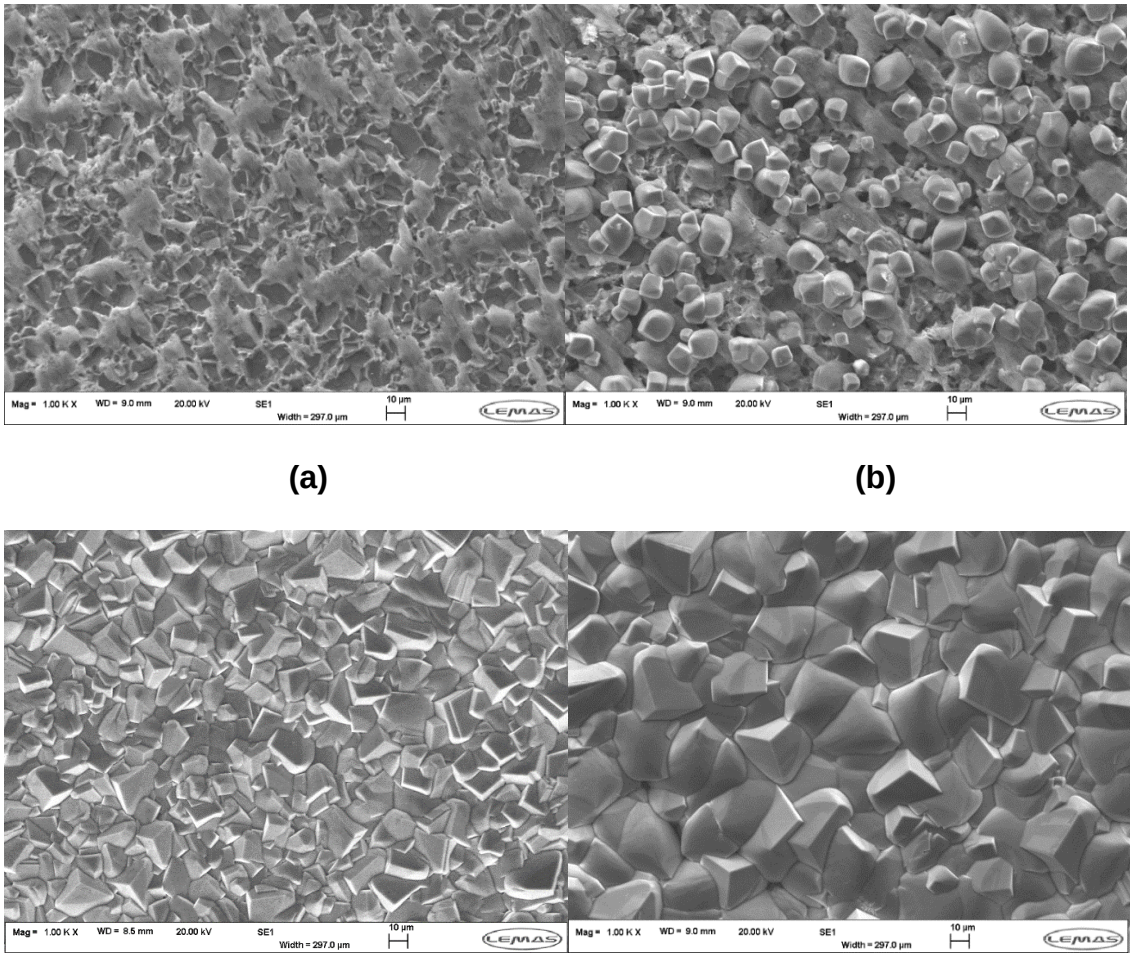

Figure 4-9 Top-view SEM images of X65 carbon steel specimens after (a) 6 h, (b) 24 h, (c) 48 h and (d) 96 h of exposure to 3 wt.% NaCl brine at 80 ºC

Cross-sectional SEM images after 24 and 96 hours of exposure at 80 ºC confirmed that surface coverage was low within the first 24 hours of exposure, as shown by Figure 4-10. However the thickness of the corrosion product layer increased from approximately 7 µm to 35 µm after 96 hours of exposure. The corrosion product appeared to be tightly retained to the steel substrate after 96 hours of exposure.

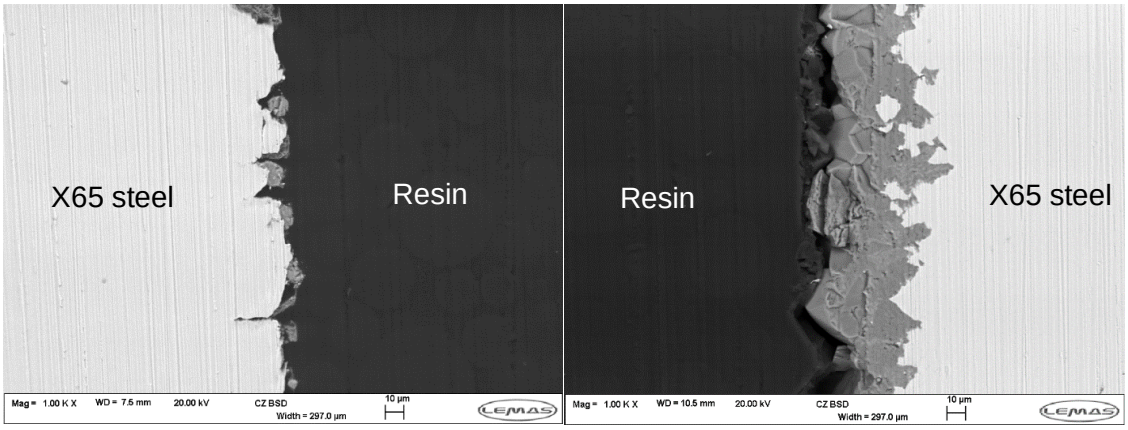

(a) **(b)**

Figure 4-10 Cross-sectional SEM images of X65 carbon steel after (a) 24 h and (b) 96 h at 80 ºC in 3 wt.% NaCl brine

X-ray diffraction patterns of specimens after 6, 24, 48 and 96 hours of exposure at 80 ºC are provided in Figure 4-11. It was confirmed that no crystalline corrosion products had precipitated onto the steel surface within the first 6 hours of exposure. However after 24 hours exposure, iron carbonate was present on the steel surfaces. The iron peak at the 45º 2.theta position was also not present after 48 hours of exposure which confirmed that a thick and dense corrosion product layer had covered the entire steel surface.

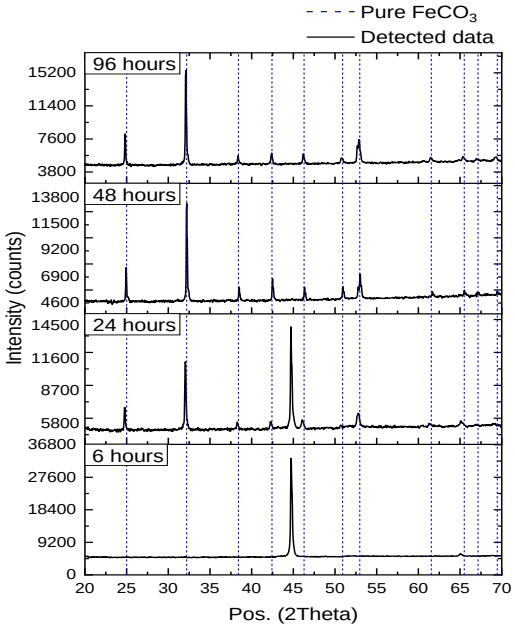

Figure 4-11 XRD patterns collected from X65 carbon steel surfaces exposed to a CO_2-saturated 3 wt.% NaCl solution for different time periods between 6 h and 96 h at 80 ˚C

A 50×50×50 µm trench was cut into the iron carbonate corrosion product which had precipitated after 96 hours of exposure at 80 ºC, as shown by Figure 4-12. The cross sectional image revealed a pit filled with corrosion products. Figure 4-13 shows EDX mapping of the pit which confirmed that the pit was filled with an iron carbonate corrosion product.

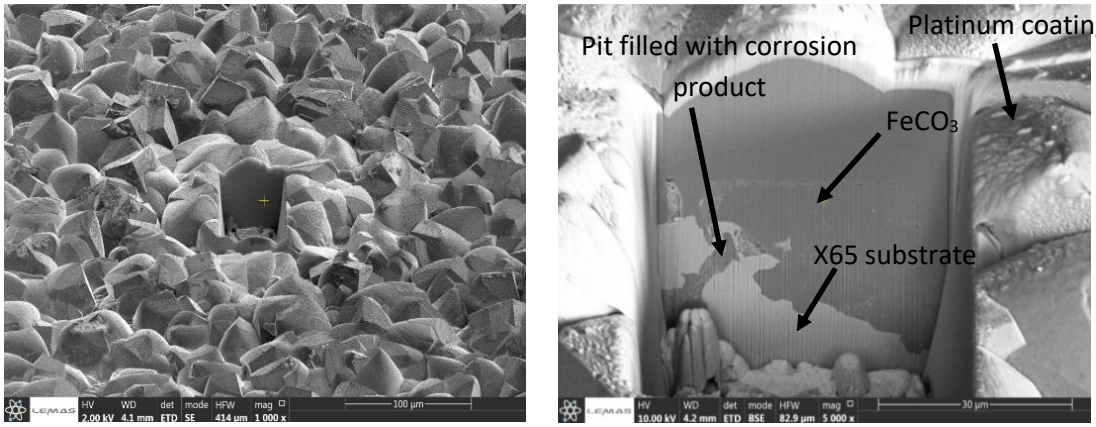

Figure 4-12 (a) Top-view and (b) cross-sectional FIB imaging of X65 carbon steel specimen exposed to 3 wt.% NaCl for 96 h at 80 ºC

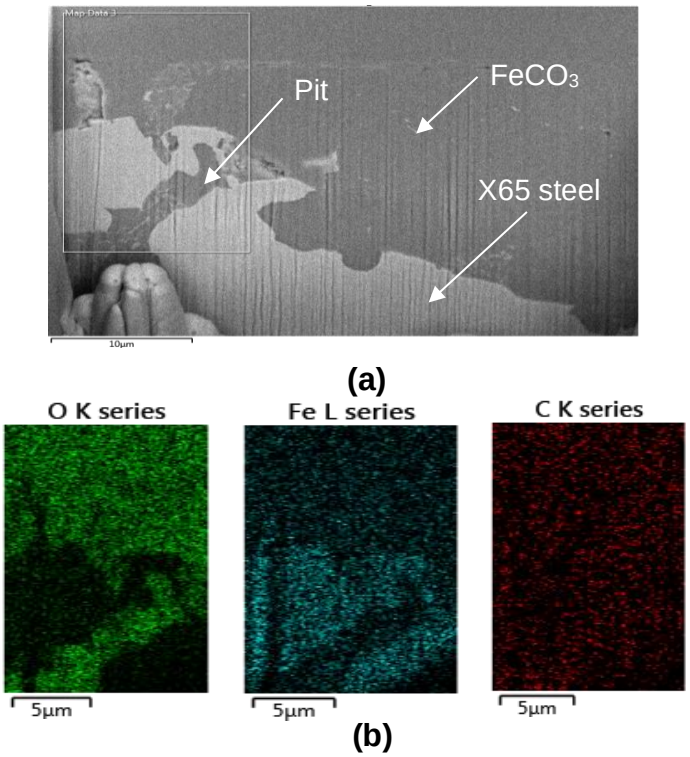

Figure 4-13 (a) SEM image of area used for EDX mapping and (b) oxygen, iron and carbon elemental mapping of specimen exposed to 3 wt.% NaCl for 96 h at 80 ºC

Top view SEM imaging of X65 carbon steel specimens after exposure at 150 ºC are provided in Figure 4-14. The SEM images confirmed that corrosion products had precipitated and covered the entire steel surface within the first 6 hours of exposure. Surface coverage did not appear to be changing with exposure time however the crystal grain sizes did increase with increasing exposure time.

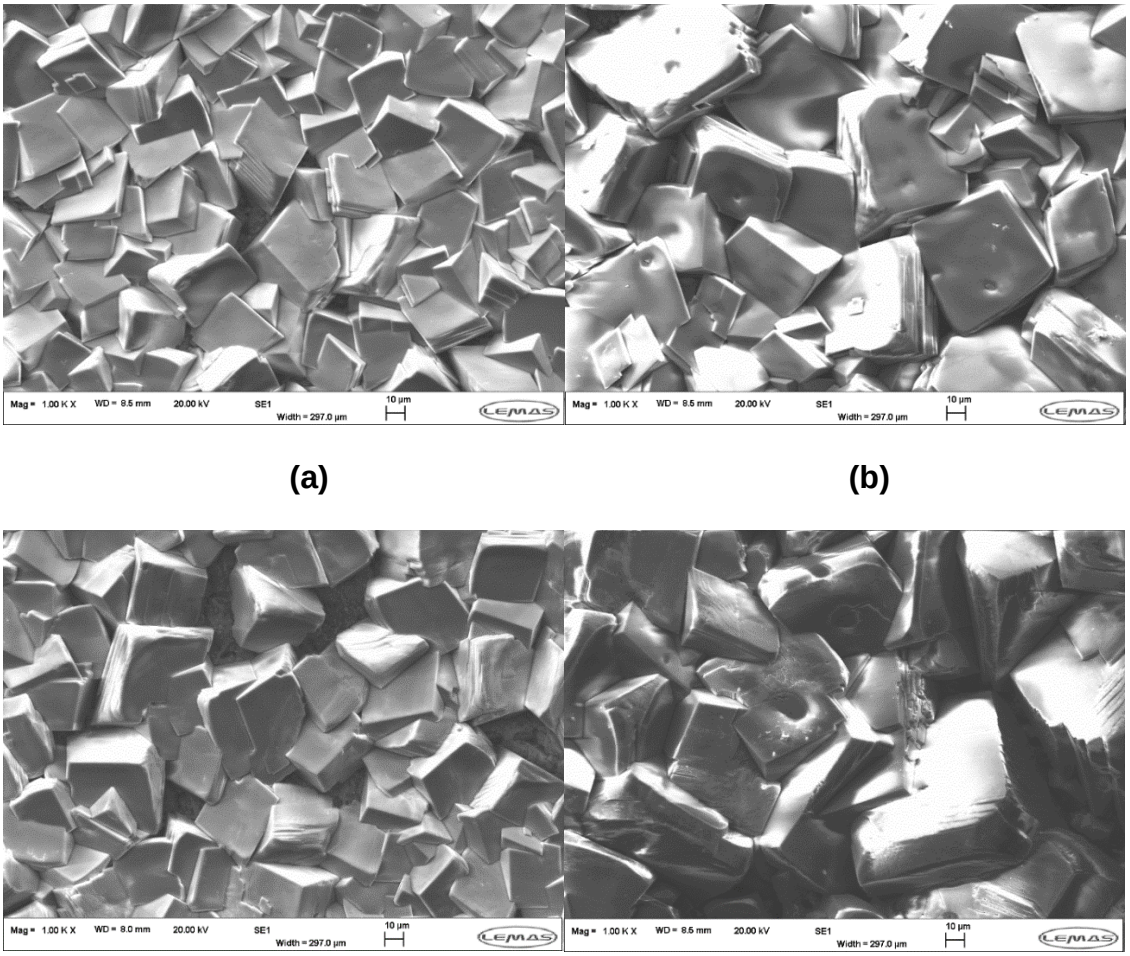

Figure 4-14 Top-view SEM images of X65 carbon steel specimens after (a) 6 h, (b) 24 h, (c) 48 h and (d) 96 h of exposure to 3 wt.% NaCl brine at 150 ºC

Figure 4-15 shows cross sectional SEM images obtained after 24 and 96 hours of exposure at 150 ºC. The SEM images indicate that the corrosion product becomes more uniform in thickness with increasing exposure periods at 150 ºC. The thickness of the corrosion product layer was approximetley 20 µm after 96 hours of exposure.

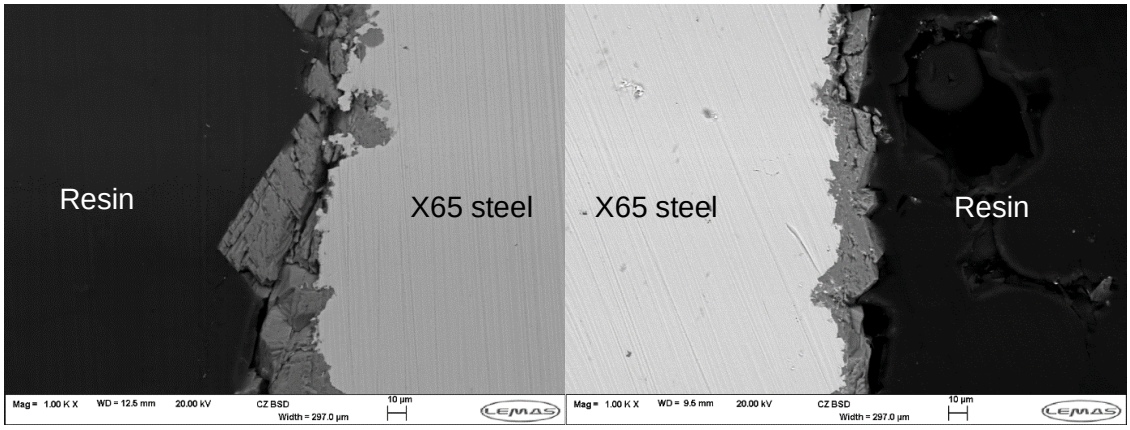

(a) **(b)**

Figure 4-15 Cross-sectional SEM images of X65 carbon steel after (a) 24 h and (b) 96 h of exposure at 150 ºC in 3 wt.% NaCl brine

Figure 4-16 shows X-ray diffraction patterns obtained after 6, 24, 48 and 96 hours of exposure at 150 ºC confirmed that iron carbonate was the only crystaline corrosion product present on the steel surfaces. They also confirmed that the corrosion products were dense and compact as iron peaks were not visible in any of the diffraction patterns.

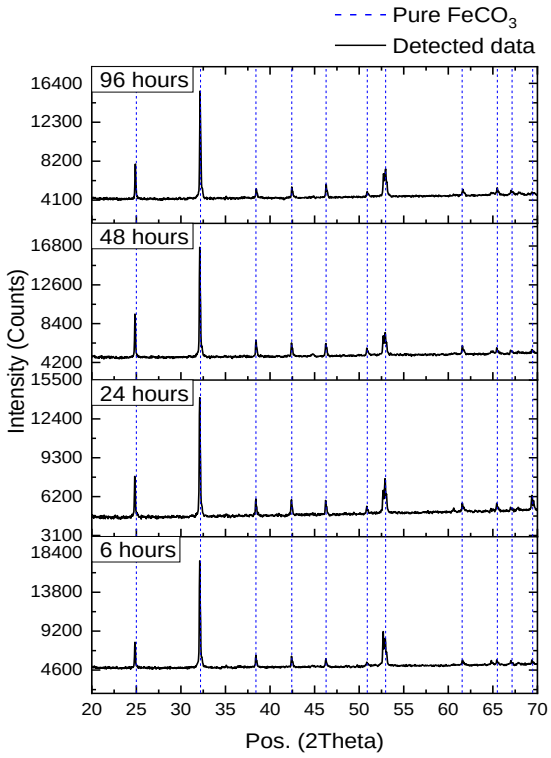

Figure 4-16 XRD patterns collected from X65 carbon steel surfaces exposed to a CO_2-saturated 3 wt.% NaCl solution for different time periods between 6 h and 96 h at 150 ˚C

4.2.4 Localised Corrosion Behaviour

The localised corrosion behaviour was assessed using NPFLEX 3D optical non-contact surface profilometry according to the procedure described in Chapter 3.5. Figure 4-17 indicates that the maximum pit depth at 80 ºC increased with increasing exposure period. The maximum pit depth increased from 8 to 46 µm for exposure periods of 6 and 96 hours respectively.

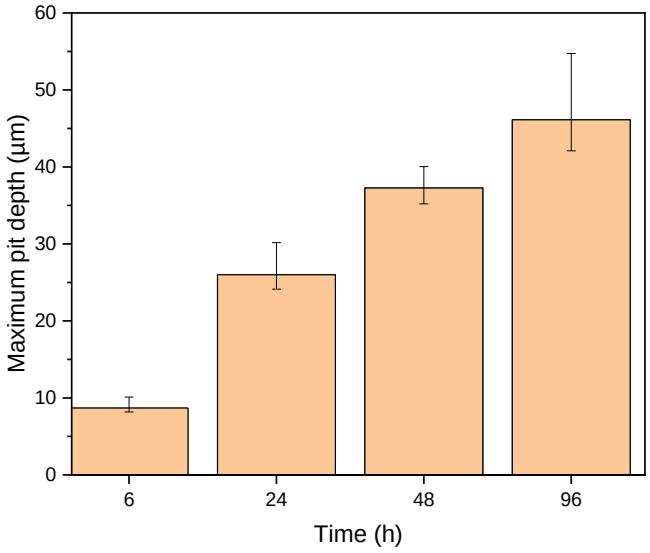

Figure 4-17 Maximum pit depth of X65 carbon steel as a function of exposure time in autoclave at 80 ºC in 3 wt.% NaCl

The localised corrosion behaviour was also assessed using the pit penetration method by assuming that mass loss due to localised corrosion is insignificant in comparison to mass loss due to uniform corrosion. Figure 4-18 shows total, uniform and pit penetration as a function of time. It was identified that the penetration caused by localised corrosion corresponds to approximately 60% of the total penetration after 96 hours of exposure. Total penetration was calculated using equation 4.1.

$$Penetration_{Total} = Penetration_{Uniform} + Penetration_{Pit} \qquad (4.1)$$

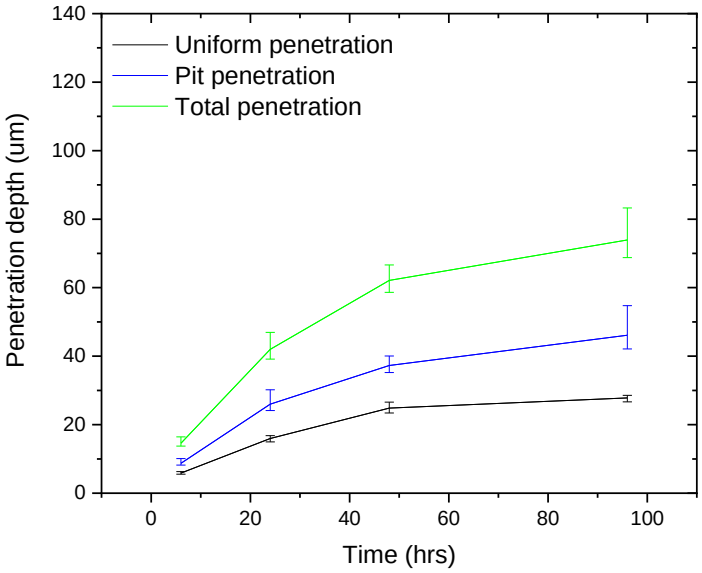

Figure 4-18 Total penetration of X65 carbon steel as a function of exposure time in autoclave at 80 ºC in 3 wt.% NaCl

Figure 4-19 provides 2D profilometry images along with micrographs after 6 and 96 hours of exposure at 80 ºC. The 2D images and micrographs were used to confirm that identified pits were in fact pits as they provide a good indication relative to the scanned 3×3 mm surface area. Figure 4-19 that pits can be clearly identified after 96 hours of exposure.

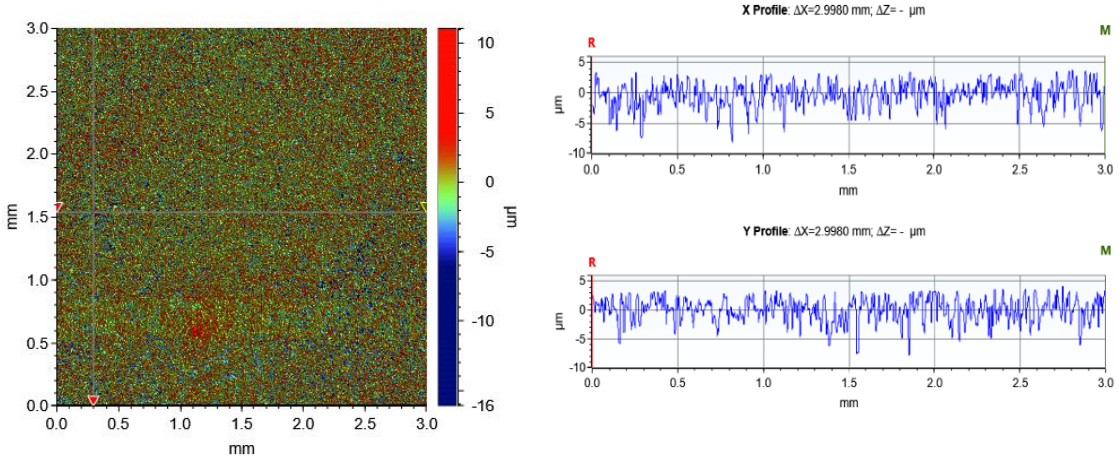

(a)

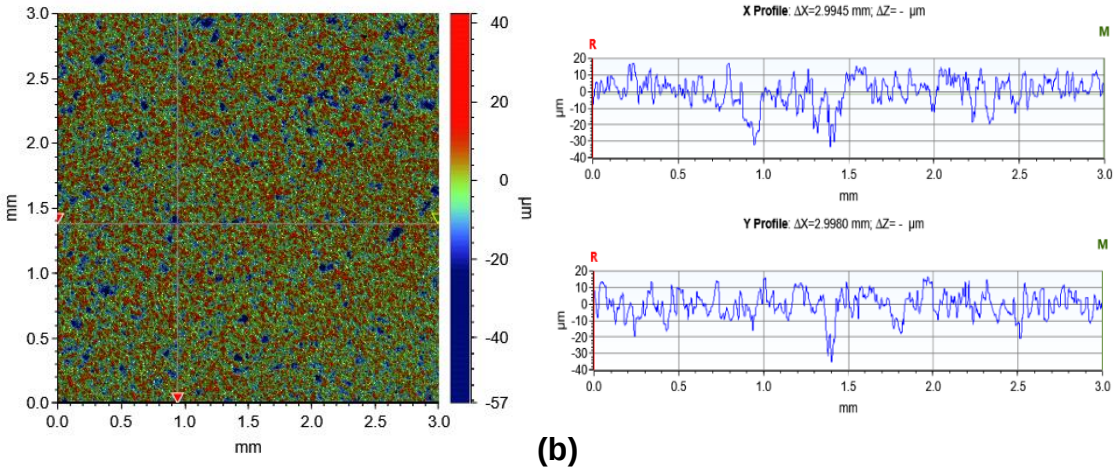

Figure 4-19 2D profilometry images of X65 carbon steel surfaces exposed to 3 wt.% NaCl brine for (a) 6 h and (b) 96 h at 80 ºC

Figure 4-20 shows that the maximum pit depth after exposure at 150 ºC was relatively stable throughout the 96 hour test, indicating that pits had developed onto the steel surface within the first 6 hours of exposure after which pit growth had completely stopped. The maximum pit depth fluctuated between 25 and 29 µm during the 96 hour test period.

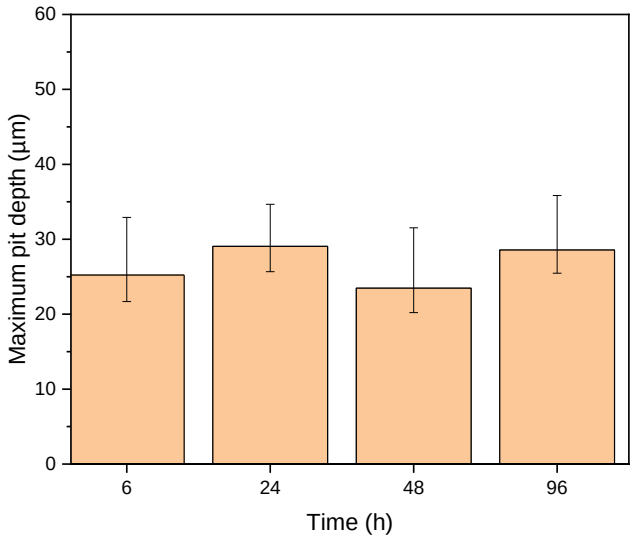

Figure 4-20 Average maximum pit depth of X65 carbon steel as a function of exposure time in autoclave at 150 ºC in 3 wt.% NaCl

The localised corrosion behaviour at 150 ºC was assessed using the total penetration method. As shown by Figure 4-21, penetration caused by localised pitting corrosion at 150 ºC constituted most of the total penetration throughout the 96 hour corrosion test due to rapid growth of pits.

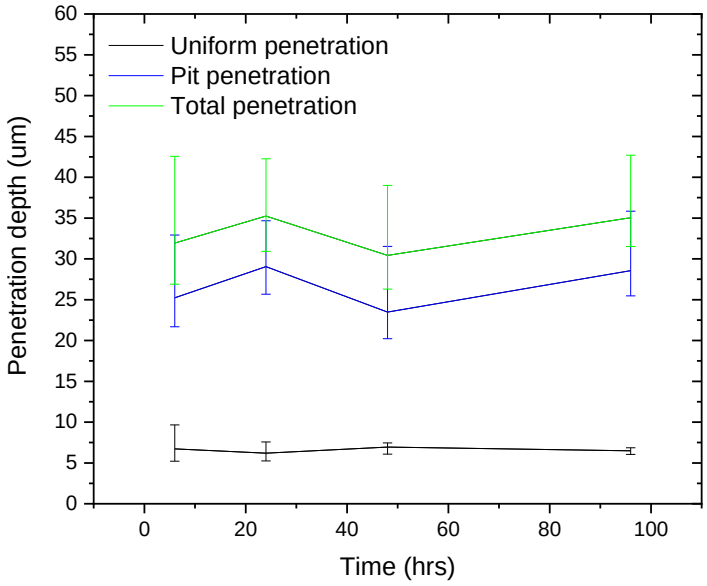

Figure 4-21 Total penetration of X65 carbon steel as a function of exposure time in autoclave at 150 ºC in 3 wt.% NaCl

2D NPFLEX surface profilometry images confirmed that pits were present on the steel surface within the first 6 hours of exposure. Figure 4-22 also confirmed that the maximum pit depth did not change with exposure time after 6 hours of exposure at 150 ºC.

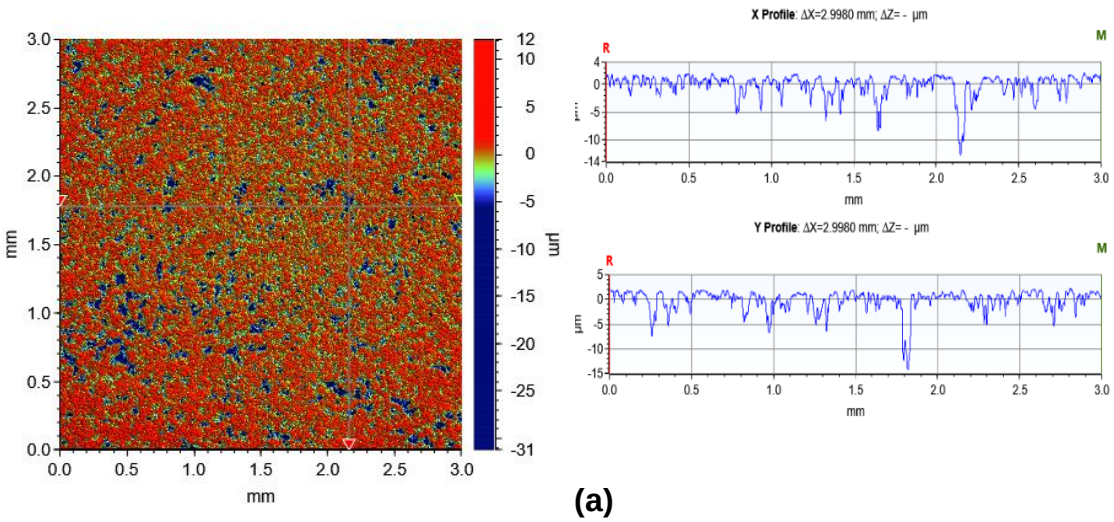

(a)

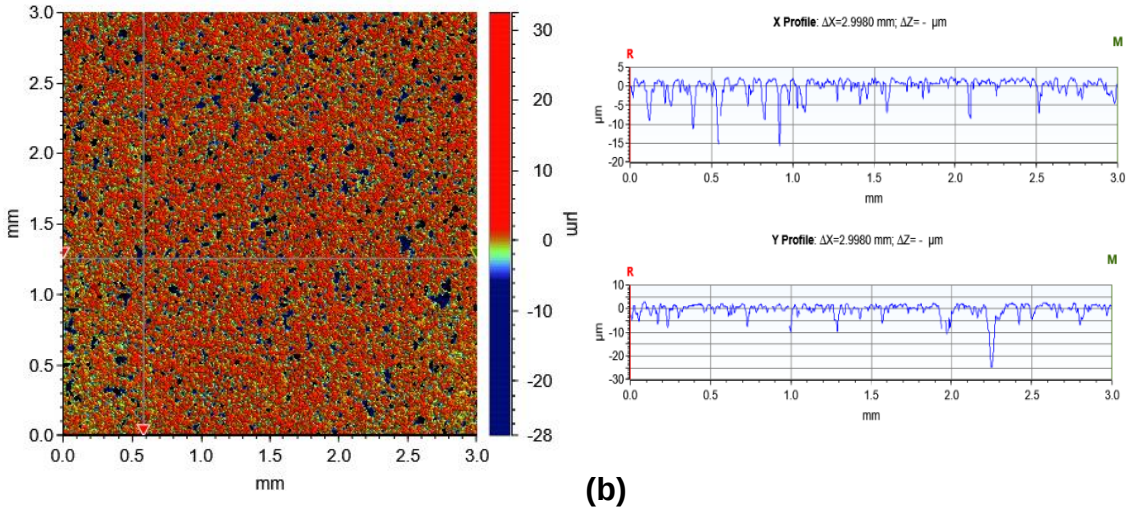

Figure 4-22 2D profilometry images of X65 carbon steel surfaces exposed to 3 wt.% NaCl brine for (a) 6 h and (b) 96 h at 150 ºC

4.3 Influence of 1.83 wt.% $CaCl_2 \cdot 2H_2O$ on the Overall Corrosion Behaviour

4.3.1 Corrosion Rate and Corrosion Product Precipitation Analysis using Mass Loss Data

The influence of Ca^{2+} ions on corrosion product kinetics/characteristics and overall corrosion behaviour was evaluated by the addition of 1.83 wt.% calcium chloride dehydrate (5000 ppm Ca^{2+}) at a maintained chloride content as described in chapter 3.2.

Figure 4-23 shows the corrosion rate and mass loss as a function of time as determined by the weight loss technique after exposure at 80 and 150 ºC. The corrosion rate at 80 ºC in the presence of Ca^{2+} decreased relatively slowly from approximately 6 mm/year after 6 hours of exposure to 3.5 mm/year after 96 hours of exposure. However at 150 ºC, the corrosion rate was initially higher after 6 hours of exposure (8.2 mm/year) but was reduced to 0.5 mm/year after 96 hours of exposure.

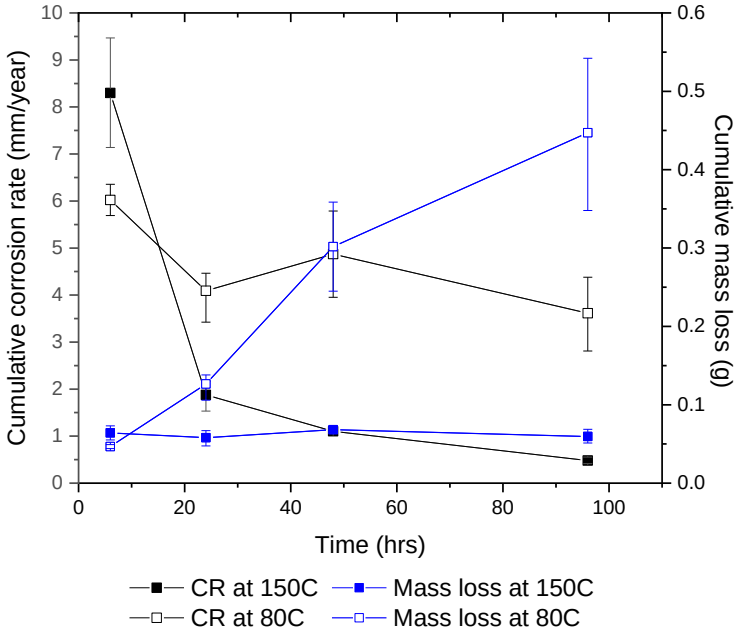

Figure 4-23 Corrosion rate and mass loss of X65 carbon steel as a function of exposure time obtained by mass loss measurements at 80 and 150 ºC in 1.83 wt.% $CaCl_2 \cdot 2H_2O$ at a maintained chloride content

Figure 4-24 indicates that the corrosion product mass increased with exposure time at 80 ºC, whereas at 150 ºC most of the corrosion product mass had precipitated onto the steel surface within the first 6 hours of exposure.

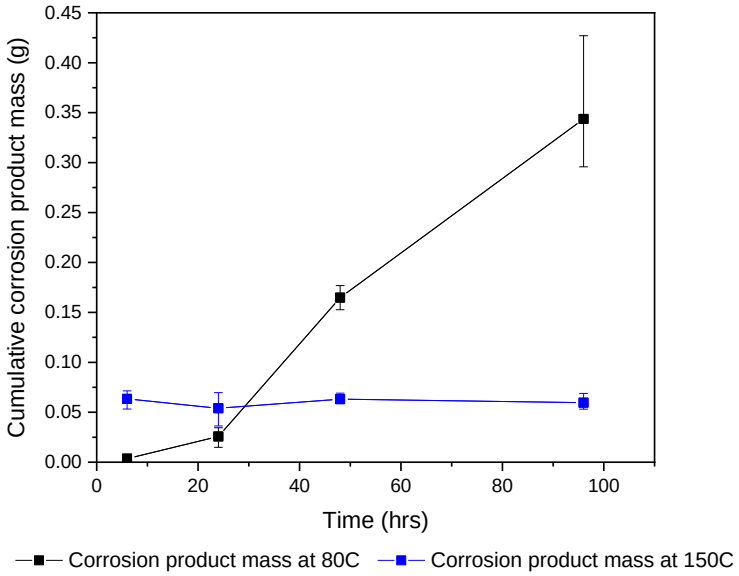

Figure 4-24 Corrosion product mass of X65 carbon steel as a function of exposure time obtained by mass loss measurements at 80 and 150 ºC in 1.83 wt.% $CaCl_2 \cdot 2H_2O$ at a maintained chloride content

4.3.2 Corrosion Rate Obtained by Electrochemical Measurements (LPR) and Validation against Weight Loss Measurements

Corrosion rates obtained by linear polarisation resistance at 80 and 150 ºC in the presence of 1.83 wt.% $CaCl_2 \cdot 2H_2O$ are shown in Figure 4-25. The corrosion rate at 80 ºC decreased from 8 mm/year to 5 mm/year after 96 hours of exposure whereas at 150 ºC the corrosion rate decreased from 6 mm/year to 0.25 mm/year.

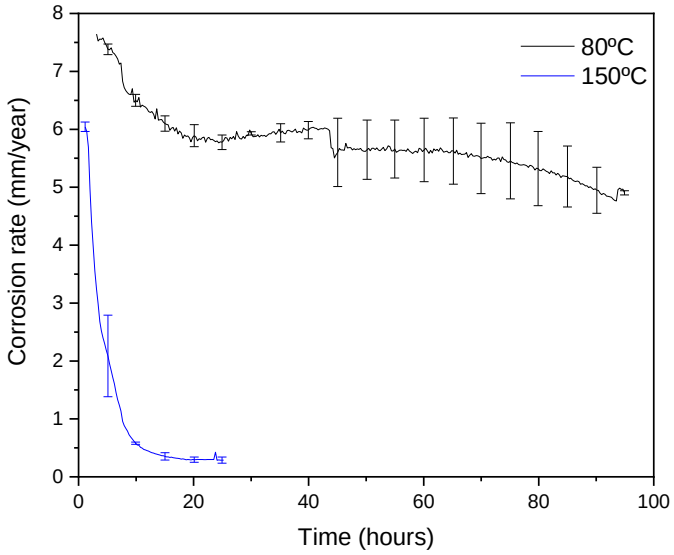

Figure 4-25 Corrosion rate of X65 carbon steel as a function of exposure time obtained by linear polarisation resistance measurements at 80 and 150 ºC in 1.8 wt.% $CaCl_2 \cdot 2H_2O$

Figure 4-26 shows indicates that the open circuit potential at 80ºC increased from -710 mV to -675 mV whereas at 150 ºC the open circuit potential increased to -630 mV within the first 24 hours of exposure.

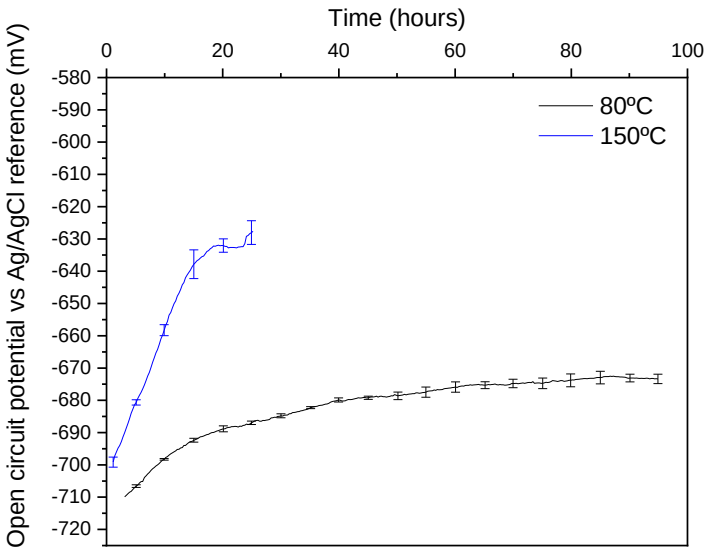

Figure 4-26 Open circuit potential of X65 carbon steel as a function of exposure time obtained by linear polarisation resistance measurements at 80 and 150 ºC in 1.8 wt.% $CaCl_2 \cdot 2H_2O$

LPR measurements were validated by comparing the accumulated mass loss (determined by LPR) with the mass loss determined by the weight loss technique, as shown by Figure 4-27 at 80 ºC and Figure 4-28 at 150 ºC. The error in the results increased with increasing exposure time at 80 ºC and decreased with increasing exposure time at 150 ºC.

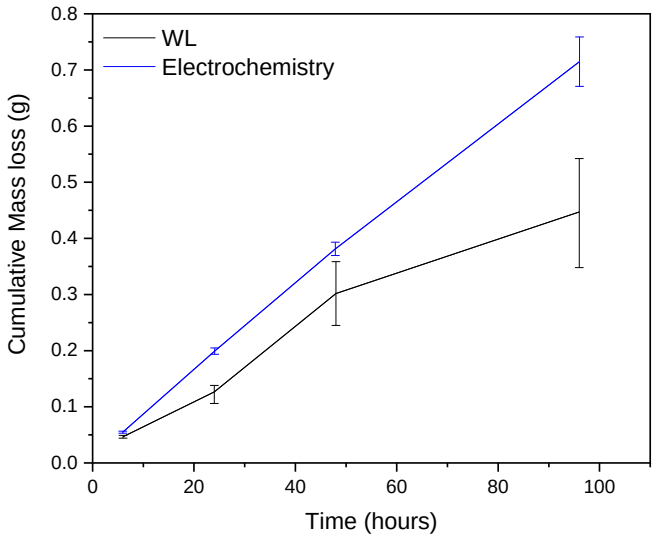

Figure 4-27 Mass loss comparison of X65 carbon steel obtained by weight loss and linear polarisation resistance measurements at 80 ºC in 1.8 wt.% $CaCl_2 \cdot 2H_2O$

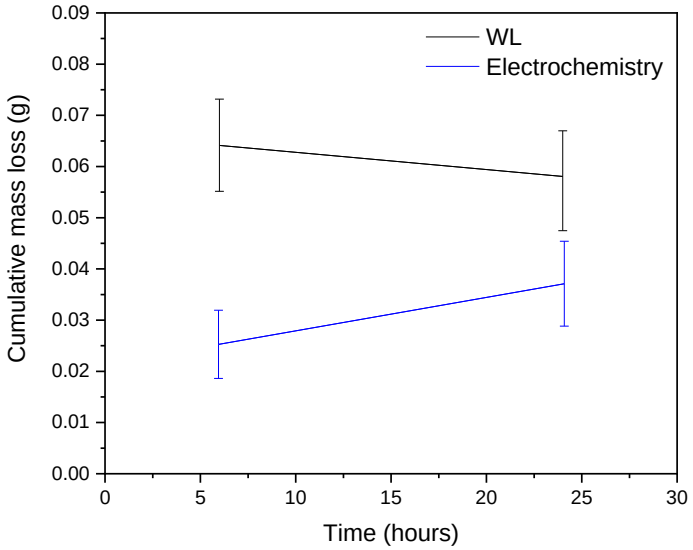

Figure 4-28 Mass loss comparison of X65 carbon steel obtained by weight loss and linear polarisation resistance measurements at 150 ºC in 1.8 wt.% $CaCl_2 \cdot 2H_2O$

4.3.3 Derivation and Validation of Equation for Fe/Ca Mole Fractions within $Fe_xCa_yCO_3$ Corrosion Products

An equation was derived using existing data within the literature to determine the molar fractions of Ca and Fe within $Fe_xCa_yCO_3$ corrosion products in order to evaluate the incorporation of calcium into the crystal lattice of $FeCO_3$. The derivation was based on the d-spacing equation for a hexagonal system (Equation 4.2) of the main Bragg reflection for $Fe_xCa_yCO_3$ located at the (104) inter-planar d-spacing. $FeCO_3$ and $CaCO_3$ are structurally similar as both are R-3c rhombohedral with similar atomic positions. However the d-spacing of $CaCO_3$ is greater than that of $FeCO_3$ due to greater space between planes of atoms as shown by Figure 4-29 and Table 3-3. This may be caused by the greater atomic radius of calcium or by its charge, however in X-ray these distances are represented by peaks. Therefore as Ca^{2+} incorporates into $FeCO_3$, it results in an increase in the atomic spacing (d-spacing).

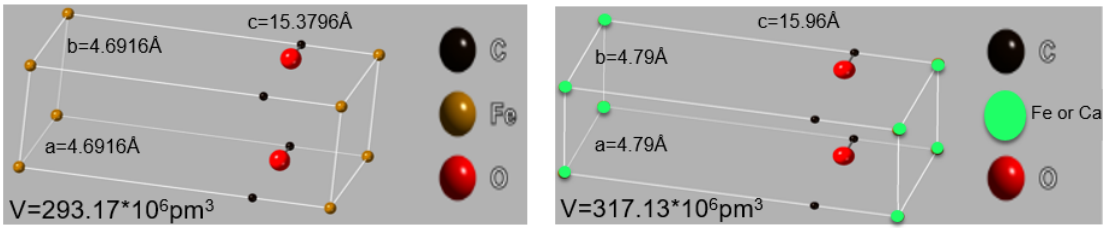

(a) **(b)**

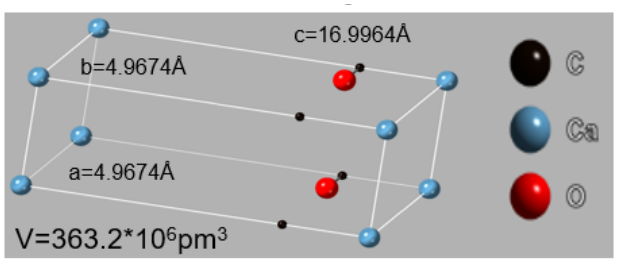

(c)

Figure 4-29 Schematics of unit cells for (a) $FeCO_3$, (b) $Fe_{0.636}Ca_{0.364}CO_3$ and (c) $CaCO_3$

The introduction of Ca into $FeCO_3$ results in an increase in the d-spacing which is represented by a larger space between atoms and an overall larger unit cell as shown by Figure 4-29. In terms of the peak positions associated with the diffraction patterns from such crystalline planes, as the Ca molar fraction within the $Fe_xCa_yCO_3$ structure increases, the peaks will shift towards lower 2θ values as illustrated by Figure 4-30.

Table 4-3 Unit cell volume and parameters for $FeCO_3$, $Fe_xCa_yCO_3$ and $CaCO_3$

	$FeCO_3$	**$Fe_{0.636}Ca_{0.364}CO_3$**	**$CaCO_3$**
a (Å)	4.6916	4.79	4.9674
b (Å)	4.6916	4.79	4.9674
c (Å)	15.3796	15.96	16.9964
α β γ (°)	90,90,120	90,90,120	90,90,120
Volume 10^6pm^3	293.17	317.13	363.20

However as perfect crystals are non-existent, small peak shifts are often associated within the same crystal compound. This is illustrated in Figure 4-30 where a shift of 0.165º can be observed across three X-ray diffraction scans of $FeCO_3$ covered surfaces. Such shifts can also be caused by specimens not being completely level with the source which results in slightly shifted peaks. However such shifts are generally significantly smaller than shifts caused by larger spacing between atoms as illustrated by Figure 4-30. The derivation explained in the following section enables the extent of this shift to be related to the stoichiometry of atoms within $Fe_xCa_yCO_3$.

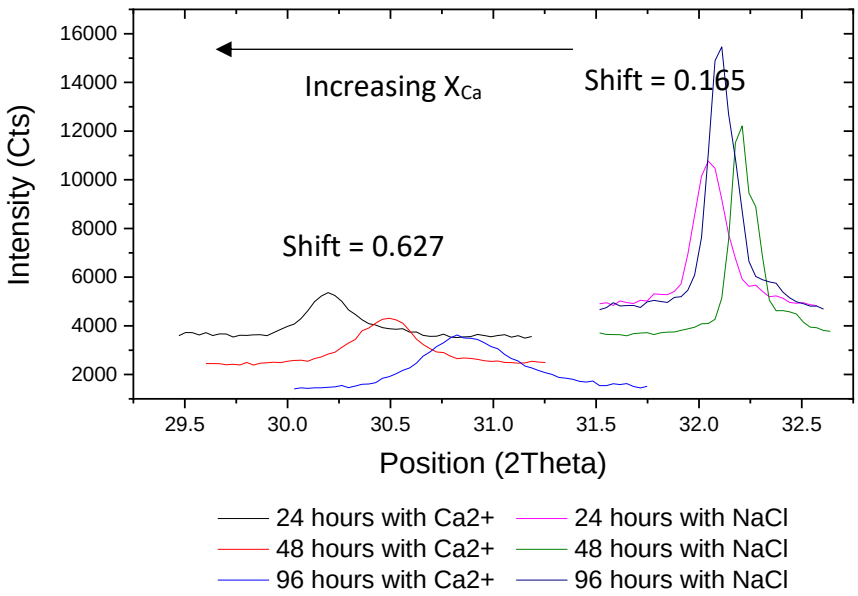

Figure 4-30 Shift in [104] X-ray peak as a function of exposure time for $FeCO_3$ (in NaCl brine) and for $Fe_xCa_yCO_3$ (in Ca^{2+} containing brine)

Equation 4.2 represents the inter-planar spacing (*d*) for a hexagonal Bravais lattice (113). This equation was used as a basis for the derivation as $FeCO_3$ and $CaCO_3$ share a hexagonal lattice structure.

$$\frac{1}{d^2} = \frac{4}{3}\left(\frac{(h^2 + hk + k^2)}{a^2}\right) + \frac{l^2}{c^2} \tag{4.2}$$

Where h, k and l are the Miller indices and a and c are the unit cell parameters, also known as the lattice constants.

Equation 4.3 represents the unit cell volume equation for a hexagonal system. Equation 4.3 was rearranged before insertion into Equation 4.2 to generate Equation 4.4. Equation 4.3 was rearranged in order to eliminate the term a^2 once substituted. This was done in order to reduce the error in the final derivation as unit cell parameter *a* is smaller than unit cell parameter c and could therefore impose greater error in the final equation derivation.

$$\mathrm{V} = \mathrm{a}^2\mathrm{c}(\sin(60)) \tag{4.3}$$

$$\frac{1}{\mathrm{d}^2} = \frac{4}{3}\left(\frac{(\mathrm{h}^2 + \mathrm{hk} + \mathrm{k}^2)\mathrm{c}\sqrt{3}}{2\mathrm{V}}\right) + \frac{\mathrm{l}^2}{\mathrm{c}^2} \tag{4.4}$$

Davidson *et al* (114) synthesised $Fe_xCa_yCO_3$ and together with data from other sources was able to present the unit cell volumes/parameters as a function of Fe

and Ca mole fractions as shown by Table 4-3. This data was used to develop linear correlations for both the unit cell volume (*V*) and unit cell parameter *c* as a function of the molar fraction of Ca (*y*) within the mixed carbonate, and are expressed in Equation 4.5 and 4.6 respectively.

Table 4-4 Unit cell volumes and parameters as a function of $Fe_xCa_yCO_3$ composition (114)

X_{Ca} (mole fraction)	X_{Fe} (mole fraction)	Unit cell volume (Å³)	Unit cell parameter a (Å³)	Unit cell parameter c (Å³)
1.0	0	367.91	-	-
0.75	0.25	346.08	4.9028	16.625
0.68	0.32	339.78	4.8788	16.483
0.5	0.5	327.38	4.8291	16.210
0	1.0	292.68	-	-

$$V = 74.107y + 291.340 \quad (4.5)$$

$$\mathrm{c} = 1.688\mathrm{y} + 15.373 \quad (4.6)$$

Inserting Equation 4.5 and 4.6 into Equation 4.4, while also inserting *h, k* and *l* values for the [104] inter planar d-spacing results in Equation 4.7. The [104] inter-planar d-spacing was used as the most intense Bragg peaks for $CaCO_3$ and $FeCO_3$ are located at 2θ positions of 29.42º and 32.07º respectively, which correspond to the [104] inter-planar d-spacing (69);

$$\frac{1}{\mathrm{d}^2} = \frac{4}{3}\left(\frac{2.924\mathrm{y} + 26.626}{148.214\mathrm{y} + 582.680}\right) + \frac{16}{(1.688\mathrm{y} + 15.373)^2} \quad (4.7)$$

Equation 4.7 was used to determine the mole fraction of Ca in $Fe_xCa_yCO_3$ using the d-spacing of the (104) peak as this was the most prominent peak for all patterns. Equation 4.7 was validated using the International centre for diffraction data (ICDD) database (Ref: 04-019-9174) and yielded an error of <4% with regards to the mole fraction of Ca. Equation 4.7 states that the mole fraction of

Ca within iron-calcium carbonate ($Fe_xCa_yCO_3$) increases linearly with an increasing d-spacing as shown by Figure 4-31.

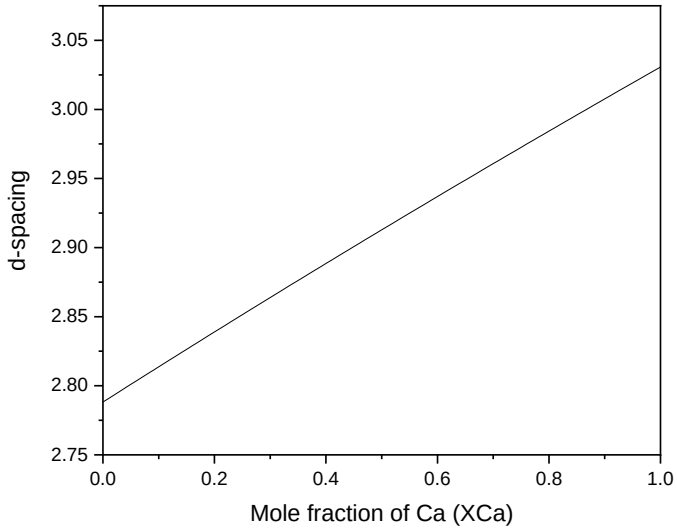

Figure 4-31 d-spacing as a function of X_{Ca} based on Equation 4.7

4.3.4 Effect on Corrosion Product Morphology and Composition

Top-view SEM images of steel surfaces exposed to a 1.8 wt.% $CaCl_2 \cdot 2H_2O$ brine at 80 ºC indicates precipitation of an amorphous iron-calcium carbonate corrosion product layer after 6 hours of exposure which was then followed by the precipitation of crystalline iron-calcium carbonate. Figure 4-32(d), indicates that after 96 hours of exposure, calcium carbonate crystals had precipitated on top of the mixed carbonate corrosion product layer.

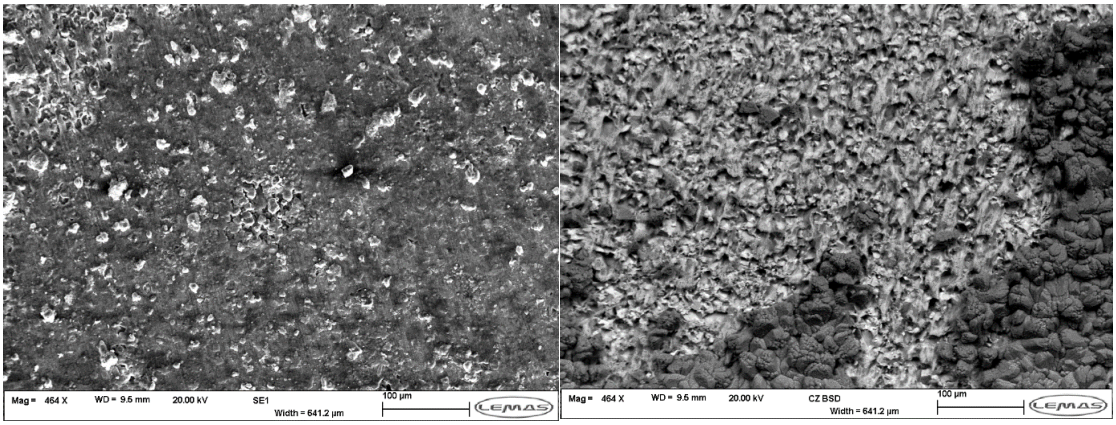

(a) **(b)**

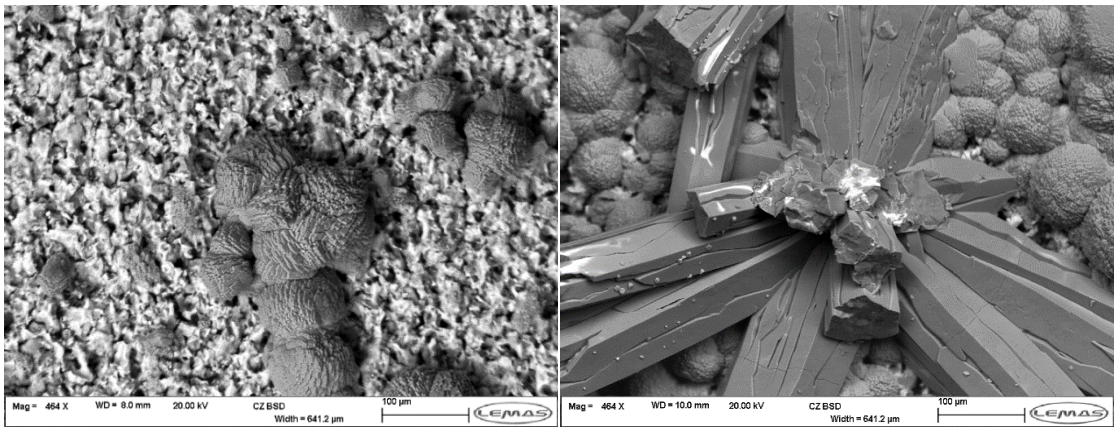

(c) **(d)**

Figure 4-32 Top-view SEM images of X65 carbon steel specimens after (a) 6h, (b) 24h, (c) 48h and (d) 96h of exposure to 1.83 wt.% $CaCl_2 \cdot 2H_2O$ brine at 80 ºC

Figure 4-33 shows cross-sectional SEM images obtained after 24 and 96 hours of exposure. The corrosion product layer increased in thickness from approximately 15 µm after 24 hours of exposure to 50 µm after 96 hours of exposure.

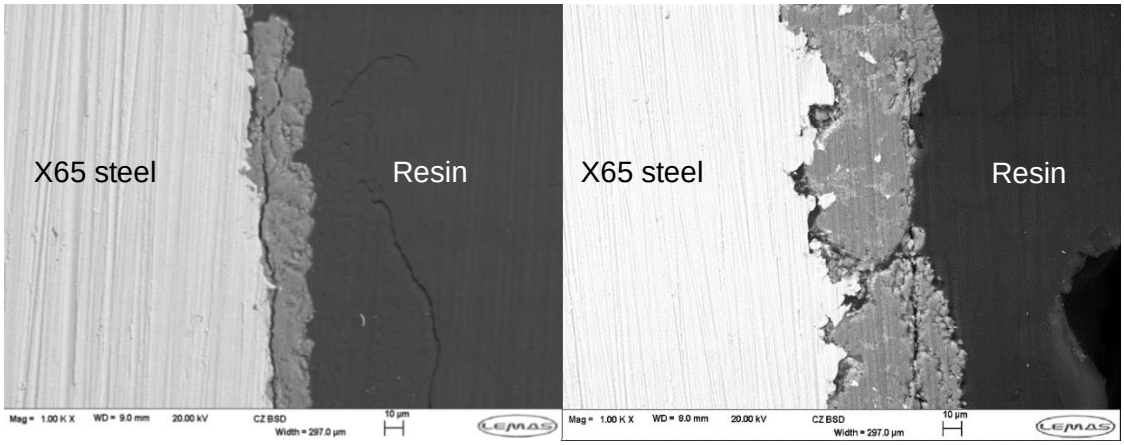

(a) **(b)**

Figure 4-33 Cross sectional SEM images of X65 carbon steel after (a) 24 h and (b) 96 h exposure to 1.83 wt.% $CaCl_2 \cdot 2H_2O$ brine at 80 ºC

X-ray diffraction patterns of the steel surfaces are provided in Figure 4-34. The diffraction patterns confirm the precipitation and presence of a crystalline mixed iron calcium carbonate corrosion product after 24 hours exposure and the presence of a calcium carbonate corrosion product after 96 hours of exposure.

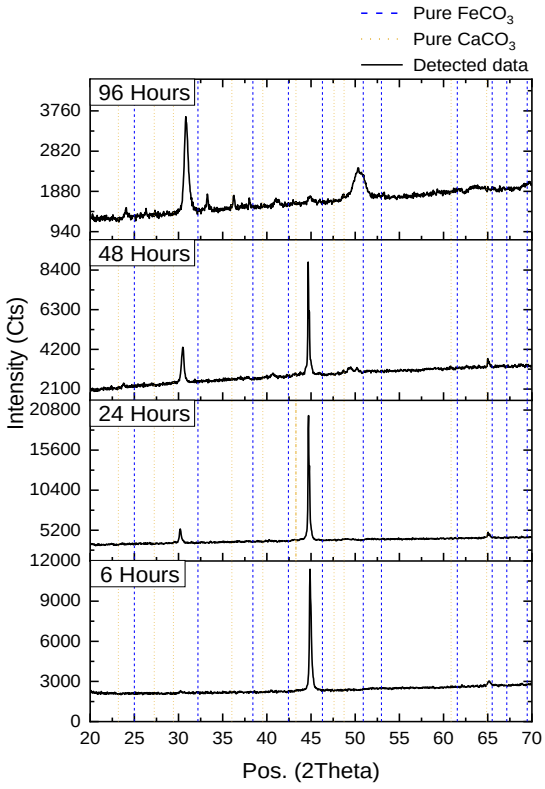

Figure 4-34 XRD patterns of X65 carbon steel after 6, 24, 48 and 96 h exposure to 1.83 wt.% $CaCl_2 \cdot 2H_2O$ brine at 80 ºC

Using Equation 4.7 and the shift in the [104] Bragg peak in Figure 4-34, the molar fraction of calcium within the mixed carbonate corrosion products ($Fe_xCa_yCO_3$) was determined at each time interval. The molar fraction was also determined using EDX point scans. The results are summarised in Table 4-5, and indicate that the molar fraction of calcium decreased with increasing exposure time at 80 ºC.

Table 4-5 Mole fraction of calcium (X_{Ca}) calculated using XRD and EDX data after 6, 24, 48 and 96 h in a 1.83 wt.% $CaCl_2 \cdot 2H_2O$ brine at 80 ºC

Temperature (˚C)	Exposure time (hours)	Calculated X_{Ca} from XRD	Calculated X_{Ca} from EDX
80	6	Amorphous	
	24	0.68	0.68
	48	0.57	0.57
	96	0.46	0.36

Figure 4-35 shows a FIB cross-section along with an EDX line scan across the thickness of the mixed carbonate layer after 96 hour exposure at 80 ºC in a 1.83 wt.% $CaCl_2 \cdot 2H_2O$ brine. The cross section confirms precipitation of calcium carbonate on top of the mixed carbonate corrosion products. The EDX line scan confirmed that the corrosion product layer was calcium rich near the steel substrate and iron rich at the top of the corrosion product layer.

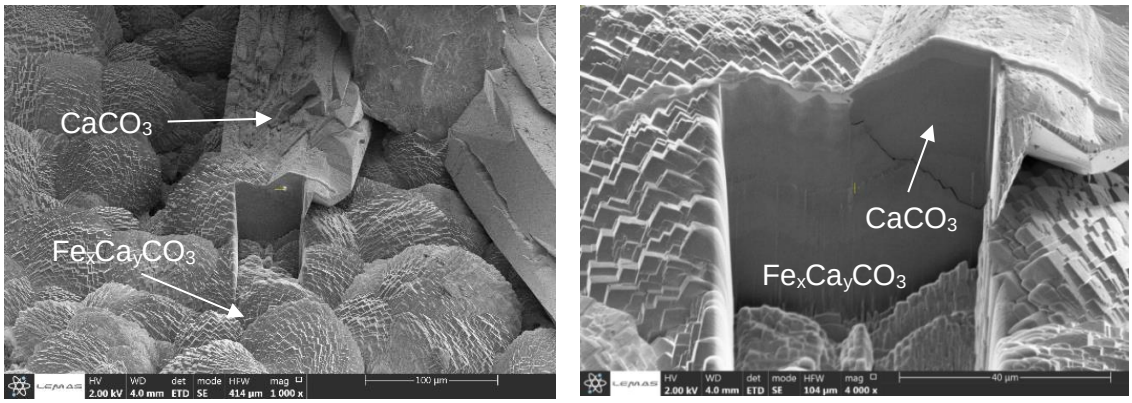

(a)

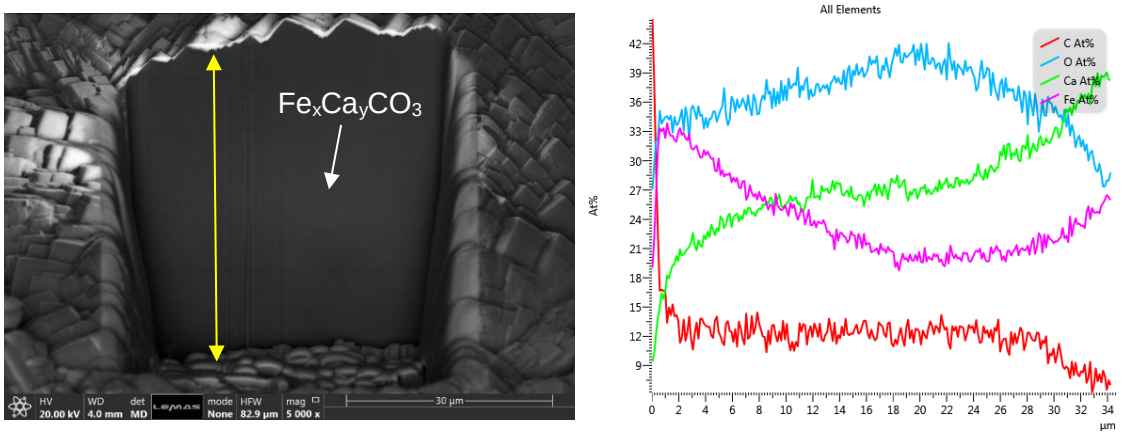

(b)

Figure 4-35 FIB cross-section of X65 carbon steel with (a) SEM images and (b) EDX linescans across thickness of corrosion product layer after 96 h exposure to 1.83 wt.% $CaCl_2 \cdot 2H_2O$ at 80 ºC

Elemental EDX mapping confirmed that calcium carbonate crystals precipitated on top of the mixed iron calcium carbonate corrosion products, as shown by Figure 4-36.

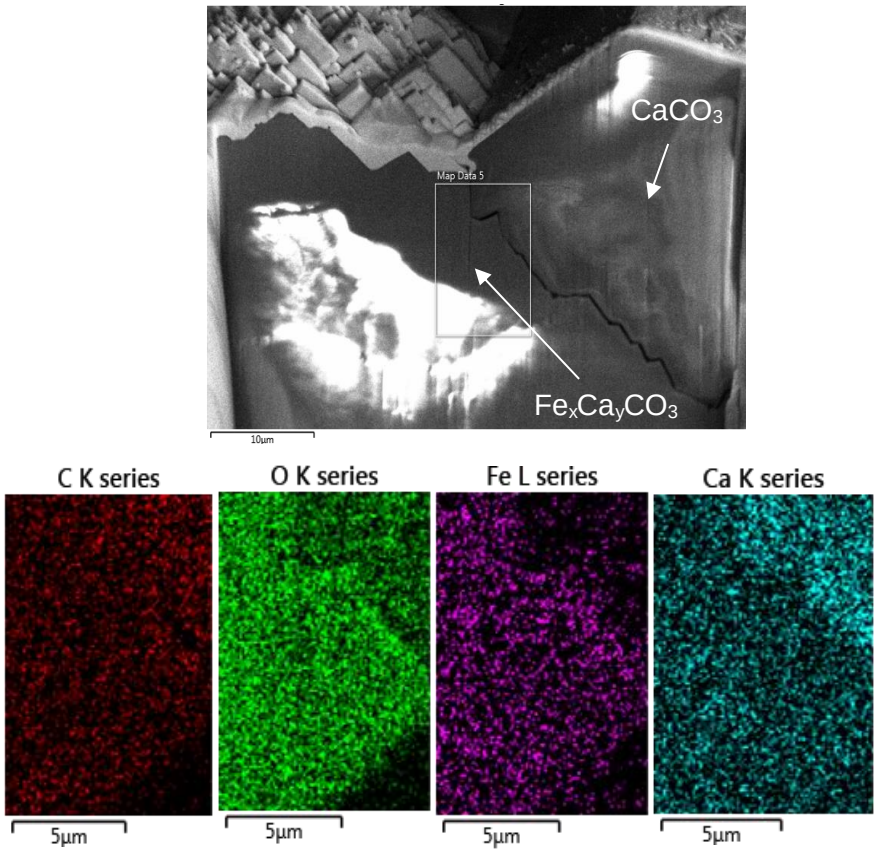

Figure 4-36 FIB cross-sectional image with elemental mapping of X65 carbon steel specimen exposed to 1.83 wt.% $CaCl_2 \cdot 2H_2O$ at 80 ºC for 96 h

Table 4-6 compares the mole fraction of calcium obtained from XRD calculations and FIB/EDX line scans. The comparison indicates that the XRD calculations overestimate the mole fraction of calcium within the mixed carbonate layer.

Table 4-6 Comparison of calcium mole fraction calculations obtained from XRD and Focused ion beam of X65 carbon steel specimen exposed to 1.83 wt.% $CaCl_2 \cdot 2H_2O$ at 80 ºC for 96 h

Exposure time (h)	X_{Ca} calculated using XRD	Height (µm)	X_{Ca} using FIB/EDX
24	0.68	23.5	0.56
96	0.46	Na	0.41

Figure 4-37 shows steel specimens after 6, 24, 48 and 96 hours of exposure to a 1.83 wt.% $CaCl_2 \cdot 2H_2O$ brine at 150 ºC. The top-view SEM images indicate that iron calcium carbonate ($Fe_xCa_yCO_3$) corrosion products had covered the entire

surface within the first 6 hours of exposure. Calcium carbonate ($CaCO_3$) crystals also appeared to be embedded within the mixed carbonate layer.

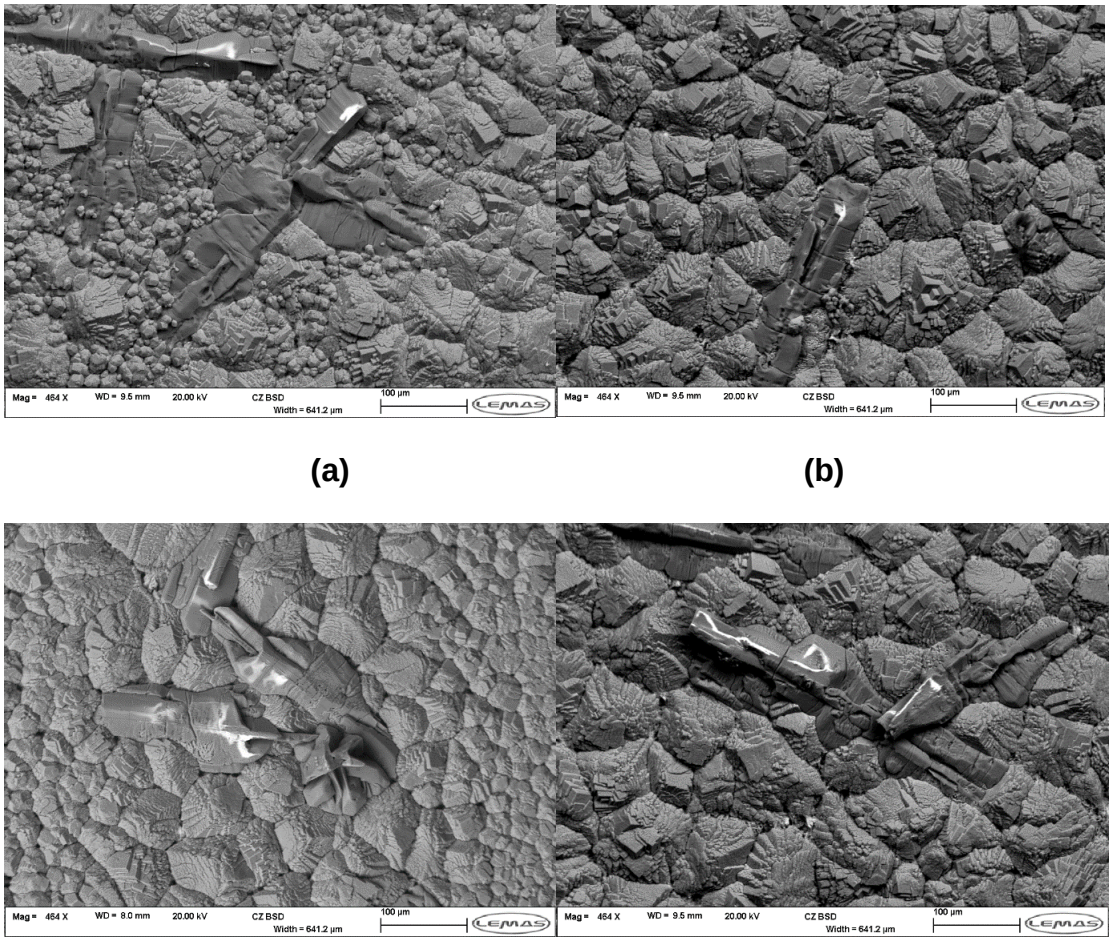

Figure 4-37 Top-view SEM images of X65 carbon steel specimens after (a) 6h, (b) 24 h, (c) 48 h and (d) 96 h of exposure to 1.83 wt.% $CaCl_2 \cdot 2H_2O$ brine at 150 ºC

Cross-sectional SEM imaging confirmed that most of the corrosion product had precipitated within the first 24 hours of exposure. Figure 4-38 also indicates that the corrosion product layer precipitated after 96 hours of exposure was non uniform in thickness. Pits filled with corrosion products can also be identified at both exposure periods.

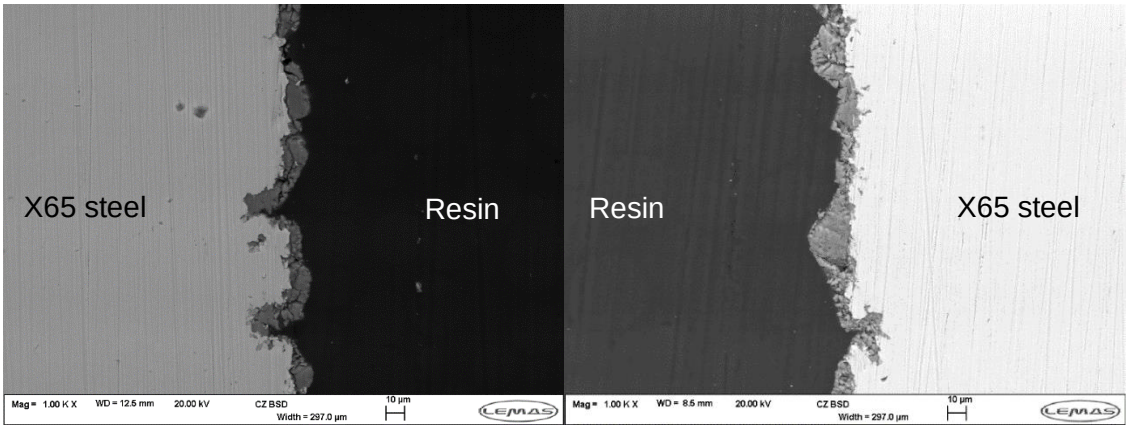

Figure 4-38 Cross sectional SEM images of X65 carbon steel after (a) 24 h and (b) 96 h exposure to 1.83 wt.% $CaCl_2 \cdot 2H_2O$ brine at 150 ºC

X-ray diffraction at 150 ºC confirmed that both iron calcium carbonate and calcium carbonate was present on the steel surfaces after 6, 24, 48 and 96 hours of exposure.

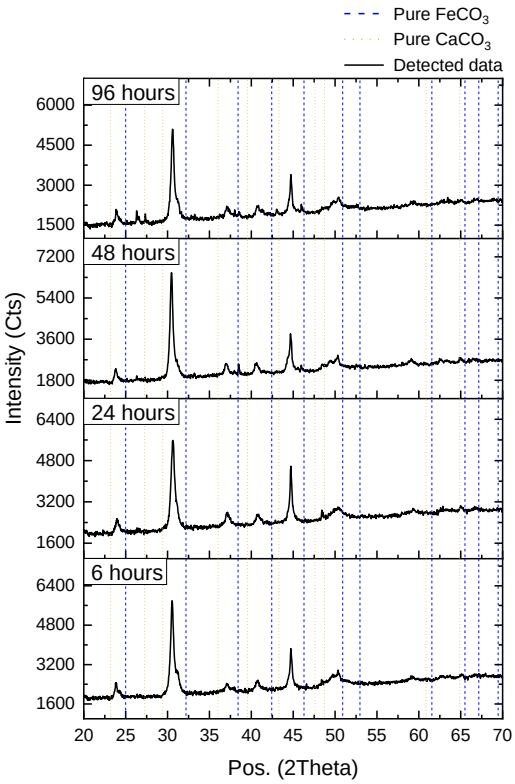

Figure 4-39 XRD patterns for X65 carbon steel after 6, 24, 48 and 96 h exposure to 1.83 wt.% $CaCl_2 \cdot 2H_2O$ brine at 150 ºCTable 4-7 indicates that there is a very small variation in both the calculated mole fraction of calcium within the mixed carbonate layer and the corrosion product mass as a function of exposure time.

Table 4-7 Mole fraction of calcium (X_{Ca}) calculated using XRD and EDX data after 6, 24, 48 and 96 h in 1.83 wt.% $CaCl_2 \cdot 2H_2O$ brine at 150 ºC

Temperature (˚C)	Exposure time (hours)	Calculated X_{Ca} from XRD	Calculated X_{Ca} from EDX
150	6	0.55	0.50
	24	0.52	0.56
	48	0.58	0.47
	96	0.54	0.38

Figure 4-40 provides a FIB cross-section with EDX line scans across the depth of the corrosion product layer. The cross sectional image shows a pit filled with corrosion products and a horizontal line across the cross section of the corrosion product layer. FIB/EDX line scans indicate that there are concentration gradients with respect to iron and calcium within the corrosion product layer, where the corrosion product is iron rich near the steel substrate and calcium rich at the top of the corrosion product layer.

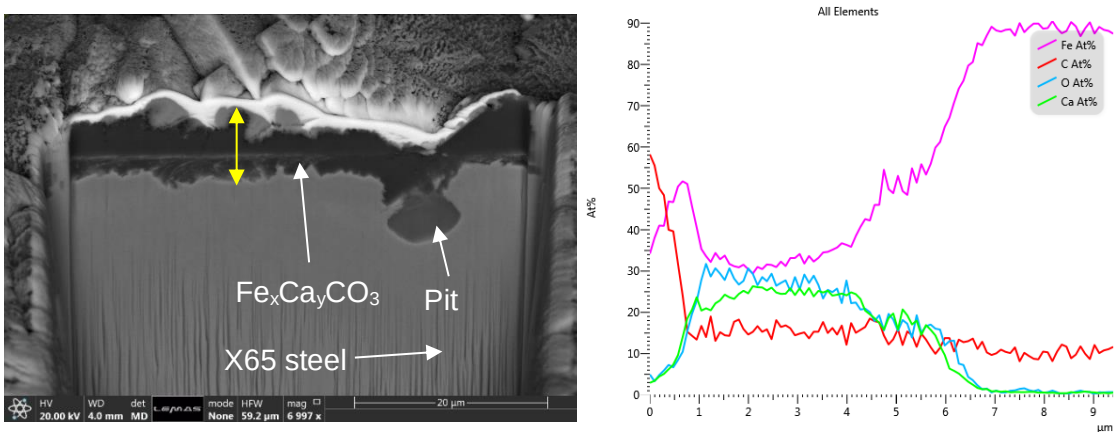

(a) **(b)**

Figure 4-40 (a) FIB cross-section of X65 carbon steel with (b) EDX line scan for corrosion product precipitated in 1.83 wt.% $CaCl_2 \cdot 2H_2O$ brine for 96 h at 150 ºC

Figure 4-41 shows EDX mapping on a pit filled with corrosion products which indicated that the pit was filled with an iron oxide corrosion product.

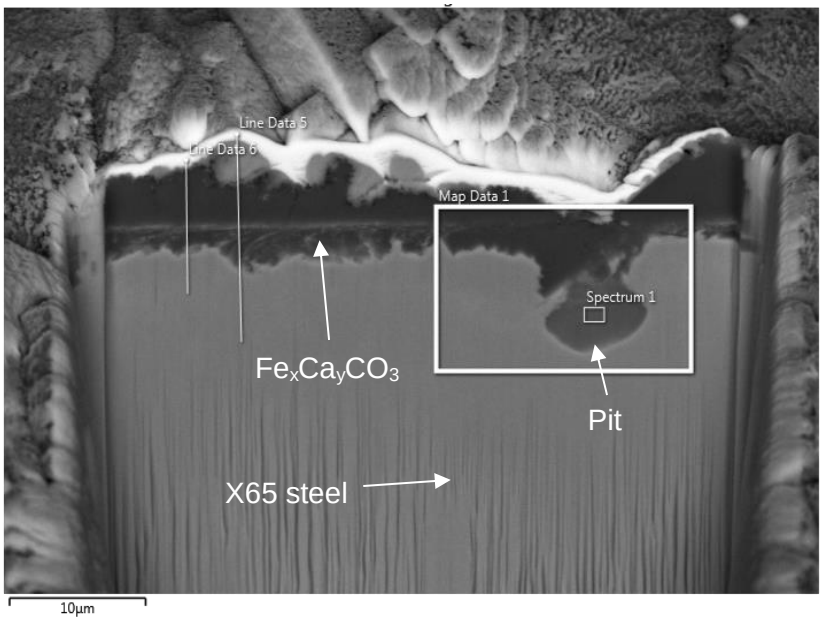

(a)

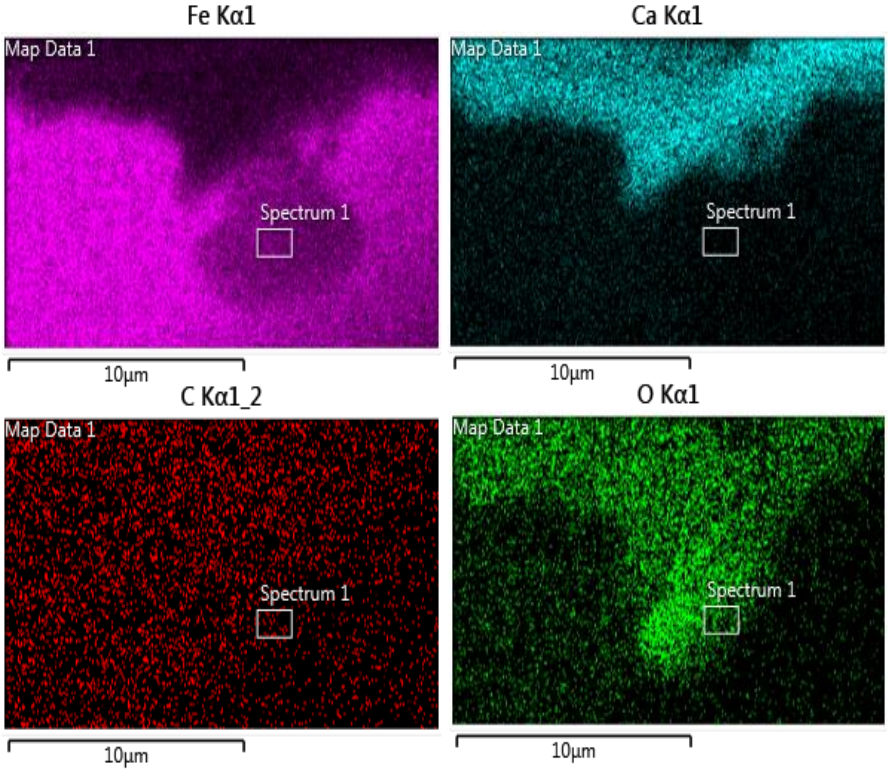

(b)

Figure 4-41 (a) FIB cross-section with (b) EDX mapping on X65 carbon steel exposed to a 1.83 wt.% $CaCl_2 \cdot 2H_2O$ brine for 96 h at 150 ºC

Data provided in Table 4-8 indicates that the mole fraction of calcium determined by XRD calculations provide an under estimation of the actual mole fraction of calcium within the corrosion product layer.

Table 4-8 Comparison of calcium mole fractions obtained by XRD calculations and FIB line scans

Exposure time (h)	X_{Ca} calculated using XRD	Height (µm)	X_{Ca} using FIB/EDX
24	0.52	Na	0.60
96	0.54	Na	0.60

4.3.5 Effect on Localised Corrosion Behaviour

The maximum pit depth increased with increasing exposure time at 80 ºC. As shown by Figure 4-42, the maximum pit depth increased from 7.5 µm after 6 hours of exposure to 50 µm after 96 hours of exposure.

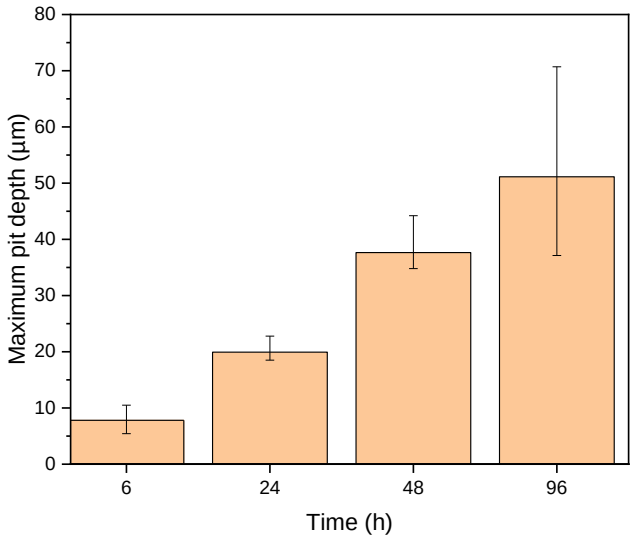

Figure 4-42 Maximum pit depth as a function of exposure time of X65 carbon steel in 1.83 wt.% $CaCl_2 \cdot 2H_2O$ at 80 ºC

Figure 4-43 examines the localised corrosion behaviour in terms of total penetration, the pit penetration was greater than uniform penetration throughout the 96 hour test period.

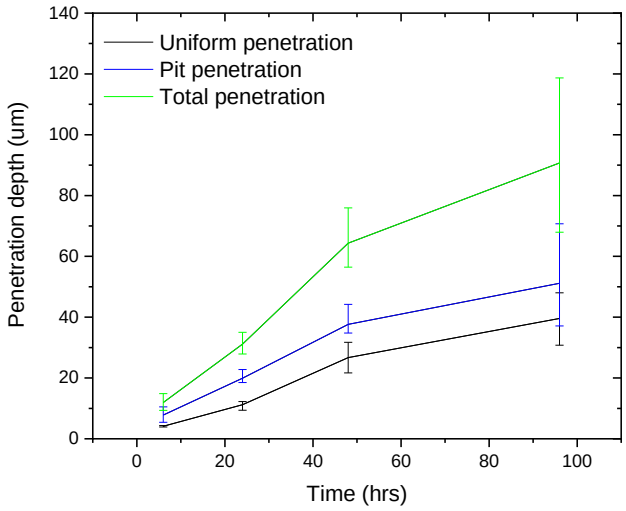

Figure 4-43 Total penetration as a function of exposure time of X65 carbon steel at in 1.83 wt.% $CaCl_2 \cdot 2H_2O$ at 80 ºC

The NPFLEX surface profilometry images show signs of pits on the steel surfaces after 96 hours of exposure. Figure 4-44 indicates pits with depths of approximately 30 and 40 µm can be observed after 96 hours of exposure.

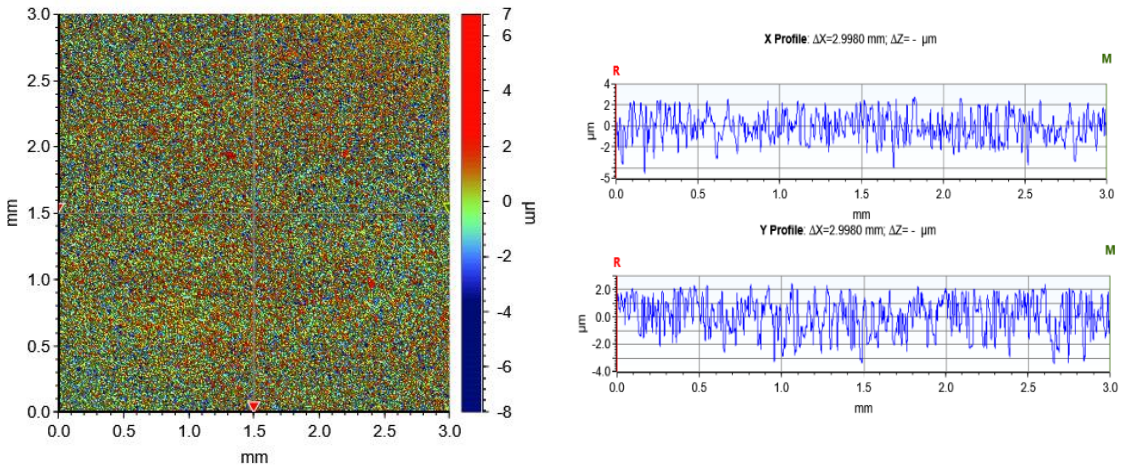

(a)

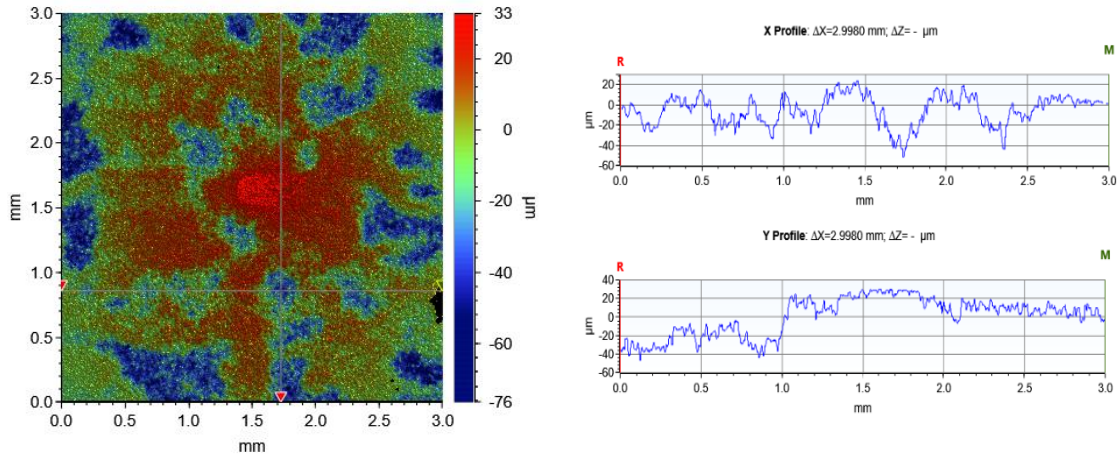

(b)

Figure 4-44 2D profilometry images of X65 carbon steel surfaces exposed to a 1.83 wt.% $CaCl_2 \cdot 2H_2O$ brine at 80 ºC for (a) 6 h and (b) 96 h

The maximum pit depth after exposure at 150 ºC provided in Figure 4-45. The bar chart shows that the maximum pit depth had developed within the first 6 hours of exposure and remained constant with exposure time at approximately 28 µm.

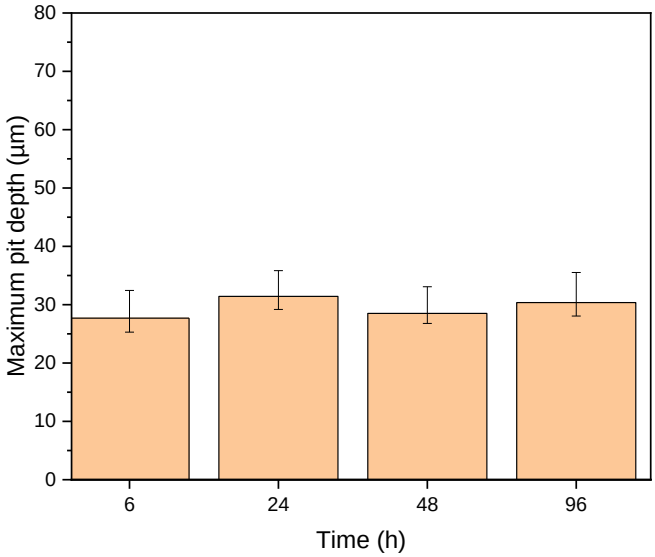

Figure 4-45 Maximum pit depth of X65 carbon steel as a function of exposure time in 1.83 wt.% $CaCl_2 \cdot 2H_2O$ brine at 150 ºC

Figure 4-46 can be used to evaluate the localised corrosion behaviour in terms of total penetration. The pit penetration contributed the most towards the total penetration throughout the 96 hour corrosion test

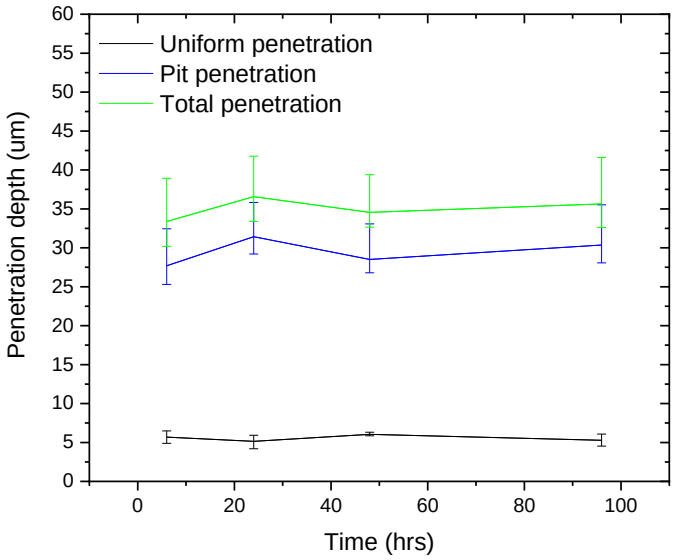

Figure 4-46 Total penetration as a function of exposure time of X65 carbon steel in 1.83 wt.% $CaCl_2 \cdot 2H_2O$ brine at 150 ºC

NPFELX surface profilometry images provided in Figure 4-47 provided indications of pits throughout test periods.

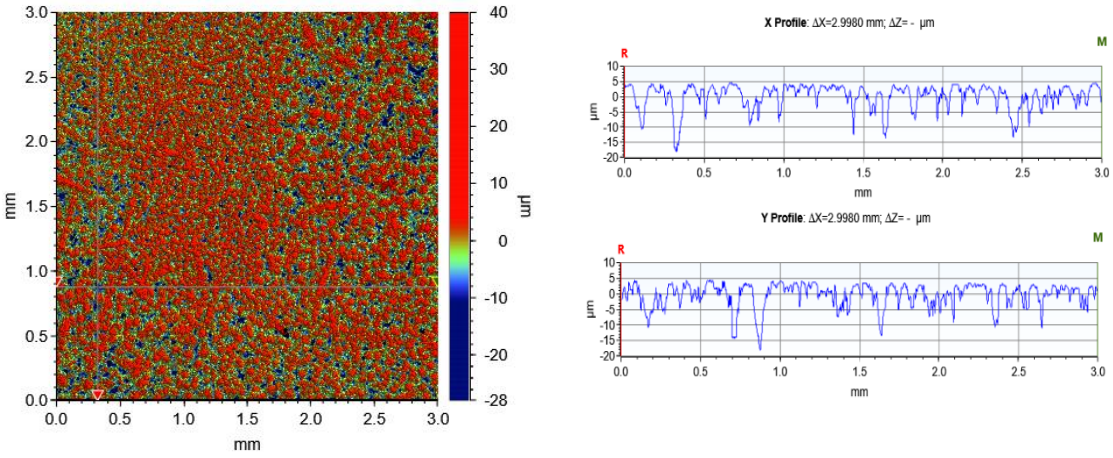

(a)

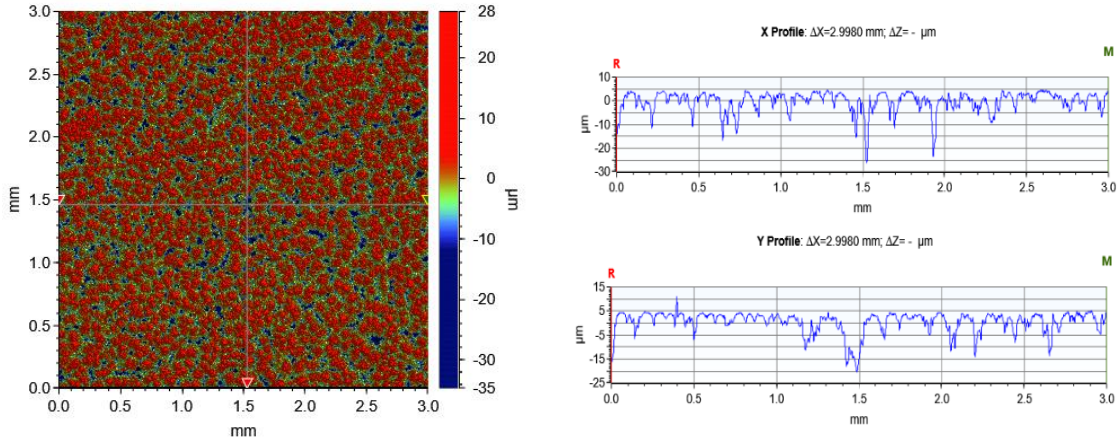

(b)

Figure 4-47 2D profilometry images of X65 carbon steel in 1.83 wt.% $CaCl_2 \cdot 2H_2O$ brine for (a) 6 h and (b) 96 h at 150 ºC

4.3.6 Influence of Intermediate Ca^{2+} Concentrations on Corrosion Product Morphology/Composition and Localised Corrosion Behaviour

The influence of Ca^{2+} on the overall corrosion behaviour was further evaluated at intermediate concentrations (0.018-0.92 wt.% $CaCl_2 \cdot 2H_2O$ at a maintained chloride content) for 48 hours of exposure at 80ºC. Experimental brine compositions are detailed in Chapter 4.1

Figure 4-48 shows top-view SEM images of surfaces exposed to calcium concentrations ranging from 0 to 1.83 wt.% $CaCl_2 \cdot 2H_2O$. The SEM images indicate that the cubic shape of iron carbonate crystals precipitated in the absence of calcium ions become more globular (iron calcium carbonate) by increasing the concentration of Ca^{2+} within the bulk solution. There was no apparent link between the calcium concentration in the bulk solution and the surface coverage, however the surface coverage was improved at calcium concentrations of 0.118 and 0.92 wt.% $CaCl_2 \cdot 2H_2O$. The introduction of calcium ions also resulted in an increase in the crystal grain sizes.

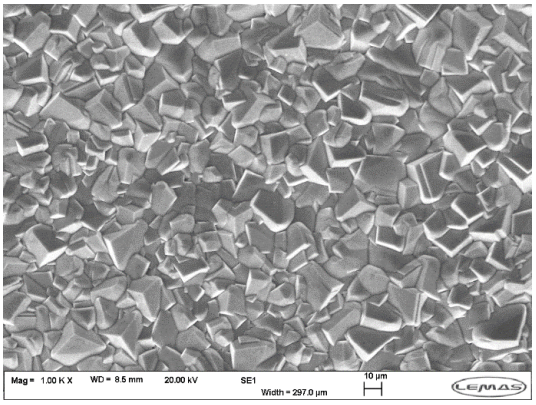
Mag = 1.00 K X
WD = 8.5 mm
20.00 kV
SE1
Width = 297.0 µm
10 µm

(a)

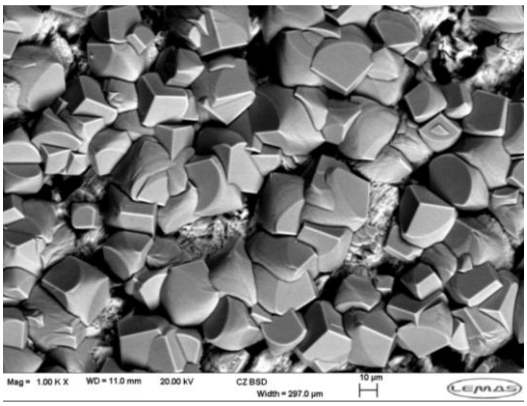
Mag = 1.00 K X
WD = 11.0 mm
20.00 kV
CZ BSD
Width = 297.0 µm
10 µm

(b)

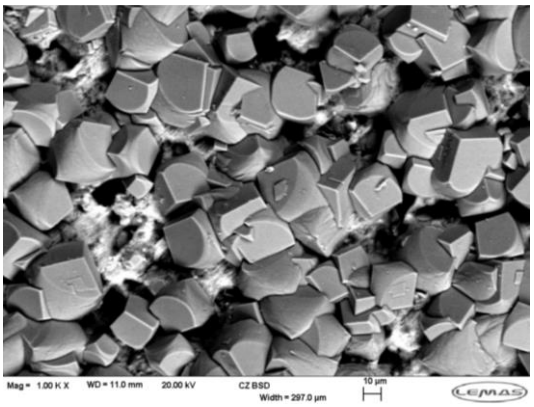
Mag = 1.00 K X
WD = 11.0 mm
20.00 kV
CZ BSD
Width = 297.0 µm
10 µm

(c)

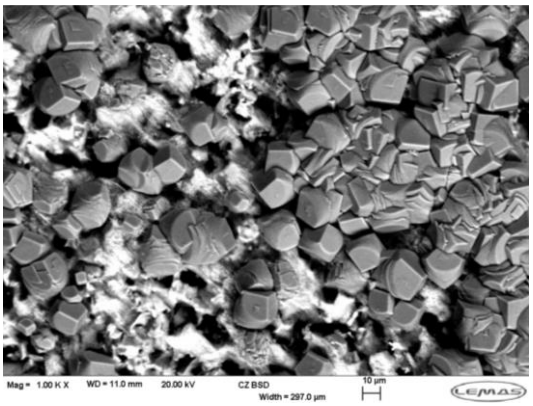
Mag = 1.00 K X
WD = 11.0 mm
20.00 kV
CZ BSD
Width = 297.0 µm
10 µm

(d)

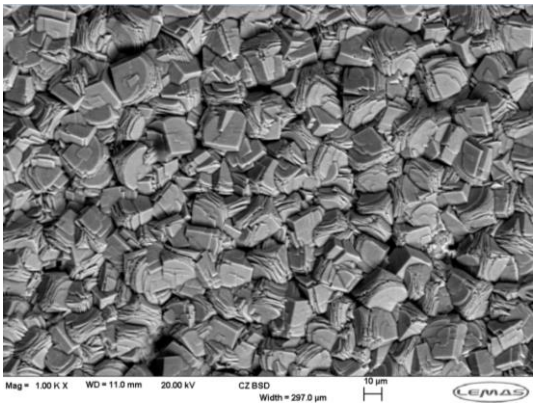
Mag = 1.00 K X
WD = 11.0 mm
20.00 kV
CZ BSD
Width = 297.0 µm
10 µm

(e)

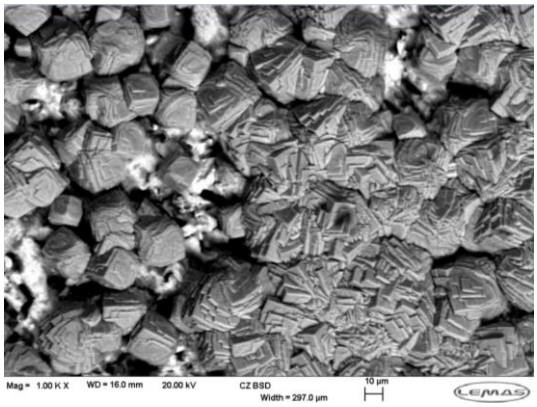
Mag = 1.00 K X
WD = 16.0 mm
20.00 kV
CZ BSD
Width = 297.0 µm
10 µm

(f)

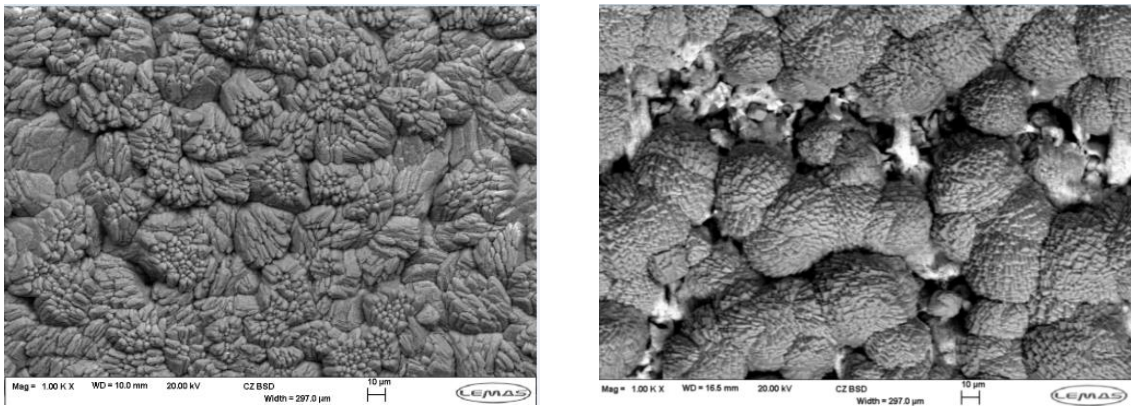

(g) **(h)**

Figure 4-48 Top-view SEM images of X65 carbon steel after exposure for 48h at 80 ºC in brines containing (a) 0, (b) 0.018, (c) 0.037, (d) 0.092, (e) 0.18, (f) 0.37, (g) 0.92 and (h) 1.83 wt.% $CaCl_2 \cdot 2H_2O$ at a maintained chloride content

The shift in [104] X-ray diffraction Bragg peaks for different calcium concentrations is provided in Figure 4-49. The [104] peaks show a clear shift from iron carbonate at 0 wt.% $CaCl_2 \cdot 2H_2O$ towards calcium carbonate with increasing Ca^{2+} concentration within the bulk solution, confirming that iron calcium carbonate was the main corrosion product present in the presence of Ca^{2+} concentration within the bulk.

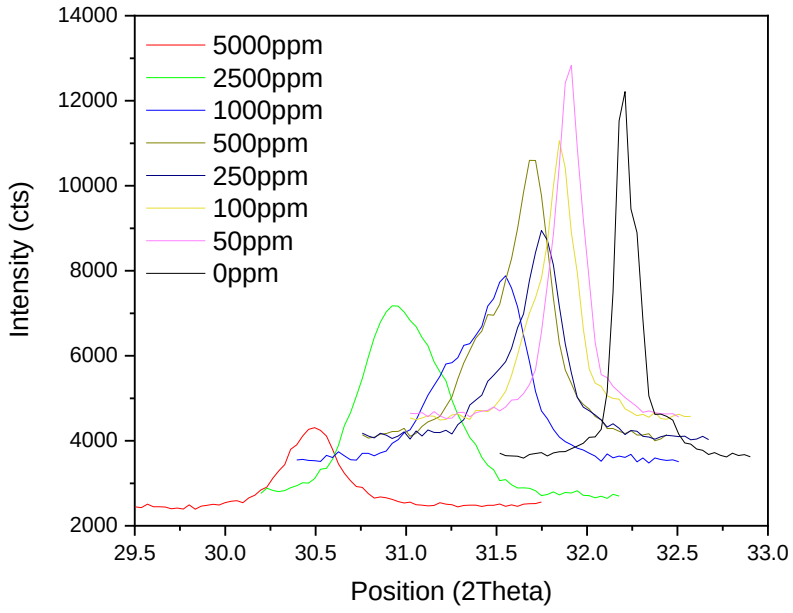

Figure 4-49 Shift in the [104] XRD peak with increasing Ca^{2+} concentration within the bulk solution at 80 ºC after exposure to brines containing 0, 0.018, 0.037, 0.092, 0.118, 0.37, 0.92 and 1.83 wt.% $CaCl_2 \cdot 2H_2O$ at a maintained chloride content

Figure 4-50 and Table 4-9 show the increase in the molar fraction of calcium and decrease in the molar fraction of iron within the iron calcium carbonate corrosion products as the Ca^{2+} concentration within the bulk solution is increased.

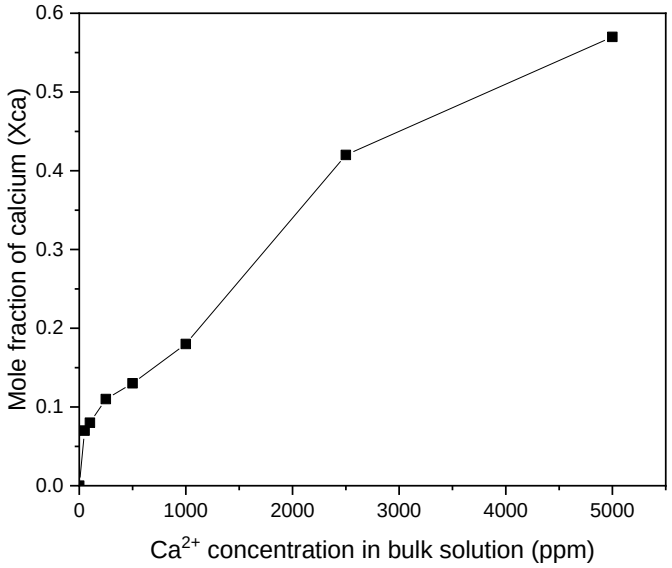

Figure 4-50 Calculated mole fraction of calcium (X_{Ca}) within corrosion product layer as a function of Ca^{2+} concentration within the bulk solution after 48 h exposure at 80 ºC

Table 4-9 Calculated mole fractions of calcium and iron within corrosion product layers after 48 h exposure to different bulk concentrations of Ca^{2+} at 80 ºC

Temperature (˚C)	Exposure time (h)	Chloride content (ppm)	Ca^{2+} concentration (ppm)	Calculated X_{Ca}	Calculated X_{Fe}
80	48	18197	0	0	1
			50	0.07	0.93
			100	0.08	0.92
			250	0.11	0.89
			500	0.13	0.87
			1000	0.18	0.82
			2500	0.42	0.58
			5000	0.57	0.43

Figure 4-51 shows that the maximum pit depth after 48 hours of exposure at different Ca^{2+} concentrations within the bulk solution did not appear to change significantly, with most of the change being within the error.

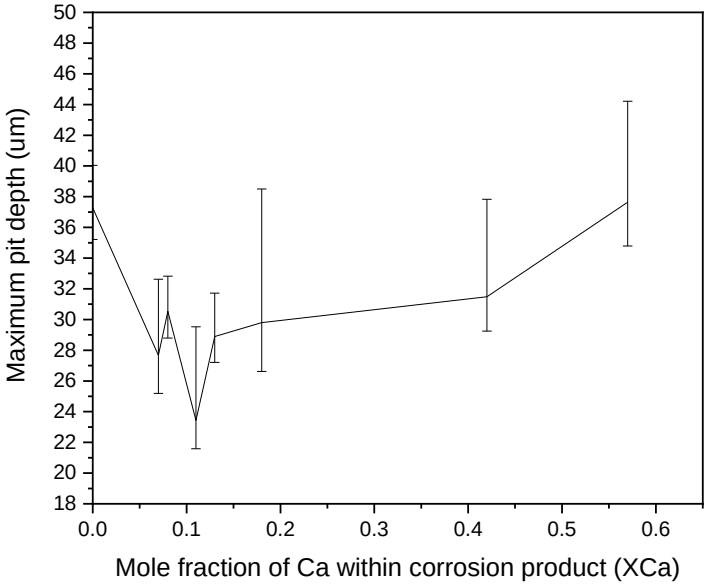

Figure 4-51 Maximum pit depth on X65 carbon steel as a function of X_{Ca} after 48 h exposure at 80 ºC

Figure 4-52 provides NPFLEX profilometry images which did not show any clear signs of localised corrosion attack at any of the intermediate Ca^{2+} concentrations.

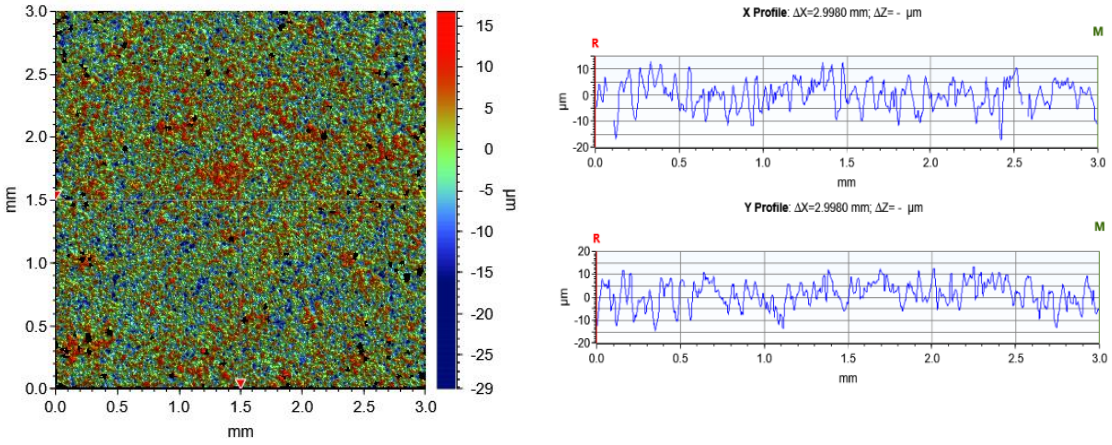

(a)

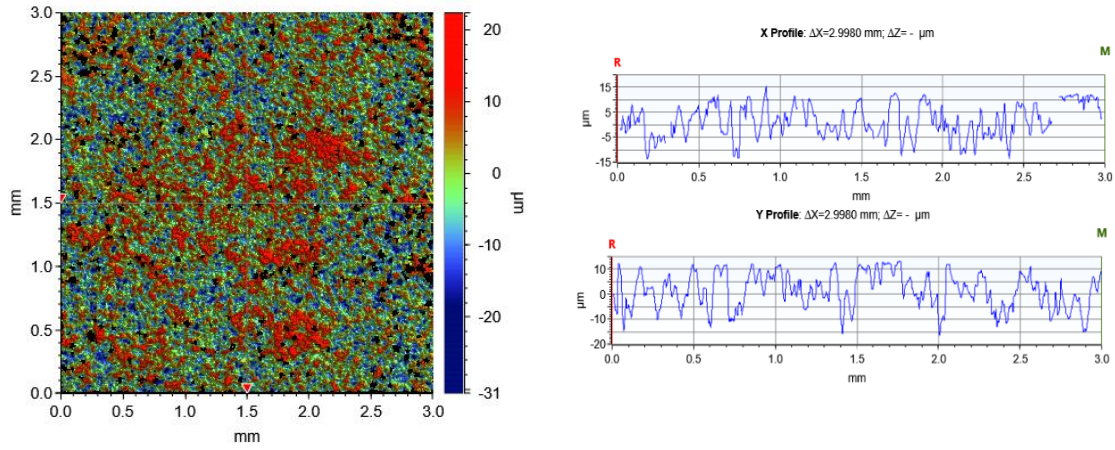
mm
µm
X Profile: ΔX=2.9980 mm; ΔZ= - µm
Y Profile: ΔX=2.9980 mm; ΔZ= - µm

(b)

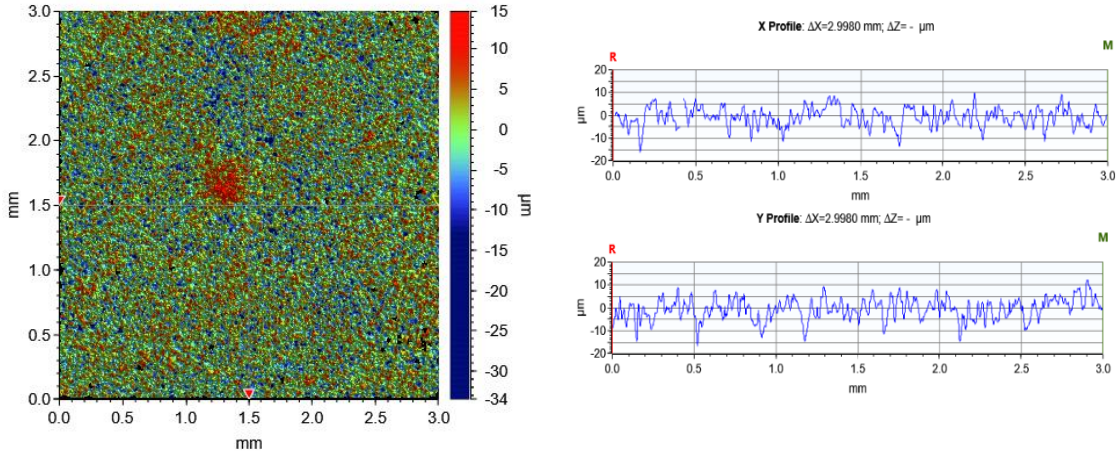
mm
µm
X Profile: ΔX=2.9980 mm; ΔZ= - µm
Y Profile: ΔX=2.9980 mm; ΔZ= - µm

(c)

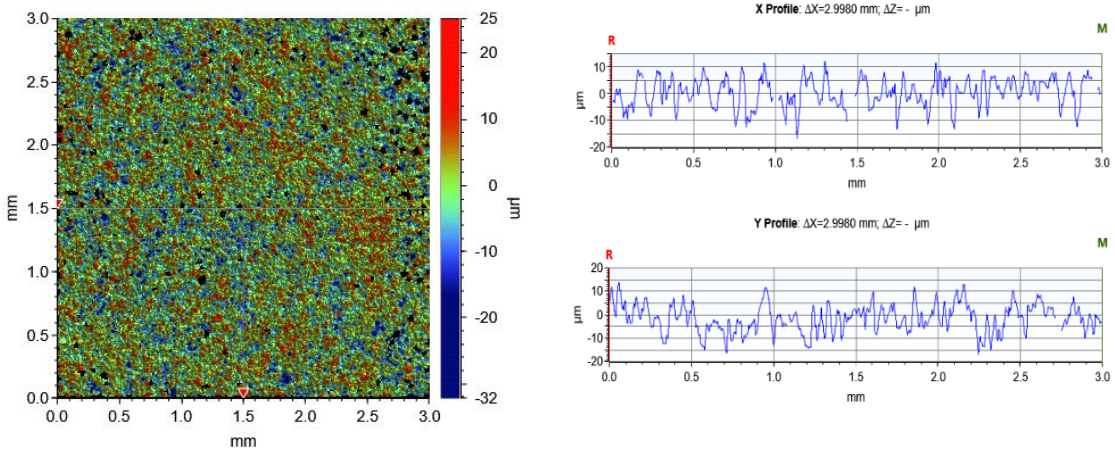
mm
µm
X Profile: ΔX=2.9980 mm; ΔZ= - µm
Y Profile: ΔX=2.9980 mm; ΔZ= - µm

(d)

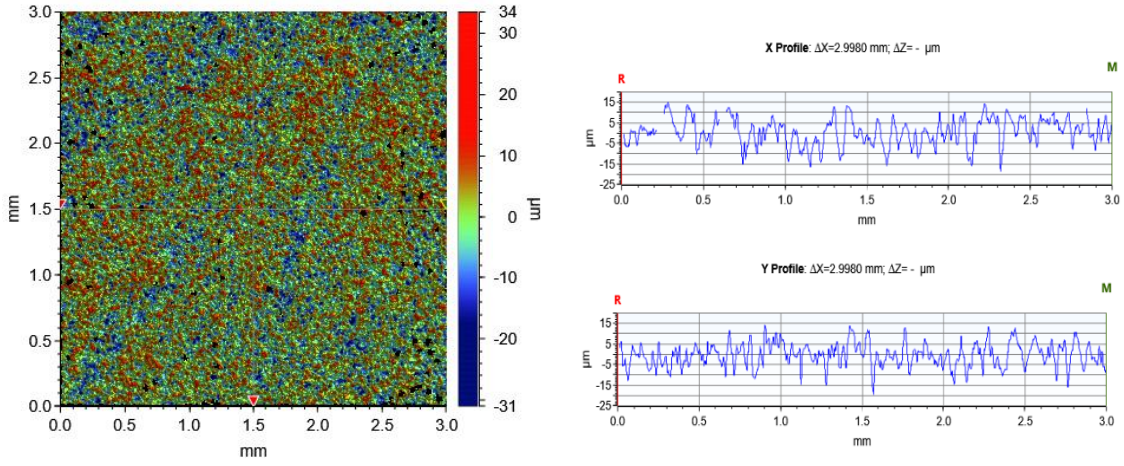

(e)

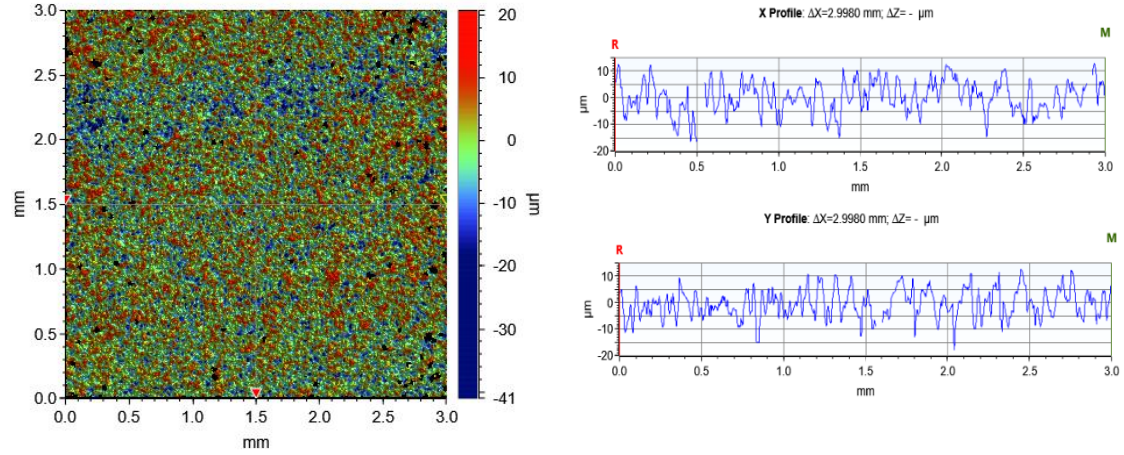

(f)

Figure 4-52 2D profilometry images of X65 carbon steel surfaces exposed to brines containing (a) 0.018, (b) 0.037, (c) 0.092, (d) 0.118, (e) 0.37 and (f) 0.92 wt.% $CaCl_2 \cdot 2H_2O$ at a maintained chloride content at 80 ºC for 48 h

4.4 Summary of Results

The role of Ca^{2+} ions on the corrosion behaviour of carbon steel in CO_2-corrosion environments was evaluated at 80 ºC and 150 ºC. In the presence of Ca^{2+} ions there was a more significant effect on the general corrosion rate at the lower temperature of 80 ºC where the protection afforded by the corrosion product layer was reduced. In the absence of calcium ions the corrosion products solely consisted of iron carbonate and in the presence of calcium ions the corrosion products consisted mainly of mixed iron-calcium carbonates, however with some precipitation of calcium carbonate. The addition of calcium ions within the bulk

solution resulted in the precipitation of globular structured crystals rather than cubic which resulted in poor coverage even after 96 hours at 80 ºC. In both the absence and presence of calcium ions the corrosion products precipitated at 150 ºC were more compact with greater surface coverage and larger crystal grain sizes.

XRD based calculations, along with focused ion beam EDX-line scans confirmed that mixed Ca/Fe carbonates precipitated with concentration gradients across their thicknesses at both 80 and 150 ºC. Greater Ca^{2+} concentrations within the bulk solution resulted in the precipitation of mixed iron-calcium carbonates with greater mole fractions of calcium. The extent of localised/pitting corrosion increased through the addition of Ca^{2+} ions indicating that Ca^{2+} plays a role in promoting localised corrosion. Corrosion rate measurements determined by linear polarisation resistance were validated against mass loss measurements. The associated error in corrosion rates determined by electrochemical measurements increased with increasing exposure time at 80 ºC and decreased with increasing exposure time at 150 ºC.

Chapter 5 Corrosion Inhibitor Performance Evaluation

5.1 Introduction

This chapter focuses on the evaluation of both uniform and localised corrosion behaviours in the presence of an imidazoline-based corrosion inhibitor and the influence of localised corrosion evaluation on the determination of the optimum inhibitor dosage at 80 °C in a CO_2-saturated sodium chloride (NaCl) brine. The influence of short term pre-corrosion and inhibitor aging on the overall performance of an imidazoline based corrosion inhibitor is also evaluated in terms of both uniform and localised corrosion within this Chapter. Findings within this chapter will be used to discuss the importance and effect of localised corrosion consideration in the determination of the optimum inhibitor dosage and on the overall evaluation of inhibitor performance.

Figure 5-1 provides an outline of the methodology structure used for the performance evaluation. The corrosion inhibitor was first evaluated in terms of inhibitor dosage (ranging from 10-100 ppm) and assessed based on its ability to retard both uniform and localised corrosion. The influence of short term pre-corrosion (2 hour pre-corrosion) was also assessed in order to determine the corrosion inhibitors' ability to perform on a pre-corroded surface in the absence of corrosion products. This was then followed by the evaluation of the inhibitor after it had undergone chemical aging at 80 ºC and 120 ºC. The performance of the corrosion inhibitor was evaluated in terms of both uniform and localised corrosion throughout this chapter.

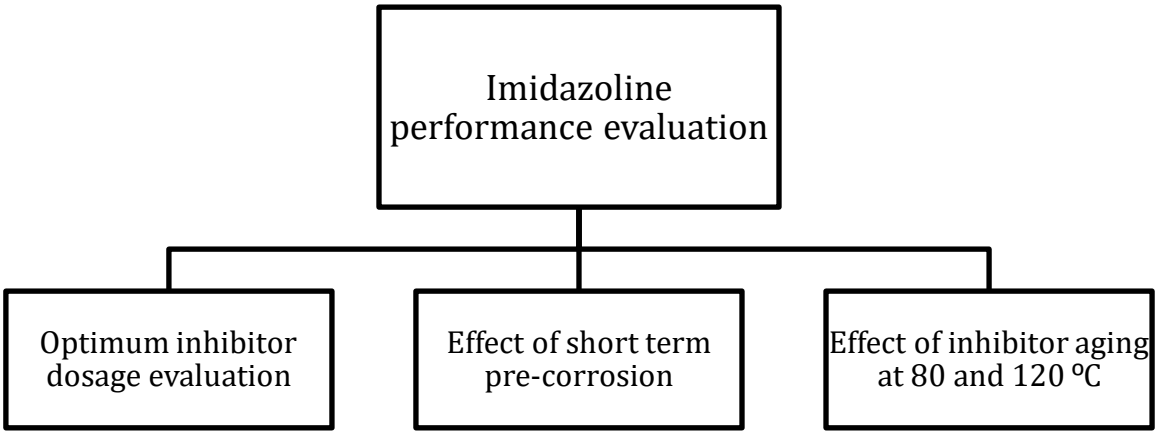

Figure 5-1 Outline of corrosion inhibitor performance tests

Data obtained by LPR measurements were presented in the form of reciprocal polarisation resistance rather than corrosion rate in order to prevent the assumption of β_a and β_c values which may have an influence on corrosion rate prediction across different inhibitor concentrations.

5.2 Optimum Inhibitor Concentration Evaluation

5.2.1 Testing Procedure

Experiments presented within this sub chapter were conducted according to the experimental procedure described in Chapter 3.4. A single carbon steel specimen was inserted into a glass beaker containing a 3 wt.% NaCl brine and was pre-corroded for 2 hours. The imidazoline corrosion inhibitor was then injected into the non-inhibited brine containing the steel specimen after 2 h of exposure and was left to corrode for a further 46 hours. The total testing time was 48 hours. Experiments were repeated at each inhibitor concentration to enable the determination of the experimental error. Electrochemical measurements in the form of linear polarisation resistance were conducted according to the procedure described in Chapter 3.4. Post-test NPFLEX, SEM and XRD analysis of steel surfaces was carried out in accordance with procedures described in Chapter 3.5.

5.2.2 Uniform Corrosion Behaviour

Figure 5-2 shows the reciprocal polarisation resistance and open circuit potential versus exposure time for carbon steel exposed to brines containing inhibitor concentrations ranging from 0 to 40 ppm. The reciprocal polarisation resistance indicates that for inhibitor concentrations of 10 and 20 ppm, the reduction in reciprocal polarisation resistance was slow and decreased from 0.017 $ohm^{-1}cm^{-2}$ to 0.007 and 0.004 $ohm^{-1}cm^{-2}$ respectively after 48 hours of total exposure. However at inhibitor concentrations of 30 and 40 ppm the reciprocal polarisation resistance reduced to values of 0.0003 and 0.001 $ohm^{-1}cm^{-2}$ respectively. The reductions in reciprocal polarisation resistance with time during inhibition were associated with positive shifts in the open circuit potential, where the potential stabilised the fastest at 40 ppm. A two-step increase in the open circuit potential was also observed at an inhibitor concentration of 30 ppm.

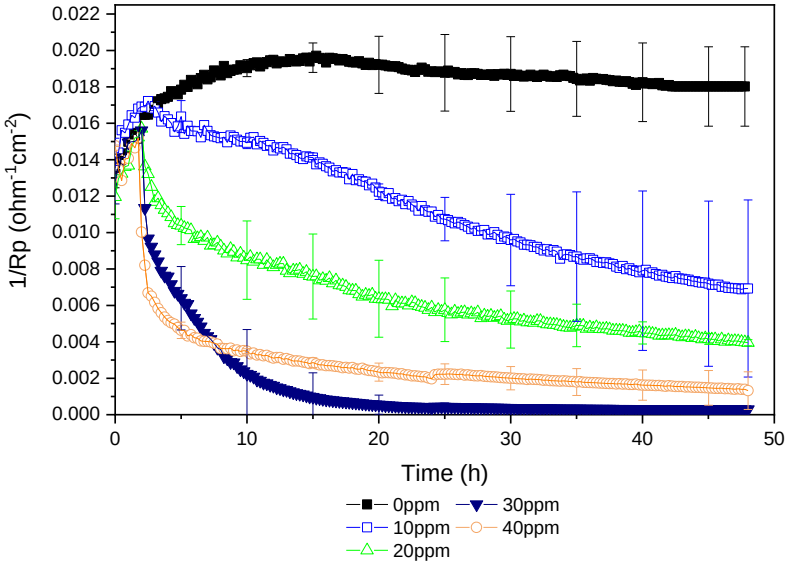

(a)

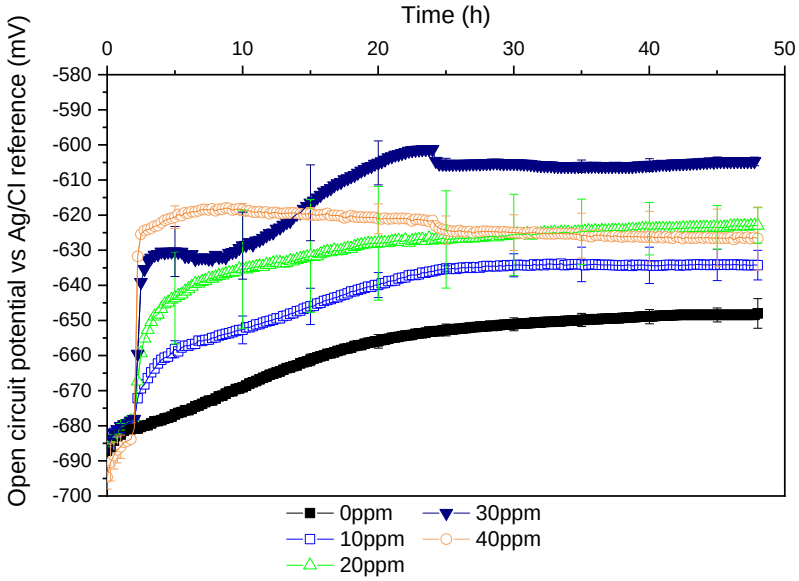

(b)

Figure 5-2 (a) Reciprocal of polarisation resistance in ohm^{-1}cm^{-2} and (b) open circuit potential in mV as a function of time determined using electrochemistry for X65 carbon steel exposed to a CO_2-saturated 3 wt.% NaCl solution at 80 $^{\circ}$C with imidazoline concentrations ranging from 0 to 40 ppm after 2 h of pre-corrosion

Figure 5-3 provides the reciprocal polarisation resistance at inhibitor concentrations of 50 and 100 ppm, where the reciprocal polarisation resistance stabilised faster relative to inhibitor concentrations below 50 ppm however at higher final reciprocal polarisation resistances (0.00049 and 0.00085 ohm^{-1}cm^{-2}

at 50 and 100ppm respectively). The open circuit potential at 50 and 100 ppm increased as the inhibitor was injected however never completely stabilised with increasing exposure time.

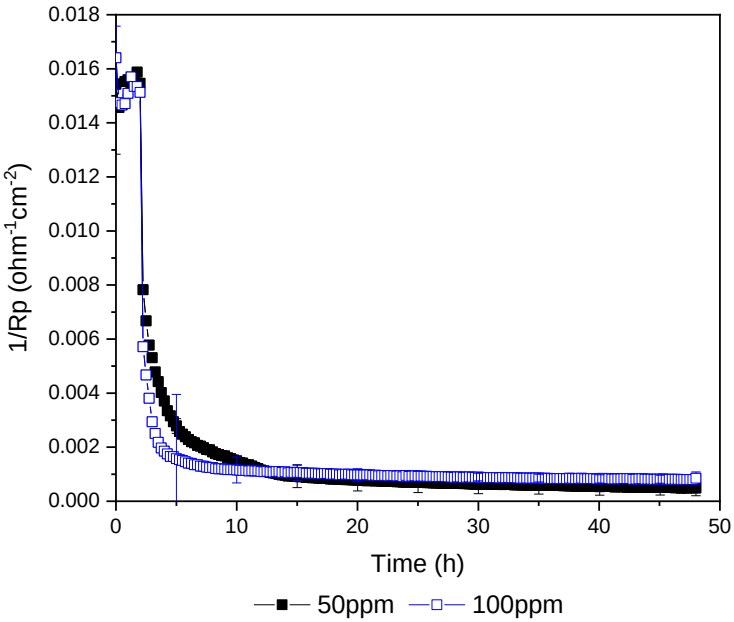

(a)

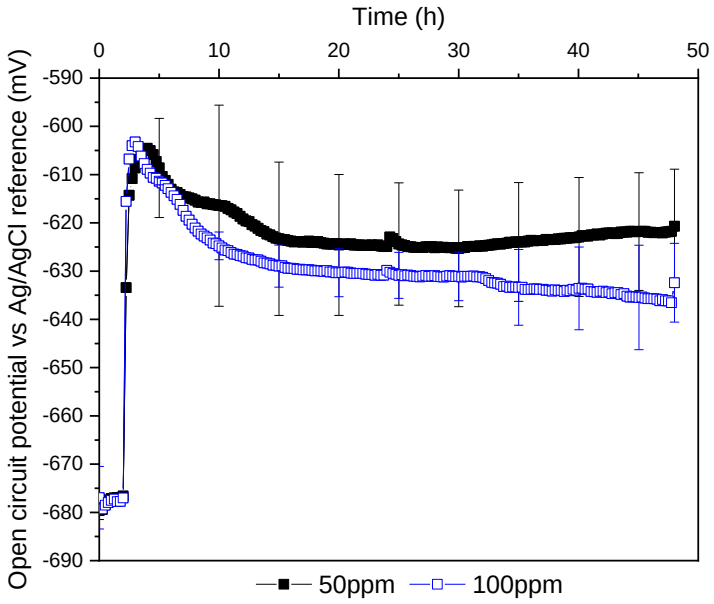

(b)

Figure 5-3 (a) Reciprocal of polarisation resistance in $ohm^{-1}cm^{-2}$ and (b) open circuit potential in mV as a function of time determined using electrochemistry for X65 carbon steel exposed to a CO_2-saturated 3 wt.% NaCl solution at 80 ˚C with imidazoline concentrations ranging from 50 to 100 ppm after 2 h of pre-corrosion

The bulk solution pH for all of the tested inhibitor concentrations are provided in Figure 5-4. The pH reduced initially with increasing inhibitor concentration as the corrosion inhibitor was introduced after the 2 hour pre-corrosion period, however by the end of the 48 hour test the bulk pH was the lowest for tests conducted at 30 and 50 ppm.

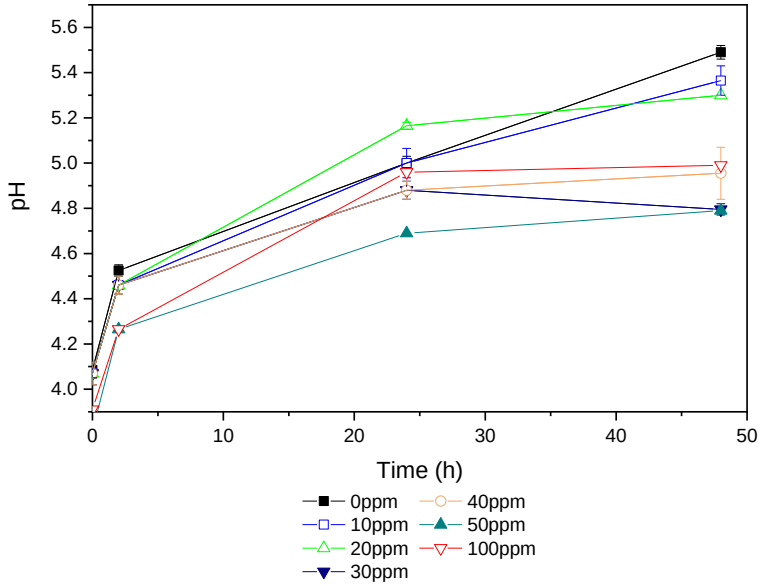

Figure 5-4 Bulk solution pH for X65 carbon steel exposed to a CO_2-saturated 3 wt.% NaCl solution at 80 °C with imidazoline concentrations ranging from 0 to 100 ppm after 2 h of pre-corrosion

The inhibitor efficiency in terms of uniform corrosion protection was determined at each inhibitor concentration as an end-point efficiency and as an integrated efficiency using Equations 5.1 and 5.2 respectively. The end-point efficiency represents the efficiency of the corrosion inhibitor based on the overall reduction in reciprocal polarisation resistance considering only the final 48 hour reciprocal polarisation resistance. However, the integrated efficiency takes into consideration every single reciprocal polarisation resistance during the corrosion tests. This efficiency is therefore also representative of the adsorption kinetics of the corrosion inhibitor. Figure 5-5 shows that the inhibitor efficiency in terms of uniform corrosion behaviour was the greatest at an inhibitor concentration of 30 ppm (98.2 and 97.1% for end-point and integrated efficiencies respectively). The integrated efficiency was greater than the end-point efficiency only at 50 ppm due to the fast rate of reduction in reciprocal polarisation resistance.

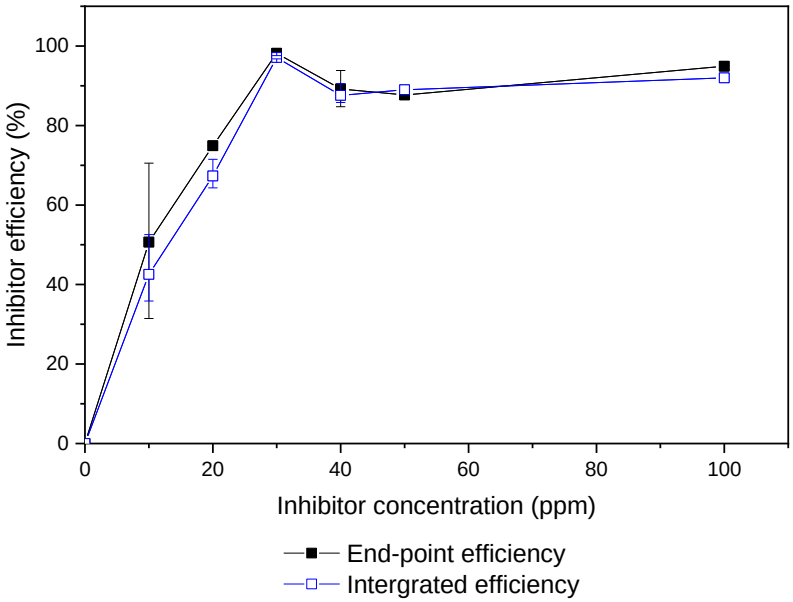

Figure 5-5 Inhibitor efficiency for X65 carbon steel exposed to a CO_2-saturated 3 wt.% NaCl solution at 80 °C with imidazoline concentrations ranging from 0 to 100 ppm after 2 h of pre-corrosion

$$E_{Endpoint}(\%) = \left[1 - \left(\frac{Rp_{Final}}{Rp_{Initial}}\right)\right] \times 100 \quad (5.1)$$

$$E_{Integrated}(\%) = \left(1 - \left[\int_{2}^{48} \left(\frac{Rp_{Final}}{Rp_{Initial}}\right)\right]\right) \times 100 \quad (5.2)$$

Where Rp_{Final} is the inhibited polarisation resistance at the end of the test (Ohm.cm^2) and $Rp_{Initial}$ is the uninhibited polarisation resistance before inhibitor addition (Ohm.cm^2).

Figure 5-6 shows top-view SEM images of steel specimens exposed to brines in the absence/presence of the corrosion inhibitor at all of the tested concentrations. In the absence of the corrosion inhibitor the surface becomes heavily corroded after 48 hours of exposure. At an inhibitor concentration of 10 ppm, the surface appears to be more heavily corroded on certain areas and less corroded on others. This can also be observed at an inhibitor concentration of 20 ppm however to a lesser extent. Steel specimens exposed to inhibitor concentrations of 30 ppm and above appeared to be less damaged by the corrosion process.

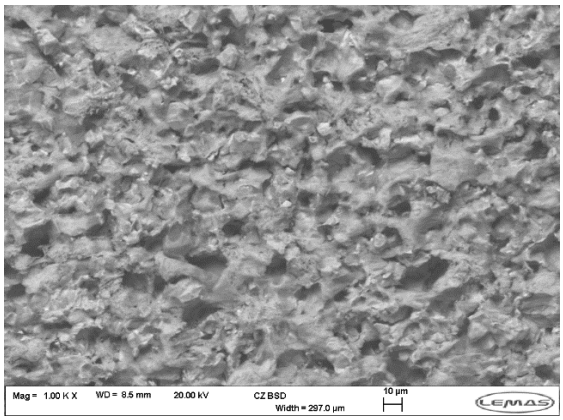
Mag = 1.00 K X WD = 8.5 mm 20.00 kV CZ BSD Width = 297.0 µm 10 µm

(a)

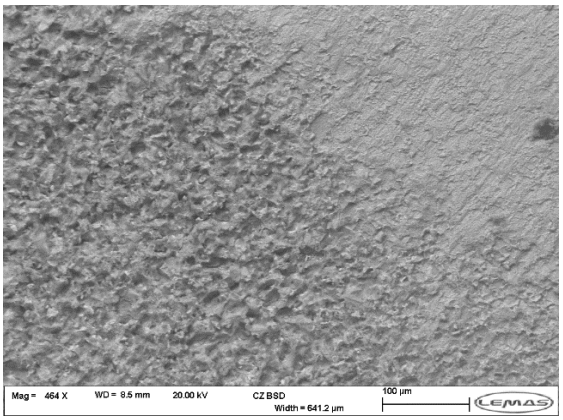
Mag = 464 X WD = 8.5 mm 20.00 kV CZ BSD Width = 641.2 µm 100 µm

(b)

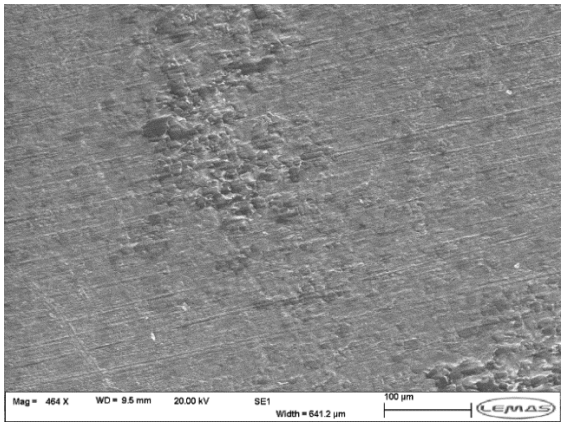
Mag = 464 X WD = 9.5 mm 20.00 kV SE1 Width = 641.2 µm 100 µm

(c)

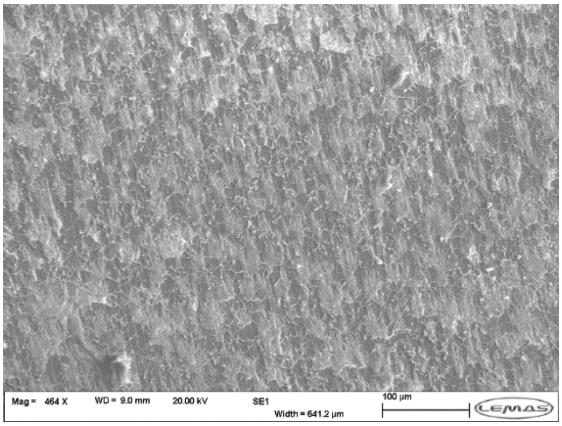
Mag = 464 X WD = 9.0 mm 20.00 kV SE1 Width = 641.2 µm 100 µm

(d)

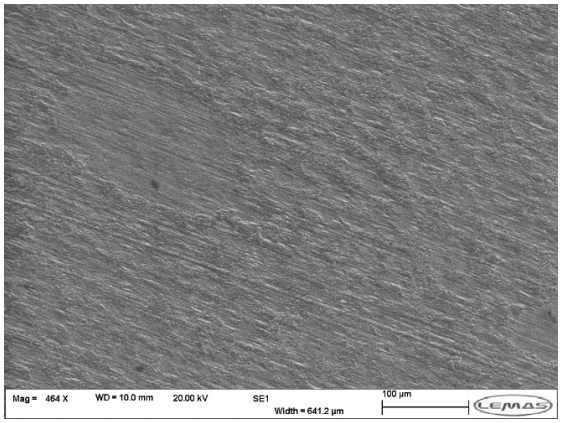
Mag = 464 X WD = 10.0 mm 20.00 kV SE1 Width = 641.2 µm 100 µm

(e)

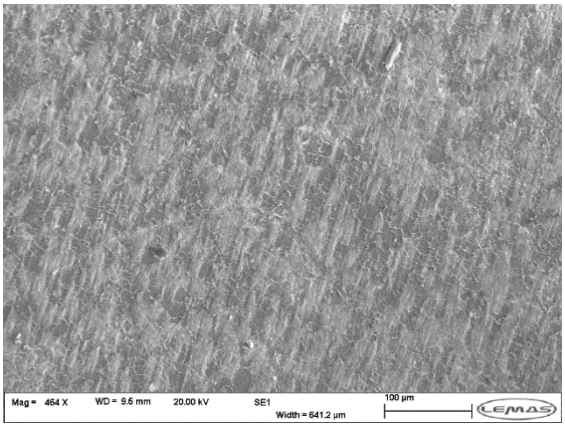
Mag = 464 X WD = 9.5 mm 20.00 kV SE1 Width = 641.2 µm 100 µm

(f)

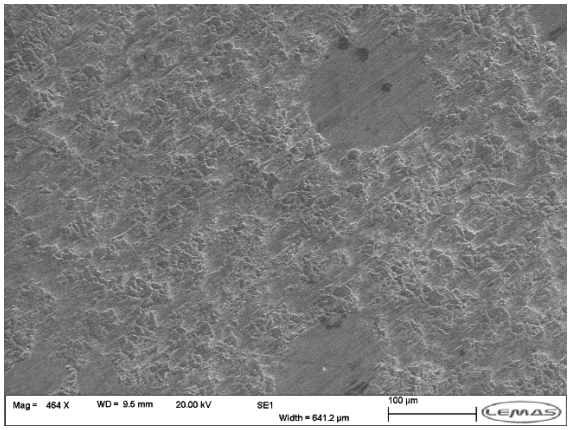

(g)

Figure 5-6 SEM images of X65 carbon steel exposed to a CO_2-saturated 3 wt.% NaCl solution at 80 °C with imidazoline concentrations of (a) 0 ppm, (b) 10 ppm, (c) 20 ppm, (d) 30 ppm, (e) 40 ppm, (f) 50 ppm and (g) 100 ppm after 2 h pre-corrosion for a total experimental time of 48 h

5.2.3 Localised Corrosion Behaviour

The localised corrosion behaviour was assessed in terms of maximum pit depth according to the procedure described in Chapter 3.5. Figure 5-7 indicates that the maximum pit depth in the absence of the corrosion inhibitor was approximately 26 µm. The maximum pit depth only decreased significantly at inhibitor concentrations of 40 ppm and above where the maximum pit depth was reduced to 1.7 µm at 40 ppm.

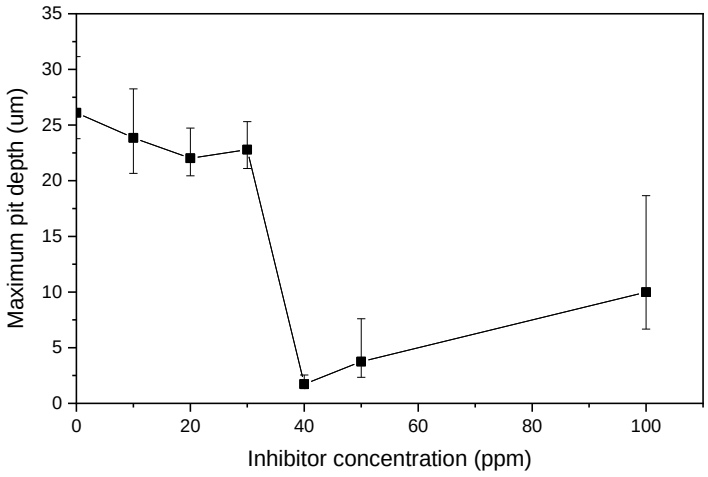

Figure 5-7 Maximum pit depth for X65 carbon steel exposed to a CO_2-saturated 3 wt.% NaCl solution at 80 °C with Imidazoline concentrations ranging from 0 to 100 ppm after 2 h of pre-corrosion with a total exposure of 48 hours

A comparison between the uniform and localised corrosion inhibition efficiencies is provided in Figure 5-8 which shows that both the uniform and localised efficiencies are the greatest at an inhibitor efficiency of 40 ppm rather than 30 ppm. The localised corrosion inhibitor efficiency was calculated using Equation (5.3).

$$IE\ (\%) = \left(1 - \frac{P_{inhibited}}{P_{uninhibited}}\right) * 100 \tag{5.3}$$

Where $P_{inhibited}$ is the maximum pit depth after exposure to the inibited brine and $P_{uninhibited}$ is the maximum pit depth after exposure to the uninhbited brine.

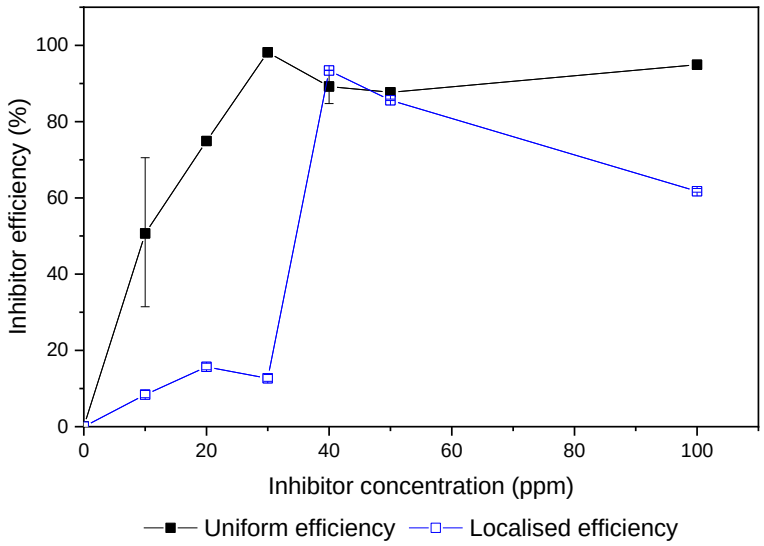

Figure 5-8 Inhibitor efficiency comparison for X65 carbon steel exposed to a CO_2-saturated 3 wt.% NaCl solution at 80 °C with Imidazoline concentrations ranging from 0 to 100 ppm after 2 h of pre-corrosion

2D and 3D surface profilometry images were used to confirm the presence of localised attacks on the steel surfaces exposed to the corrosion inhibitor. Figure 5-9 to Figure 5-14 indicate that in the absence of the corrosion inhibitor the surface had been roughened. Localised corrosion attacks could also be observed at 30 ppm.

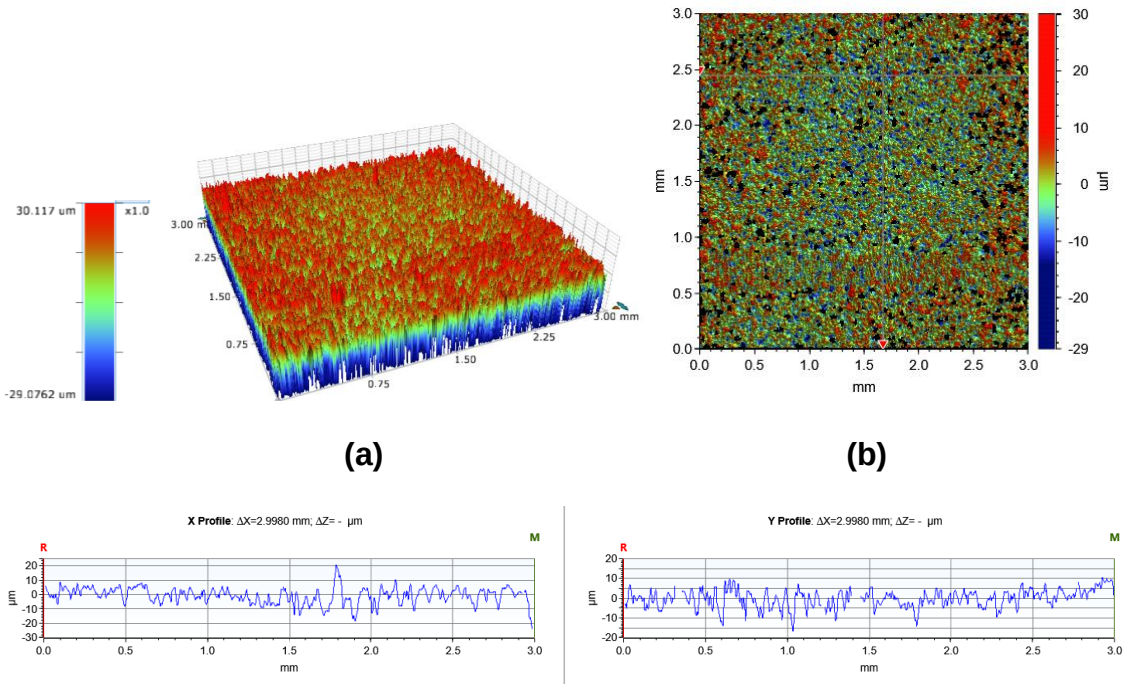

Figure 5-9 (a) 3D image, (b) 2D image and (c) 2D micrographs for X65 carbon steel exposed to a CO_2-saturated 3 wt.% NaCl solution at 80 °C for 48 h

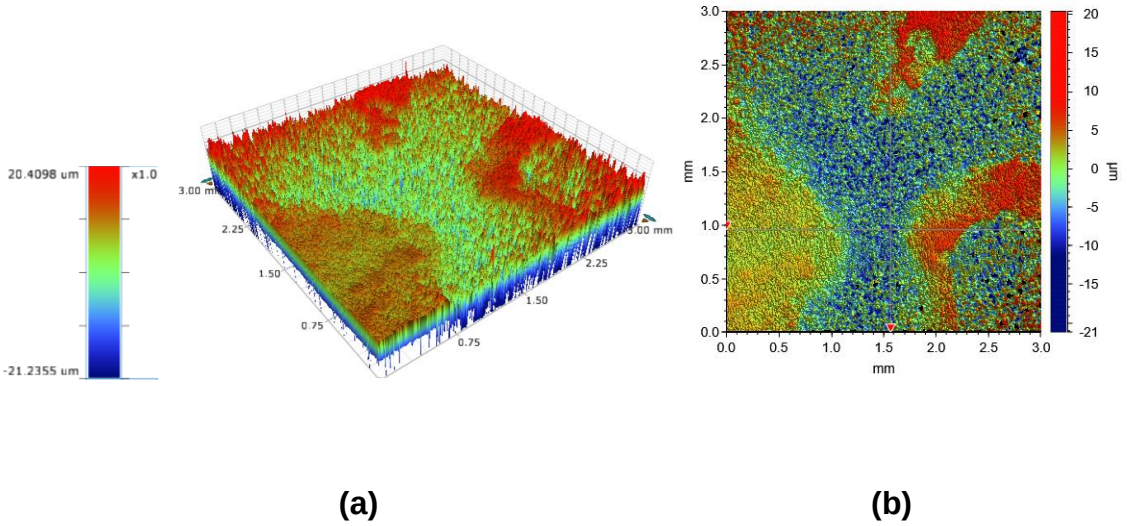

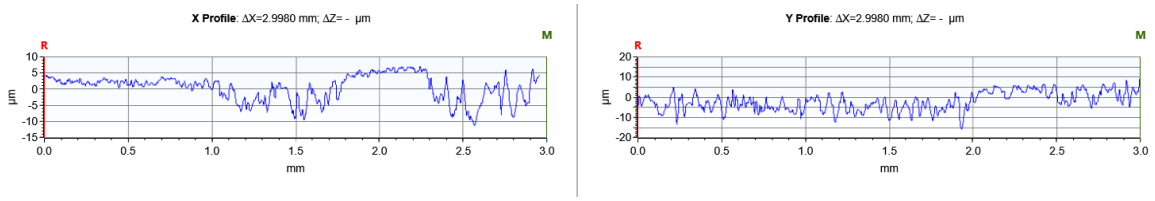

(c)

Figure 5-10 (a) 3D image, (b) 2D image and (c) 2D micrographs for X65 carbon steel exposed to a CO_2-saturated 3 wt.% NaCl solution at 80 °C with 10 ppm imidazoline inhibitor added after 2 h pre-corrosion

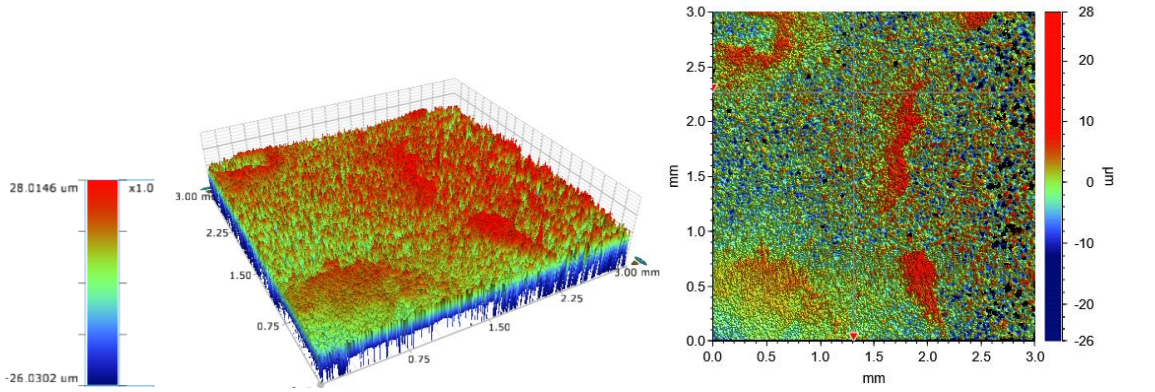

(a) **(b)**

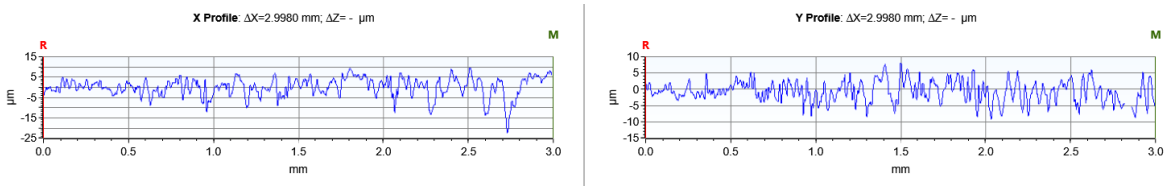

(c)

Figure 5-11 (a) 3D image, (b) 2D image and (c) 2D micrographs for X65 carbon steel exposed to a CO_2-saturated 3 wt.% NaCl solution at 80 °C with 20 ppm imidazoline inhibitor added after 2 h pre-corrosion

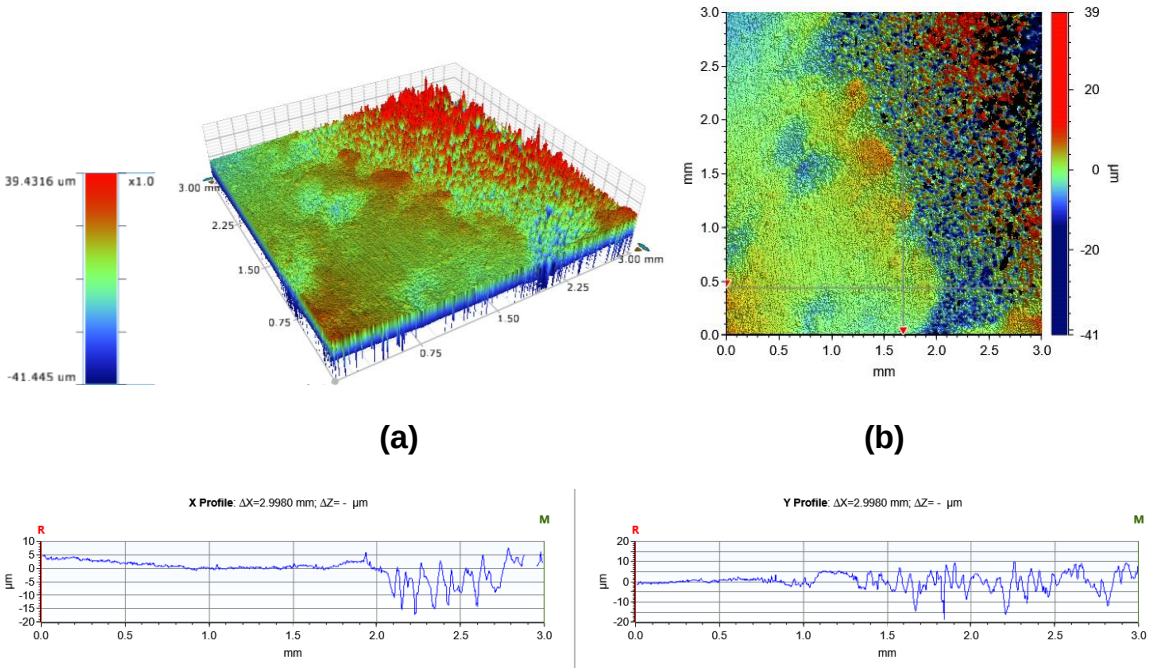

Figure 5-12 (a) 3D image, (b) 2D image and (c) 2D micrographs for X65 carbon steel exposed to a CO_2-saturated 3 wt.% NaCl solution at 80 °C with 30 ppm imidazoline inhibitor added after 2 h pre-corrosion

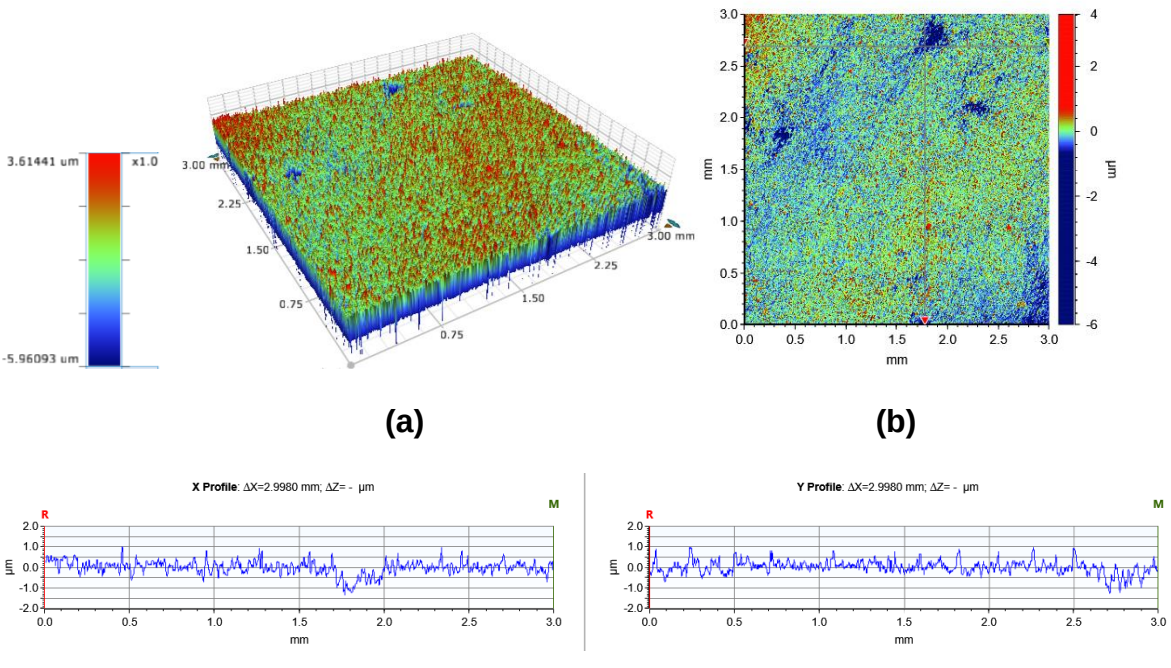

Figure 5-13 (a) 3D image, (b) 2D image and (c) 2D micrographs for X65 carbon steel exposed to a CO_2-saturated 3 wt.% NaCl solution at 80 °C with 40 ppm imidazoline inhibitor added after 2 h pre-corrosion

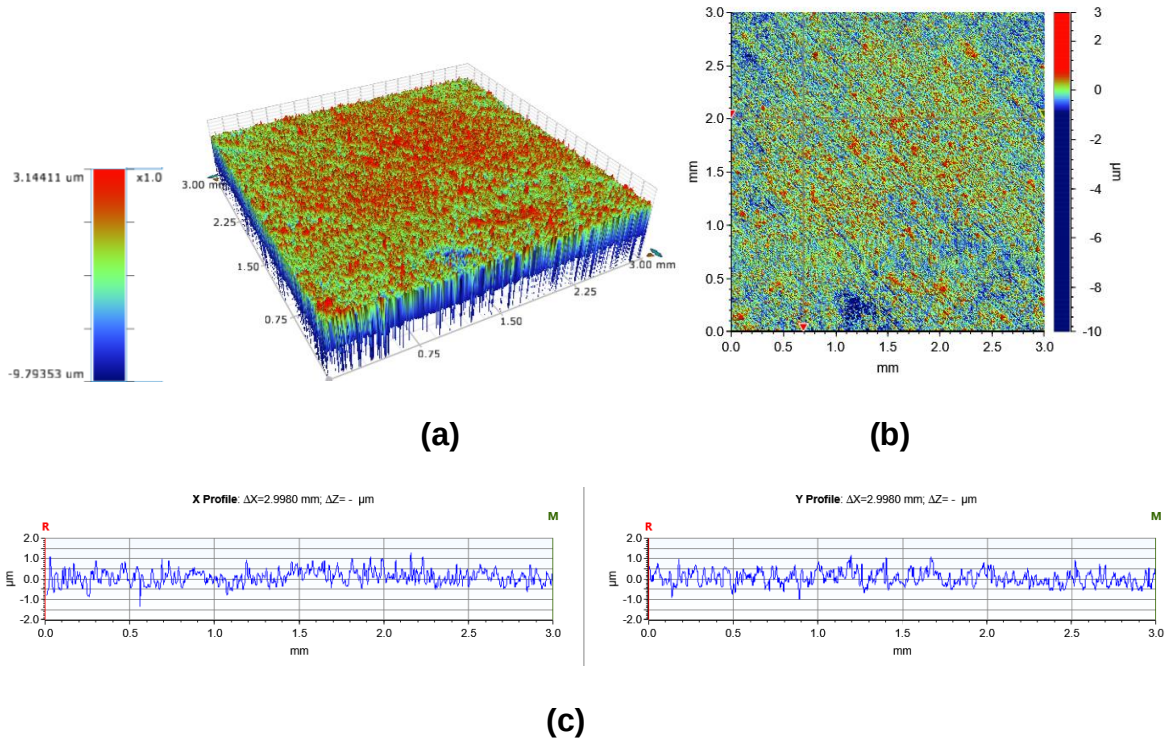

Figure 5-14 3D image, (b) 2D image and (c) 2D micrographs for X65 carbon steel exposed to a CO_2-saturated 3 wt.% NaCl solution at 80 °C with 50 ppm imidazoline inhibitor added after 2 h pre-corrosion

5.3 Effect of Short Term Pre-Corrosion on Corrosion Inhibition

5.3.1 Testing Procedure

The corrosion tests described within this sub-chapter were conducted according to the experimental procedure described in Chapter 3.4. Tests were conducted at an inhibitor concentration of 30 ppm in the absence of a pre-corrosion period where the inhibitor had been injected to the brine prior to the introduction of a steel specimen. The findings were compared to findings from Chapter 5.2 where the corrosion inhibitor was injected after a two hour pre-corrosion period.

5.3.2 Uniform Corrosion Behaviour

The reciprocal polarisation resistance in Figure 5-15 indicates that there is faster rate of reduction in the absence of a pre-corrosion period, however the stabilised reciprocal polarisation resistance was lower when a pre-corrosion period of 2 hours was established before inhibitor injection. The reciprocal polarisation resistance was 0.00096 $ohm^{-1}cm^{-2}$ in the absence of a pre-corrosion period as

compared to 0.00029 ohm^{-1}cm^{-2} by the end of the tests. This was also associated with a smaller positive shift in the open circuit potential, where it stabilised at -640 mV as compared -605 mV. A double shift in the OCP was only observed after inhibitor injection after a 2 hour pre-corrosion period.

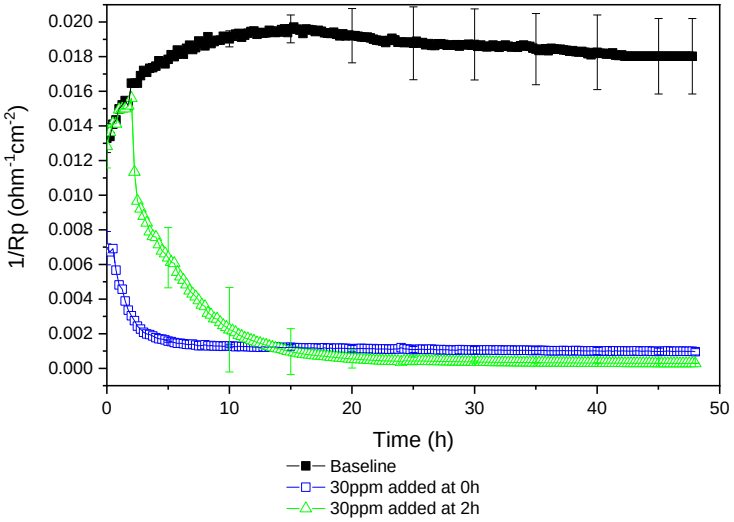

(a)

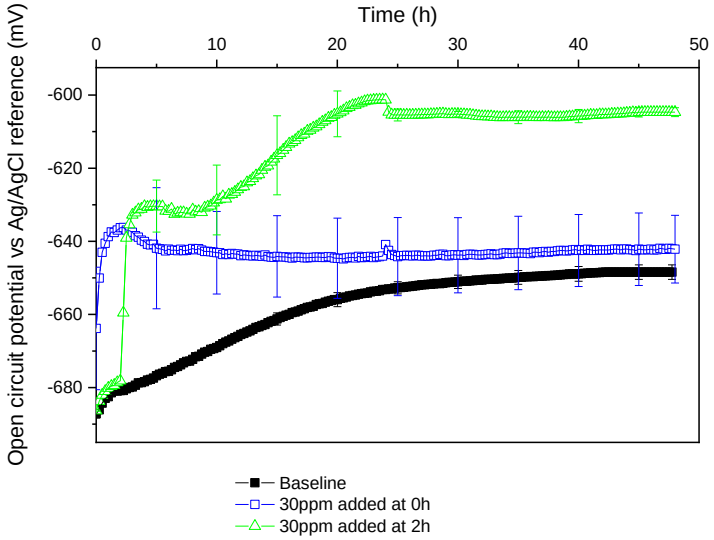

(b)

Figure 5-15 (a) Reciprocal of polarisation resistance in ohm^{-1}cm^{-2} and (b) open circuit potential in mV as a function of time determined using electrochemistry for X65 carbon steel exposed to a CO_2-saturated 3 wt.% NaCl solution at 80 $^{\circ}$C with 30 ppm imidazoline with and without 2 h pre-corrosion

The bulk solution pH remained lower in tests conducted in the absence of a pre-corrosion period and after 48 hours of exposure the bulk pH was 4.3 as

compared to a bulk pH of 4.75 in tests conducted with inhibitor injection after a 2 hour pre-corrosion period.

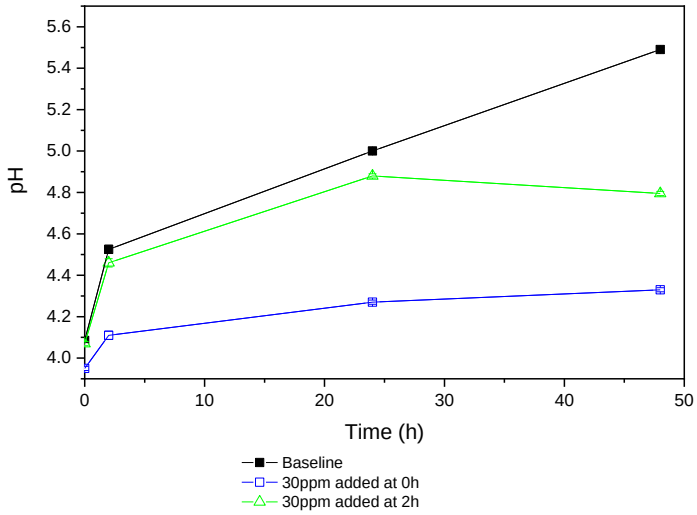

Figure 5-16 Bulk solution pH for X65 carbon steel exposed to a CO_2-saturated 3 wt.% NaCl solution at 80 °C with 30 ppm imidazoline with and without 2 h pre-corrosion

Top-view SEM images indicated that the steel specimen exposed to the inhibitor containing brine (in the absence of the pre-corrosion period) had two distinct areas of corrosion, where one area appeared to be more heavily corroded than the other as compared to a visibly uniformly roughened surface when the steel specimen had undergone a 2 hour pre-corrosion period before exposure to the corrosion inhibitor.

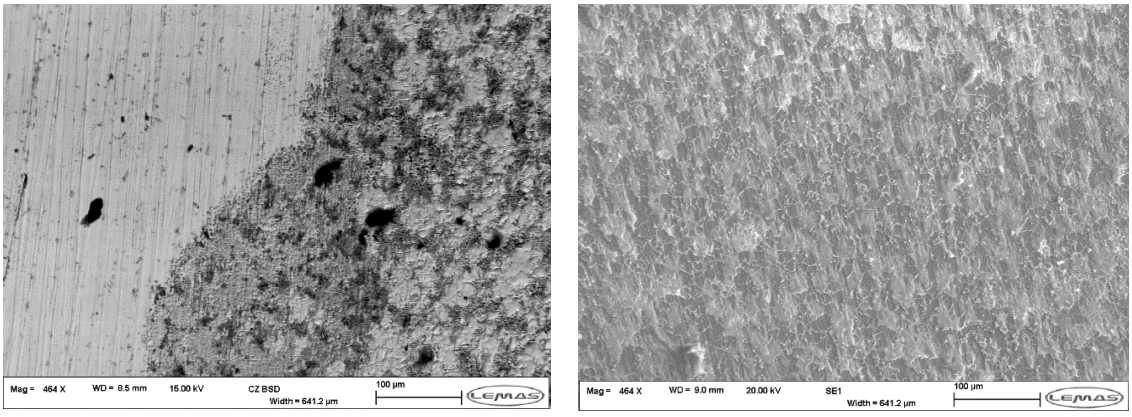

(a) **(b)**

Figure 5-17 SEM images of X65 carbon steel exposed to a CO_2-saturated 3 wt.% NaCl solution at 80 °C with imidazoline concentrations of 30 ppm (a) without pre-corrosion (b) with 2 h of pre-corrosion for a total experimental time of 48 h

Figure 5-18 indicated that although there was a faster reduction in the reciprocal polarisation resistance in the absence of a pre-corrosion period, both the end-point and integrated efficiencies were lower than they were in the presence of a 2 hour pre-corrosion period. The end-point and integrated efficiencies were 86.2 and 93.6% respectively for tests conducted in the absence of a pre-corrosion period as compared to 98 and 97.1% when the inhibitor was injected after a 2 hour pre-corrosion period.

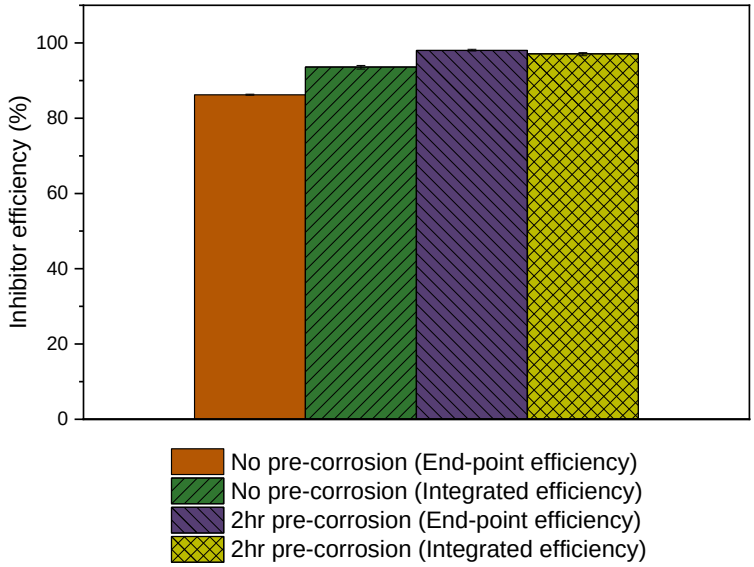

Figure 5-18 Uniform corrosion inhibitor efficiency for X65 carbon steel exposed to a CO_2-saturated 3 wt.% NaCl solution at 80 $^{\circ}$C with 30 ppm imidazoline with and without 2 h pre-corrosion

5.3.3 Localised Corrosion Behaviour

The absence of a 2 hour pre-corrosion period resulted in a reduction in the localised corrosion efficiency from 95.4% to 12.7%, as shown by Figure 5-19.

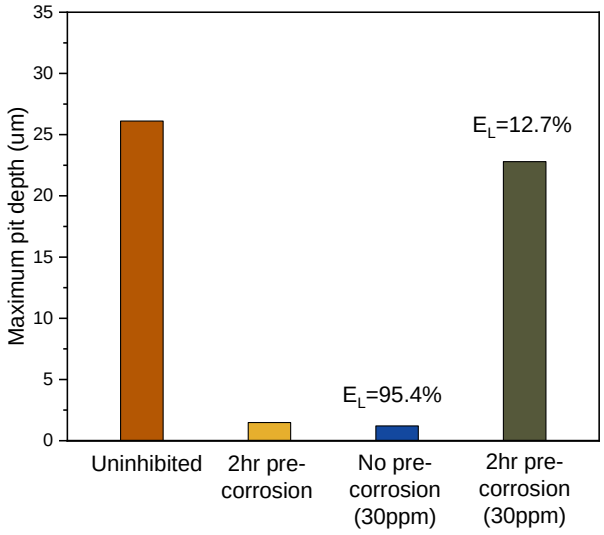

Figure 5-19 Maximum pit depth for X65 carbon steel exposed to a CO_2-saturated 3 wt.% NaCl solution at 80 °C with 30 ppm imidazoline with and without 2 h of pre-corrosion

2D and 3D surface profilometry confirmed that there was localised corrosion attacks only on steel specimens which had been inserted into brines already containing the corrosion inhibitor (absence of pre-corrosion period).

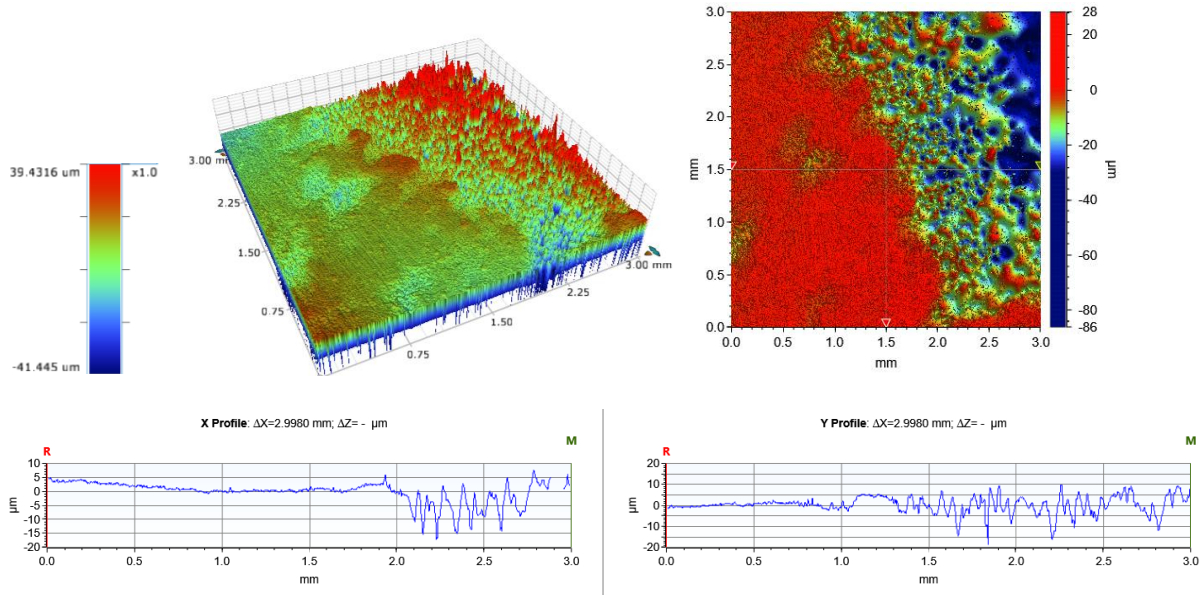

(a)

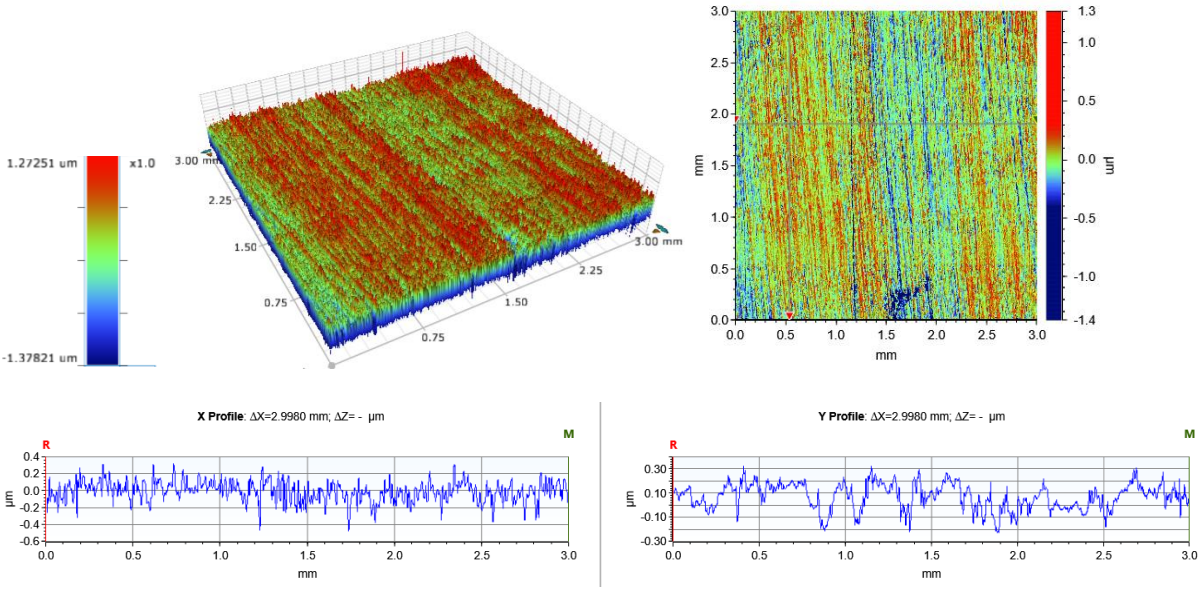

(b)

Figure 5-20 3D image, 2D image and 2D micrographs for X65 carbon steel exposed to a CO_2-saturated 3 wt.% NaCl solution at 80 °C with 30 ppm imidazoline inhibitor added (a) after 2 h pre-corrosion and (b) without pre-corrosion

5.4 Influence of Inhibitor Aging Temperature and Time on Corrosion Inhibition

5.4.1 Testing Procedure

Test results presented within this sub-chapter were conducted according to the experimental procedure described in Chapter 3.4. 30 ppm of an imidazoline based corrosion inhibitor was aged at 80 and 120 ºC in glass cells and autoclaves respectively for different time periods in 3 wt.% NaCl brines. Brines containing the aged corrosion inhibitor were then transferred to glass cells where the performance tests of the aged inhibitors were conducted under CO_2 saturation at 80 ºC on a single X65 carbon steel specimen. The test started as soon as a single carbon steel specimen was inserted into the glass beaker containing the aged inhibitor within the 3 wt.% NaCl brine. The total testing time was 48 hours. Experiments were repeated to enable the determination of experimental error. Electrochemical measurements in the form linear polarisation resistance was conducted according to the procedure described in Chapter 3.4.

5.4.2 Inhibitor Aging at 80 ºC

The imidazoline corrosion inhibitor was aged for 24, 48 and 120 hours at 80 ºC before the performance of the aged inhibitor was evaluated on X65 carbon steel. The reciprocal polarisation resistance in Figure 5-21 indicates that aging of the imidazoline corrosion inhibitor results in a faster reduction in the reciprocal polarisation resistance. Inhibitor aging for 24 and 48 hours also resulted in a greater overall reduction in the reciprocal polarisation resistance where they had reduced to 0.00086 and 0.0003 $ohm^{-1}cm^{-2}$ respectively as compared to 0.00096 $ohm^{-1}cm^{-2}$ for a non-aged inhibitor. The open circuit potential in Figure 5-21b increased to -625 mV for inhibitor aged for 48 hours as compared to -640 mV for the non-aged imidazoline inhibitor.

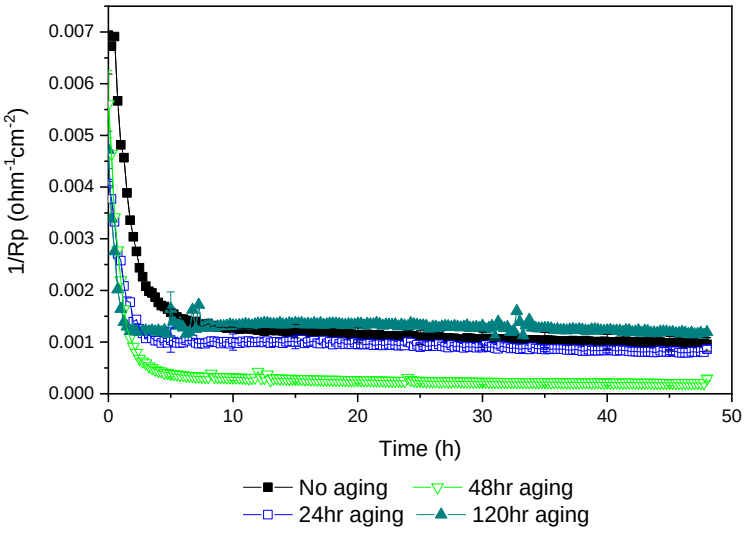

(a)

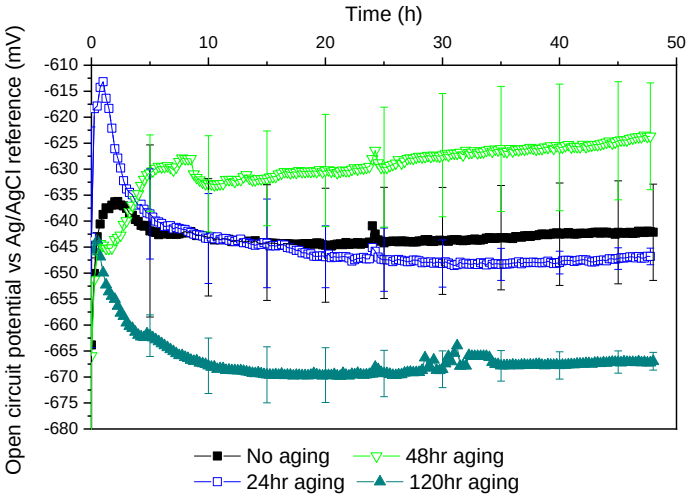

(b)

Figure 5-21 (a) Reciprocal of polarisation resistance in $ohm^{-1}cm^{-2}$ and (b) open circuit potential in mV as a function of time determined using electrochemistry for X65 carbon steel exposed to a CO_2-saturated 3 wt.% NaCl solution at 80 °C with 30 ppm imidazoline aged for 0 to 120 h at 80 °C

Figure 5-22 indicates that inhibitor aging results in an initial increase in the bulk solution pH, where the maximum initial pH was 4.11 for the 24 hour aged inhibitor as compared to a pH of 3.95 for the non-aged compound. The highest pH was observed after 48 hours of testing of the 120 hour aged compound (pH 4.57).

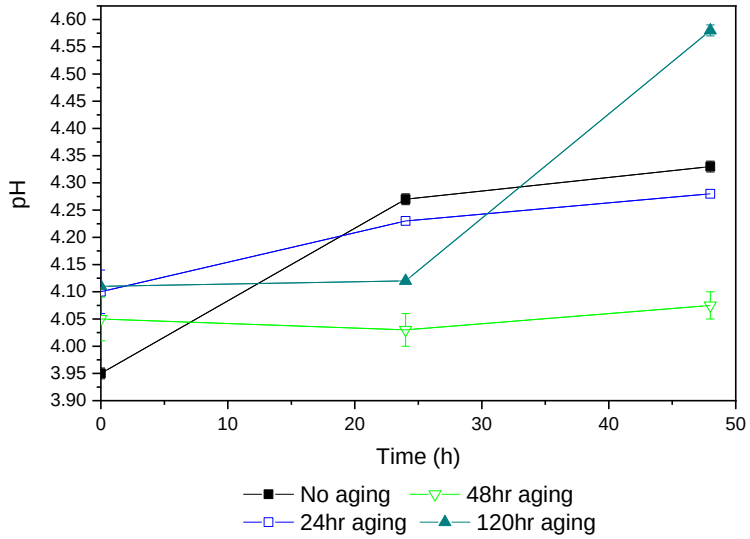

Figure 5-22 Bulk solution pH for X65 carbon steel exposed to a CO_2-saturated 3 wt.% NaCl solution at 80 °C with 30 ppm imidazoline aged for 0 to 120 h

Top-view SEM images of steel surfaces exposed to the non-aged and aged corrosion inhibitors after 48 hours of exposure are provided in Figure 5-23. The images confirm that 24 hour aging of the corrosion inhibitor resulted in improved surface conditions, with less heavily corroded zones as compared to the surface exposed to the non-aged inhibitor. This was also observed for the steel surface exposed to the inhibitor aged for 48 hours, where the entire surface appeared to have been protected from corrosion as wet-grinding marks could still be observed across the entire surface with no heavily corroded zones. However the surface exposed to the 120 hour aged inhibitor was more heavily corroded on certain areas and less corroded on others.

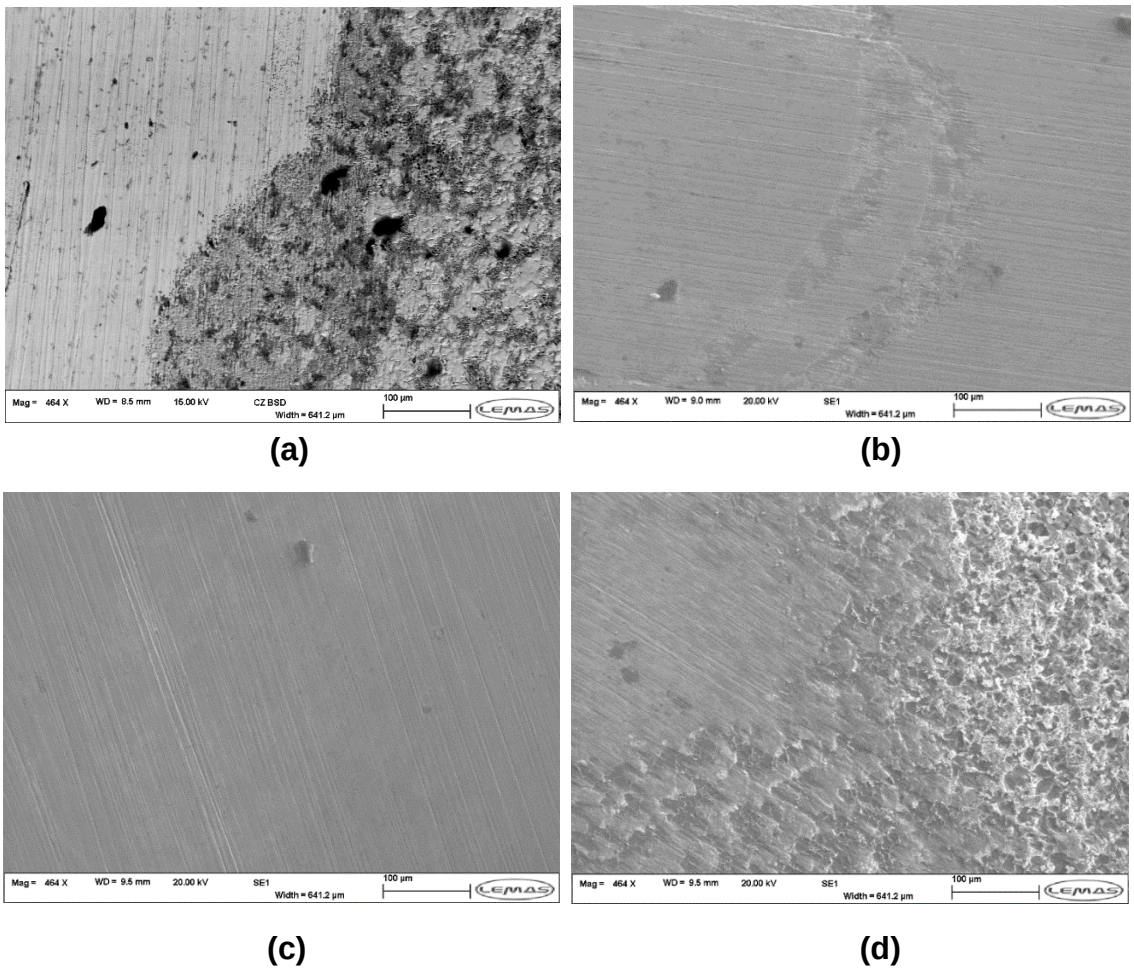

Figure 5-23 SEM images of X65 carbon steel exposed to a CO_2-saturated 3 wt.% NaCl solution at 80 ^{o}C with 30 ppm imidazoline aged for (a) 0 h, (b) 24 h, (c) 48 h and (d) 120 h at 80 ^{o}C

Figure 5-24 shows the efficiencies of the corrosion inhibitors as a function of aging time period. Efficiencies were calculated in terms of end-point and integrated efficiencies using Equation 5.1 and 5.2 respectively. Both methods indicate that the inhibitor efficiency increased with inhibitor aging up to an aging time of 48 hours after which the efficiency then decreased to its lowest values after 120 hours. The integrated efficiency was greater than the end-point efficiency for all the performance tests due to the fast reductions in reciprocal polarisation resistance.

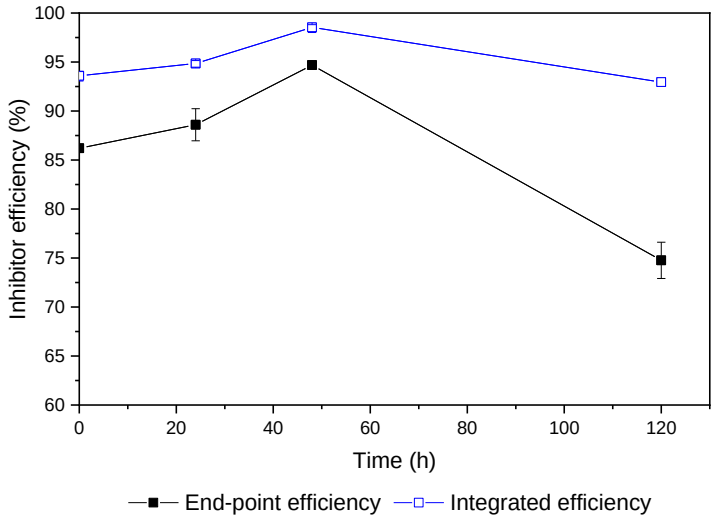

Figure 5-24 Inhibitor efficiency for X65 carbon steel exposed to a CO_2-saturated 3 wt.% NaCl solution at 80 °C with 30 ppm imidazoline as a function of inhibitor aging time at 80 ºC

The performance of the non-aged and aged corrosion inhibitors in terms of localised corrosion was evaluated using NPFLEX surface profilometry, provided in Figure 5-25. The localised inhibitor efficiency decreased with increasing aging time, from 95% for the non-aged compound to 86% for the 120 hour aged compound.

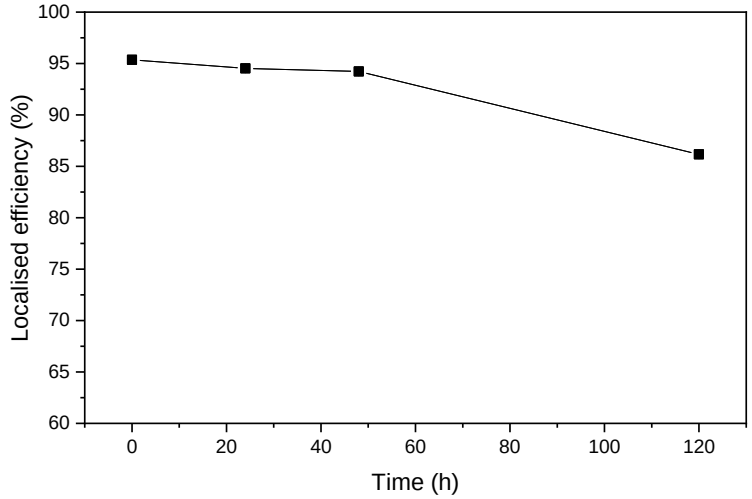

Figure 5-25 Localised efficiency for X65 carbon steel exposed to a CO_2-saturated 3 wt.% NaCl solution at 80 °C with 30 ppm imidazoline as a function of inhibitor aging time at 80 ºC

2D and 3D profilometry images along with their associated micrographs were used to confirm the presence of localised corrosion attacks on steel surfaces

exposed for 48 hours. Figure 5-26 indicates that inhibitor aging of up to 120 hours at 80 ºC did not induce localised attack however it did result in roughening of the steel surfaces.

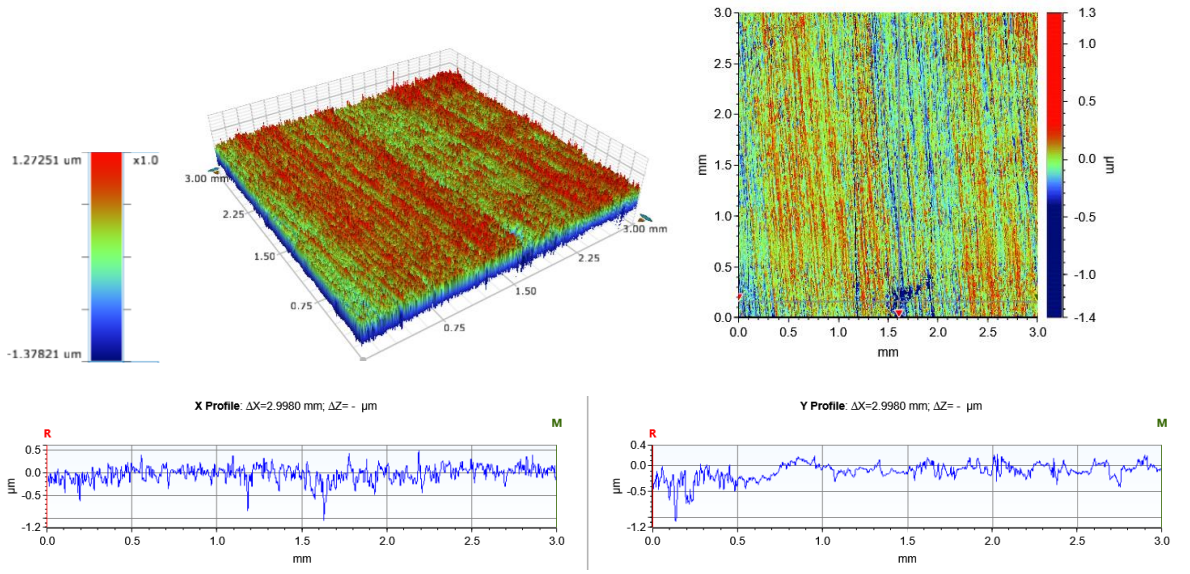

(a)

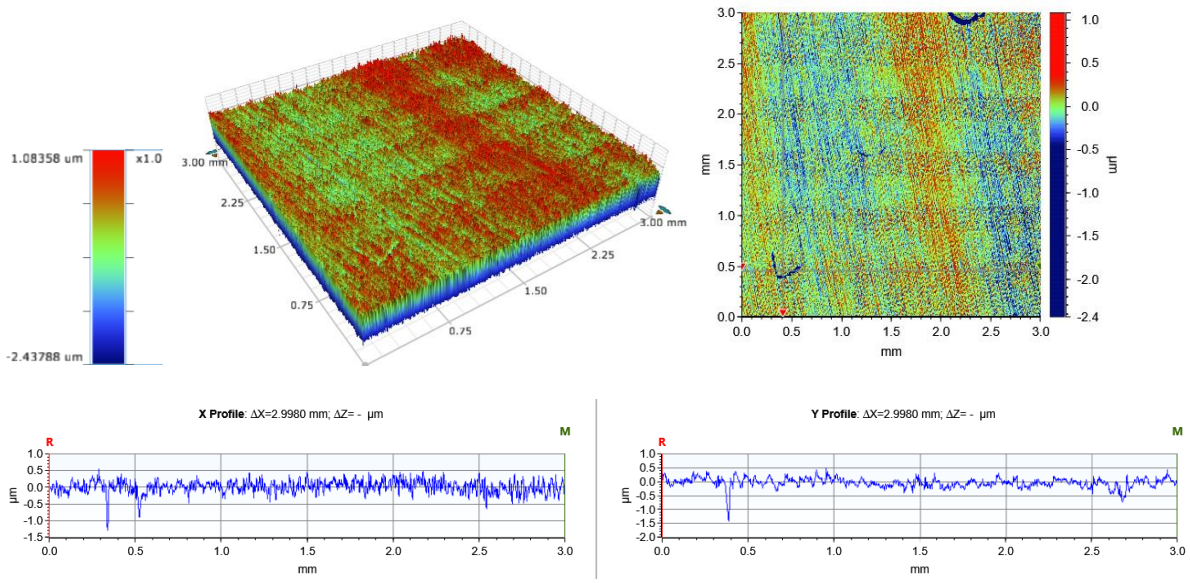

(b)

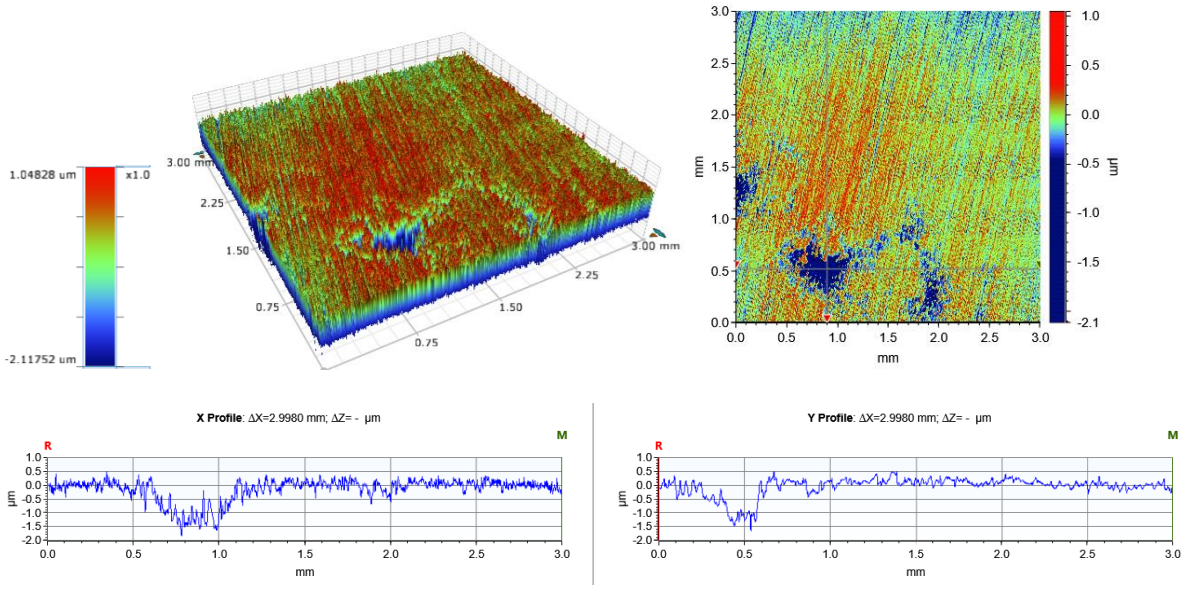

(c)

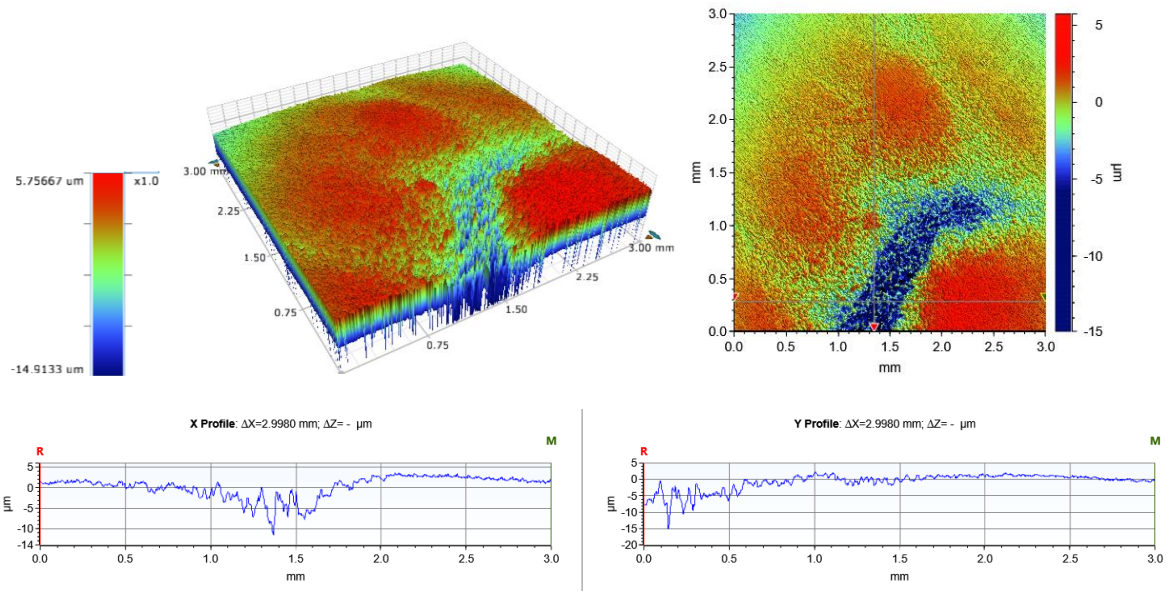

(d)

Figure 5-26 3D image, 2D image and 2D micrographs for X65 carbon steel exposed to a CO_2-saturated 3 wt.% NaCl solution at 80 °C with 30 ppm imidazoline inhibitor (a) without aging, (b) 24 h aging, (c) 48 h aging, and (d) 120 h aging at 80 ºC

5.4.3 Inhibitor Aging at 120 ºC

The performance of imidazoline corrosion inhibitors aged for 2, 6 and 24 hours at 120 ºC was evaluated using linear polarisation resistance at 80 ºC. Figure 5-27 shows that the reduction in reciprocal polarisation resistance for non-aged and

aged compounds initially reduced at similar rates however the overall reduction in reciprocal polarisation resistance reduced with increasing aging time at 120 ºC. The reciprocal polarisation resistance after 48 hours of exposure for the 24 hour aged compound was 0.0022 ohm^{-1}cm^{-2} in comparison to 0.00096 ohm^{-1}cm^{-2}. The open circuit potential remained higher for the aged compounds throughout the 48 hour tests.

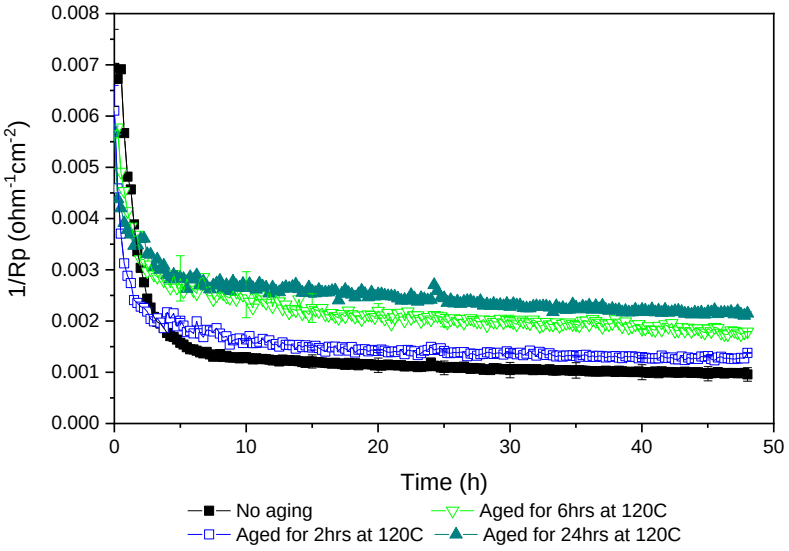

(a)

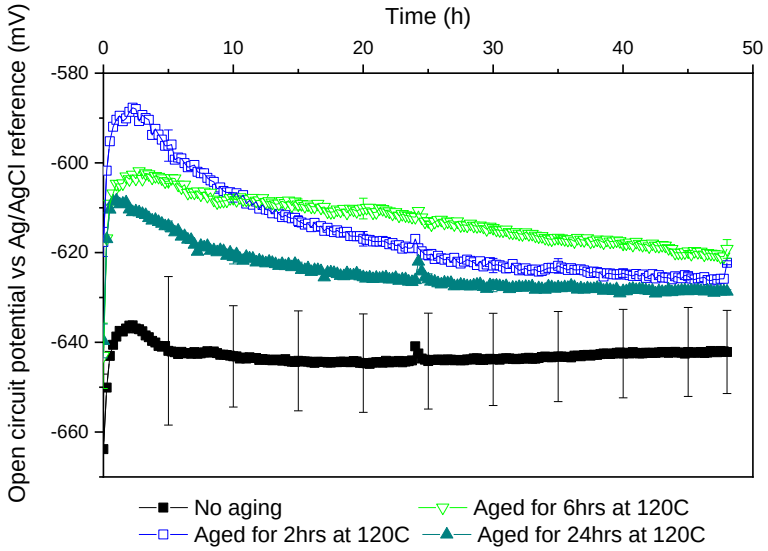

(b)

Figure 5-27 (a) Reciprocal of polarisation resistance in ohm^{-1}cm^{-2} and (b) open circuit potential in mV as a function of time determined using electrochemistry for X65 carbon steel exposed to a CO_2-saturated 3 wt.% NaCl solution at 80 ˚C with 30 ppm imidazoline aged for 0 to 24 h at 120 ºC

Figure 5-28 shows that inhibitor aging at 120 ºC resulted in a higher initial bulk pH which remained higher for the aged inhibitors throughout the 48 hour tests. The final pH increased with increasing aging time and was as a result the greatest in tests conducted with the inhibitor compound aged for 24 hours (pH 5) in comparison to a pH of 4.33 for the non-aged compound.

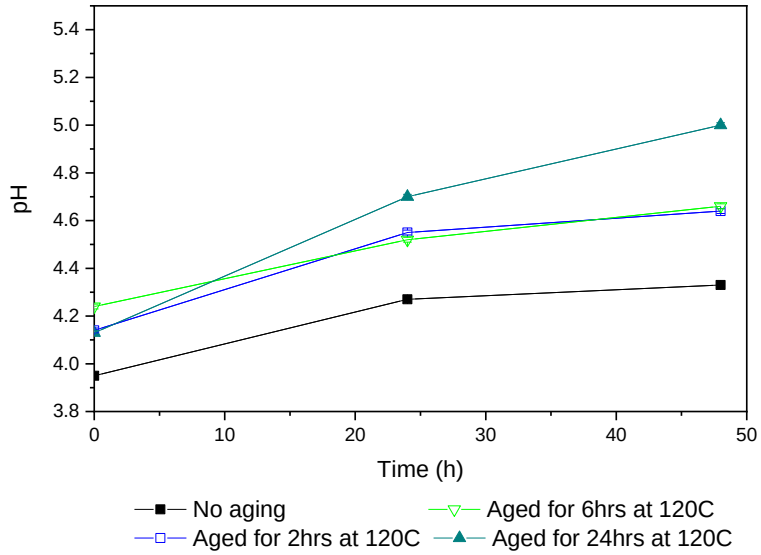

Figure 5-28 Bulk solution pH for X65 carbon steel exposed to a CO_2-saturated 3 wt.% NaCl solution at 80 ˚C with 30 ppm imidazoline aged for 0 to 24 h at 120 ºC

Top-view SEM imaging shows that aging of the corrosion inhibitor for 2 hours at 120 ºC did not result in any significant changes to the surface conditions after testing at 80 ºC for 48 hours. However Figure 5-29 shows that aging for 6 and 24 hours resulted in worsened surface conditions where there appeared to be more severe corrosion attacks on the steel surfaces.

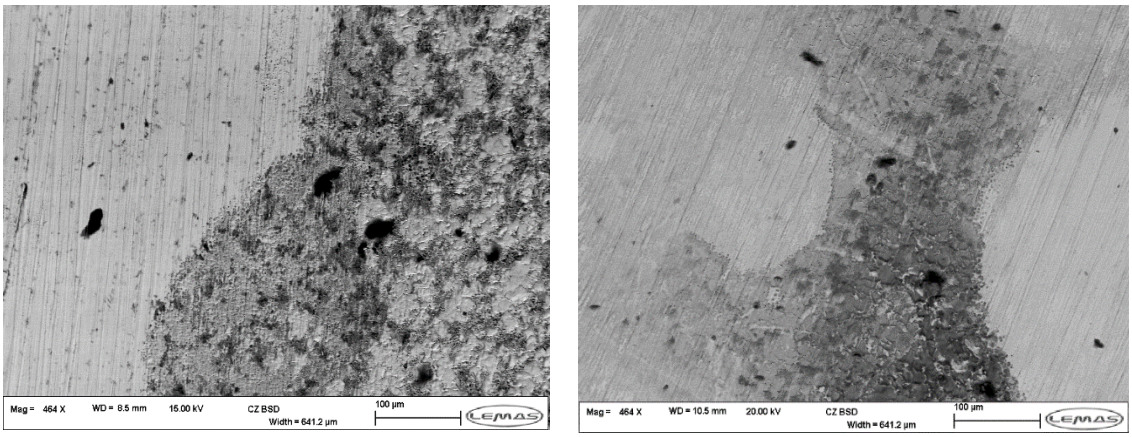

(a) **(b)**

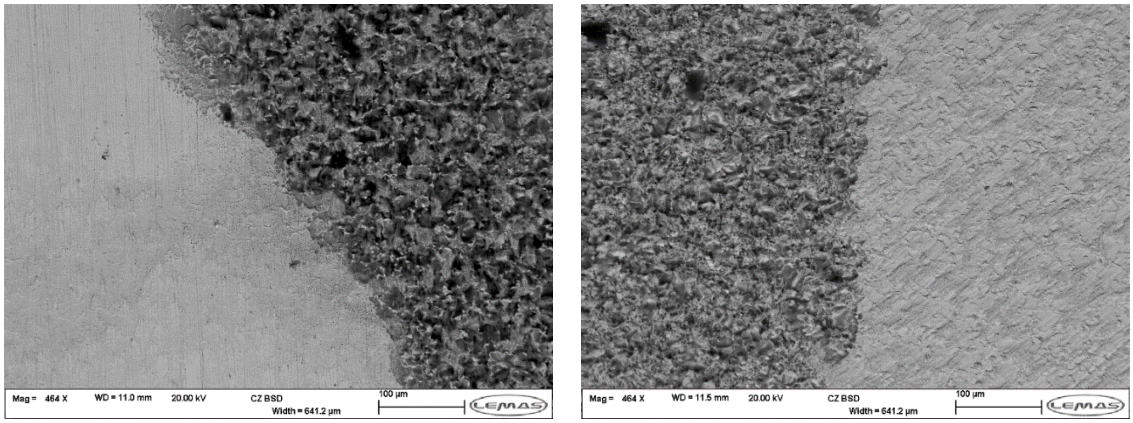

(c) **(d)**

Figure 5-29 SEM images of X65 carbon steel exposed to a CO_2-saturated 3 wt.% NaCl solution at 80 ºC with 30 ppm imidazoline aged for (a) 0 h, (b) 2 h, (c) 6 h and (d) 24 h at 120 ºC

The inhibitor efficiency in terms of uniform corrosion suppression was examined in terms of end-point and integrated efficiency using Equation 5.1 and 5.2 respectively. Figure 5-30 indicates that the inhibitor efficiencies determined by both methods decreased with increasing aging time from 86.2 and 93.6% to 62.4 and 86.6% for the 24 hour aged compound in terms of integrated and end-point efficiencies respectively.

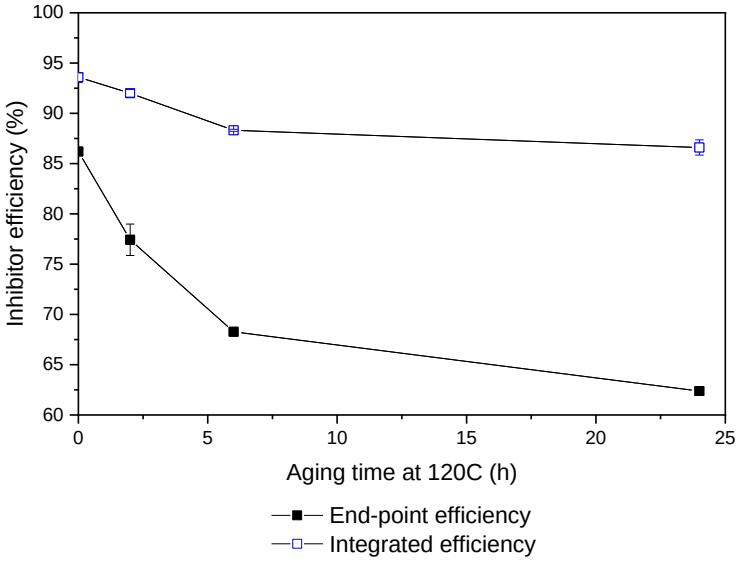

Figure 5-30 Inhibitor efficiency for X65 carbon steel exposed to a CO_2 saturated 3 wt.% NaCl solution at 80 °C with 30 ppm imidazoline as a function of inhibitor aging time at 120 ºC

The inhibitor efficiency in terms of localised corrosion suppression is provided in Figure 5-31 which decreased with increasing inhibitor aging time at 120 ºC. The

efficiency reduced from 95.4% to 83.4% when aged for 2 hours, to 73.7% when aged for 6 hours and 73.2% when aged for 24 hours.

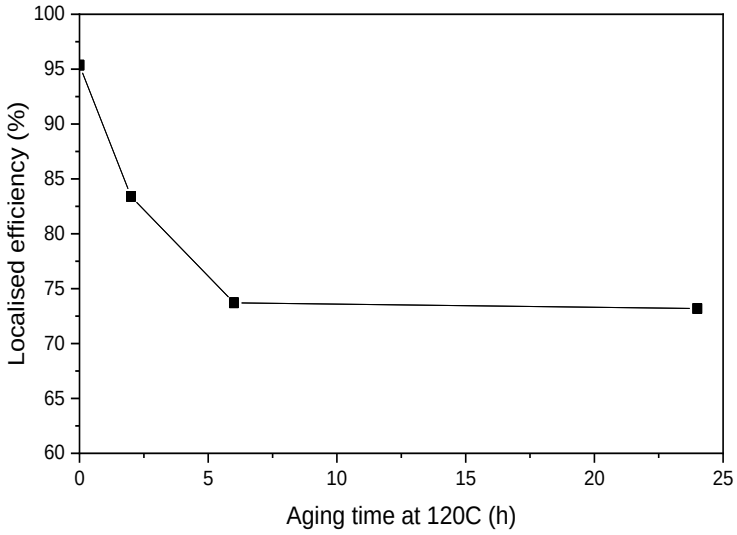

Figure 5-31 Localised efficiency for X65 carbon steel exposed to a CO_2 saturated 3 wt.% NaCl solution at 80 °C with 30 ppm imidazoline as a function of inhibitor aging time at 120 ºC

The severity of localised corrosion attack on steel surfaces exposed to aged inhibitor compounds was further evaluated using 2D and 3D surface profilometry images. Figure 5-32 confirms that the steel surfaces exposed to the aged inhibitor compounds had not undergone any identifiable localised corrosion attack. However, the surfaces were found to have greater surface roughness.

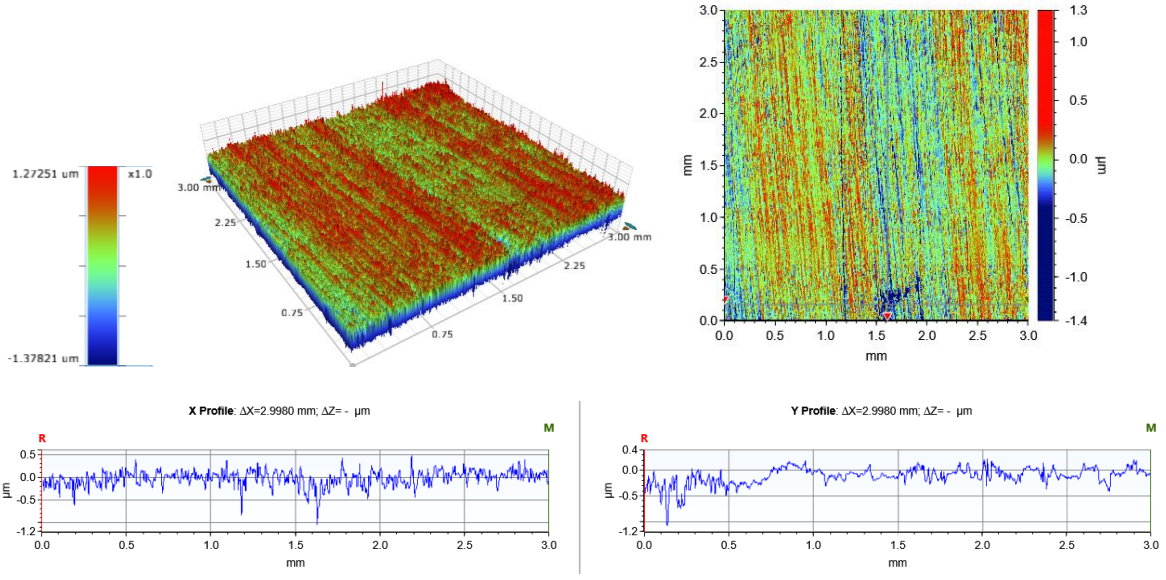

(a)

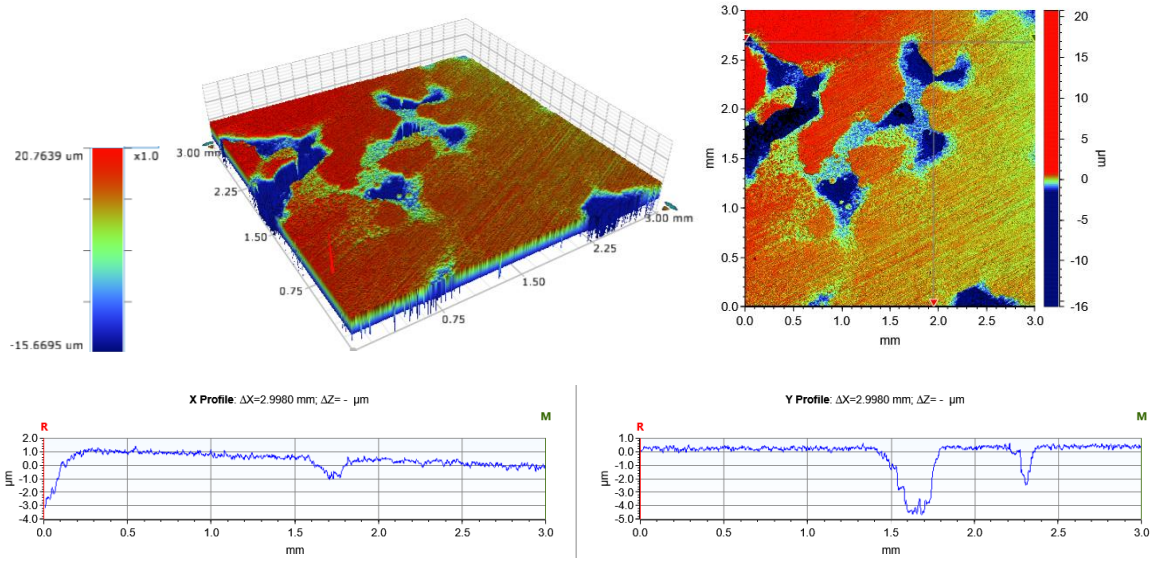
20.7639 um
x1.0
-15.6695 um
3.00 mm
2.25
1.50
0.75
mm
µm
X Profile: ΔX=2.9980 mm; ΔZ= - µm
Y Profile: ΔX=2.9980 mm; ΔZ= - µm
R
M

(b)

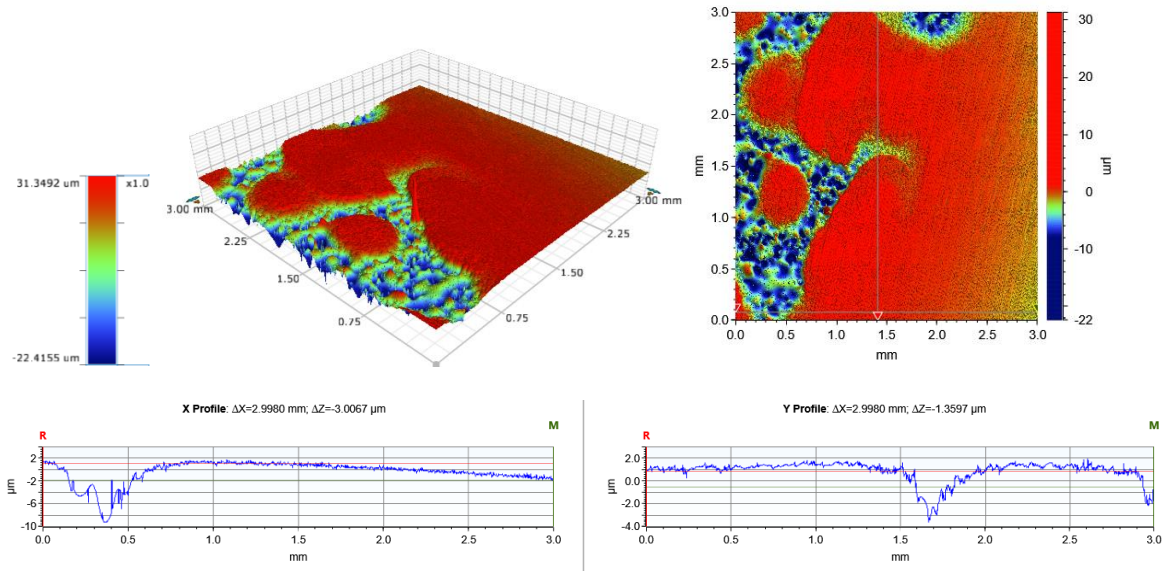
31.3492 um
x1.0
-22.4155 um
3.00 mm
2.25
1.50
0.75
mm
µm
X Profile: ΔX=2.9980 mm; ΔZ=-3.0067 µm
Y Profile: ΔX=2.9980 mm; ΔZ=-1.3597 µm
R
M

(c)

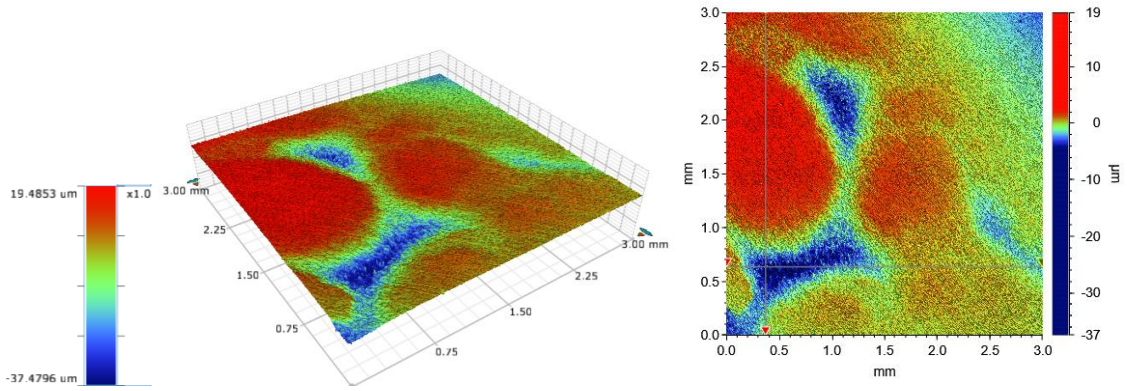
19.4853 um
x1.0
-37.4796 um
3.00 mm
2.25
1.50
0.75
mm
µm

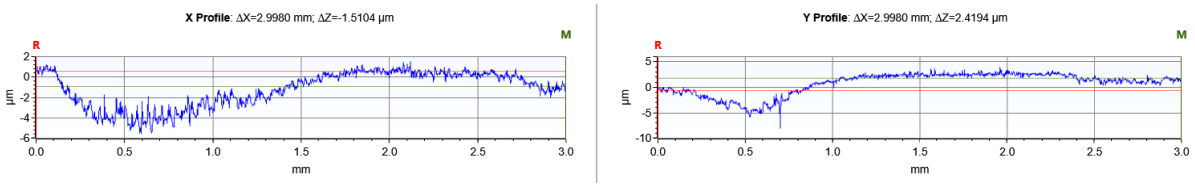

(d)

Figure 5-32 3D image, 2D image and 2D micrographs for X65 carbon steel exposed to a CO_2-saturated 3 wt.% NaCl solution at 80 °C with 30 ppm imidazoline inhibitor (a) without aging, (b) 2 h aging, (c) 6 h aging, and (d) 24 h aging at 120 ºC

Figure 5-33 provides a comparison of uniform corrosion inhibitor efficiencies for non-aged and 24 hour aged compounds at 80 and 120 ºC. The comparison shows that there is a small increase in inhibitor efficiency (2.4% increase in end-point and 1.3% in integrated efficiency) after aging for 24 hours at 80 ºC. However 24 hour aging at 120 ºC resulted in a reduction in the efficiency (23.8% in end-point and 7% in integrated).

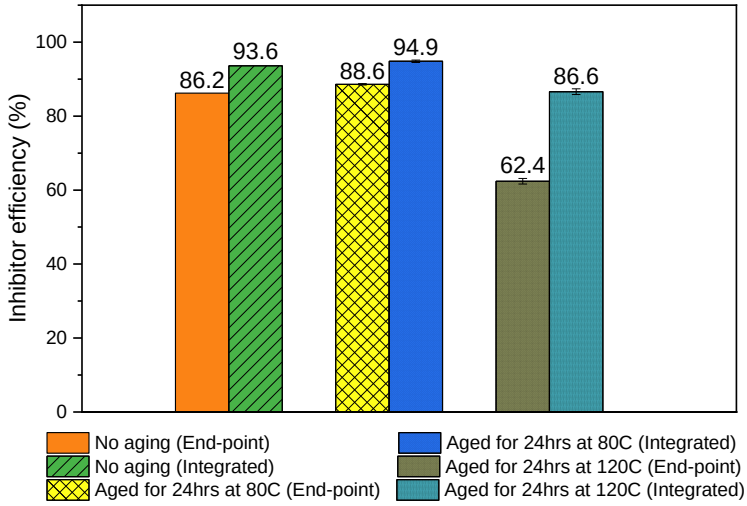

Figure 5-33 Uniform corrosion inhibitor efficiency for X65 carbon steel exposed to a CO_2-saturated 3 wt.% NaCl solution at 80 °C with 30 ppm imidazoline with and without inhibitor aging at 80 and 120 ºC for 24 h

Figure 5-34 compares the efficiency in terms of localised corrosion, which shows a reduction in the efficiency from 95.4% to 94.5 and 73.2% after aging at 80 and 120 ºC respectively for 24 hours.

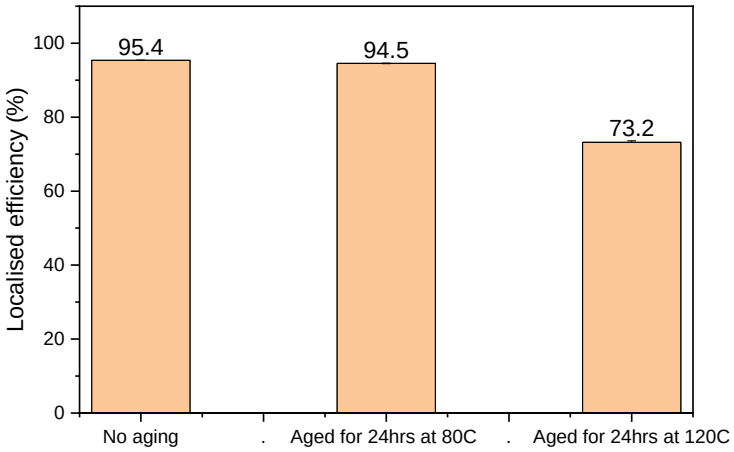

Figure 5-34 Localised corrosion efficiency for X65 carbon steel exposed to a CO_2-saturated 3 wt.% NaCl solution at 80 °C with 30 ppm imidazoline with and without inhibitor aging at 80 and 120 ºC for 24 h

5.5 Summary of Results

The performance of an imidazoline derivative was evaluated in its ability to provide corrosion protection for X65 carbon steel in a CO_2-saturated sodium chloride (NaCl) solution at 80 °C. The performance of the corrosion inhibitor was investigated with respect to both uniform and localised corrosion using *in situ* linear polarisation resistance electrochemical measurements and *ex situ* non-contact surface profilometry, respectively. The findings demonstrate that the optimum inhibitor concentration required for suppression of uniform corrosion is significantly lower than that for localised corrosion protection, highlighting the importance of systematic, post-test topographical measurements of the steel surface in the selection and optimisation of inhibitor dose rates. The findings show that short-term pre-corrosion can lead to improved uniform corrosion suppression in the presence of the inhibitor however it will also result in worsened performance with respect to localised corrosion which will ultimately result in the reduction of its overall performance. The results indicate that in the context of uniform corrosion, aging of this corrosion inhibitor may lead to improved or worsened performance depending on the aging temperature and exposure period.

Chapter 6 Corrosion Inhibitor Interaction with Corrosion Product Covered Surfaces

6.1 Introduction

This Chapter focuses on the interaction of an imidazoline corrosion inhibitor with corrosion product covered surfaces. The ability of an imidazoline based corrosion inhibitor to supress uniform and localised corrosion in the presence of iron carbide (Fe_3C), partial coverage iron carbonate ($FeCO_3$) and full coverage $FeCO_3$ corrosion product layers was evaluated using a two stage experimental methodology. The development and implementation of a two stage testing methodology enabled different corrosion product covered surfaces to be tested in both the absence and presence of the corrosion inhibitor in an initially standardised environment, allowing for more accurate comparison of inhibitor performance on different corrosion product covered surfaces which enabled the estimation of the decoupled contributions towards overall corrosion protection as afforded by the inhibitor and the corrosion product layer. Finally this chapter also examines the influence of the imidazoline corrosion inhibitor on the wettability of different surfaces initially wetted by either oil or water. The inhibitor performance on the pre-corroded X65 carbon steel specimens was compared to the performance of the corrosion inhibitor on wet-ground X65 carbon steel. Data obtained by LPR measurements were presented in the form of reciprocal polarisation resistance rather than corrosion rate in order to prevent the assumption of β_a and β_c values which may have an influence on corrosion rate prediction across different inhibitor concentrations.

6.2 Testing Procedure

The experimental procedure consisted of a two-stage experimental process (Figure 6-1), where X65 carbon steel specimens were pre-corroded in autoclaves to generate three different corrosion product surfaces. Pre-corrosion in autoclaves was conducted according to the experimental procedure described in Chapter 3.3. Pre-corrosion was carried out for 6, 24 and 96 hours at 80 ºC and 1 bar Pco_2 at 25 ºC in 3 wt.% NaCl brines (Table 6-1) to generate an iron carbide layer, partial coverage iron carbonate layer and full coverage iron carbonate layer (Figure 6-2). The pre-corroded specimens were then characterised using SEM, XRD and NP_{flex} in order to determine the corrosion products present, their morphology and the extent of localised corrosion on the surfaces. The pre-corroded specimens were then individually tested in glass cells (Table 6-2) both in the absence and presence of an imidazoline corrosion inhibitor for 48 h durations using linear polarisation resistance (LPR) measurements according to the experimental procedure described in Chapter 3.4. The pre-corroded steel specimens were tested in glass cells containing 3 wt.% NaCl brines at 80 ºC under CO_2 saturation. In tests where corrosion inhibition performance was evaluated, the inhibitor was pre-injected before the steel specimen was inserted at an inhibitor concentration of 30 ppm. After the second stage (Testing in the absence and presence of the corrosion inhibitor), the steel specimens were once again characterised using SEM, XRD and NP_{flex}. This experimental procedure enabled the different corrosion product covered specimens to be tested with an inhibitor under the same initial brine chemistry, eliminating the effect of bulk pH which allowed for a more accurate performance evaluation and comparison between the different corrosion product specimens.

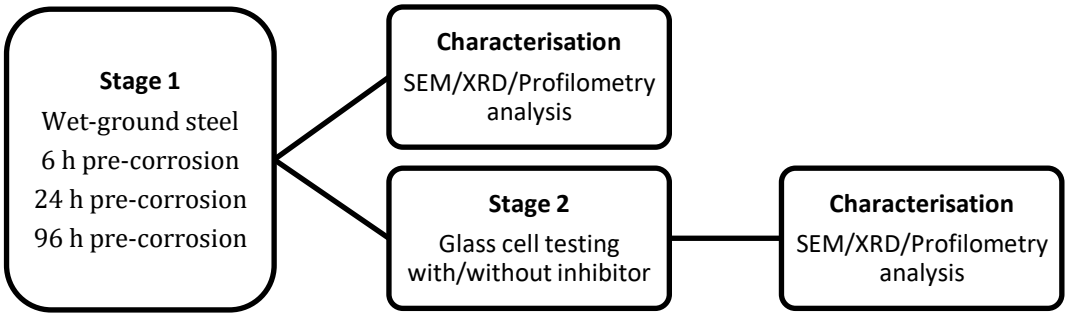

Figure 6-1 Flow chart of experimental process

Table 6-1 Autoclave pre-corrosion conditions (Stage 1)

Pre-corrosion period (h)	NaCl content (wt.%)	Total Cl^- (wt.%)	Temperature (˚C)	P_{CO2} at 25 ˚C (bar)
6	3	1.82	80	1
24				
96				

Table 6-2 Glass cell testing conditions (Stage 2)

Test condition	Inhibitor concentration (ppm)	Temperature (ºC)	P_{CO2} (bar)	Duration (h)	NaCl content (wt.%)
Un-inhibited	0	80	1	48	3
Inhibited	30				

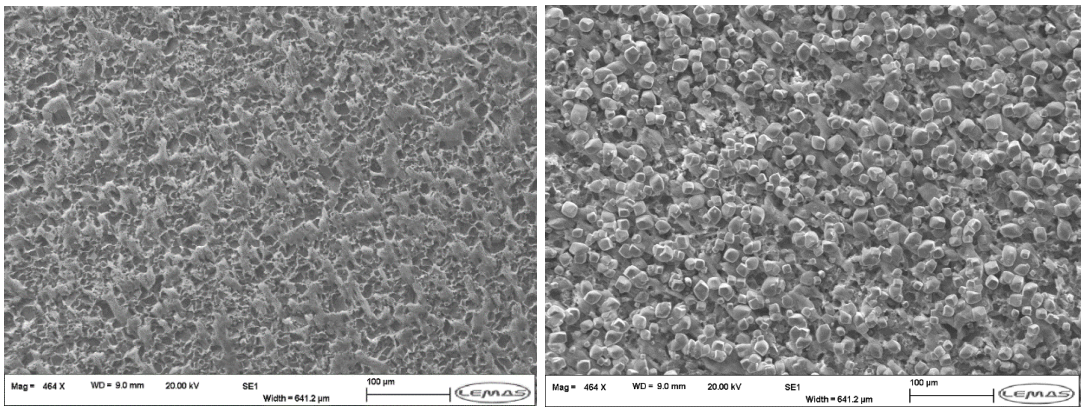

(a) **(b)**

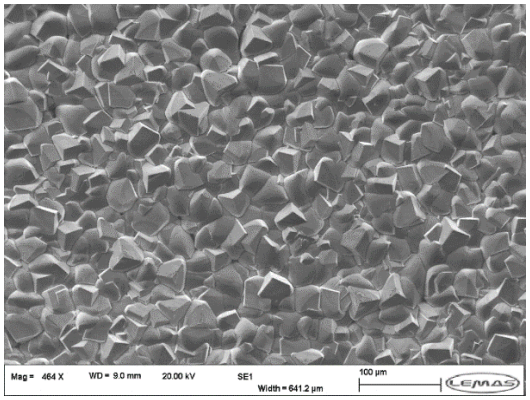

(c)

Figure 6-2 X65 carbon steel specimens after pre-corrosion in autoclaves for (a) 6 h (iron carbide), (b) 24 h (partial coverage iron carbonate) and (c) 96 h (full coverage iron carbonate) at 80 ºC

6.3 Inhibition on Wet-Ground X65 Carbon steel

Figure 6-3 shows the reciprocal polarisation resistance and open circuit potential as functions of exposure time for wet-ground X65 carbon steel in the absence and presence of 30 ppm of the imidazoline corrosion inhibitor where inhibitor addition was performed prior to immersion of the specimen into the electrolyte. The reciprocal polarisation resistance decreased at a rapid rate to 0.007 $ohm^{-1}cm^{-2}$ in the presence of the corrosion inhibitor accompanied by a 50 mV increase in the open circuit potential. The end-point and integrated inhibitor efficiencies with respect to the uniform corrosion behaviour were determined to be 92 and 93.6% using Equation 5.1 and 5.2 respectively.

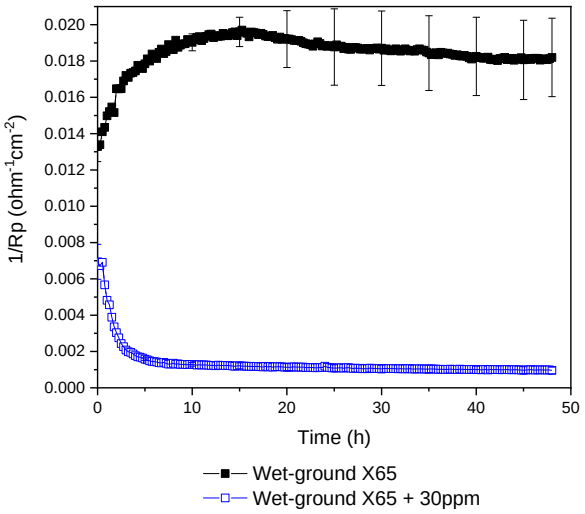

(a)

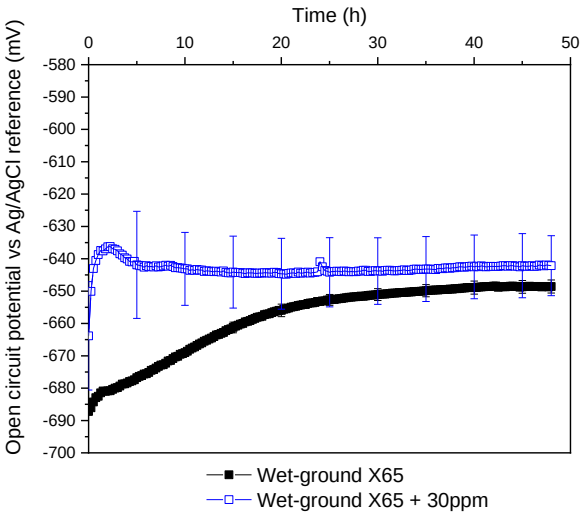

(b)

Figure 6-3 (a) Reciprocal values of polarisation resistance and (b) open circuit potential vs Ag/AgCl reference as a function of time for wet-ground X65 carbon steel specimens exposed to inhibited and uninhibited CO_2-saturated 3 wt.% NaCl solution at 80 ºC. Note that inhibitor addition was performed prior to immersion of the specimen in the electrolyte.

The bulk solution pH was initially lower in the presence of the corrosion inhibitor and remained lower throughout the test duration, resulting in a final pH of 4.3 as compared to 5.5 in the absence of the corrosion inhibitor as shown in Figure 6-4.

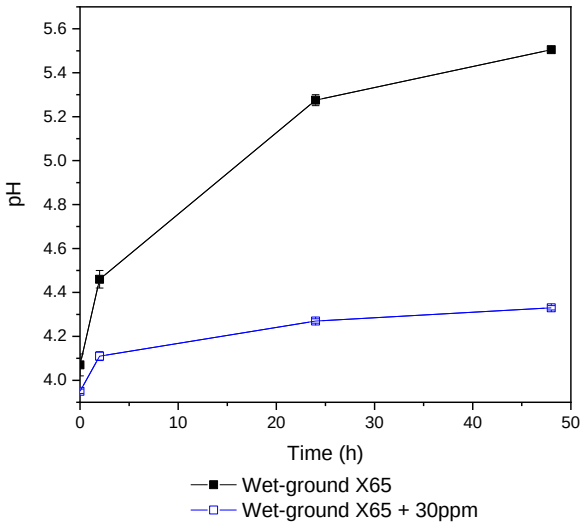

Figure 6-4 Bulk pH as a function of time for wet-ground X65 carbon steel specimens exposed to inhibited and uninhibited CO_2-saturated 3 wt.% NaCl solution at 80 ºC. Note that inhibitor addition was performed prior to immersion of the specimen in the electrolyte.

Figure 6-5 shows SEM images of the carbon steel specimens after 48 h of exposure in the presence and absence of the corrosion inhibitor, where the surface exposed to the corrosion inhibitor shows two distinct areas.

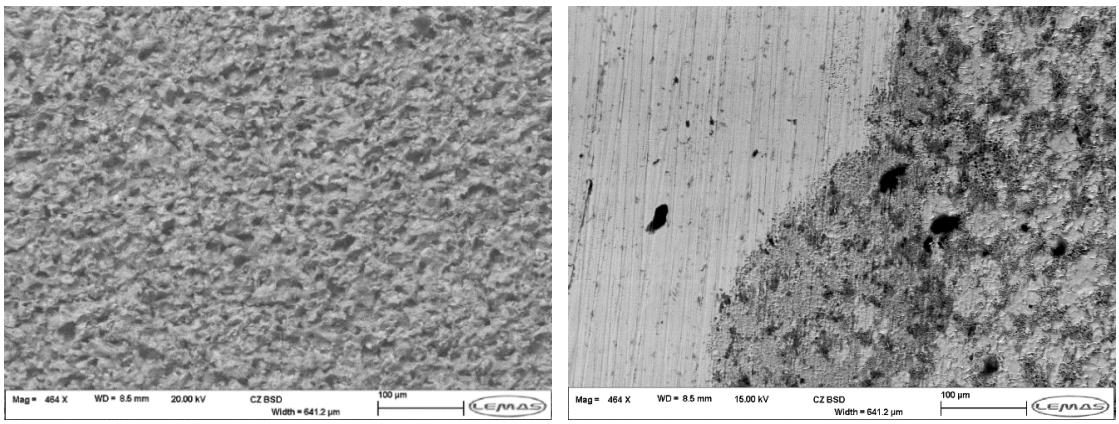

Figure 6-5 SEM top-view images for wet-ground X65 steel specimens after exposure to a CO_2-saturated 3 wt.% NaCl brine at 80 ºC containing (a) 0 ppm and (b) 30 ppm of imidazoline corrosion inhibitor for 48 h

X-ray diffraction patterns of carbon steel specimens exposed to the inhibited and uninhibited brines after 48 h of exposure are shown in Figure 6-6, which confirm that no crystalline corrosion products were present on either of the surfaces.

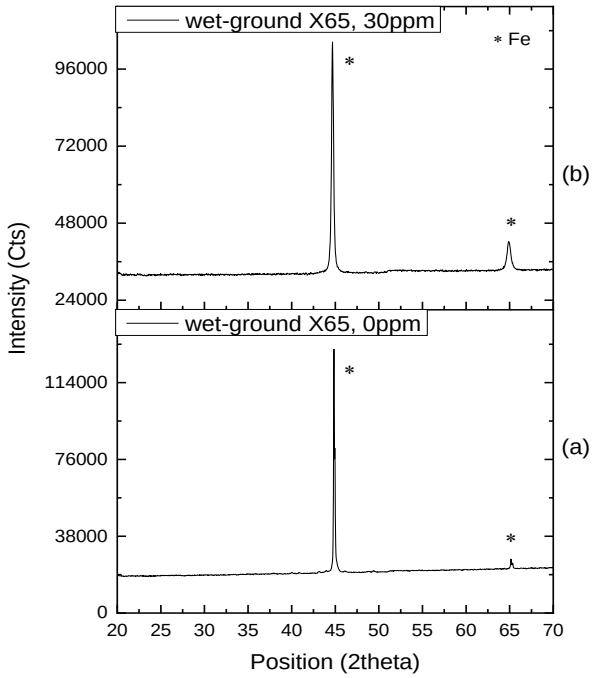

Figure 6-6 XRD pattern for wet-ground X65 steel specimens after exposure to a CO_2-saturated 3 wt.% NaCl brine at 80 ºC containing (a) 0 ppm and (b) 30 ppm of imidazoline corrosion inhibitor for 48 h

Figure 6-7 shows the maximum pit depth on carbon steel specimens after 48 h of exposure to inhibited and uninhibited brines as gathered by non-contact profilometry. The inhibitor efficiency with respect to the localised corrosion behaviour was found to be 95.4%.

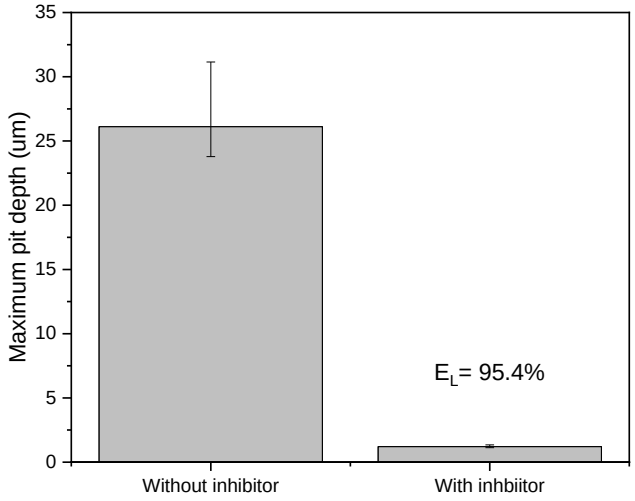

Figure 6-7 Maximum pit depth for wet-ground X65 steel specimens after exposure to a CO_2-saturated 3 wt.% NaCl brine at 80 ºC containing 0 ppm and 30 ppm of imidazoline corrosion inhibitor for 48 h

6.4 Inhibition on Iron Carbide Covered Surface

Figure 6-8 shows the reciprocal polarisation resistance and open circuit potential as a function of exposure time for a pre-corroded iron carbide layer evaluated in the absence and presence of an imidazoline corrosion inhibitor at 80 ºC in glass cells. The reciprocal polarisation resistance decreased with time in the absence of the corrosion inhibitor, from 0.017 $ohm^{-1}cm^{-2}$ to 0.011 $ohm^{-1}cm^{-2}$. In the presence of the corrosion inhibitor the reciprocal polarisation resistance decreased at a greater rate down to 0.00041 $ohm^{-1}cm^{-2}$ which was associated with a greater increase in the open circuit potential resulting in a final OCP of -586 mV after 48 hours of exposure as compared to an OCP of -649 mV in the absence of the corrosion inhibitor. The inhibitor efficiencies for uniform corrosion suppression were determined using Equation 5.1 and 5.2, and were found to be 95 and 96.3% in terms end-point and integrated efficiency respectively.

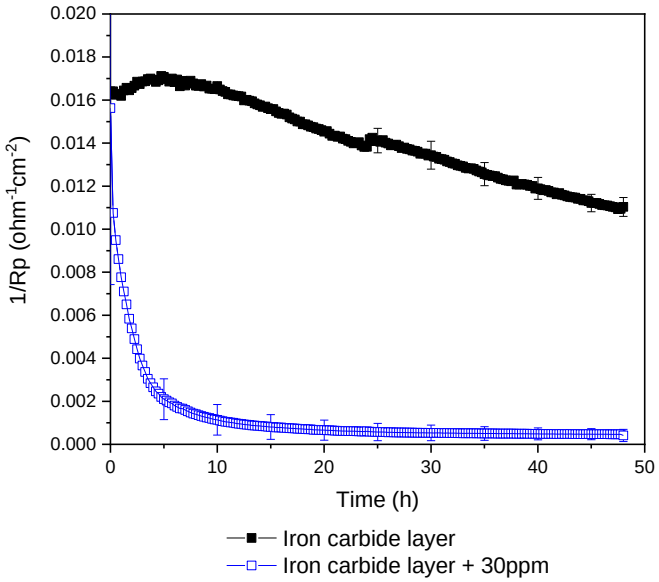

(a)

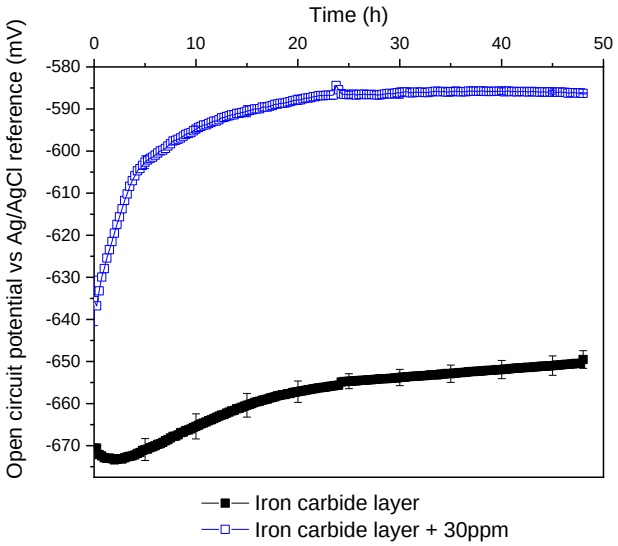

(b)

Figure 6-8 (a) Reciprocal of polarisation resistance and (b) open circuit potential vs Ag/AgCl reference as a function of time for X65 steel (with a pre-formed iron carbide rich layer) exposed to inhibited and uninhibited CO_2-saturated 3 wt.% NaCl solution at 80 ºC. Note that inhibitor addition was performed prior to immersion of the specimen in the electrolyte.

The faster and greater reduction in reciprocal polarisation resistance in the presence of the corrosion inhibitor resulted in a lower pH throughout the 48 hour test duration, as shown by Figure 6-9, with a final pH of 4.57 as compared to a pH of 5.95 for tests conducted in the absence of the corrosion inhibitor.

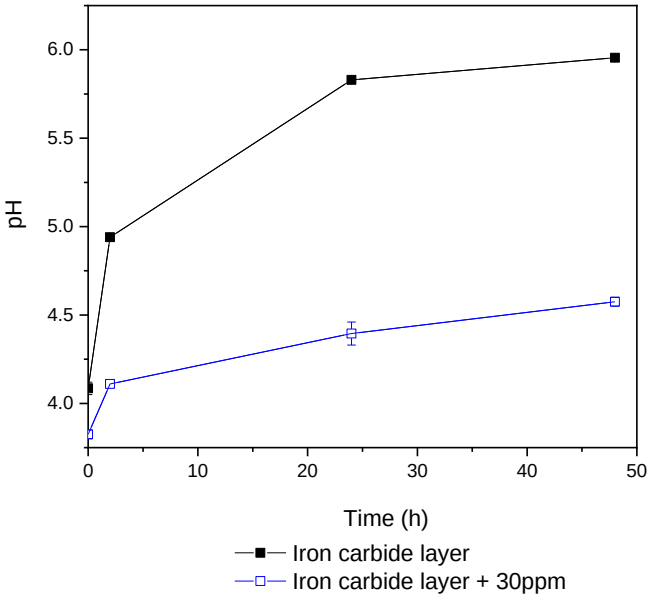

Figure 6-9 Bulk pH as a function of time for X65 steel (with a pre-formed iron carbide rich layer) exposed to inhibited and uninhibited CO_2-saturated 3 wt.% NaCl solution at 80 ºC. Note that inhibitor addition was performed prior to immersion of the specimen in the electrolyte.

The pre-corroded iron carbide layer was examined using top-view SEM in order to compare the state of surface conditions after exposure to un-inhibited and inhibited brines in glass cells. Figure 6-10 confirmed that the pre-corroded specimen exposed to the un-inhibited brine had been further corroded, however the pre-corroded iron carbide layer exposed to the inhibited brine appeared to have undergone less corrosion.

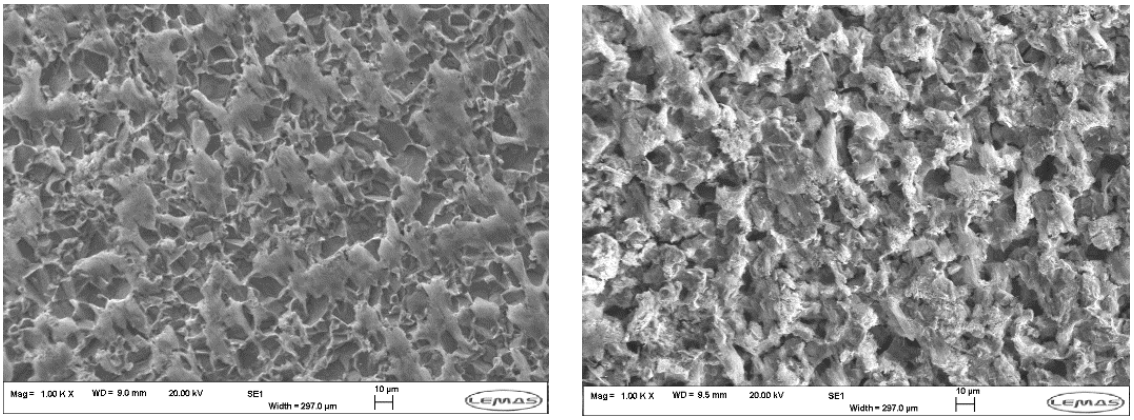

(a) **(b)**

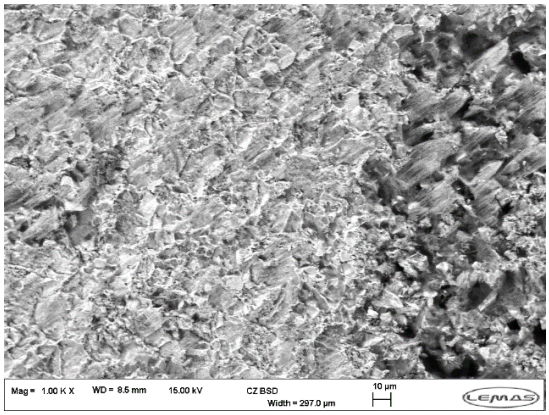

(c)

Figure 6-10 SEM top-view images for (a) iron carbide layer after 6 hour pre-corrosion in autoclave at 80 ºC, (b) Iron carbide layer after uninhibited exposure to 3 wt.% NaCl brine at 80 ºC and (c) Iron carbide layer after exposure to 30 ppm inhibited 3 wt.% NaCl brine at 80 ºC

X-ray diffraction of the iron carbide layer covered surfaces after autoclave pre-corrosion and after glass cell testing in un-inhibited and inhbited brines are provided in Figure 6-11, and confirmed that no crystaline corrosion products were present on either of the surfaces.

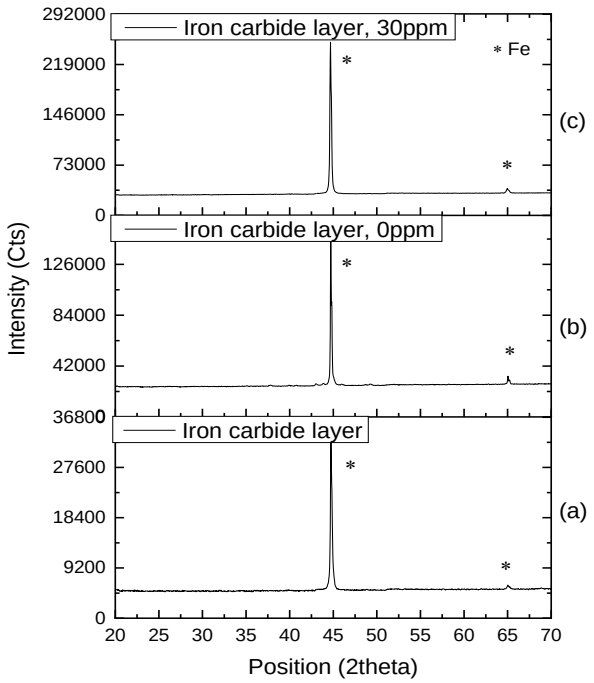

Figure 6-11 XRD pattern for (a) Iron carbide layer after 6 hour pre-corrosion in autoclave at 80 ºC, (b) Iron carbide layer after uninhibited exposure to 3 wt.% NaCl brine at 80 ºC and (c) Iron carbide layer after exposure to 30 ppm inhibited 3 wt.% NaCl brine at 80 ºC

The extent of localised corrosion on pre-corroded iron carbide covered surface before and after exposure to un-inhibited and inhibited brines was assessed using NPFLEX non-contact profilometry in terms of maximum pit depth. Figure 6-12 indicates that the maximum pit depth increased from 8.7 µm to 28.2 µm after exposure to the un-inhibited brine, however only increased to 11.1 µm after exposure to the inhibited brine. The inhibitor efficiency on the pre-corroded surface (iron carbide layer) was determined using Equation 6.1 and was found to be 87.4%.

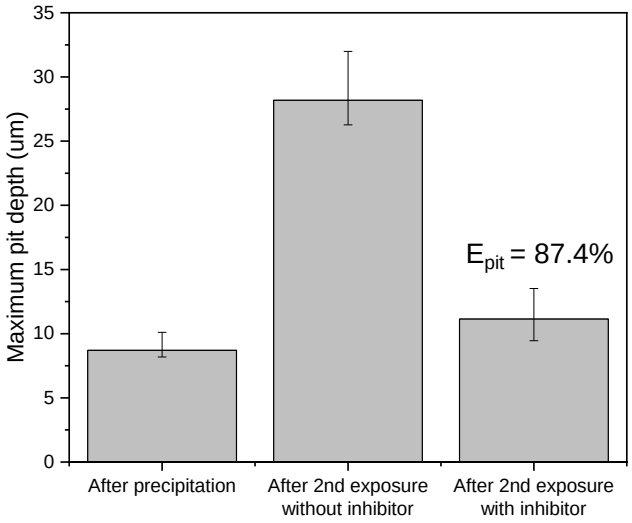

Figure 6-12 Maximum pit depth for iron carbide layer after 6 hour pre-corrosion in autoclave at 80 ºC, after uninhibited exposure to 3 wt.% NaCl brine at 80 ºC and after exposure to 30 ppm inhibited 3 wt.% NaCl brine at 80 ºC

$$E_{pit}(\%) = \left(1 - \frac{P_3 - P_1}{P_2 - P_1}\right) \times 100 \qquad (6.1)$$

Where P_3 is the maximum pit depth after exposure to the inhibited brine (µm), $P_1$is the maximum pit depth after pre-corrosion (µm) and P_2 is the maximum pit depth after exposure to the uninhbited brine (µm).

The extent of localised corrosion was further evaluated using 2D and 3D profilometry images provided in Figure 6-13, which confirmed that there were no signs of localised corrosion on the iron carbide covered surface before testing in glass cells. 2D and 3D profilometry images of the iron carbide layer exposed to the un-inhibited brine confirmed signs of localised corrosion attack. Figure 6-13c confirmed localised corrosion attacks on the iron carbide layer exposed to the inhibited brine however to a lesser extent.

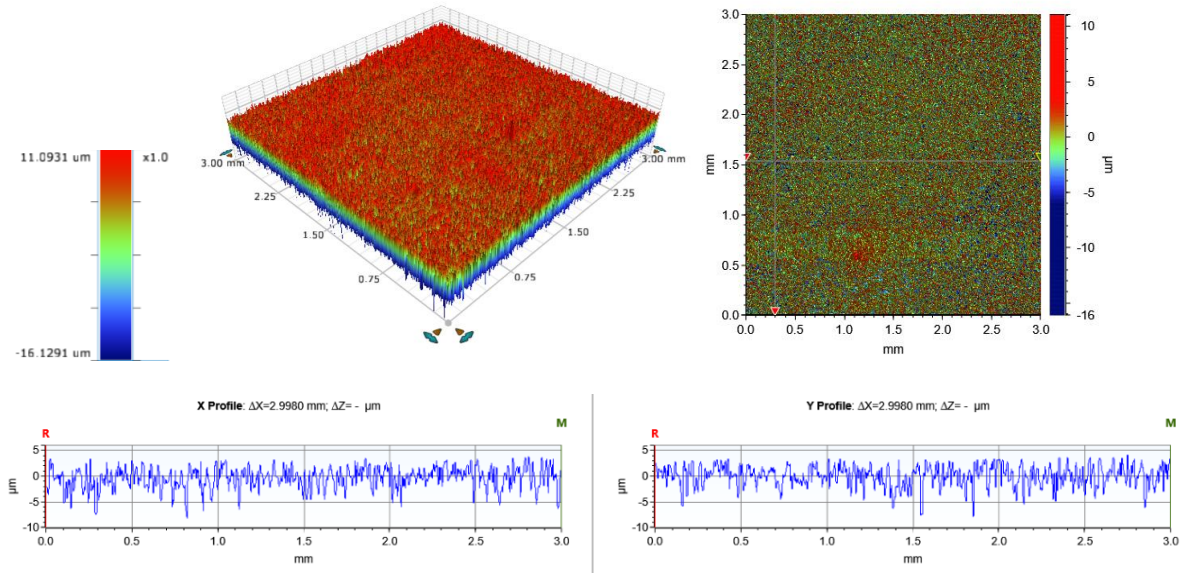
11.0931 um
x1.0
-16.1291 um
3.00 mm
2.25
1.50
0.75
mm
µm
X Profile: ΔX=2.9980 mm; ΔZ= - µm
Y Profile: ΔX=2.9980 mm; ΔZ= - µm
R
M

(a)

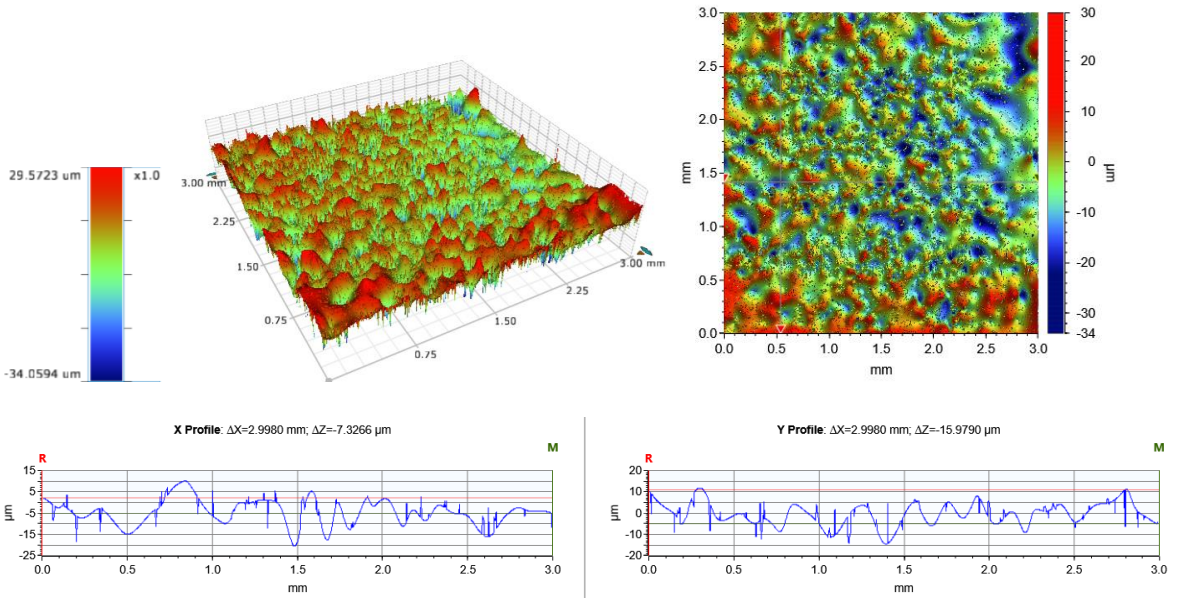
29.5723 um
x1.0
-34.0594 um
3.00 mm
2.25
1.50
0.75
mm
µm
X Profile: ΔX=2.9980 mm; ΔZ=-7.3266 µm
Y Profile: ΔX=2.9980 mm; ΔZ=-15.9790 µm
R
M

(b)

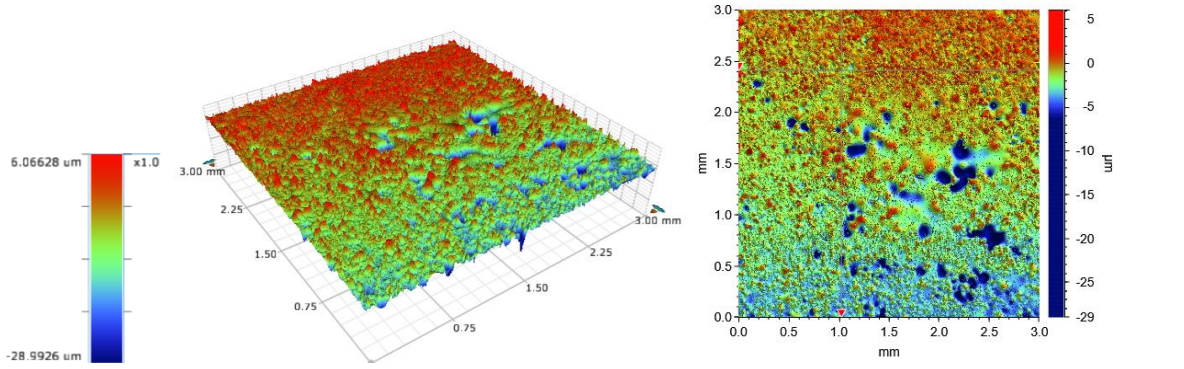
6.06628 um
x1.0
-28.9926 um
3.00 mm
2.25
1.50
0.75
mm
µm

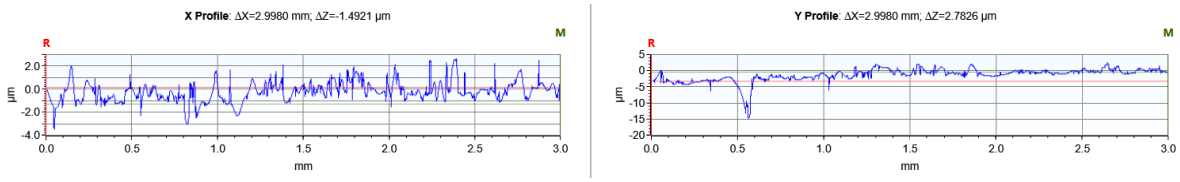

(c)

Figure 6-13 3D images, 2D images and 2D micrographs for X65 carbon steel after (a) 6 h pre-corrosion period in autoclave at 80 ºC, (b) after exposure to uninhibited brine in glass cell at 80 ºC and (c) after exposure to 30 ppm inhibited brine in glass cell at 80 ºC

6.5 Inhibition of Surfaces with Partial Coverage of $FeCO_3$

The reciprocal polarisation resistance for steel specimens with partial coverage $FeCO_3$ is provided in Figure 6-14a. The reciprocal polarisation resistance in the absence of the corrosion inhibitor decreased from 0.016 $ohm^{-1}cm^{-2}$ to 0.011 $ohm^{-1}cm^{-2}$ and decreased at a faster rate in the presence of the corrosion inhibitor to 0.00048 $ohm^{-1}cm^{-2}$. The greater reduction in reciprocal polarisation resistance in tests conducted in inhibited brines was associated with greater positive shifts in the open circuit potential, as shown by Figure 6-14b. The open circuit potential in the inhibited brine was -596 mV as compared to an open circuit potential of -647 mV in the uninhibited brine. The inhibitor efficiencies for uniform corrosion suppression were determined using Equation 5.1 and 5.2, and were found to be 96 and 95% in terms end-point and integrated efficiency respectively.

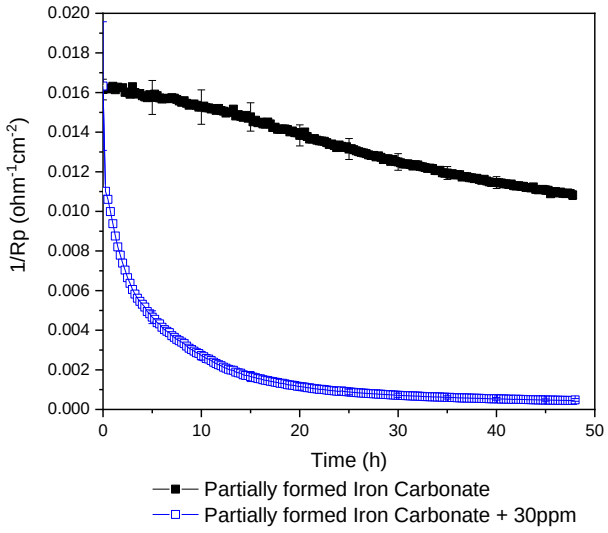

(a)

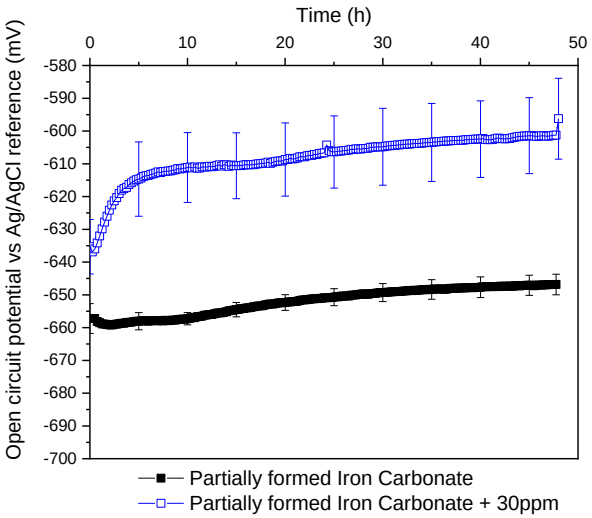

(b)

Figure 6-14 (a) Reciprocal of polarisation resistance and (b) open circuit potential vs Ag/AgCl reference as a function of time for X65 steel (with a pre-formed partial coverage $FeCO_3$ layer) exposed to inhibited and uninhibited CO_2-saturated 3 wt.% NaCl solution at 80 ºC. Note that inhibitor addition was performed prior to immersion of the specimen in the electrolyte

The bulk solution pH was lower for tests conducted in the inhibited brine throughout the 48 hour testing period, as shown by Figure 6-15. The pH after 48 hours of exposure was 5.98 in the uninhibited brine and 4.86 in the inhibited brine.

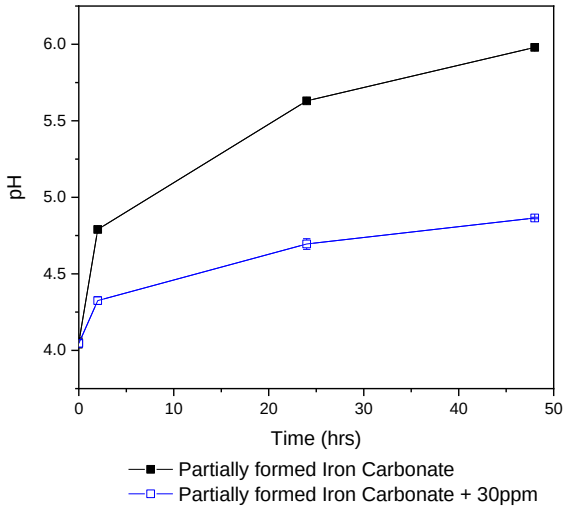

Figure 6-15 Bulk pH as a function of time for X65 steel (with a pre-formed partial coverage $FeCO_3$ layer) exposed to inhibited and uninhibited CO_2-saturated 3 wt.% NaCl solution at 80 ºC. Note that inhibitor addition was performed prior to immersion of the specimen in the electrolyte

Top-view SEM images of the surfaces before and after exposure to the un-inhibited and inhibited brines are provided in Figure 6-16, and show that exposure to the un-inhibited brine for 48 hours resulted in partial dissolution of the iron-carbonate layer and that exposure to the inhibited brine resulted in further dissolution of the iron carbonate corrosion product.

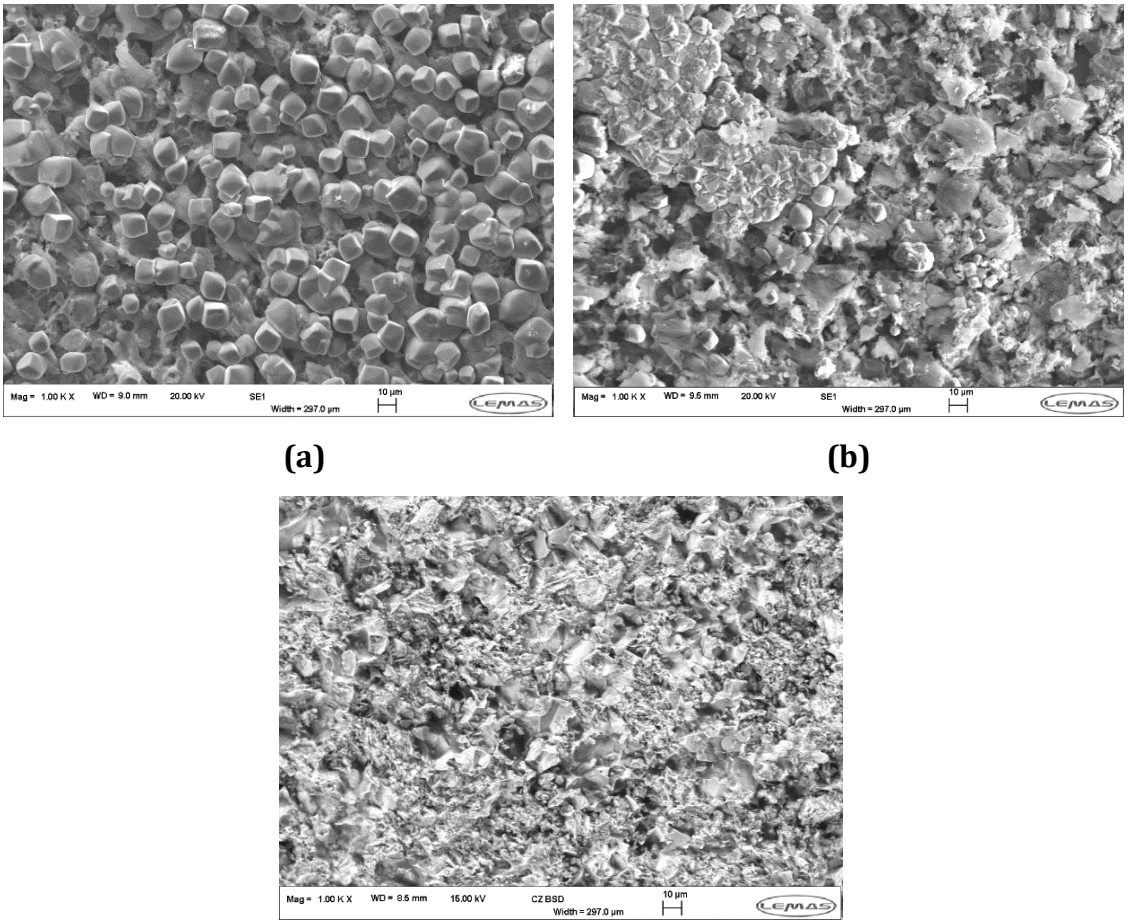

(a) **(b)**

(c)

Figure 6-16 SEM top-view images for (a) partial coverage $FeCO_3$ layer after 24 hour pre-corrosion in autoclave at 80 ºC, (b) partial coverage $FeCO_3$ layer after uninhibited exposure to 3 wt.% NaCl brine at 80 ºC and (c) partial coverage $FeCO_3$ layer after exposure to 30 ppm inhibited 3 wt.% NaCl brine at 80 ºC

X-ray diffraction of the surfaces is provided in Figure 6-17, and confirms the partial dissolution of iron carbonate after exposure to the un-inhibited brine. It was also confirmed that the iron carbonate had completely dissolved after 48 hour exposure to the inhibited brine.

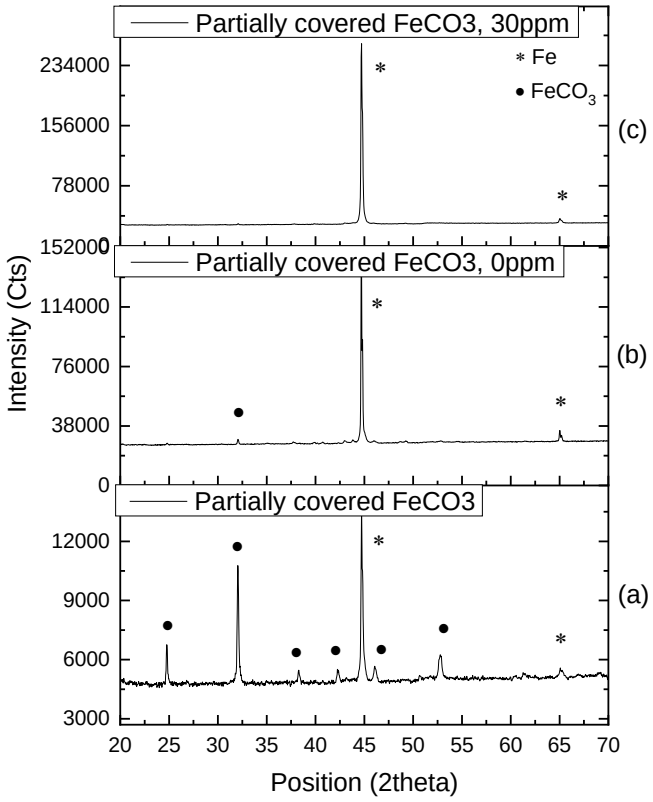

Figure 6-17 XRD pattern for (a) partial coverage $FeCO_3$ layer after 24 hour pre-corrosion in autoclave at 80 ºC, (b) partial coverage $FeCO_3$ layer after uninhibited exposure to 3 wt.% NaCl brine at 80 ºC and (c) partial coverage $FeCO_3$ layer after exposure to 30 ppm inhibited 3 wt.% NaCl brine at 80 ºC

The maximum pit depth of the pre-corroded partial coverage iron carbonate specimen decreased from 26 µm to 25.5 µm after 48 hour exposure to the un-inhibited brine, as shown by Figure 6-18. However after exposure to the inhibited brine, the maximum pit depth increased to 34.1 µm resulting in a localised corrosion inhibitor efficiency of -19.5%.

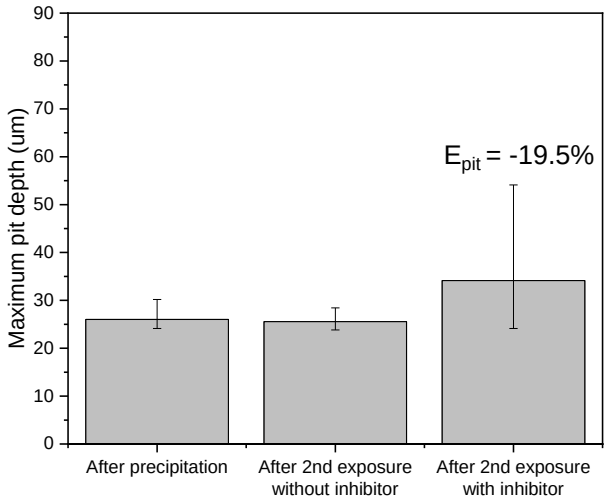

Figure 6-18 Maximum pit depth for partial coverage $FeCO_3$ layer after 24 hour pre-corrosion in autoclave at 80 ºC, partial coverage $FeCO_3$ layer after uninhibited exposure to 3 wt.% NaCl brine at 80 ºC and partial coverage $FeCO_3$ layer after exposure to 30 ppm inhibited 3 wt.% NaCl brine at 80 ºC

The extent of localised corrosion was further examined using 2D and 3D NPFLEX surface profilometry images and micrographs. Figure 6-19 confirms that exposure to the un-inhibited brine results in a less smooth surface however with some localised attacks. Figure 6-19c confirmed that exposure to the inhibited brine had led to a lesser extent of surface roughening however at the cost of a greater localised corrosion attack.

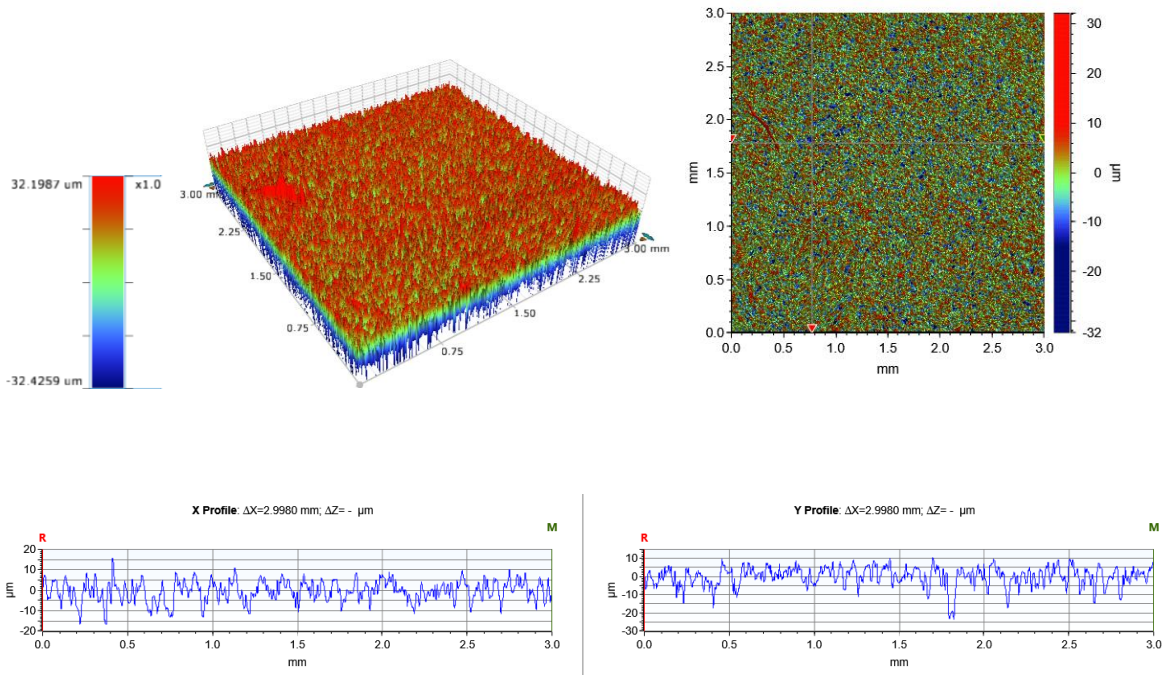

(a)

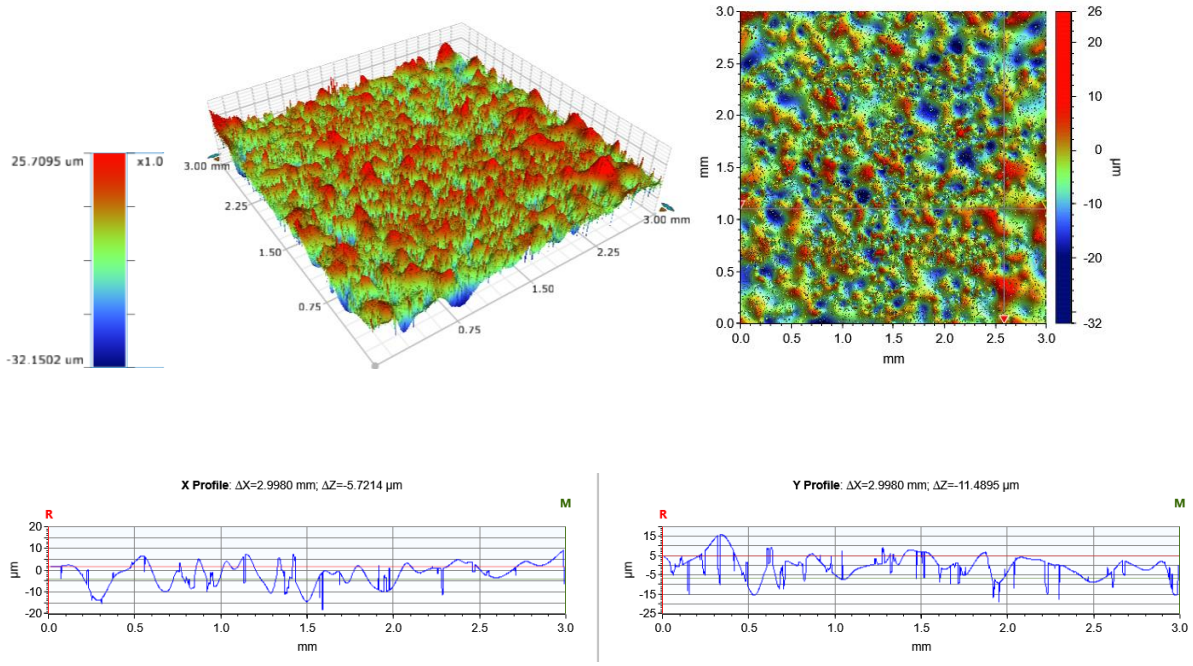

(b)

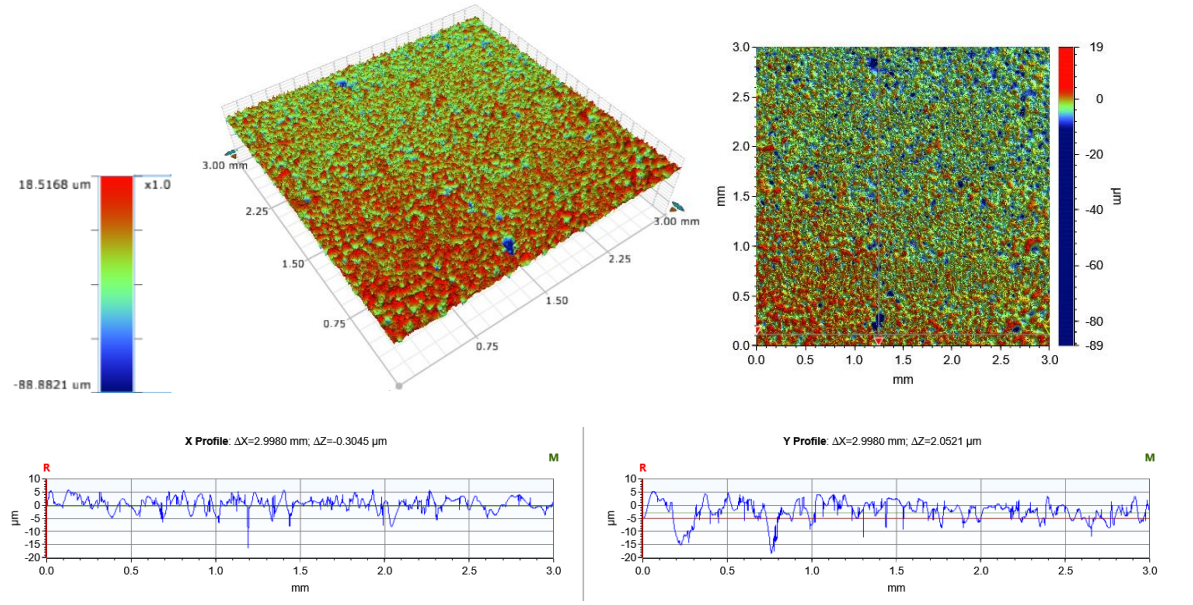

(c)

Figure 6-19 3D image, 2D image and 2D micrographs for X65 carbon steel after (a) 24h precipitation period in autoclave at 80 ºC, (b) after exposure to uninhibited brine in glass cell at 80 ºC and (c) after exposure to 30 ppm inhibited brine in glass cell at 80 ºC

6.6 Inhibition of Surfaces with Full Coverage of $FeCO_3$

Figure 6-20 shows the reciprocal polarisation resistance and open circuit potential as a function of exposure time for 96 hour pre-corroded X65 steel (Full coverage $FeCO_3$) after exposure to glass cell tests in un-inhibited and inhibited brines. The reciprocal polarisation resistance for the test conducted in the un-inhibited brine stabilised after approximately 20 hours of exposure before slowly decreasing to 0.0033 $ohm^{-1}cm^{-2}$ by the end of the test. However in the test conducted in the inhibited brine, the reciprocal polarisation resistance quickly reduced and stabilised at 0.00124 $ohm^{-1}cm^{-2}$. The resulting open circuit potentials after 48 hours of exposure to the un-inhibited and inhibited brines were -640 mV and -598 mV respectively. The inhibitor efficiencies for uniform corrosion suppression were determined using Equation 5.1 and 5.2, and were found to be 83 and 93.4% in terms end-point and integrated efficiency respectively.

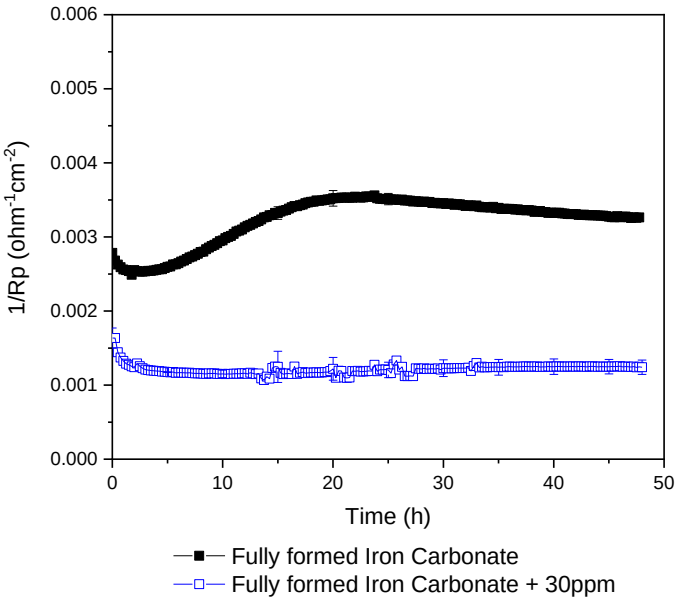

(a)

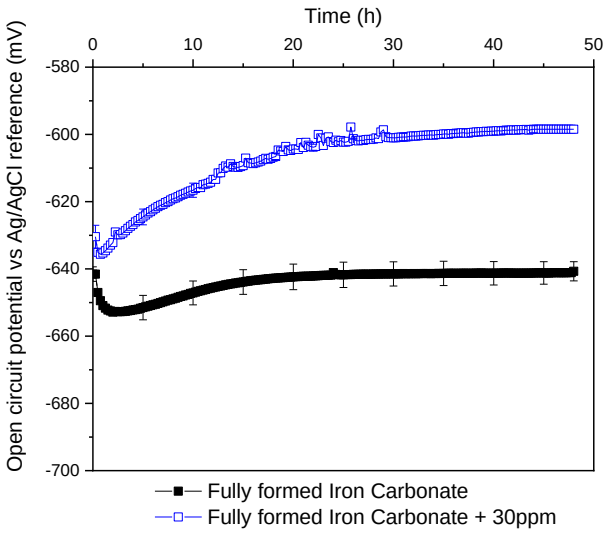

(b)

Figure 6-20 (a) Reciprocal of polarisation resistance and (b) open circuit potential vs Ag/AgCl reference as a function of time for X65 steel (with a pre-formed full coverage $FeCO_3$ layer) exposed to inhibited and uninhibited CO_2-saturated 3 wt.% NaCl brines at 80 ºC. Note that inhibitor addition was performed prior to immersion of the specimen in the electrolyte.

The bulk solution pH increased with increasing exposure time from 3.95 to 6.1 and 4.7 after exposure to the un-inhibited and inhibited brines respectively, as shown by Figure 6-21.

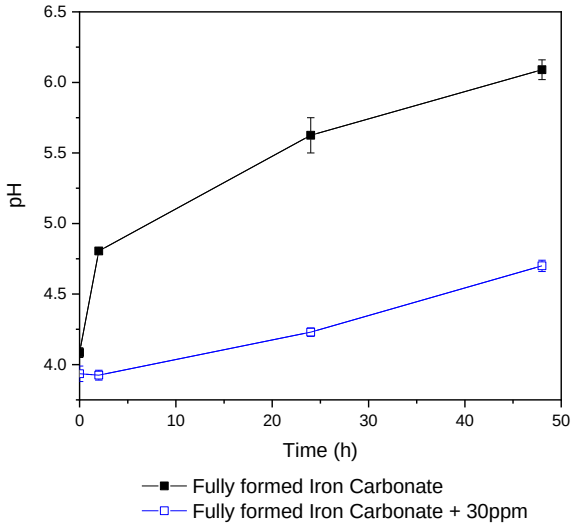

Figure 6-21 Bulk pH as a function of time for X65 steel (with a pre-formed full coverage $FeCO_3$ layer) exposed to inhibited and uninhibited CO_2-saturated 3 wt.% NaCl brines at 80 ºC. Note that inhibitor addition was performed prior to immersion of the specimen in the electrolyte.

Figure 6-22 illustrates the partial dissolution of iron carbaonte after 48 hour exposure to both un-inhibted and inhbited brines withitin the glass cell tests.

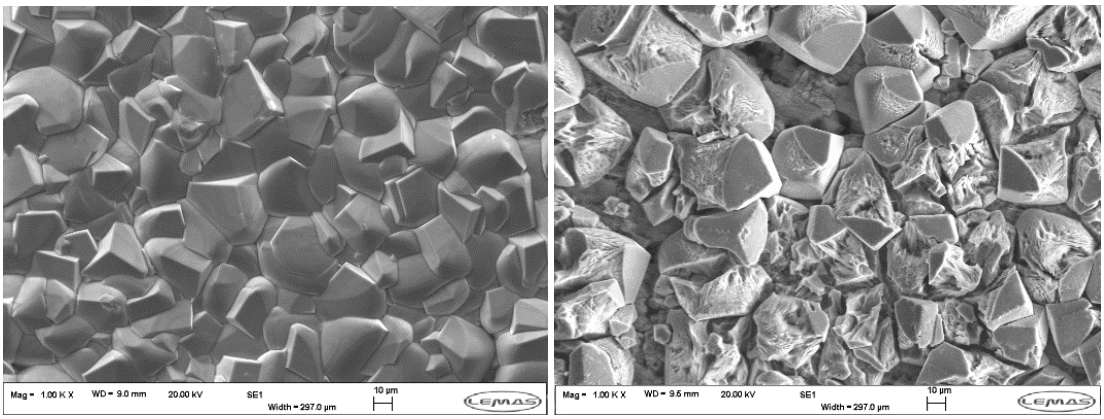

(a) **(b)**

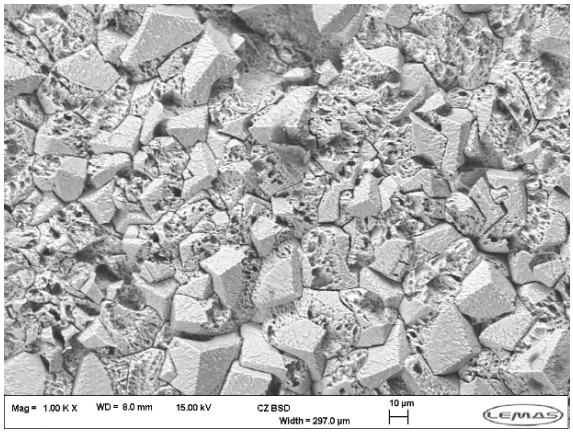

(c)

Figure 6-22 SEM top-view images for (a) full coverage $FeCO_3$ layer after 96 hours pre-corrosion in autoclave at 80 ºC, (b) full coverage $FeCO_3$ layer after uninhibited exposure to 3 wt.% NaCl brine at 80 ºC and (c) full coverage $FeCO_3$ layer after exposure to 30 ppm inhibited 3 wt.% NaCl brine at 80 ºC

X-ray diffraction confirmed the presence of iron carbonate corrosion products on the pre-corroded specimens after exposure to the un-inhibited and inhibited glass cell tests, as shown by Figure 6-23.

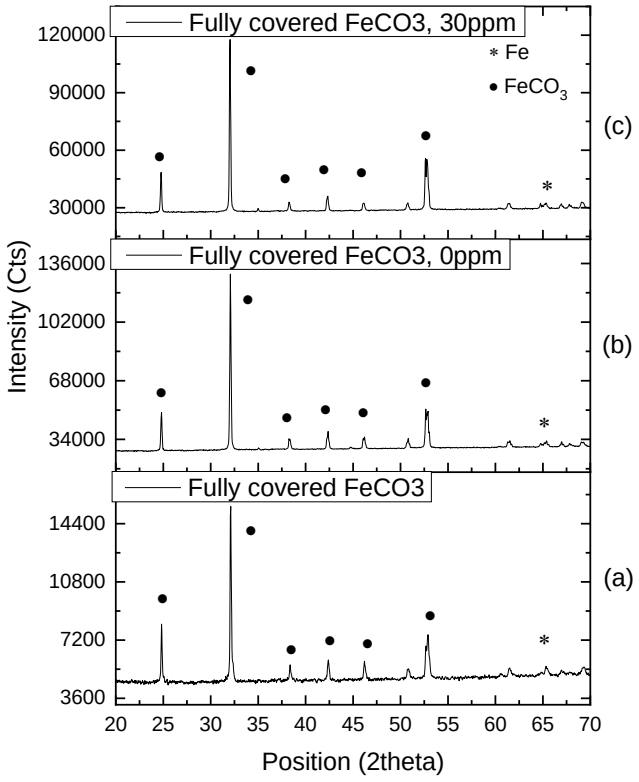

Figure 6-23 XRD patterns for (a) full coverage $FeCO_3$ layer after 96 hours pre-corrosion in autoclave at 80 ºC, (b) full coverage $FeCO_3$ layer after uninhibited exposure to 3 wt.% NaCl brine at 80 ºC and (c) full coverage $FeCO_3$ layer after exposure to 30 ppm inhibited 3 wt.% NaCl brine at 80 ºC

The maximum pit depth of the pre-corroded full coverage iron carbonate specimen increased after exposure to the un-inhibited brine, from 46.1 µm to 51.4 µm. There was a further increase in the maximum pit depth to 54.1 µm after exposure to the inhibited brine, as shown by Figure 6-24. The inhibitor efficiency in terms of localised corrosion was calculated using Equation 6.1 and was found to be -0.5%.

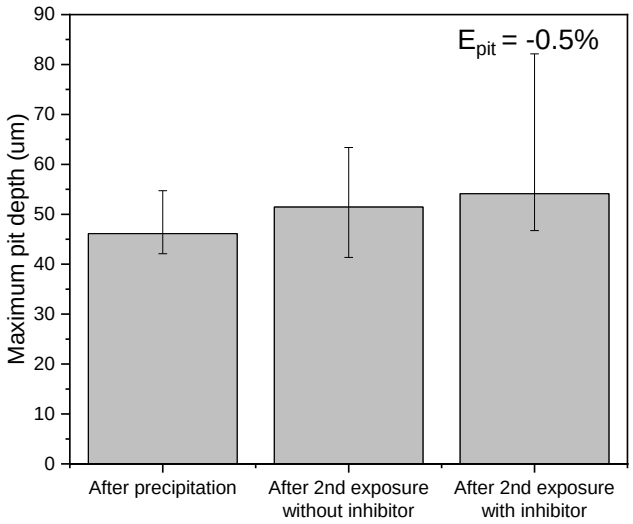

Figure 6-24 Maximum pit depth for (a) full coverage $FeCO_3$ layer after 96 hours pre-corrosion in autoclave at 80 ºC, full coverage $FeCO_3$ layer after uninhibited exposure to 3 wt.% NaCl brine at 80 ºC and full coverage $FeCO_3$ layer after exposure to 30 ppm inhibited 3 wt.% NaCl brine at 80 ºC

NPFLEX 2D and 3D profilometry images together with 2D micrographs were used to confirm the presence of pits on the pre-corroded surfaces. Figure 6-25 confirms that the extent of localised corrosion increased after exposure to the un-inhibited brine and further increased after exposure to the inhibited brine.

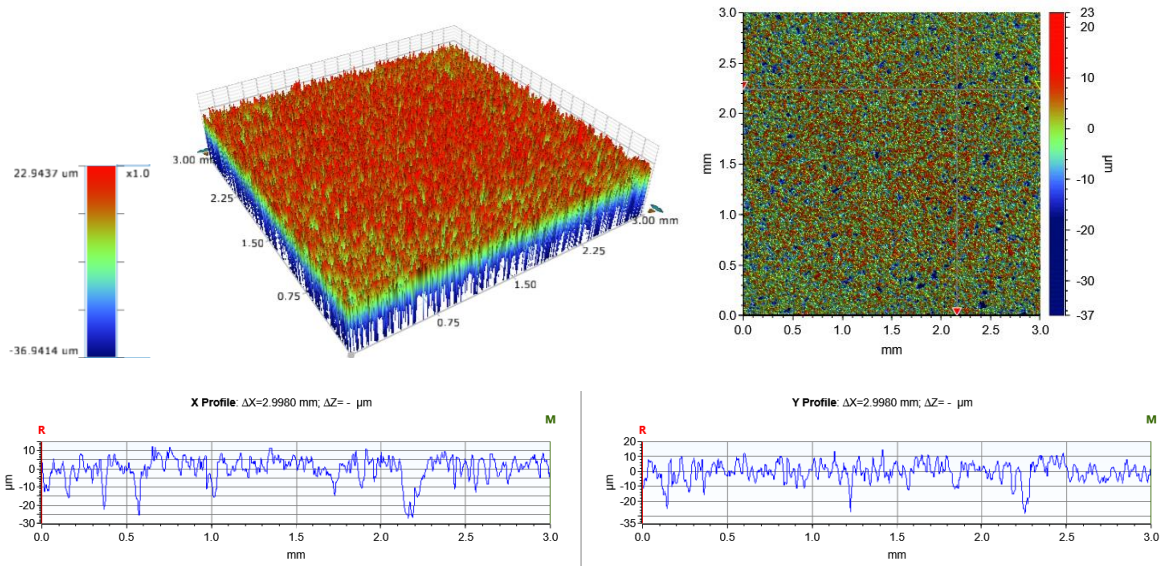

(a)

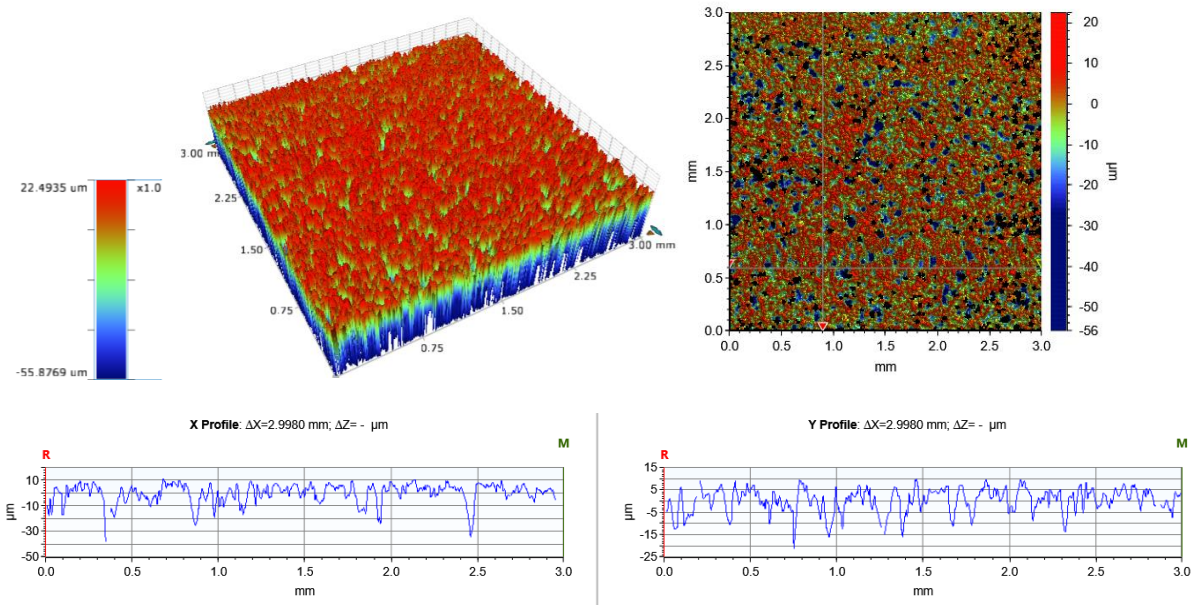

(b)

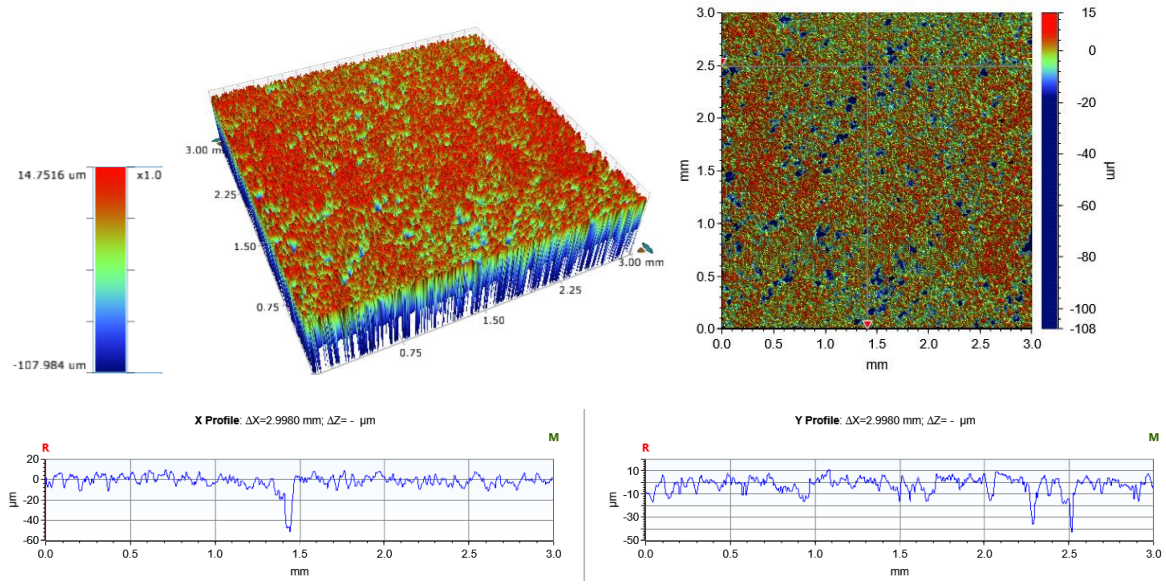

(c)

Figure 6-25 3D image, 2D image and 2D micrographs for X65 carbon steel after (a) 96 h precipitation period in autoclave at 80 ºC, (b) after exposure to uninhibited brine in glass cell at 80 ºC and (c) after exposure to 30 ppm inhibited brine in glass cell at 80 ºC

6.7 Overall Performance Comparison

Figure 6-26 compares the inhibitor efficiency with respect to the uniform corrosion behaviour for all of the pre-corroded specimens, iron carbide (6 hour pre-corrosion), partial coverage iron carbonate (24 hour pre-corrosion) and full coverage iron carbonate (96 hour pre-corrosion). The comparison shows that the overall efficiency in terms of uniform corrosion was the greatest for the iron carbide covered steel specimen (6 hour pre-corrosion). The inhibitor efficiency was 3% (end-point) and 2.4% (integrated) greater than that of steel which had not undergone pre-corrosion. In terms of uniform corrosion efficiency, partial coverage iron carbonate had similar efficiencies however full coverage iron carbonate resulted in a reduction of inhibitor efficiency to 83% (end-point) and 93.4% (integrated).

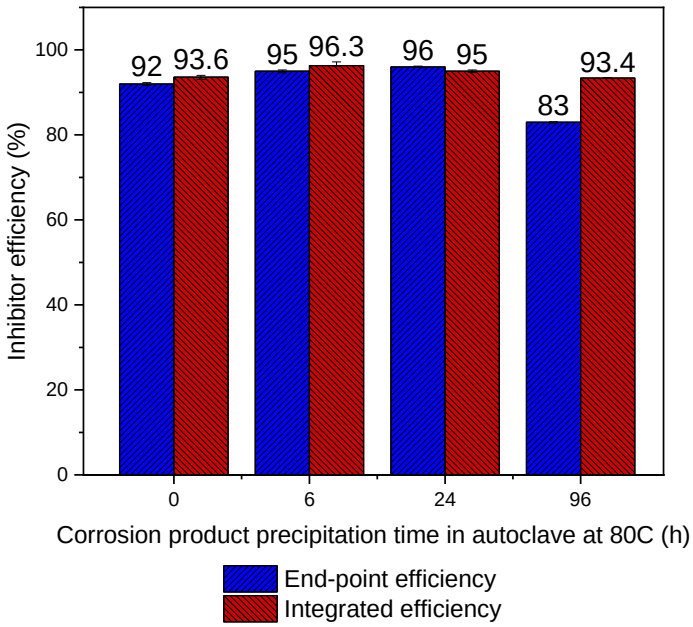

Figure 6-26 Comparison of end-point and integrated uniform corrosion inhibitor efficiencies on wet-ground X65 carbon steel, 6 h pre-corroded steel (iron carbide layer), 24 h pre-corroded steel (partial coverage iron carbonate) and 96 h pre-corroded steel (full coverage iron carbonate) after exposure to 30 ppm inhibited 3 wt.% NaCl brines at 80 ºC

The individual contributions towards overall corrosion protection afforded by the corrosion product and corrosion inhibitor for each of the tested steel specimens were estimated by calculation of protection afforded by the corrosion product within the un-inhibited brine, as shown by Figure 6-27. The contribution towards

overall protection as afforded by the corrosion inhibitor was then determined by subtracting the protection afforded by the corrosion product from the overall efficiency. The estimations indicate that the protection afforded by the corrosion inhibitor decreases with increasing pre-corrosion time.

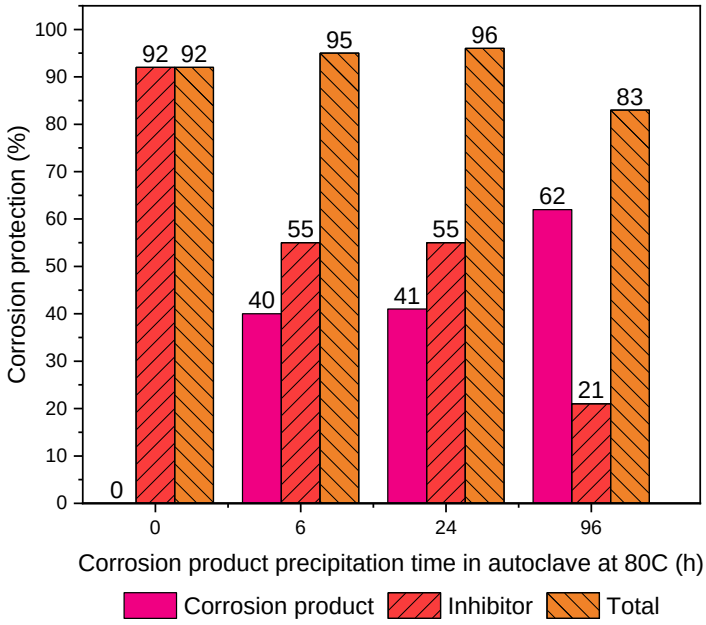

Figure 6-27 Estimation of individual corrosion protection afforded by corrosion products and corrosion inhibitors for wet-ground X65 (0 h pre-corrosion), Iron carbide layer (6 h pre-corrosion), Partial coverage iron carbonate (24 h pre-corrosion) and full coverage iron carbonate (96 h pre-corrosion) after exposure to 30 ppm inhibited 3 wt.% NaCl brine at 80 ºC

Figure 6-28 compares the inhibitor efficiencies in terms of uniform and localised corrosion for the different pre-corroded steel specimens, where pre-corrosion of up to 24 hours results in an increase in end-point uniform corrosion efficiency from 92% to 96% while the localised efficiency decreases from 95% to -19.5%. At a pre-corrosion time of 96 hours the uniform efficiency decreases by 12% however decreases by 95.9% in terms of localised corrosion efficiency.

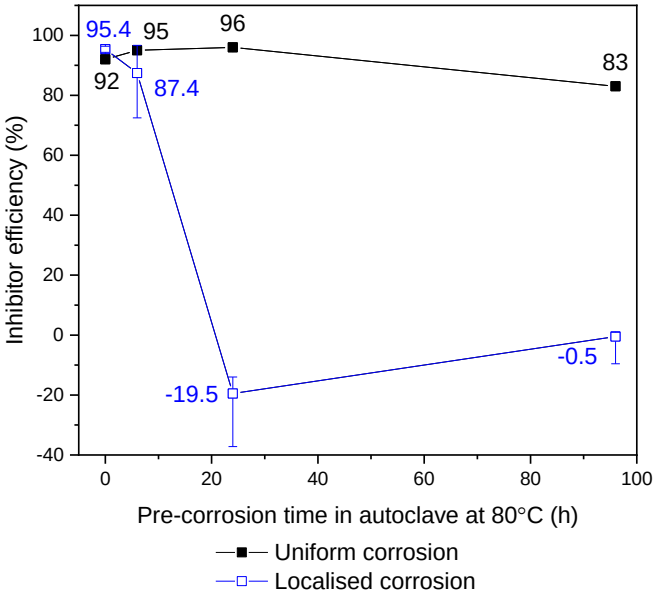

Figure 6-28 Uniform and localised inhibitor efficiencies for Wet-ground X65 (0 h pre-corrosion), Iron carbide layer (6 h pre-corrosion), Partial coverage iron carbonate (24 h pre-corrosion) and full coverage iron carbonate (96 h pre-corrosion) after exposure to 30 ppm inhibited 3 wt.% NaCl brine at 80 ºC

6.8 Influence of Corrosion Inhibition on Surface Wettability

Water-in-oil and oil-in-water contact angle measurements were conducted on wet-ground X65 carbon steel and full coverage iron carbonate surfaces as shown by Figure 6-29, in order to determine the influence of an imidazoline corrosion inhibitor on surface wettability in the absence and presence of iron carbonate corrosion products. The tests were conducted according to the experimental procedure described in Chapter 3.5.

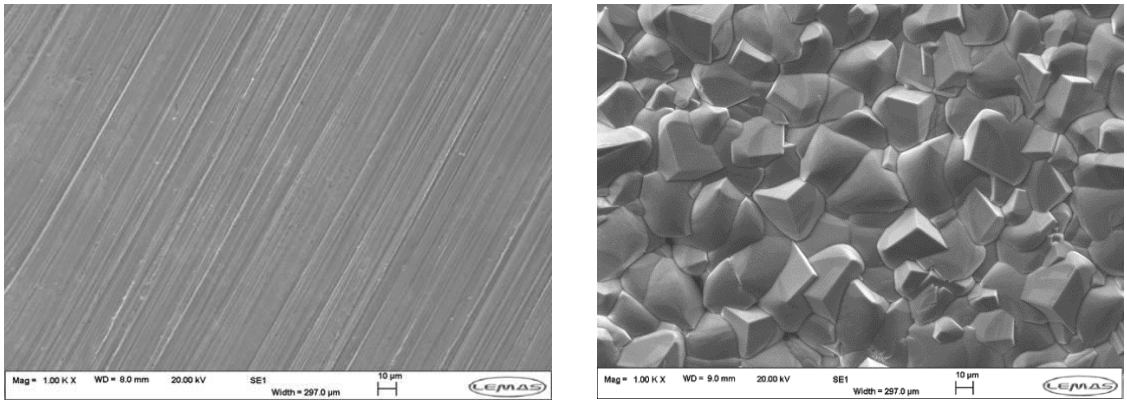

(a) **(b)**

Figure 6-29 (a) Wet-ground X65 and (b) iron carbonate surfaces used for contact angle measurements where iron carbonate was precipitated in autoclaves at 80 ºC, 1 bar Pco_2 at 25 ºC for 96 hours

6.8.1 Wet-Ground X65

6.8.1.1 Water-in-Oil

Figure 6-30 shows the water phase contact angle as a function of inhibitor concentration for a droplet of water on wet-ground X65 carbon steel submerged in oil. The water phase contact angle increased from 106 degrees at 0 ppm to 148 degrees at 30 ppm and remained stable up to a concentration of 100 ppm. The wetting behaviour was hydrophobic at all inhibitor concentrations as well as in the absence of the corrosion inhibitor.

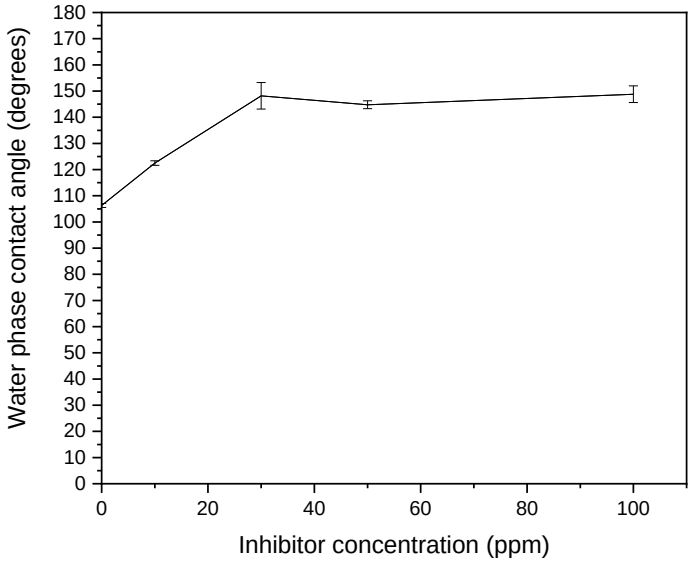

Figure 6-30 Water phase contact angle as a function of inhibitor concentration on wet-ground X65 carbon steel in a water in oil system

The water phase contact angle of the water droplet as a function of time is shown in Figure 6-31. The contact angle decreased with time in the absence of the corrosion inhibitor, from 113 degrees to 79 degrees after 1000 seconds of exposure which resulted in a hydrophobic to hydrophillic wetting transition after approximetely 400 seconds of exposure. The contact angle at 10 ppm slowly increased and reached its maximum of 170 degrees after 500 seconds. However at concentrations above 10 ppm the contact angles increased rapidly and had reached their maximum values (150-170 degrees) within the first 250 seconds.

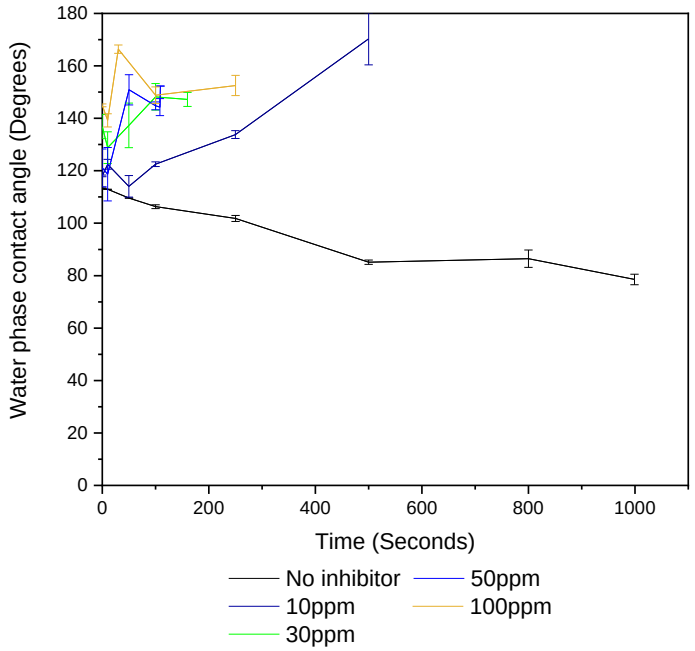

Figure 6-31 Water phase contact angle as a function of time on wet-ground X65 carbon steel in a water in oil system

6.8.1.2 Oil-in-Water

The water phase contact angle of an oil droplet on wet-ground X65 steel submerged in water increased from 47 degrees at 0 ppm to a maximum of 134 degrees at 10 ppm and remained above 90 degrees at all inhibitor concentrations, as shown by Figure 6-32.

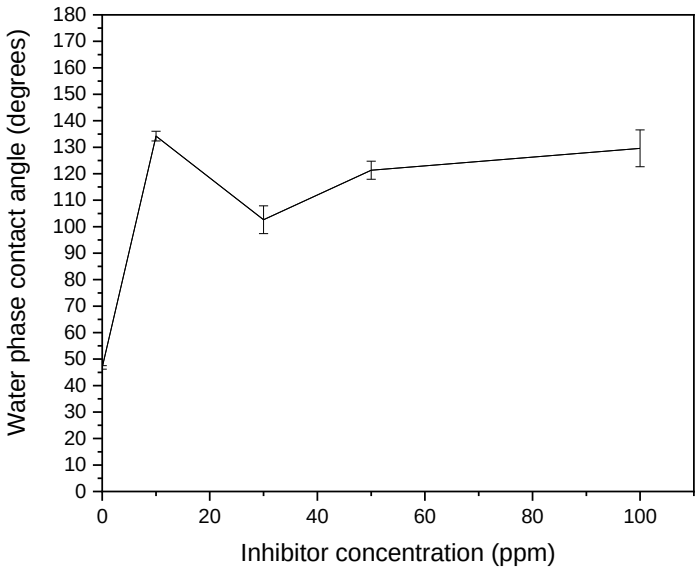

Figure 6-32 Water phase contact angle as a function of inhibitor concentration on wet-ground X65 carbon steel in an oil in water system

Figure 6-33 indicates that the contact angles remained stable with increasing exposure time at all of the inhibitor concentrations confirming that the wetting behaviour was hydrophillic in the absence of the inhbitor and hydrophobic in the presence of the corrosion inhbitor throughout the 1000 seconds of the test.

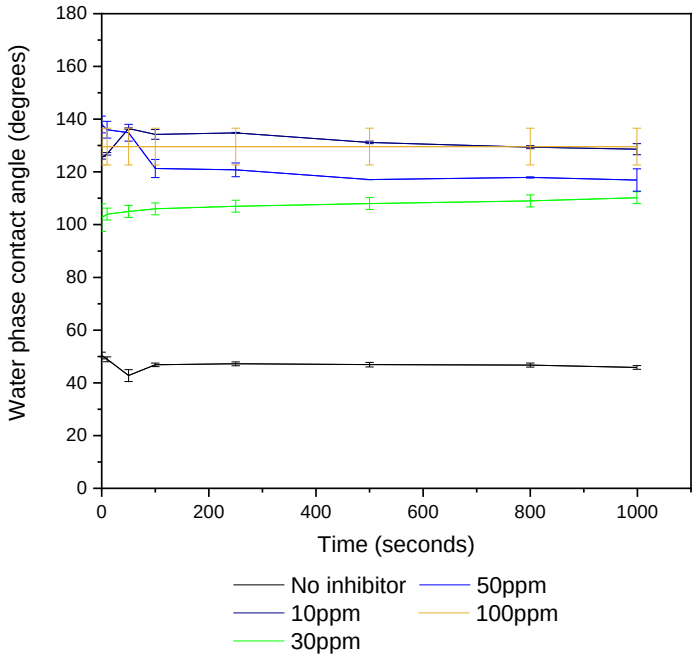

Figure 6-33 Water phase contact angle as a function of time on wet-ground X65 carbon steel in a oil in water system

6.8.2 Iron Carbonate Covered Surface

6.8.2.1 Water-in-Oil

Figure 6-34 shows the water phase contact angle of a water droplet on an iron carbonate covered steel surface submerged in oil as a function of inhibitor concentration. The contact angle increased from 63 degrees at 0 ppm to a maximum of 122.5 degrees at an inhibitor concentration of 30 ppm. The contact angle decreased with further increases in inhibitor concentration and was found to be 100 degrees at an inhibitor concentration of 100 ppm however the wetting behaviour remained hydrophobic at all inhibitor concentrations.

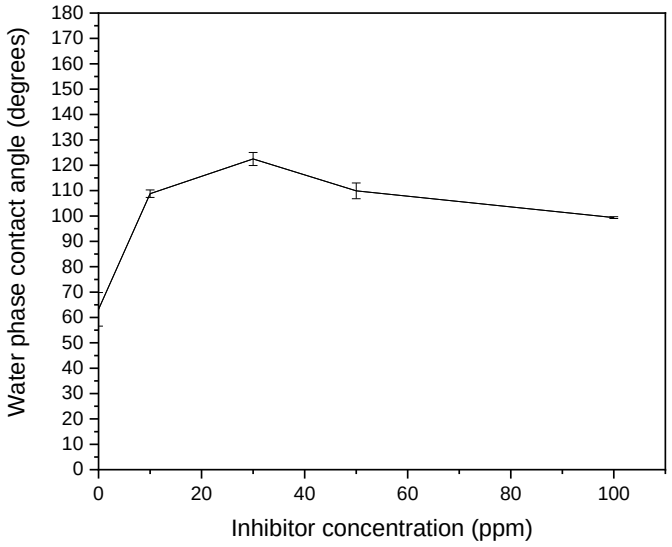

Figure 6-34 Water phase contact angle as a function of inhibitor concentration on an iron carbonate covered surface in a water in oil system

Figure 6-35 shows the contact angle as a function of exposure time. The contact angles remained reasonably stable with increasing exposure time with no significant changes in the wetting behaviour which confirmed that the surface was hydrophilic in the absence of the inhibitor and hydrophobic in the presence of the inhibitor throughout the duration of the tests.

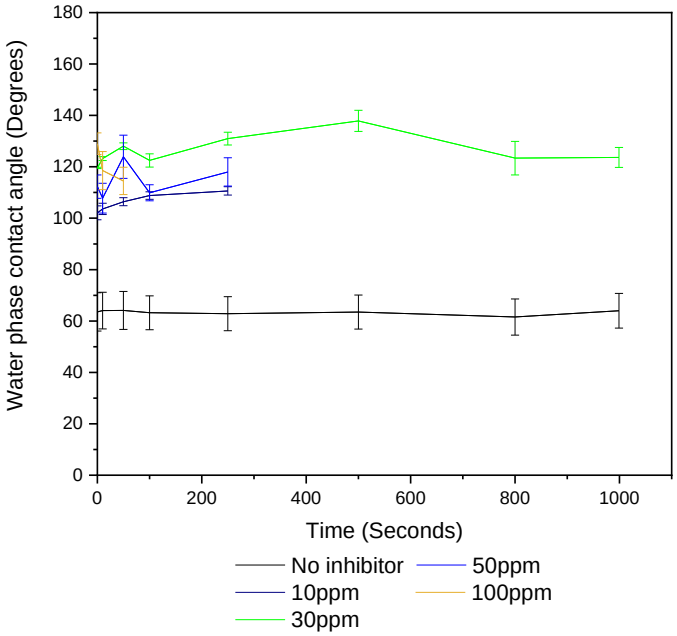

Figure 6-35 Water phase contact angle as a function of time on an iron carbonate covered surface in a water in oil system

6.8.2.2 Oil-in-Water

The water phase contact angle of a droplet of oil on an inverted iron carbonate surface submerged in water is shown in Figure 6-36 as a function of inhibitor concentration. The water phase contact angle was initially 51.7 degrees in the absence of the corrosion inhibitor and decreased to 29.8 degrees after exposure to 30 ppm of the corrosion inhibitor and the wetting behaviour therefore remained hydrophilic at all of the tested inhibitor concentrations.

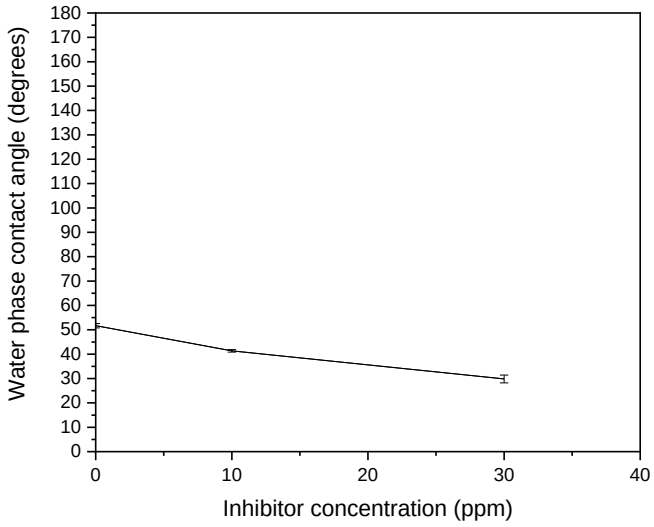

Figure 6-36 Water phase contact angle as a function of inhibitor concentration on an iron carbonate covered surface in an oil in water system

The water phase contact angle of the oil droplets remained constant with increasing exposure time at inhibitor concentrations of up to 30 ppm and remained hydrophillic for the duration of the tests.

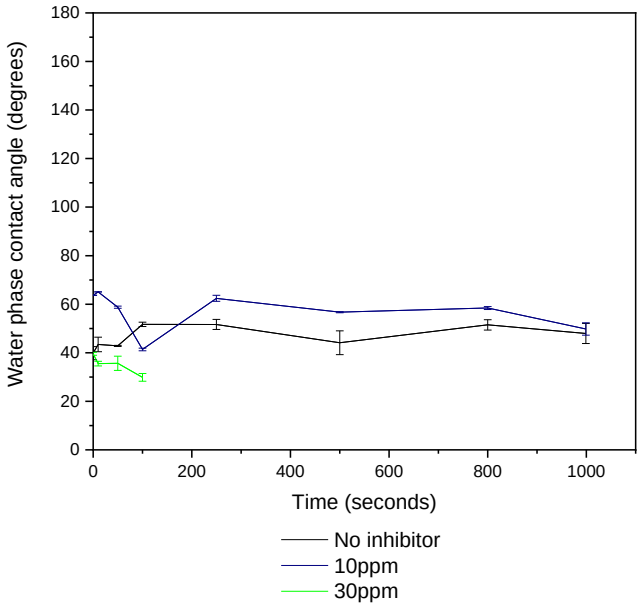

Figure 6-37 Water phase contact angle as a function of time on iron carbonate covered surface in an oil in water system

6.9 Summary of Results

The role of pre-corrosion on the performance of an imidazoline corrosion inhibitor was evaluated with respect to inhibition of uniform and localised corrosion in CO_2 environments at 80 ºC using a two stage testing procedure with autoclave pre-corrosion and glass cell inhibition testing of X65 carbon steel. The inhibitor performance was assessed on iron carbide and partially/fully covered iron carbonate ($FeCO_3$) and compared against inhibition on wet-ground X65 carbon steel. In terms of uniform corrosion suppression the performance of the imidazoline corrosion inhibitor was improved by up to 4% on steel surfaces which had a partial coverage of iron carbonate however this resulted in a 114.9% drop in its ability to suppress localised/pitting attacks. Further pre-corrosion (full coverage iron carbonate) was found to result in a reduction in the inhibitors uniform efficiency (-9%) and was also found to cause the inhibitor to directly promote localised/pitting attacks. Baseline tests conducted under all environmental conditions in the absence of the corrosion inhibitor enabled the estimation of the individual contributions provided by the inhibitor and the

corrosion products towards overall corrosion protection, which indicated that the protection afforded by the inhibitor was approximately 58% on iron carbide covered surfaces and surfaces partially covered by iron carbonate. The individual contribution of the corrosion inhibitor towards overall protection was further reduced to 25% on a surface with a full coverage of iron carbonate.

Chapter 7 Overall Discussion

7.1 Introduction

Results presented in chapters 4, 5 and 6 have demonstrated findings with respect to the role of Ca^{2+} on corrosion product growth kinetics and characteristics, corrosion inhibitor performance evaluation and corrosion inhibitor interaction with corrosion product covered surfaces, respectively. This chapter will provide a discussion to link these findings and provide detailed explanations for specific behaviours. The discussion is divided into three main sections. A map illustrating the main topics of discussion for each section is provided in Figure 7-1. For each main topic of discussion, at least one finding will be highlighted and its contribution towards existing literature will be emphasised.

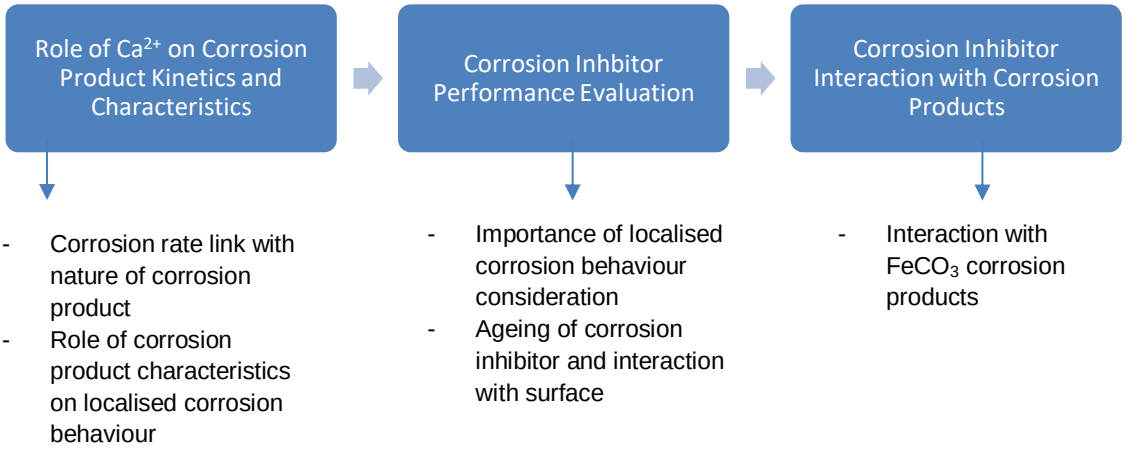

Figure 7-1 Map for main topics of discussion

7.2 Role of 1.83 wt.% $CaCl_2 \cdot 2H_2O$ on Corrosion Behaviour at 80 and 150 ºC

This sub-chapter discusses the influence of calcium ions on the overall corrosion behaviour in CO_2 environments at 80 and 150 ºC based on results from Chapter 4. The characteristics of corrosion products based on results obtained by SEM/EDX, XRD/Molar calculations and FIB are discussed in order to provide an assessment of exactly how calcium ions can influence the overall corrosion behaviour. The influence of calcium ions on the localised corrosion behaviour is discussed and compared to the behaviour observed in sodium chloride based brines. Finally, the influence of intermediate $CaCl_2 \cdot 2H_2O$ concentrations on the

characteristics/composition of corrosion product and on the localised corrosion behaviour is discussed at the end of this sub-chapter.

7.2.1 Corrosion Rate Link with Nature of Corrosion Product formed at 80 ºC

Mass gain measurements in Figure 4-2 indicate that at 80 ºC and 6 h, there is minimal corrosion product on the steel surface. As the test progresses at 80 ºC, a reduction in corrosion rate occurs in conjunction with an increase in the mass of the corrosion product, which appears to decline in growth rate towards the end of the 96 h experiment. In comparison to the experiments performed in 3 wt.% NaCl, the initial corrosion rates after 6 h at 80 ºC were lower in the presence of 1.83 wt.% Ca^{2+}, as indicated by Figure 4-23. Furthermore, the corrosion product film formed at 80 ºC resulted in a less protective layer after 96 h (3.6 mm $year^{-1}$ in comparison to 2.5 mm $year^{-1}$ in pure NaCl), which precipitated more slowly over the first 48 h, but ultimately possessed a greater mass by the end of the 96 h experiments. The slower kinetics of film formation over 48 h may be attributed to the effect of Ca^{2+} on the solubility of the formed precipitate, as discussed and observed by Alsaiari *et al*. (115), or it could be partly caused by the lower corrosion rate over the first 24 h of the experiments compared to tests in the absence of Ca^{2+} (as shown in Figure 4-23 and Figure 4-1) which would delay Fe^{2+} saturation of the test solution and hence, the onset of precipitation. However, after 48 h, total mass loss of carbon steel is higher in the presence of Ca^{2+} compared to that in the NaCl solution over the same time period *but* the inverse relationship is observed with regards to the corrosion product mass i.e. the amount of precipitation relative to the corrosion rate is lower in the presence of Ca^{2+}.

This observation of a lower precipitation rate relative to the overall dissolution rate of the steel over the first 48 h suggests that less corrosion product layer is retained at the steel surface. Given that no bulk precipitation was observed at the end of any of the experiments performed in this study (i.e. the solution appeared completely clear upon immediate opening of the autoclave), it is suggested that Ca^{2+} does play a role in increasing the solubility of the overall corrosion product within the system. The greater mass of the corrosion product after a duration of 96 h in the presence of Ca^{2+} can be attributed to the reduction in corrosion rate compared to tests in the pure NaCl system which provides a

greater flux of Fe^{2+} ions into the bulk solution to facilitate further precipitation back onto the specimen surface.

Across both environments there was a distinct inverse relationship between corrosion product mass and the corrosion rate of the underlying steel, with the greatest mass of corrosion product providing the least protection to the substrate after 96 h. This indicates that a large mass or thick corrosion product does not necessarily ensure efficient suppression of general corrosion rate for carbon steels. The low mass gain measurement in the absence of 1.83 wt.% Ca^{2+} which was previously discussed is supported by the top-view SEM image of the steel surface in Figure 4-9(a), where no crystalline corrosion product is evident after 6 h, only the presence of a porous iron carbide (Fe_3C) structure as a result of the selective dissolution of the ferrite phase within the steel microstructure. Consequently, the corrosion rate recorded after 6 h can be regarded as the anticipated dissolution rate in the absence of a protective layer. The resulting corrosion layer after 96 h is shown in the SEM images within Figure 4-9(d) (top view) and Figure 4-10(b) (cross-section), depicting a crystalline layer with a thickness exceeding 30 µm as shown by Figure 4-12.

The top-view SEM image corresponding to the specimen exposed to the 1.54 wt.% NaCl solution with 1.83 wt.% Ca^{2+} in Figure 2-32(a) shows that at 80 ˚C a seemingly amorphous layer (which was very thin due to the low mass gain value recorded and rich in iron and calcium based on EDX measurements) had precipitated after 6 h of exposure. This can be contrasted with the absence of a layer on X65 steel in the 3 wt.% NaCl solution in Figure 4-9(a). In the presence of Ca^{2+}, the formation of the initial amorphous layer was followed by the precipitation of a crystalline corrosion product (also rich in iron and calcium – confirmed later as $Fe_xCa_yCO_3$) exhibiting a different morphology to that of $FeCO_3$ in the pure NaCl system as shown by Figure 4-32(b). After 96 h, the deposition of calcium rich crystals (confirmed later as $CaCO_3$) had occurred on top of the already precipitated $Fe_xCa_yCO_3$ film as shown by Figure 4-32(d). The figure also indicates that this layer is substantially more porous than that of the film formed in the presence of purely NaCl after 96 h, correlating with its poor ability to inhibit general corrosion. FIB-SEM images in Figure 4-35(a) and Figure 4-36 also indicate $CaCO_3$ precipitation on top of the mixed carbonate layer.

The cross-sectional SEM images shown in Figure 4-33 show that the corrosion product layer at 80 ºC after 96 h is 50 µm thick, which is around twice the thickness of that in the 3 wt.% NaCl solution. However, the layer appears to be less well adhered to the substrate in comparison to the one formed in the pure NaCl experiment at the same temperature. Furthermore, the layer formed in the presence of Ca^{2+} is known to be very porous, as shown in Figure 4-32 where some areas exist on the steel surface are completely absent of corrosion product. Both these observations correlate with the poor protection offered by the film in the presence of Ca^{2+}.

Figure 4-34 shows the XRD patterns of the precipitated films in the presence of Ca^{2+} at 80ºC as a function of time. The results confirm that a crystalline layer of $Fe_xCa_yCO_3$ had precipitated after 24 h of exposure and that $CaCO_3$ was present on the surface after 96 h of exposure. The results also show that the main (104) peak for $Fe_xCa_yCO_3$ shifts to the right towards that associated with the same miller plane for $FeCO_3$, whilst also increasing in intensity with increasing exposure time. The Bravais lattices for $CaCO_3$ and $FeCO_3$ are located at 2θ angles of 29.42º and 32.07º, respectively, and a shift can be observed from the latter to the former with increased exposure time within Figure 4-34.

It is possible to calculate the mole fraction of Ca within the $Fe_xCa_yCO_3$ based on the shift in the (104) peak. Such calculations are outlined in Chapter 4.3, providing the derivation of Equation (4.7). Calculations were performed using Equation (4.7) and are provided in Table 4-5 and Table 4-7 for tests conducted at 80 and 150 ºC respectively. The results were correlated with EDX measurements which evaluate the ratio between the atomic wt.% of Ca to the combined atomic wt.% of Fe and Ca. Table 4-5 shows that the calculated mole fraction of Ca within the corrosion product layer decreased with increasing exposure time at 80 °C. These observations suggest that the corrosion product at 80 °C has different iron and calcium compositions along its thickness. An extended 192 h experiment was conducted at 80 °C to further observe the decrease in the mole fraction of Ca with time. The results show that the average mole fraction of Ca decreased further to 0.17.

Figure 4-35 shows EDX line scan results of the corrosion product layer formed in the presence of Ca^{2+} at 80 ºC. The image indicates the variability in Ca concentration through the film. The variation at 80 ºC shows a higher

concentration closer to the steel surface, although this line scan does not extend all the way to the substrate. Studies conducted by Esmaeely *et al* (69) have indicated that the presence of high calcium concentrations within the bulk solution results in the solution being supersaturated with respect to both $FeCO_3$ and $CaCO_3$ however with greater initial supersaturation with respect to $CaCO_3$ due to the higher concentration of Ca^{2+}. This can result in greater incorporation of calcium ions within the mixed $Fe_xCa_yCO_3$ layer. However due to high dissolution rates of the steel surface, the solution can become more supersaturated with respect to $FeCO_3$ due to greater consumption of Ca^{2+} relative to the consumption Fe^{2+} which results in a reduction in the incorporation of calcium ions. This results in the precipitation of a $Fe_xCa_yCO_3$ layer consisting of higher mole fractions of calcium near the steel substrate. This mechanism of crystal growth is demonstrated by the schematics in Figure 7-2 which demonstrates the initial formation of a calcium rich layer of $Fe_xCa_yCO_3$ and the incorporation of Fe^{2+} with increasing exposure time. The findings presented in Chapter 4 have indicated that this is indeed the case, where $Fe_xCa_yCO_3$ corrosion products can precipitate onto steel surfaces with concentration gradients across their depths. This finding is of extreme importance in terms of predicting the relative properties and stability of mixed Fe/Ca carbonate corrosion products.

Figure 7-2 Growth mechanism of $Fe_xCa_yCO_3$ corrosion product at 80 ºC as a function of exposure time

7.2.2 Corrosion Rate Link with Nature of Corrosion Product formed at 150 ºC

The rate of reduction in corrosion rate is noticeably faster at higher temperature (150 ºC) as shown by Figure 4-1 and can be attributed to the faster kinetics and development of a more compact corrosion product layer, as will be discussed later, however it may also be partly attributed to an increase in the bulk pH. At 150 ºC after 6 h there is a considerable amount of corrosion product (0.1 g) on the X65 steel surface based on mass gain measurements in Figure 4-2. Figure 4-2 shows that the corrosion product mass on the steel surface remains relatively constant throughout the duration of the experiment at 150 ºC, demonstrating that the majority of precipitation occurs within the first 6 h. Such observations highlight that the precipitation is much more rapid at 150 ºC, but also that the corrosion rate of 9.8 mm/year is not an accurate reflection of the corrosion rate for X65 in the absence of a protective corrosion product film; i.e. the corrosion rate under these conditions is under-estimated.

The film formed at 150 ºC in the presence of Ca^{2+} resulted in a final corrosion rate of 0.5 mm/year for the underlying steel which is similar to the 0.6 mm/year recorded in the 3 wt.% NaCl solution. The kinetics of corrosion product formation were rapid and indistinguishable at 150 ºC in both the presence and absence of Ca^{2+}. However, the mass of corrosion product on the steel surface when Ca^{2+} was present in the brine was half that of the layer generated in the pure NaCl solution, yet offered similar levels of protection towards general corrosion. The low corrosion rate after 96 h of exposure at 150 ºC may once again be partly attributed to an increase in the bulk pH of the solution brine. However in both the presence and absence of calcium ions at 150 ºC there was a rapid reduction in the corrosion rate.

The precipitation of a new crystalline entity such as $FeCO_3$ from a brine solution starts through the nucleation process. The nucleation process is a series of atomic processes by which the atoms rearrange into a cluster of the product phase large enough as to have the ability to grow irreversibly to a larger size (116). The driving force required for nucleation and growth of crystals is known to be the supersaturation as discussed in Chapter 2. The mechanism of $FeCO_3$ formation was discussed in Chapter 2, however other mechanisms have been proposed in the past. It has been proposed that at a low bulk pH (pH ~ 4) the

carbonate ion is a minority species by which case the bicarbonate ion is regarded as the precipitable ion (117, 118) and $FeCO_3$ precipitates according to Equation 7.1.

$$Fe^{2+} + HCO_3^- \leftrightarrow FeCO_3 + H^+ \quad (7.1)$$

Mora and Turgoose proposed a different mechanism for $FeCO_3$ formation (117, 118) (Equation 7.2).

$$\mathrm{Fe} + H_2CO_3 \leftrightarrow FeCO_3 + 2H^+ + 2e^- \quad (7.2)$$

However crystals grow due to a series of processes by which an atom or a molecule is incorporated into the surface of a crystal. There is transport of atoms through the solution and attachment to the surface. This is followed by movement of atoms on the surface and further attachment of atoms (116). These processes are dependent upon the level of supersaturation which explains why crystals grow with increasing exposure periods and grow even further at higher temperatures. The top view SEM image of the steel surface at 150 ºC after 6 h, shown in Figure 4-14(a) can be contrasted with those on the carbon steel surface at 80 ºC after the same exposure period in Figure 4-9(a). At 150 ºC, a 10-15 µm thick film has already developed compared to no protective film formation at the lower temperature, as shown by Figure 4-15(b). After 96 h exposure to the test solution at 150 ºC, there is no significant change in the corrosion product thickness which is representative of all cross-sections examined between 6 and 96 h or mass in Figure 4-2. However, the crystal grain size has increased dramatically based on the top view images in Figure 4-14. Given that the mass of corrosion product remains stable throughout the entire test, yet the crystal size increases, this perhaps indicates that some crystals are growing on the surface at the expense of others.

The corrosion product present at 150 ºC after 96 h offers superior protection to the steel substrate compared to that formed at 80 ºC after the same exposure time. However, after 4 days of immersion in the test solution the corrosion product layer formed at 150 ºC possesses half the mass and half the thickness of the film precipitated at 80 ºC, which corresponds to approximately the same average film porosity in both experiments, yet the film formed at 150 ºC is substantially more protective. Figure 4-11 and Figure 4-16 show the XRD patterns of corrosion products at 80 and 150 ºC respectively in the absence of

Ca^{2+} as a function of time, highlighting that both corrosion products possess the same composition (purely $FeCO_3$) and that the difference in protectiveness is not attributed to different film chemistries in this instance.

At 150 ºC, $Fe_xCa_yCO_3$ crystals and $CaCO_3$ crystals were evident on the steel surface after 6 h of exposure as shown by Figure 4-37(a). However, unlike the calcium-rich crystals that had precipitated at 80 ˚C after 96 h, these appeared to be embedded within the mixed iron-calcium layer, although it is not clear as to whether these crystals were in contact with the steel substrate. The corrosion film formed at 150 ºC with 1.83 wt.% Ca^{2+} after 96 h, shown by Figure 4-38(b) is more compact and protective than that formed in the pure NaCl solution at the same temperature, as illustrated by Figure 4-15(b), although not as uniform in thickness. This indicates that the uniformity of coverage is affected by the presence of Ca^{2+} in the brine.

The XRD results at 150 ˚C within Figure 4-39 confirmed that both $Fe_xCa_yCO_3$ and $CaCO_3$ were present on the steel surface within the first 6 h of exposure to the 1.83 wt.% Ca^{2+} solution and remained present throughout the 4 day experiment. Table 4-7 shows that at 150 ˚C (unlike 80 ˚C) the mole fraction of Ca remains constant with time. However due to extremely fast kinetics at 150 ˚C most of the corrosion product had precipitated within the first 6 hours of exposure and ceased to continue developing which meant that mole fraction determined at 6, 24, 48 and 96 hours of exposure were in fact the same corrosion product as indicated by Figure 4-23. Figure 4-40 shows an EDX line scan of the corrosion product layer formed in the presence of Ca^{2+} at 150 ºC. At 150 ºC, the opposite trend is observed as compared to the observations made at 80 ºC. The Ca concentration reduces closer towards the steel surface. This can be attributed to the extremely fast corrosion product precipitation and steel dissolution rates at 150 ºC. Precipitation of a calcium rich corrosion product occurs first, however as the steel surface recedes due to dissolution, an iron rich corrosion product starts to precipitate at the interface between the steel surface and the calcium rich corrosion product layer. This is supported by a horizontal line across the corrosion product layer indicating a duplex layered corrosion product where both layers consist of $Fe_xCa_yCO_3$. The growth mechanism of $Fe_xCa_yCO_3$ at 150 ºC is illustrated by the schematics in Figure 7-3.

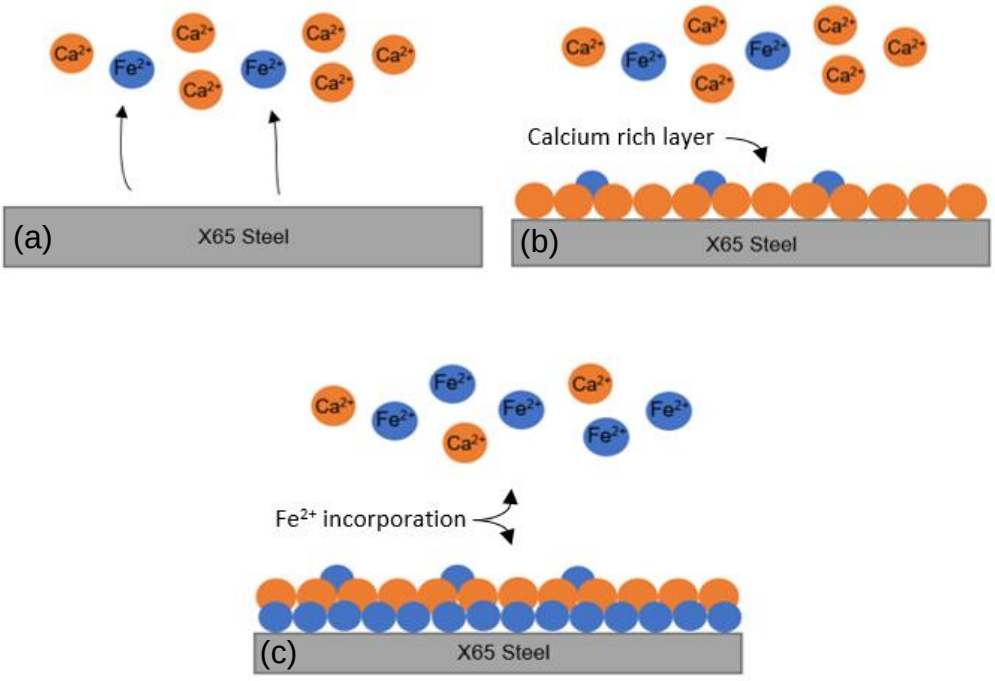

Figure 7-3 Growth mechanism of $Fe_xCa_yCO_3$ corrosion product at 150ºC

7.2.3 Role of Corrosion Product Characteristics on Localised Corrosion Behaviour at 80 ºC

Figure 4-17 and Figure 4-42 show the maximum pit depth as a function of exposure time for X65 carbon steel exposed to 80 ºC in the absence and presence of 1.83 wt.% Ca^{2+} respectively. The maximum pit depth recorded across both conditions indicate that the maximum pit depth increases with increasing exposure time up to maximum pit depths of 46 µm and 51 µm in the absence and presence of calcium ions respectively after 96 hours of exposure. Figure 4-18 and Figure 4-43 relate to experiments at 80 ºC and make for an interesting comparison. As previously mentioned, the pit depth relative to the corroding surface increases steadily in both the presence and absence of Ca^{2+}, with no discernible difference being evident between the two, suggesting that Ca^{2+} does not influence the pitting kinetics in this environment. However, there is a difference in the level of uniform thickness loss between the two experiments as a function of time towards the latter stages of each test, with the rate of thickness loss reducing more significantly in the absence of Ca^{2+} due to the more protective nature of the film formed. When considering the combined effect of uniform thickness loss and pit depth relative to the corroded surface, a total penetration depth can be quantified, and here lies a distinction between the specimens exposed to each environment. The higher uniform thickness loss in

the presence of Ca^{2+} towards the end of the experiments creates a more discernible difference between the two total penetration depths in Figure 4-18 and Figure 4-43. It could be argued that the higher uniform thickness loss in the presence of Ca^{2+} somewhat masks the true pit growth kinetics as the area surrounding the pits are receding at a comparatively substantial rate. As an example, the uniform thickness loss comprises over 40% of the total penetration depth after 96 h in the presence of Ca^{2+}. These results lead to the conclusion that Ca^{2+} does appear to promote pit growth in the 80 ^{o}C environment, however, this is overshadowed somewhat by the ion's additional effect of maintaining a higher uniform corrosion rate due to the establishment of a less protective corrosion product layer compared to the environment in the absence of Ca^{2+}.

In addition to accentuating the pitting kinetics at 80 ^{o}C, the presence of Ca^{2+} influences the topography of the corroded surface at the end of the experiment and the morphology of the form of attack. Figure 4-19, Figure 4-22, Figure 4-44 and Figure 4-47 illustrate the surface characteristics of the carbon steel surfaces after removal of the corrosion product using surface profilometry. The addition of Ca^{2+} changes the topography significantly and the form of attack changes from a very non-uniform/locally corroded surface, to one with clearly distinguishable micro-pits. Esmaeely *et al* (119) reported that the presence of Ca^{2+} can cause localised corrosion however without proposing a mechanism of action. As previously discussed, the presence of calcium ions within the bulk solution has a major influence on the characteristics and chemical composition of corrosion products where the presence of 1.83 wt.% $CaCl_2 \cdot 2H_2O$ results in the precipitation of a $Fe_xCa_yCO_3$ corrosion product layer rather than $FeCO_3$. The morphology of the $Fe_xCa_yCO_3$ layer is more globular in structure in comparison to the $FeCO_3$ layer formed in the absence of calcium ions, resulting in a layer which is visually more porous as indicated by SEM images in Figure 4-9 and Figure 4-32. This may cause corrosive species within the electrolyte to permeate through pores which results in localised corrosion attack. This suggests that Ca^{2+} promotes localised corrosion indirectly through the establishment of corrosion product layers consisting of more globular and therefore more porous crystal grains as demonstrated by the schematic diagrams in Figure 7-4. Figure 4-12 and Figure 4-13 confirmed the presence of corrosion products within pits which indicated

that these were non-protective films which enabled pits to further grow at greater rates (relative to entire surface).

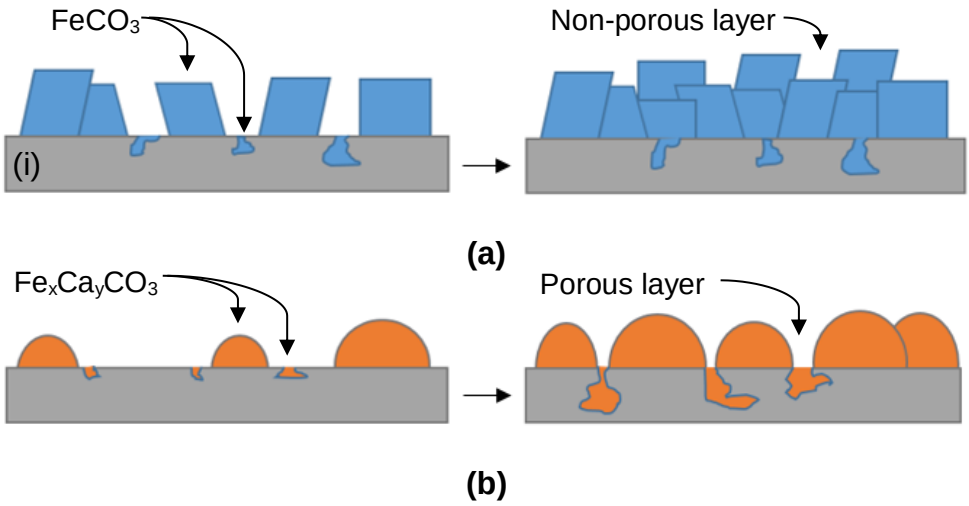

Figure 7-4 Schematic diagrams of mechanisms for (a) $FeCO_3$ and (b) $Fe_xCa_yCO_3$ corrosion product growth and localised attack initiation and growth at 80 ºC

The influence of Ca^{2+} ions on the corrosion behaviour at 80 ºC was further evaluated at a range of Ca^{2+} concentrations at a maintained chloride content. In addition to the discussed tests at 5000 ppm Ca^{2+} (1.83wt.% Ca^{2+}), tests were conducted at concentrations of 50, 100, 250, 500, 1000 and 2500 ppm of Ca^{2+}, as illustrated by Table 3-2 at a fixed exposure period of 48 hours. Figure 4-48 shows top-view SEM images of X65 carbon steel surfaces exposed to Ca^{2+} concentrations ranging from 0 to 5000 ppm after 48 hours of exposure. The SEM images indicate corrosion product precipitation at all concentrations however with varying crystal grains sizes, surface coverage and morphology. The crystal grain size was greater in the presence of Ca^{2+} however no apparent link between the Ca^{2+} concentration within the bulk solution and the crystal grain size was observed. The crystal grain size increased even in the presence of small concentrations of Ca^{2+} (50 ppm) from approximately 10 µm to 20 µm, however at 250 ppm the crystal grain size reduced to approximately 15 µm. The largest crystal grain size was observed at 5000 ppm (approximately 30 µm) which meant that although there was no apparent link between the concentration of Ca^{2+} and crystal grain size, the crystal grain size was always greater in the presence of Ca^{2+}.

Figure 4-48 also indicates that the surface coverage of corrosion products was poor in the presence of calcium ions and remained relatively poor at Ca^{2+} concentrations of up to 250 ppm. However at 500 ppm, the surface coverage had improved dramatically however pores in between the crystal grains were visually apparent even from top-view SEM imaging. At a Ca^{2+} concentration of 1000 ppm the surface coverage had worsened where the steel substrate was visible on some areas of the surface. The surface coverage dramatically improved once again at 2500 ppm where there appeared to have been greater nucleation of crystals onto the steel surface. As previously discussed, the surface coverage on the steel specimen exposed to the 5000 ppm Ca^{2+} brine was also poor where the steel substrate could also be observed through top-view SEM images. The morphology of the corrosion product crystals which had precipitated onto the steel surfaces varied with the Ca^{2+} concentration within the bulk solution. In the absence of Ca^{2+} (3 wt.% NaCl), the crystals where cubic. With increasing Ca^{2+} concentrations within the bulk solution a vertex within the cubic crystals had become sphered. This behaviour can be observed at Ca^{2+} concentrations ranging from 50 to 500 ppm. At concentrations of 1000 and 2500 ppm the entire crystals had become more spherical. At 5000 ppm the crystals are extremely globular which has improved the interconnectivity of crystals which is of extreme importance in terms of the protectiveness that they can provide. It is apparent that single crystals are bounding together to form aggregates which makes it difficult to separate what once used to be a single crystal from another due to the lack of crystal grain boundaries. However as the surface coverage is poor after 48 h of exposure, it results in a porous corrosion product layer. This behaviour is schematically illustrated by Figure 7-5.

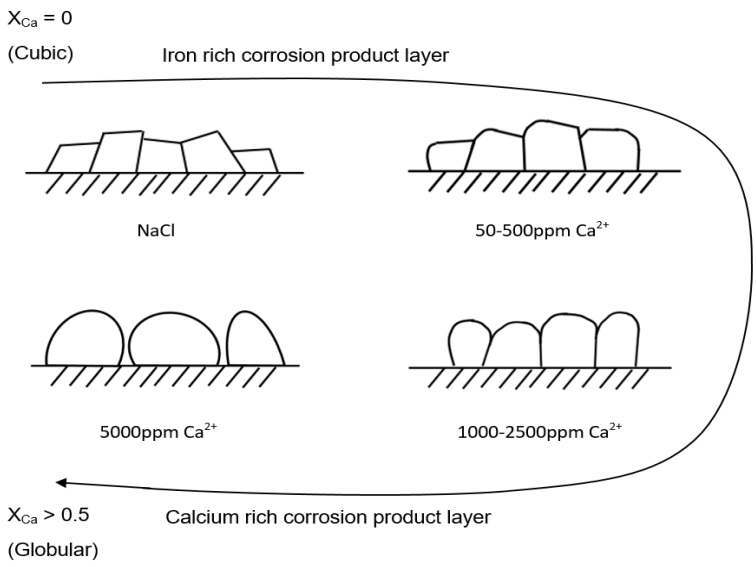

Figure 7-5 Cross-sectional schematic diagrams of corrosion product layers after precipitation in brines containing pure NaCl and varying concentrations of Ca^{2+}

The change in crystal grain size and morphology in the presence of calcium ions can be attributed to the greater ionic radius of calcium, and as a result of calcium incorporation into the crystal lattice of $FeCO_3$, it therefore results in larger unit cells and a greater spacing between planes of atoms. This results in an overall increase in the crystal grain size, however it also results in an overall change in the three-dimensional structure of the crystal lattice which influences the morphology of the crystals which precipitate. This is illustrated by Figure 4-29 which indicates the greater ionic radius of calcium as compared to iron.

X-ray diffraction was used to determine the composition of the corrosion products which had precipitated in tests conducted at varying Ca^{2+} concentrations. Figure 4-49 shows the main [104] peaks for iron carbonate and iron-calcium carbonate at bulk solution Ca^{2+} concentrations ranging from 0 to 5000 ppm, where there is a clear link between the intensity/position of the [104] peaks and the Ca^{2+} concentration within the bulk solution. The intensity and position reduce and decrease respectively with increasing Ca^{2+} concentrations within the brines. The positions of the [104] peaks were used in conjunction with Equation (4.7) to determine the molar fractions of calcium and iron within the corrosion products and thereby evaluate the incorporation of calcium within iron carbonate corrosion products. Figure 4-50 illustrates the relationship between the calculated mole fraction of calcium within the corrosion products and the Ca^{2+} concentration within the bulk solution. The results indicate that the mole fraction of calcium

within the corrosion product increases with increasing Ca^{2+} within the bulk solution. Table 4-9 provides a summary of these findings. The calculated molar fractions of calcium and iron indicate that the corrosion product remains iron rich at Ca^{2+} concentrations within the bulk of up to 2500 ppm. However at 5000 ppm, the corrosion product is calcium rich with a molar fraction of calcium (X_{Ca}) of 0.57.

Referring back to Figure 4-48, it was previously mentioned that corrosion product crystals were more spherical after 48 hours of exposure to brines containing Ca^{2+} and that at 5000 ppm the crystals had become globular. With the XRD calculations indicating that greater Ca^{2+} concentrations within the bulk lead to greater incorporation of calcium within the corrosion product layer, it is clear that the corrosion product crystals only completely lose their description as cubic or somewhat cubic when the corrosion product consists of mainly calcium (calcium rich) rather than iron. The resulting globular corrosion product layer which precipitates due to incorporation of Ca^{2+} can then result in more severe localised attacks according to the mechanism proposed in Figure 7-4.

7.2.4 Role of Corrosion Product Characteristics on Localised Corrosion Behaviour at 150 ºC

Figure 4-20 and Figure 4-45 indicate that at 150 ºC in both the absence and presence of 1.83 wt.% Ca^{2+}, pits had developed within the first 6 hours of exposure. The recorded maximum pit depths were therefore fairly constant with increasing exposure time and were found to be approximately 26.6 and 29.5 µm in the absence and presence of Ca^{2+} respectively. As previously discussed, the uniform corrosion rate was significantly lower at 150 ºC and the precipitated corrosion products appeared to be more protective. As a result of these observations a greater pitting tendency was expected at the elevated temperature. And, as previously mentioned the presence of Ca^{2+} also resulted in greater maximum pit depths. This meant that not only was the pitting tendency greater at 150 ºC but it was also greater in the presence of calcium ions. The localised to uniform corrosion rate ratios (pitting tendencies) after 96 hours of exposure at 150 ºC were found to be 4 and 5.4.

Referring back to the total penetration plots, Figure 4-21 and Figure 4-46 relate to experiments performed at 150 ºC in the absence and presence of Ca^{2+} respectively. Across all time periods, there is no significant difference between either the uniform thickness, localised/pit depth relative to the corroding surface,

and the total penetration depth. The kinetics of pit initiation and propagation at 150 ºC are significantly quicker than at 80 ºC, with a pit penetration depth reaching in excess of 30 µm after only 6 h in both 150 ºC environments. This depth is twice that of the values obtained at 80ºC after the same time period. However, unlike the experiments at 80 ºC, pit propagation completely ceases after 6 h at 150 ºC, regardless of the presence of Ca^{2+}. The highly protective nature of both films formed at 150 ºC completely prevents pit propagation and also minimises the extent of general corrosion. These results indicate that protective film formation is possible in the presence of Ca^{2+} containing brines and that $Fe_xCa_yCO_3$ layers can offer just as much protection to steel surfaces as $FeCO_3$ when formed at higher temperatures (150 ºC). This is true not only from the perspective of general corrosion, but also localised corrosion. Profilometry images of the steel surface after exposure to the 150 ºC brines for 96 hours are provided in Figure 4-22 and Figure 4-47 after removal of corrosion products in the absence and presence of Ca^{2+} ions. The images show clear pits in both conditions which have developed within the first 6 hours of exposure and then completely ceased due to the establishment of protective corrosion product layers. The extremely protective nature of these corrosion product layers can be attributed to several factors such as temperature, CO_2 partial pressure and pH. The higher test temperature (150ºC) was associated with a higher CO_2 partial pressure (1.5 bar) relative to tests conducted at 80ºC which would have further reduced the solubility of both $FeCO_3$ and $CaCO_3$. However increasing temperature also results in an increase in the rates of chemical and electrochemical reactions as well as the rate of transport of species, therefore resulting in greater corrosion rates prior to corrosion product precipitation. Theoretically this suggests that the bulk solution pH would have been evolving at a substantially faster rate at 150ºC due to an increase in the flux of Fe^{2+} from the corroding steel surface. This would have caused a further reduction in the solubility of both $FeCO_3$ and $CaCO_3$ which further accelerates precipitation and growth of corrosion products, due to the reduction in the Fe^{2+} and CO_3^{2-} concentrations required to reach saturation.

7.3 Corrosion Inhibitor Performance Evaluation on Wet-Ground X65 Carbon Steel

A comprehensive review of existing literature on performance evaluation of corrosion inhibitors (provided in Chapter 2) revealed that corrosion inhibitors are mainly performance tested with respect to their capability to retard uniform corrosion (24, 26, 96-99, 101, 102). However the evaluation of corrosion inhibitors to suppress localised corrosion is of extreme importance as it may have an influence on the determination of the optimum dosage. This sub-chapter aims to emphasise the importance of localised corrosion evaluation in the context of performance evaluation of corrosion inhibitors.

7.3.1 Importance of Localised Corrosion Behaviour Consideration on Determination of Optimum Inhibitor Dosage

The reciprocal of R_p and OCP as determined by electrochemical measurements for different inhibitor concentrations ranging from 0 to 40 ppm are presented in Figure 5-2 as a function of time over 48 h. The reciprocal of R_p shows that in the absence of the imidazoline corrosion inhibitor the corrosion rate remains stable throughout the duration of the experiment. The corrosion inhibitor was injected after 2 h of pre-corrosion and even with relatively small dosages of 10 and 20 ppm there was a subsequent response in the form of a reduction in the corrosion rate, with $\frac{1}{R_p}$ reducing from 0.017 and 0.015 $ohm^{-1}cm^{-2}$ to 0.007 and 0.004 $ohm^{-1}cm^{-2}$ as shown by Figure 5-2 (a) and an increase in the OCP from -690 mV to -650 and -625 mV at 10 and 20 ppm respectively after 48 h, as illustrated by Figure 5-2 (b). However at an inhibitor concentration of 30 ppm, $\frac{1}{R_p}$ exhibited a faster decline to a significantly lower value of 0.0003 $ohm^{-1}cm^{-2}$. In terms of OCP, two ‘waves’ of OCP increase could be observed where the potential increases initially to -635 mV and stabilises for 6 hours before increasing at a slower rate to a maximum value of -600 mV. Such behaviour could theoretically indicate two stages of adsorption/interaction of the inhibitor with the steel surface.

At inhibitor concentrations of 40 ppm and above, the corrosion response with time was very similar, where the reciprocal of polarisation resistance decreased to values greater than at an inhibitor concentration of 30 ppm, indicating less effective inhibition of general corrosion as shown by Figure 5-2 and Figure 5-3

(a). However the rate of reduction in $\frac{1}{R_p}$ was greater at higher inhibitor concentration within the first 6 h, indicating faster initial adsorption, despite being less effective.

The bulk solution pH was measured as a function of time, shown by Figure 5-4 and the initial bulk solution pH was found to be 4 and increased with time to approximately 5.5 in the absence of the imidazoline corrosion inhibitor. The addition of the imidazoline corrosion inhibitor led to a reduction in the extent to which the bulk pH increased, with the most significant suppression being observed at a concentration of 30 ppm where the final pH was 4.8. At concentrations above 30 ppm (i.e. 40 ppm) the final pH was still lower than that in the blank condition, but higher than that recorded at 30 ppm. These results are consistent in terms of the ranking of the corrosion rate based on the electrochemical measurements in Figure 5-2 and Figure 5-3 (a).

Ex-situ scanning electron microscopy (SEM) analysis of the surfaces exposed to varying inhibitor concentration are provided in Figure 5-6. Figure 5-6 revealed that the X65 carbon steel had been substantially corroded in the absence of the imidazoline corrosion inhibitor based on visual observations. However, no corrosion products appeared to have precipitated onto the steel surface under the experimental conditions within the 48 h experimental period, as shown by Figure 5-6 (a). In the presence of 10 ppm of the corrosion inhibitor, two distinctive areas where observed on the steel surface. One of the areas appeared to be rougher and more severely corroded, analogous to that of the uninhibited sample. Such behaviour could be attributed to heterogeneous inhibitor adsorption onto the steel surface which enabled protection by inhibitor film formation only in certain areas and not on the entire steel surface, as illustrated by Figure 5-6 (b). At inhibitor concentrations of 30 ppm and above, Figure 5-6 (c and d) indicate that the steel surface is much smoother with very little corrosion haven taken place on the surface, suggesting that at concentrations of 30 ppm or above, improved protection of the carbon steel surface was provided, consistent with results gathered by electrochemical measurements.

The carbon steel surfaces were analysed post-test using NPFLEX surface profilometry to determine the extent of localised corrosion. Figure 5-7 shows the measured depths after 48 h of exposure at varying inhibitor concentrations which

revealed that the maximum pit depth decreased with increasing inhibitor concentration up to a concentration of 40 ppm and then started to increase with any further increase in the inhibitor concentration. The maximum pit depth was approximately 26 µm, recorded in the absence of the inhibitor and reached a minimum value of 1.7 µm at an inhibitor concentration of 40 ppm. The reduction in maximum pit depth was calculated as a localised inhibitor efficiency for each inhibitor concentration and compared to the uniform inhibitor efficiency in Figure 5-8. The results indicate that the inhibitor is the most efficient in terms of the localised corrosion behaviour at 40 ppm, however, it is determined to be the most efficient in terms of uniform corrosion behaviour at 30 ppm. The important aspect to note here is that at an inhibitor concentration of 30 ppm, the localised corrosion inhibitor efficiency is only 12.7% whereas at 40 ppm the uniform and localised efficiencies are 89 and 93% respectively which when combined is greater than at any other inhibitor concentration, as shown by Figure 7-6. This means that if the optimum inhibitor concentration is selected based purely on the uniform corrosion behaviour then localised corrosion attacks will not be sufficiently supressed. The extent of localised corrosion at 30 and 40 ppm can be seen in Figure 5-12 and Figure 5-13 where areas of localised corrosion can be seen at 30 ppm however no clear pits can be identified at an inhibitor concentration of 40 ppm. This is believed to be due to the initially faster rate of adsorption of the inhibitor at concentrations above 30 ppm, where faster adsorption of the inhibitor limits pit initiation during the initial hours of the 48 hour tests. However the faster initial rates of adsorption at concentrations above 30 ppm also result in less uniform coverage of the corrosion inhibitor which causes a slight reduction in the uniform corrosion efficiency of the inhibitor as shown by Figure 7-6.

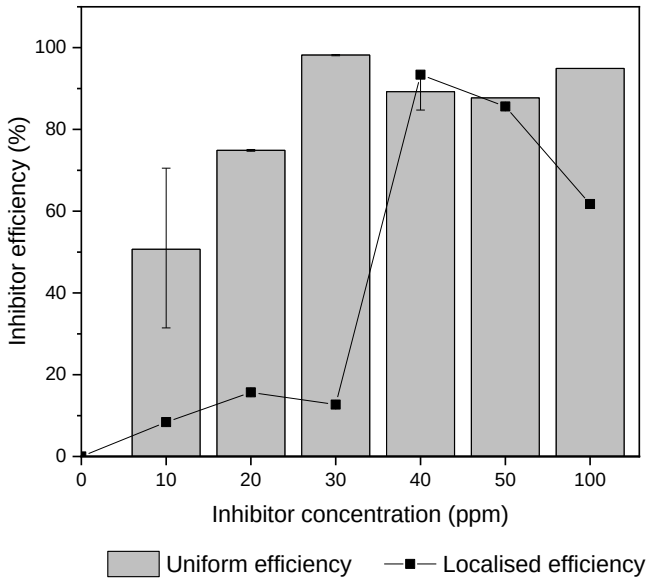

Figure 7-6 Uniform and localised corrosion inhibitor efficiencies at inhibitor concentrations ranging from 0 to 100 ppm after exposure for 48 h at 80 ºC with a 2 h pre-corrosion period

Analysis of the localised corrosion behaviour concluded that the determination of the optimum inhibitor concentration can be influenced when localised corrosion behaviour is taken into consideration and that in the present case, the optimum inhibitor concentration appeared to be 30 ppm upon consideration of the general corrosion response. However, after analysing the localised corrosion behaviour, 40 ppm was found to be the optimum inhibitor concentration. Palmer *et al* (96) determined that once a pit has developed, extremely high inhibitor dosages are required to reduce pit growth and concluded that performance testing of corrosion inhibitors with respect to the localised corrosion behaviour should be an integral part of any inhibitor selection programme and that corrosion inhibitors which are effective in reducing uniform corrosion rates may not be as effective with respect to the localised corrosion behaviour. The findings presented and discussed within this sub-chapter have emphasised the importance of localised corrosion evaluation in the context of determining the optimum dosage of a corrosion inhibitor.

7.3.2 Ageing of Corrosion Inhibitor and Interaction with Surface

The imidazoline corrosion inhibitor was aged for 24, 48 and 120 h at 80 ºC before being tested under the same conditions as in the initial study. The results in Figure 5-21 indicate that the reciprocal of the polarisation resistance decreased at a greater rate and reached a lower value when aged for a maximum time of

48 h at 80 ºC, suggesting that the imidazoline compound had partially converted into a product which resulted in improved performance, consistent with the findings of Jenkins (81) who observed similar behaviour at an aging temperature of 100 ºC. However aging of the imidazoline compound in this study for 120 h led to changes in chemistry which led to a reduction in the performance, resulting in a greater reciprocal of polarisation resistance and reduction in the OCP at the end of the 48 h experiment.

pH measurements recorded during the performance tests of the aged imidazoline compounds in Figure 5-22 revealed that the bulk pH was initially higher for the aged products however changed less with time with increasing aging time for inhibitors aged for 24 and 48 h. As a result the final pH was lower for product aged for 24 and 48 h however significantly greater for the imidazoline product aged for 120 h which confirmed that less iron ions had been released to the bulk in the performance tests of imidazoline products aged for 24 and 48 h due to their improved performance. Further analysis of the steel surfaces after the performance tests using SEM in Figure 5-23 confirmed that the carbon steel specimens exposed to the 24 and 48 h aged imidazoline compound had experienced very little corrosion, where the surfaces were very smooth in comparison to the non-aged compound. The specimen exposed to the 48 h aged product had the least damage with grinding marks still visible across the whole specimen as shown by Figure 5-23 (c), whereas the carbon steel specimen exposed to the 120 h aged imidazoline product appeared to be more corroded with a visually rougher surface which was consistent with the previously discussed results.

Analysis of the end-point and integrated efficiencies of the aged inhibitors in Figure 5-24 showed that the inhibitor efficiency increased from 86.2 and 93.3% to 94.7 and 98.5% for end-point and integrated efficiencies respectively for the 48 h aged imidazoline compound. However with 120 h of aging time, the efficiencies decreased to 74.8 and 92.9% for end-point and integrated efficiencies, respectively. The integrated efficiencies were greater than the end-point efficiencies for all inhibitors due to fast rate of reduction of the reciprocal R_p, as previously indicated by Figure 5-21. However, although aging of the corrosion inhibitor for 24 and 48 h led to improved performance with respect to the uniform corrosion behaviour, the same was not observed with respect to the

localised corrosion behaviour as shown by Figure 5-25. Figure 5-26 indicated that increasing the inhibitor aging time at 80 ºC resulted in the formation of deeper pits on the steel surface which led to a decrease in the localised inhibitor efficiency from 95.4% to 94.5, 94.2 and 86.1% for products aged for 24, 48 and 120 h, respectively. Since localised corrosion accounts for the majority of oil and gas pipeline failures, the results suggest that imidazoline compounds aged for more than 48 h at 80 ºC can promote failure due to insufficient protection against localised corrosion.

Figure 7-7 shows the chemical structure of a typical imidazoline based corrosion inhibitor which consists of three main parts; a hydrophilic imidazoline five membered ring (head), a hydrophobic tail consisting of a hydrocarbon chain and an amine side chain (pendant) (120-123). The primary protection/adsorption of an imidazoline corrosion inhibitor has been reported to be through bonding of the five membered nitrogen ring however the amine side chain is also known to provide protection by itself. The chemical breakdown of an imidazoline based compound results in breakdown into its amine precursor as shown by Figure 7-7, which can result in improved corrosion protection. However amine compounds are known to be more water soluble and therefore more susceptible to hydrolysis which is beneficial in terms of the synthesis of more environmentally acceptable corrosion inhibitors however not beneficial in terms of being persistent corrosion inhibiting compounds (123, 124). As a result, high temperature exposure of imidazoline based compounds results in hydrolysis which results in a reduction in protection against corrosion.

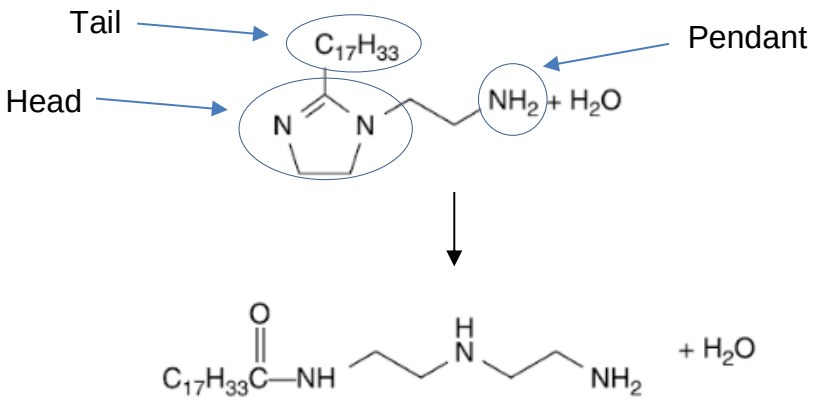

Figure 7-7 Chemical breakdown of imidazoline into amine precursor

The imidazoline corrosion inhibitor was aged at 120 ºC for 2, 6 and 24 h and then performance tested at 80 ºC. Contrary to the corrosion behaviour observed with imidazoline products aged at 80 ºC, all the aged products at 120 ºC deteriorated in performance where the stabilised reciprocal of R_p increased with increasing inhibitor aging time at 120 ºC, as shown by Figure 5-27. Aging at 120 ºC also resulted in an increase in the OCP which suggested that the aging of the inhibitor at 120 ºC had led to hydrolysis of the compound which resulted in the degradation of the corrosion inhibitor. These finding were consistent with those of Ding *et al* (98) who observed a 40-50% loss of the corrosion inhibitor due to hydrolysis when tested at 120 and 150 ºC. These findings indicate that greater inhibitor concentrations are required in such conditions in order to compensate for inhibitor loss caused by hydrolysis.

pH measurements of the imidazoline corrosion inhibitor aged at 120 ºC in Figure 5-28 revealed that aging the inhibitor at 120 ºC had resulted in an increase in the bulk pH of the brine solution. The pH for all of the aged products remained higher than that of the non-aged inhibitor containing brine solution. The final pH of the aged inhibitors also increased in order with increasing final reciprocal R_p after 48 h of exposure. Analysis of the carbon steel specimens exposed to brine solutions containing the aged imidazoline corrosion inhibitors was carried out using the SEM. Figure 5-29 indicated that all the specimens had two distinct areas, where one was more heavily corroded than the other indicating slower adsorption of the inhibitor molecules onto certain areas. In all cases the lightly corroded areas corresponded to the majority of the specimen surface area and the heavily corroded zones where the minority. All specimens exposed to aged inhibitors contained a more severely corroded area which had been more severely corroded than the heavily corroded area of the specimen exposed to the non-aged imidazoline corrosion inhibitor. The SEM top-view images also revealed that the conditions of both the light and heavy corroded zones worsened with increasing corrosion inhibitor aging time at 120 ºC, where the surface appears to have become rougher with increasing aging time.

Inhibitor efficiency calculations of the 120 ˚C aged inhibitors presented in Figure 5-30 revealed that the inhibitor efficiency with respect to uniform corrosion decreased at a much more significant rate with increasing aging time as compared to the reduction in efficiency of inhibitors aged at 80 ºC which is due

to increased rate of hydrolysis associated with increasing temperature which resulted in further degradation of the corrosion inhibitor. The end-point and integrated inhibitor efficiencies decreased from 86.2 and 93.6% to 62.4 and 86.6% respectively for the imidazoline inhibitor aged for 24 h. Nonetheless the decrease in inhibitor performance with respect to the general corrosion behaviour was also associated with large drop in performance with respect to the localised corrosion behaviour as shown by Figure 5-31 and Figure 5-32. The localised corrosion inhibitor efficiency was reduced from 95.4 to 73.2% for the imidazoline inhibitor aged for 24 h at 120 ºC. The greater localised corrosion attacks observed for compounds aged at 120 ºC are believed to be due to the slower rates of adsorption onto certain areas of the steel specimens as previously discussed and observed by Figure 5-29, resulting in both greater uniform and localised corrosion attacks before the inhibitor is able to adsorb onto the unprotected areas. This mechanism is demonstrated by Figure 7-8.

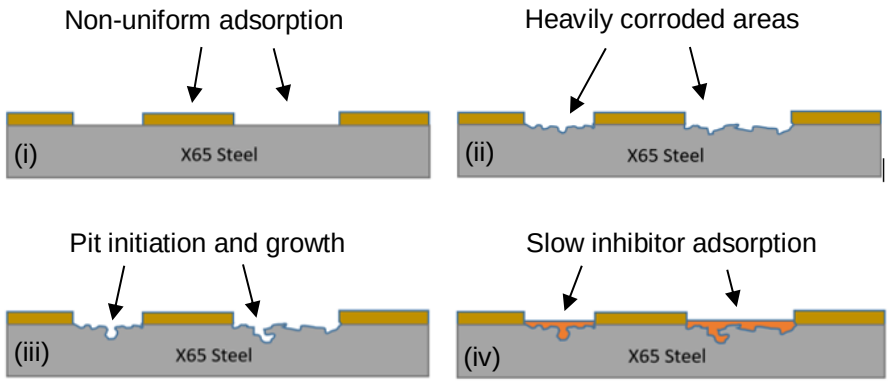

Figure 7-8 Mechanism for localised corrosion attacks in the presence of aged inhibitor compounds

7.4 Interaction between Corrosion Inhibitor and $FeCO_3$ Corrosion Products

Performance evaluation of an imidazoline corrosion inhibitor in the presence of corrosion products (pre-corroded surfaces) can help improve our knowledge of how inhibitors operate, interact, transport and incorporate with/within corrosion products, however existing literature within this area of study is extremely restricted (29-32, 84, 97, 103-106). This sub-chapter aims to present a novel method for testing corrosion inhibitors on corrosion product covered surfaces

which enables more effective comparison of overall inhibitor performance on different corrosion product covered surfaces and the de-coupling of individual contributions provided by the corrosion inhibitor and by the corrosion product.

7.4.1 Partial Coverage $FeCO_3$

Pre-corrosion of X65 steel for 24 h at 80 ºC in an autoclave led to the precipitation of a $FeCO_3$ layer which partially covered the steel surface and offered poor general corrosion protection to the substrate. The corrosion behaviour of the partially covered steel was evaluated using glass cells containing a CO_2-saturated 3 wt.% NaCl solution with and without 30 ppm of the imidazoline corrosion inhibitor to determine the efficiency compared to a wet-ground X65 steel surface, and a 6 h pre-corroded specimen with a Fe_3C rich layer. The reciprocal values of polarisation resistance in the uninhibited system provided in Figure 6-14 showed a decrease as a function of time which is believed to be predominantly as a result of the increase in the bulk solution pH as a result of an increase in iron ions in the bulk solution with time, as shown by Figure 6-15. The reciprocal values of polarisation resistance in the inhibited test showed a relatively slow reduction during the 48 h test, where it decreased from 0.016 to 0.00048 $ohm^{-1}cm^{-2}$ after 48 h of exposure which occurred in conjunction with a positive shift in the open circuit potential from -640 to -600 mV. The rate of reduction in corrosion rate with time for the inhibited test was slower than that of wet-ground X65 steel and the pre-corroded Fe_3C layer. These findings indicate that the presence of a crystalline corrosion product diminishes the adsorption kinetics and hinders formation of the inhibitor film. The bulk solution pH remained lower for the inhibited experiment throughout the duration of the tests due to a reduction in the number of iron ions emitted into the bulk solution as a result of the suppression of the corrosion rate. The end-point efficiency in terms of uniform corrosion was 96% as compared to 92 and 95% for wet-ground X65 and pre-corroded Fe_3C respectively. This indicated that although the adsorption of the corrosion inhibitor was hindered by the crystalline $FeCO_3$ layer, the efficiency in terms of uniform corrosion was comparable after 48 h of exposure.

Examination of the X65 carbon steel surfaces post precipitation in the autoclave in Figure 6-16 (a) and after the glass cell tests with and without the imidazoline corrosion inhibitor in Figure 6-16 (b-c) showed that most of the $FeCO_3$ had dissolved in the uninhibited glass cell tests, however there remained some areas

with individual $FeCO_3$ crystals and minor areas where the $FeCO_3$ crystals had aggregated to form a conglomorate of crystals. In glass cell tests with 30 ppm of the imidazoline corrosion inhibitor, it was confirmed that the inhibitor had led to further dissolution of the $FeCO_3$ corrosion product where neither single crystals or conglomorates of $FeCO_3$ crystals could be visually identified. X-ray diffraction results of the partially $FeCO_3$ covered steel before and after exposure to uninhibited and inhibited glass cell testing in Figure 6-17 confirmed that $FeCO_3$ was present after precipiation in the autoclaves. However, after testing in the uninhibited glass cell experiment, only a small [104] $FeCO_3$ peak was present which confirmed that most of the $FeCO_3$ had dissolved even in the absence of the corrosion inhibitor. In the presence of the corrosion inhibitor there was no longer an $FeCO_3$ peak present which confirmed that the inhibitor had led to further dissolution as suggested by the scanning electon microscopy images in Figure 6-16.

The extent of localised corrosion on the pre-corroded specimens with the partial coverage of $FeCO_3$ were evaluated using non-contact profilometry before and after exposure to uninhibited and inhibited glass cell experiments. Figure 6-18 and Figure 6-19 show the maximum pit depth and profilometry images where the maximum pit depth was 26 µm for the pre-corroded layer prior to glass cell testing and the maximum pit depth was found to have remained fairly stable (25.5 µm) after exposure to the uninhibited glass cell test which was within the experimental error. However after glass cell testing with the corrosion inhibitor, the maximum pit depth had increased to 34 µm resulting in a localised inhibitor efficiency of -19.5% as compared to a uniform end-point efficiency of 96% which further indicates that pre-corrosion can lead to improved uniform corrosion efficiency however this comes at the cost of a dramatic reduction in the localised corrosion efficiency. It should be noted that the provided maximum pit depths are representative of an average taken of the 10 deepest pits taken across 3 different scanned 3×3 mm areas across three different specimens. As a result the error bars represent the range in the maximum pit depth across the scanned areas. Further analysis of the maximum pit depth data indicates that the maximum pit depth was greater on the 24 h pre-corroded X65 steel specimen exposed to the inhibited glass cell test rather than the uninhibited glass cell test which indicated that the corrosion inhibitor had promoted localised corrosion when used on a pre-

corroded partially covered $FeCO_3$ corrosion product as indicated by the negative value of the calculated efficiency.

Results from surface wettability studies conducted on wet-ground steel and $FeCO_3$ covered surfaces in Figure 6-30, Figure 6-32, Figure 6-34 and Figure 6-36 indicated that the imidazoline corrosion inhibitor was able to adsorb onto carbon steel however not onto $FeCO_3$. Using these results in conjunction with findings from SEM, XRD and surface profilometry, a mechanism for the localised corrosion attacks in the presence of partial coverage $FeCO_3$ and the imidazoline corrosion inhibitor can be proposed. It is believed that the previously discussed dissolution of $FeCO_3$ in the presence of the corrosion inhibitor results in un-protected local areas (by corrosion inhibitor) which result in localised corrosion attacks. This is demonstrated by Figure 7-9. These localised corrosion attacks are believed to be initiating faster than the inhibitor can adsorb a protective hydrophobic film onto the un-protected free local surface areas. This results in the corrosion inhibitor indirectly promoting localised corrosion as the remainder of the surface is protected by a protective hydrophobic inhibitor film.

7.4.2 Full Coverage $FeCO_3$

A $FeCO_3$ corrosion product providing significant coverage and protection to the X65 steel specimen was generated in autoclaves after 96 h pre-corrosion. Again, these specimens were transferred to glass cell experiments in uninhibited and inhibited CO_2-saturated 3 wt.% NaCl brines and their corrosion response was assessed using the linear polarisation resistance technique in Figure 6-20. The uninhibited glass cell experiments on the $FeCO_3$ covered steel surfaces indicated that the reciprocal values of polarisation resistance initially started to increase before it started to stabilise and slowly decrease after 20 h of exposure to the uninhibited brine. The increase in the reciprocal values was a possible indication of dissolution of the corrosion product layer which had a subsequent effect of increasing the bulk solution pH in Figure 6-21, which was 5.6 after 24 h of exposure. The progressive increase in pH then led to a slow decline in the corrosion rate. The reciprocal values of polarisation resistance for the fully $FeCO_3$ covered steel surface exposed to the inhibited brine solution was lower than that of the uninhibited glass cell experiment (both at the start and end of the experiment), stabilising faster (within 3 h) at a value of 0.00125 $ohm^{-1}cm^{-2}$ as compared to a maximum value of 0.0035 $ohm^{-1}cm^{-2}$ for the uninhibited glass cell

test. The open circuit potential shifted positively by 40 mV after 48 h of exposure to the inhibited brine solution. The end-point uniform corrosion efficiency was 83% which was significantly lower than the previously discussed uniform corrosion efficiencies observed for wet-ground X65 steel, 6 h pre-corroded X65 and 24 h pre-corroded X65 (92, 95 and 96% respectively) which is due to the presence of a fully developed $FeCO_3$ layer which limits adsorption and formation of an inhibitor film onto the steel surface.

Top-view images from the scanning electron microscope for the $FeCO_3$ covered specimens before and after exposure to the uninhibted and inhibited glass cell tests in Figure 6-22 confirmed that the corrosion product layer had been slowly dissolving in both uninhibited and inhbited glass cell tests. This is due to the fact that the $FeCO_3$ covered surface was tested in an undersaturated brine (with respect to $FeCO_3$). The dissolution led to an increase in both primary and secondary porosity (Intergranular porosity and single crystal porosity respectively) which led to a reduction in corrosion protection offered by the corrosion product layer. The increase in porosity both within and around the $FeCO_3$ crystals shown by Figure 6-22 may also have a been a signifcant factor influencing the localised corrosion behaviour which will be further discussed.

XRD results in Figure 6-23 from the $FeCO_3$ covered steel specimens before and after exposure to the uninhibited and inhibited glass cell environments confirmed that crystalline $FeCO_3$ was still present on the X65 carbon steel surfaces after exposure to both the uninhibited and inhibited glass cell tests. The maximum pit depth was evaluated and compared for the $FeCO_3$ covered X65 specimens before and after exposure to the uninhibited and inhibited glass cell tests in Figure 6-24 and Figure 6-25 using non-contact surface profilometry. The data shows that the maximum pit depth after precipitation of the corrosion product layer in the autoclave was 46 µm which then increased to 51 and 54 µm after exposure to the uninhibited and inhibited glass cell tests respectively. The maximum pit depth was greater after glass cell testing in the inhibited brine as compared to after testing in the uninhibited brine which once again suggests that the use of a corrosion inhibitor in the presence of crystalline corrosion products can promote localised corrosion. The efficiency of the corrosion inhibitor with respect to the localised corrosion behaviour was calculated using Equation (5.3) and was found to be -0.5% which confirmed that the inhibitor did not provide any

protection against localised corrosion and was in fact directly promoting localised corrosion due to the presence of a fully covered and crystalline corrosion product layer on the steel surface. As previously mentioned and observed by Figure 6-22, there was a greater extent of dissolution of the $FeCO_3$ layer in the presence of the corrosion inhibitor causing an increase in both intergranular porosity and single crystal porosity. This is belived to have a direct infleunce on the localised corrosion behaviour and can be explained by the schematic diagrams in Figure 7-9. The schemtic diagrams indicate that dissolution of $FeCO_3$ in the presence of the inhibitor can cause an increase in the overall porosity of the corrosion product layer which may be permeable and cause corrosive species within the electrolyte to permeate through pores which results in localised corrosion attacks. This can occur between individual crystal grains and within single crystals. Existing literature (Chapter 2) suggests that corrosion inhibitors can behave in either a synergistic or antagonistic manner with corrosion product covered surfaces depending on their molecular chemistry. However this has only been confirmed with respect to the uniform corrosion behaviour. The findings in the current study extends the current literature in the context of interaction between corrosion inhibitors with corrosion product covered surfaces by revealing the antagonistic behaviour corrosion inhibitors can have with respect to the localised corrosion behaviour in the presence of $FeCO_3$.

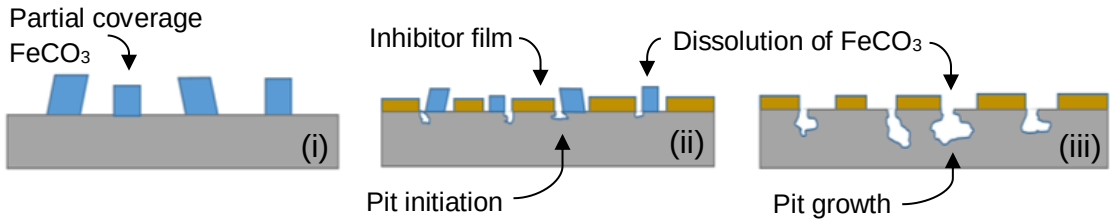

(a)

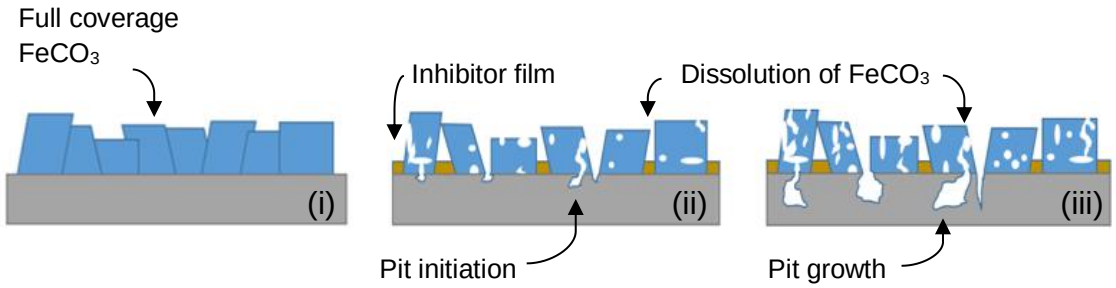

(b)

Figure 7-9 Schematic diagrams illustrating mechanism for localised corrosion attacks on X65 carbon steel in the presence of imidazoline corrosion inhibitor with (a) partial coverage $FeCO_3$ and (b) full coverage $FeCO_3$

A thorough literature review (Chapter 2) indicated that the individual contributions provided by inhibitor and corrosion products towards corrosion protection have never been de-coupled in an attempt to understand the true synergistic/antagonistic interaction between a corrosion inhibitor and a corrosion product (29-32, 84, 97, 103-106). In order to determine the individual protection afforded by the inhibitor and the corrosion products, the efficiency of the corrosion products in relation to protection provided was calculated relative to the corrosion rate of the uninhibited glass cell test of wet-ground X65 steel. These were then subtracted from the total efficiency to estimate the amount of protection afforded by the corrosion inhibitor on pre-corroded X65 specimens. However as previously discussed all corrosion products had undergone some extent of dissolution which meant that the data provided in Figure 6-27 had underestimated the inhibitor contribution towards overall corrosion protection and overestimated the overall corrosion protection afforded by the corrosion products. In spite of this, the data provided does provide an indication as to how the individual contributions of the corrosion product and the inhibitor change with

increasing pre-corrosion time (More protective corrosion product layers). The data shows that similar protection was afforded by the Fe_3C corrosion product layer and the partially covered $FeCO_3$ surface, however the fully covered $FeCO_3$ layer provided 50% more protection and as a result of this the corrosion inhibitor was less effective and only provided 25% of the overall protection.

The uniform and localised corrosion efficiencies were compared in Figure 6-28 for all the pre-corrosion times in order to evaluate the optimum pre-corrosion time for maximum protection against both uniform and localised corrosion. The data indicated that although 24 h of pre-corrosion (partially covered $FeCO_3$) resulted in the highest inhibitor efficiency with respect to uniform corrosion behaviour (96%), the highest set of uniform and localised corrosion efficiencies was for zero hours of pre-corrosion which indicated that the imidazoline corrosion inhibitor provided optimum protection on wet-ground X65 carbon steel. These findings also indicate that the presence of crystalline $FeCO_3$ will always result in severe localised attacks. The present study has contributed to the existing literature by demonstrating not only the influence/presence of corrosion products on the uniform corrosion behaviour but also on the localised corrosion behaviour.

Chapter 8 Conclusions and Recommendations for Future Research

8.1 Conclusions

In solely NaCl based brines, it has been demonstrated that $FeCO_3$ is one of the main corrosion products which can accumulate onto steel surfaces of internal pipelines. Several studies have focused on evaluating the protectiveness of this corrosion product, spanning a wide range of operating and environmental conditions, however very little research has been directed towards the precipitation of mixed iron-calcium carbonates in comparison to other carbonates within the literature. This is surprising given that that the formation of $Fe_xCa_yCO_3$ has been observed in several water treatment plants and oil wells. It has been established that the presence of Ca^{2+} ions can result in the formation of a mixed carbonate scale which appears to influence both the general and localised corrosion behaviour of carbon steel, at least in low pressure environments. However, such characteristics have not been considered at elevated temperatures (beyond 80 ^oC). Consequently, Chapter 4 focuses on the corrosion behaviour of X65 carbon steel, the characteristics of the surface corrosion products and their protective properties at 80 and 150 ^oC in the absence and presence of calcium chloride di-hydrate ($CaCl_2{\cdot}2H_2O$) to enhance understanding of CO_2 corrosion in more complex brine chemistries at elevated temperatures.

As described in Chapter 3, an autoclave capable of *in-situ* electrochemical measurements was developed to aid the study by providing continuous corrosion rate monitoring. The corrosion rate measurements gathered by linear polarisation resistance were validated against corrosion rates obtained by mass loss measurements. The influence of 1.83 wt.% $CaCl_2{\cdot}2H_2O$ on the kinetics/characteristics of corrosion products and on the overall corrosion behaviour was assessed using corrosion rate measurements (LPR and mass loss), scanning electron microscopy (SEM), X-ray diffraction (XRD) and Focused ion beam (FIB). The localised corrosion behaviour was assessed using NPFLEX non-contact surface profilometry. Furthermore, the influence of intermediate $CaCl_2{\cdot}2H_2O$ concentrations on the characteristics/composition and pitting behaviour of $Fe_xCa_yCO_3$ corrosion products was evaluated. The following conclusions could be drawn based on findings from Chapter 4.

- In the presence of Ca^{2+} ions there was a more significant effect on the general corrosion rate at the lower temperature of 80 ºC where the protection afforded by the corrosion product layer was reduced.
- In the absence of calcium ions the corrosion products solely consisted of iron carbonate and in the presence of calcium ions the corrosion products consisted mainly of mixed iron-calcium carbonates however in some cases with co-precipitation of calcium carbonate.
- The addition of calcium ions within the bulk solution resulted in the precipitation of globular structured crystals rather than cubic which resulted in poor corrosion product coverage and increased visual porosity between crystal grains, even after 96 hours exposure at 80 ºC.
- In both the absence and presence of calcium ions the corrosion products which had precipitated at 150 ºC were more compact with improved surface coverage and larger crystal grain sizes even after 6 hours of exposure to the brine solutions.
- XRD based calculations, along with focused ion beam EDX-line scans confirmed that the mixed Ca/Fe carbonates had precipitated with concentration gradients across their depth at both 80 and 150 ºC.
- Greater Ca^{2+} concentrations within the bulk solution resulted in the precipitation of mixed iron-calcium carbonates with greater mole fractions of calcium.
- The extent of localised/pitting corrosion increased through the addition of Ca^{2+} ions indicating that Ca^{2+} plays a role in promoting localised corrosion.
- Corrosion rate measurements determined by linear polarisation resistance were validated against mass loss measurements. The associated error in the corrosion rates determined by electrochemical measurements increased with increasing exposure time at 80 ºC and decreased with increasing exposure time at 150 ºC due to the different precipitation behaviours observed at the two temperatures.

The economic losses attributed to corrosion both directly and indirectly within the oil and gas industry can be exceptionally large, making it paramount to combat corrosion in a cost effective manner. The majority of corrosion inhibitors consist of nitrogen-containing compounds which function by forming a protective film on the steel surface. In order to successfully use corrosion inhibitors in the oil and

gas industry, they must be evaluated thoroughly using laboratory tests before application in the field. Amongst other factors, all inhibitors should be tested for compatibility with the environment, provide sufficient protection against corrosion and most importantly not cause antagonistic effects with other chemicals in the process fluid, which could result in the initiation or accentuation of localised corrosion. In terms of the evaluation of corrosion control only, this requires rigorous corrosion inhibitor testing with respect to both the general and localised corrosion behaviour to ensure both corrosion mechanisms are successfully mitigated.

Chapter 5 focuses on the evaluation of both the general and localised corrosion behaviour of carbon steel in the presence of an imidazoline based corrosion inhibitor and the influence of localised corrosion evaluation on the determination of the optimum inhibitor dosage at 80 °C in CO_2-saturated sodium chloride (NaCl) brines. Chapter 5 also focuses on examining the effects of short term pre-corrosion and inhibitor aging on the overall performance of this specific corrosion inhibitor. Literature suggests that the localised corrosion behaviour has only been considered by a few researchers in the context of corrosion inhibitor performance evaluation. Although some authors have assessed the localised corrosion behaviour when evaluating corrosion inhibitors, it has mostly been done at a fairly low temperature range (25-55 ºC). The purpose of Chapter 5 was to contribute to existing literature by providing a wider range of corrosion inhibitor tests which help evaluate both the general and localised corrosion performance of corrosion inhibitors. The following conclusions could be drawn based on the findings from Chapter 5.

- It was demonstrated that the optimum inhibitor concentration required for suppression of uniform corrosion is significantly lower than that for localised corrosion protection, highlighting the importance of systematic, post-test topographical measurements of the steel surface in the selection and optimisation of inhibitor dose rates.
- Selection of the optimum inhibitor dosage based on solely the uniform corrosion behaviour can result in great protection against uniform corrosion at the cost of severe localised corrosion attacks.
- Short-term pre-corrosion can lead to improved uniform corrosion suppression in the presence of the inhibitor however it will also result in

worsened performance with respect to the localised corrosion behaviour which will ultimately result in the reduction of the corrosion inhibitors overall performance.

- The results show that in the context of uniform corrosion, aging of this corrosion inhibitor may lead to improved or worsened performance depending on the aging temperature and exposure period.
- Inhibitor aging of imidazoline corrosion inhibitors at temperatures below their stability limit can result in improved protection afforded by the inhibitor due to chemical breakdown to their amine precursor.
- Protection against localised corrosion is always compromised when this particular inhibitor is aged above 80 °C, with the performance worsening with increased aging time due to hydrolysis.

Existing literature has shown that the influence of pre-corrosion on inhibition has mainly been evaluated on non-protective crystalline corrosion products or in the presence of Fe_3C with little attention to the performance of corrosion inhibitors with respect to the localised corrosion behaviour. Chapter 6 evaluates the role of pre-corrosion on the performance of an imidazoline corrosion inhibitor with respect to inhibition of uniform and localised corrosion in CO_2 environments at 80 ºC using a two stage testing procedure where pre-corrosion was conducted in autoclaves at 80 ºC and inhibitor testing was conducted in glass cells at 80 ºC. The inhibitor performance was assessed on iron carbide and partially/fully covered iron carbonate ($FeCO_3$) and compared against inhibition on wet-ground X65 carbon steel.

- In terms of uniform corrosion suppression the performance of the imidazoline corrosion inhibitor was improved by up to 4% on partial coverage iron carbonate surfaces.
- All pre-corrosion periods resulted in worsened localised/pitting attacks with the lowest inhibitor efficiency with respect to localised corrosion being observed on partial coverage $FeCO_3$, resulting in a localised inhibitor efficiency of -19.5%.
- Inhibition on crystalline $FeCO_3$ results in the promotion of localised/pitting corrosion.
- Baseline tests conducted under all environmental conditions in the absence of the corrosion inhibitor enabled the estimation of the individual

contributions by the inhibitor and the corrosion products towards overall corrosion protection, which indicated that the protection afforded by the inhibitor was approximately 58% on iron carbide and partial coverage iron carbonate surfaces.

- The individual contribution of the corrosion inhibitor towards overall protection was further reduced to 25% on full coverage iron carbonate surfaces indicating that the presence of iron carbonate has an antagonistic effect on the corrosion inhibitor.

8.2 Recommendations for Future Research

The research findings demonstrated within this thesis provide significant scientific and industrial benefits by expanding the knowledge surrounding mixed carbonates in the form of $Fe_xCa_yCO_3$ and their influence on the overall corrosion behaviour, demonstrating their capability in influencing the localised corrosion behaviour. The research findings have also demonstrated the importance of localised corrosion consideration in the performance evaluation of corrosion inhibitors, where consideration of the localised corrosion behaviour can result in improved overall inhibition as well as cost savings by reducing under and over dosing in real life applications. The research has also demonstrated the antagonistic interaction between corrosion inhibitors and corrosion product layers, where inhibition on wet-ground steel has been found not to be representative of inhibition on pre-corroded steel surfaces and in some cases can result in severe localised corrosion attacks demonstrating the importance of corrosion inhibition in the early stages of corrosion processes. To build on the knowledge obtained from this research, the following recommendations are suggested.

Recommendation 1

At high temperatures the corrosion kinetics are extremely fast resulting in rapid precipitation of corrosion products. In Chapter 4, results have shown that localised corrosion attacks result in pitting corrosion where pits develop within the first 6 hours of exposure to the experimental brines at 150 ºC. This raises the question of whether the pits develop before or during corrosion product precipitation.

Due to the long heat-up and cooling periods experienced with single autoclave systems, it would not be feasible to conduct experiments for durations shorter than 6 hours. However, localised corrosion kinetics at elevated temperatures can be evaluated for experimental tests shorter than 6 hours using twin autoclave systems. A twin autoclave system would enable shorter heat-up and cooling periods of brines which would allow for shorter test durations.

Localised corrosion kinetics at elevated temperatures can also be evaluated more accurately by conducting tests at extremely small surface area to volume ratios (A/V). Smaller A/V ratios will result in slower precipitation of corrosion products by delaying saturation with respect to $FeCO_3$.

Recommendation 2

Chapter 4 has demonstrated that in the presence of calcium ions within brine solutions can result in the precipitation of complex corrosion products such as $Fe_xCa_yCO_3$ which exist with Ca/Fe concentration gradients across their depths. However the reason for concentration gradients with respect to iron and calcium within $Fe_xCa_yCO_3$ is still unknown. It is of extreme importance to understand the mechanism behind the concentration gradients as it will enable more accurate predictions of the protectiveness of these corrosion products and their solubility.

The concentration gradients may be attributed to two factors; the consumption of calcium ions within the brine solution and the bulk solution pH. It is recommended that *in-situ* pH measurements are conducted during the precipitation of mixed iron-calcium carbonates to understand how the bulk pH changes with increasing exposure time, before, during and after precipitation of corrosion products. It is also recommended that brine solution is sampled during the tests for atomic emission spectroscopy to enable the determination of the elements present within brine solutions and their quantities.

Recommendation 3

The performance of an imidazoline corrosion inhibitor was evaluated on corrosion product covered surfaces in Chapter 6, however this study was conducted at an inhibitor of 30 ppm which was found to be the optimum concentration with respect to the uniform corrosion behaviour in Chapter 5. It would be extremely beneficial to conduct the same tests under the same conditions however at the optimum inhibitor concentration with respect to the

localised corrosion behaviour (40 ppm) to determine whether or not severe localised corrosion attacks can be prevented in the presence of the corrosion inhibitor on pre-corroded steel surfaces.

Recommendation 4

The inhibitor performance tests on pre-corroded steel surfaces were conducted in un-buffered bulk solution conditions which resulted in a reduction in the accuracy of the estimated individual contributions provided by both the corrosion inhibitor and the corrosion product layer. It may therefore have had an influence on the overall performance comparison of the inhibitor in the presence of different corrosion product layers. It is suggested that for future research, the bulk pH is maintained constant throughout the test period in order to more accurately compare the inhibitor performance on different pre-corroded steel surfaces. This can be successfully achieved by conducting the tests in a flow cell.

Recommendation 5

Experiments were conducted in autoclave and glass cell systems. For the autoclave tests appropriate measures were implemented in order to minimise oxygen contamination. These measures included purging the autoclave with CO_2 prior to the test and pumping the CO_2 saturated brine into the autoclave. However such measures were not implemented for glass cell tests and it is therefore important to ensure that the minimum oxygen content possible is present within the glass cell systems used for future tests. This can be achieved by preparing and CO_2 saturating the brine in a separate glass cell to the cell where the test is conducted. A specimen can therefore be inserted into the second glass cell prior to pumping of the brine from the first glass cell to the second. This methodology would therefore ensure that a specimen would not have to be inserted into the glass cell containing the saturated brine and therefore minimise the possibility of oxygen ingress.

References

1. KERMANI, M.B. and A. MORSHED. Carbon Dioxide Corrosion in Oil and Gas Production—A Compendium. *CORROSION*, 2003, 59(8), pp.659-683.
2. YARO, A.S., K.R. ABDUL-KHALIK and A. KHADOM. Effect of CO_2 corrosion behavior of mild steel in oilfield produced water. 2015, 38, pp.24-38.
3. LIU, Z.G., X.H. GAO, C. YU, L.X. DU, J.P. LI and P. HAO. Corrosion Behavior of Low-Alloy Pipeline Steel with 1% Cr Under CO_2 Condition. 2015, 28(6), pp.739-747.
4. TRAN, T., B. BROWN and S. NESIC. Corrosion of mild steel in an aqueous CO_2 environment—basic electrochemical mechanisms revisited. 2015.
5. SCHMITT, G. Global needs for knowledge dissemination, research, and development in materials deterioration and corrosion control. 2009, 38.
6. NOR, A.M., M. SUHOR, M. MOHAMED, M.M. SINGER and S. NESIC. Corrosion of carbon steel in high CO_2 environment: flow effect. 2011.
7. SUHOR, M., M. MOHAMED, A.M. NOR, M. SINGER and S. NESIC. 2012.
8. MANSOORI, H., D. YOUNG, B. BROWN, S. NESIC and M. SINGER. Effect of $CaCO_3$-Saturated Solution on CO_2 Corrosion of Mild Steel Explored in a System with Controlled Water Chemistry and Well-Defined Mass Transfer Conditions. *Corrosion Science*, 2019.
9. BLATT, H., R. TRACY and B. OWENS. *Petrology: igneous, sedimentary, and metamorphic.* Macmillan, 2006.
10. RAYMOND, L.A. *Petrology: the study of igneous, sedimentary, metamorphic rocks.* Wm. C. Brown Dubuque, Iowa, 1995.
11. HUNT, J.M. Distribution of hydrocarbons in sedimentary rocks. *Geochimica et Cosmochimica Acta*, 1961, 22(1), pp.37-49.
12. WILSON, J. Limestone and dolomite reservoirs. 1980, 2.
13. HOBSON, G.D. *Developments in petroleum geology.* Elsevier Science Ltd, 1980.
14. ALSAIARI, H.A., N. ZHANG, S. WORK, A.T. KAN and M.B. TOMSON. A New Correlation to Predict the Stoichiometry of Mixed Scale: Iron-Calcium Carbonate. *In: SPE International Conference on Oilfield Scale*, 2012/1/1/, Aberdeen, UK. Society of Petroleum Engineers, 2012.
15. SHENG, J. *Modern chemical enhanced oil recovery: theory and practice.* Gulf Professional Publishing, 2010.
16. ALVARADO, V. and E.J.E. MANRIQUE. Enhanced oil recovery: an update review. 2010, 3(9), pp.1529-1575.
17. GREEN, D.W. and G.P. WILLHITE. *Enhanced oil recovery.* Henry L. Doherty Memorial Fund of AIME, Society of Petroleum Engineers. 1998.
18. LAKE, L.W. Enhanced oil recovery. 1989.

19. CAMPBELL, C.J. and J.H. LAHERRÈRE. The End of Cheap Oil. *Scientific American*, 1998, 278(3), pp.78-83.

20. OWYANG, M.T. *The Rise of Shale Oil* [online]. 2018. [Accessed 04/02].

21. XU, C., W. ZOU, Y. YANG, Y. DUAN, Y. SHEN, B. LUO, C. NI, X. FU and J. ZHANG. Status and prospects of deep oil and gas resources exploration and development onshore China. *Journal of Natural Gas Geoscience*, 2018, 3(1), pp.11-24.

22. BJØRLYKKE, K. Introduction to petroleum geology. *In: Petroleum Geoscience*. Springer, 2015, pp.1-29.

23. RAHUMA, M. and M. BOBBY KANNAN. Corrosion in Oil and Gas Industry: A Perspective on Corrosion Inhibitors. *J Material Sci Eng*, 2014, 3, p.e110.

24. JENKINS, A. Performance of High-Temperature, Biodegradable Corrosion Inhibitors. *In: CORROSION 2011*, 2011/1/1/, Houston, Texas. NACE International, 2011, p.12.

25. VERMA, C., E.E. EBENSO and M.A. QURAISHI. Ionic Liquids as Green Corrosion Inhibitors for Industrial Metals and Alloys. *In: Green Chemistry*. InTech, 2018.

26. PALENCSÁR, A., E. GULBRANDSEN and K. KOSORÚ. High Temperature Testing of Corrosion Inhibitor Performance. *In: CORROSION 2013*, 2013/3/17/, Orlando, Florida. NACE International, 2013, p.15.

27. BRZESZCZ, J. and A. TURKIEWICZ. Corrosion inhibitors–application in oil industry. *Nafta-Gaz*, 2015, 71(2), pp.67--75.

28. PAOLINELLI, L.D., T. PÉREZ and S.N.J.C.S. SIMISON. The effect of pre-corrosion and steel microstructure on inhibitor performance in CO_2 corrosion. 2008, 50(9), pp.2456-2464.

29. GULBRANDSEN, E., S. NESIC, S. MORTEN HESJEVIK, S. SKJFRVE, B. SUNDFER, T. BURCHARDT and A.J.C. STANGELAND. Effect of precorrosion on the performance of inhibitors for CO_2 corrosion of carbon steel. 1998.

30. ZHANG, H.H., X. PANG, M. ZHOU, C. LIU, L. WEI and K. GAO. The behavior of pre-corrosion effect on the performance of imidazoline-based inhibitor in 3 wt.% NaCl solution saturated with CO_2. 2015, 356, pp.63-72.

31. GULBRANDSEN, E., M. FOSS and J. SJÖBLOM. Interaction of carbon dioxide corrosion inhibitors with corrosion products deposit. *In: CORROSION 2008*: NACE International, 2008.

32. KVAREKVAL, J. and E.J.C. GULBRANDSEN, PAPER. High temperature and high flow velocity tests for CO_2 corrosion inhibitors. 2001.

33. SNOW, D.A. *Plant engineer's reference book.* Elsevier, 2001.

34. KAIN, V, PREPARATION, PROCESSING, E.B.S.B. APPLICATIONS" and E.I. A. TYAGI. Chapter 12,". 2012.

35. ECM, E.M. Reference module in materials science and materials engineering. 2016.

36. WAN, R. Advanced Well Completion Engineering: Oil and Gas Well Corrosion and Corrosion Prevention. 2011.

37. SPEIGHT, J.G. *Oil and Gas Corrosion Prevention: From Surface Facilities to Refineries.* Gulf Professional Publishing, 2014.

38. EL-SHERIK, A. *Trends in Oil and Gas Corrosion Research and Technologies: Production and Transmission.* Woodhead Publishing, 2017.

39. AHMAD, Z. *Principles of corrosion engineering and corrosion control.* Elsevier, 2006.

40. MCCAFFERTY, E. *Introduction to corrosion science.* Springer Science & Business Media, 2010.

41. KOLESAR, S.C. Principles of corrosion. *In: 12th International Reliability Physics Symposium*: IEEE, 1974, pp.155-167.

42. TAIT, W.S. *An introduction to electrochemical corrosion testing for practicing engineers and scientists.* PairODocs Publications, 1994.

43. GAMRY. *Understanding the Specifications of your Potentiostat* [online]. 2019. [Accessed]. Available from: https://www.gamry.com/application-notes/instrumentation/understanding-specs-of-potentiostat/.

44. BADEA, G., A. CARABAN, M. SEBESAN, S. DZITAC, P. CRET and A. SETEL. Polarisation measurements used for corrosion rates determination. 2010.

45. NORDSVEEN, M., S. NEŠIC, R. NYBORG and A. STANGELAND. A mechanistic model for carbon dioxide corrosion of mild steel in the presence of protective iron carbonate films—part 1: theory and verification. 2003, 59(5), pp.443-456.

46. UHLIG, H.H., R. REVIE and I. SONS. Corrosion and Corrosion Control: an Introduction to Corrosion Science and Engineering. (Book). 1985, p.1985.

47. SCHMITT, G., CORROSION 83/43, NACE, HOUSTON, TX. Fundamental aspects of CO_2 corrosion. 1984.

48. BENTISS, F., M. LAGRENEE, M. TRAISNEL and J.C. HORNEZ. The corrosion inhibition of mild steel in acidic media by a new triazole derivative. *Corrosion Science*, 1999, 41(4), pp.789-803.

49. FRANKEL, G.S. and N. SRIDHAR. Understanding localized corrosion. *Materials Today*, 2008, 11(10), pp.38-44.

50. SOLTIS, J. Passivity breakdown, pit initiation and propagation of pits in metallic materials – Review. *Corrosion Science*, 2015, 90, pp.5-22.

51. HUA, Y., R. BARKER and A. NEVILLE. Effect of temperature on the critical water content for general and localised corrosion of X65 carbon steel in the transport of supercritical CO_2. 2014, 31, pp.48-60.

52. G46-94, A. Standard guide for examination and evaluation of pitting corrosion. 2005.

53. DE MORAES, F., J.R. SHADLEY, J. CHEN and E.F. RYBICKI. Characterization of CO_2 Corrosion Product Scales Related to

Environmental Conditions. *In: CORROSION 2000*, 2000/1/1/, Orlando, Florida. NACE International, 2000, p.27.

54. GAO, M., X. PANG and K. GAO. The growth mechanism of CO_2 corrosion product films. *Corrosion Science*, 2011, 53(2), pp.557-568.

55. CROLET, J.L., N. THEVENOT and S. NESIC. *Role of conductive corrosion products on the protectiveness of corrosion layers*. NACE International, Houston, TX (United States), 1996.

56. FARELAS, F., B. BROWN and S. NESIC, PAPER. Iron carbide and its influence on the formation of protective iron carbonate in CO_2 corrosion of mild steel. 2013, 2291.

57. SUN, W., S. NEŠIĆ and R. WOOLLAM. The effect of temperature and ionic strength on iron carbonate ($FeCO_3$) solubility limit. 2009, 51(6), pp.1273-1276.

58. SUN, W., K. CHOKSHI and S. NESIC. Iron Carbonate Scale Growth and the Effect of Inhibition in CO_2 Corrosion of Mild Steel. *In: CORROSION 2005*, 2005/1/1/, Houston, Texas. NACE International, 2005, p.23.

59. TANUPABRUNGSUN, T., B. BROWN and S. NESIC. Effect of pH on CO_2 corrosion of mild steel at elevated temperatures. 2013, (48).

60. BARKER, R., I. AL SHAAILI, R. DE MOTTE, D. BURKLE, T. CHARPENTIER, S. VARGAS and A. NEVILLE. Iron carbonate formation kinetics onto corroding and pre-filmed carbon steel surfaces in carbon dioxide corrosion environments. 2019, 469, pp.135-145.

61. NEŠIC, S. and K. LEE. A mechanistic model for carbon dioxide corrosion of mild steel in the presence of protective iron carbonate films—part 3: film growth model. 2003, 59(7), pp.616-628.

62. HUA, Y., R. BARKER and A. NEVILLE. The effect of O_2 content on the corrosion behaviour of X65 and 5Cr in water-containing supercritical CO_2 environments. 2015, 356, pp.499-511.

63. BARKER, R., Y. HUA and A. NEVILLE. Internal corrosion of carbon steel pipelines for dense-phase CO_2 transport in carbon capture and storage (CCS)–a review. 2017, 62(1), pp.1-31.

64. CRAIG, B. *Corrosion product analysis - A road map to corrosion in oil and gas production.* 2002.

65. PLUMMER, L.N. and E. BUSENBERG. The solubilities of calcite, aragonite and vaterite in CO_2-H_2O solutions between 0 and 90ºC, and an evaluation of the aqueous model for the system $CaCO_3$-CO_2-H_2O. 1982, 46(6), pp.1011-1040.

66. FALINI, G., S. ALBECK, S. WEINER and L. ADDADI. Control of aragonite or calcite polymorphism by mollusk shell macromolecules. 1996, 271(5245), pp.67-69.

67. ALSAIARI, H.A., A.T. KAN and M.B. TOMSON. Molar Ratio of Ca^{2+} to Fe^{2+} in the Supersaturated Solution of Iron Carbonate and Calcium Carbonate and in the Precipitate: Relation and Interpretation. *In: SPE International Symposium on Oilfield Chemistry*: Society of Petroleum Engineers, 2009.

68. NAVABZADEH ESMAEELY, S., Y.S. CHOI, D. YOUNG and S. NEŠIĆ. Effect of calcium on the formation and protectiveness of iron carbonate layer in CO_2 corrosion. 2013, 69(9), pp.912-920.

69. ESMAEELY, S.N., Y.S. CHOI, D. YOUNG and S. NEŠIĆ. Effect of Calcium on the Formation and Protectiveness of Iron Carbonate Layer in CO_2 Corrosion. *CORROSION*, 2013, 69(9), pp.912-920.

70. ALSAIARI, H.A., S. YEAN, M.B. TOMSON and A.T. KAN. Iron Calcium Carbonate: Precipitation Interaction. *In: SPE International Oilfield Scale Conference*, 2008/1/1/, Aberdeen, UK. Society of Petroleum Engineers, 2008, p.16.

71. SCHMITT, G. and M. HORSTEMEIER. Fundamental aspects of CO_2 metal loss corrosion-Part II: Influence of different parameters on CO_2 corrosion mechanisms. *In: CORROSION 2006*: NACE International, 2006.

72. NAZARI, M.H., S. ALLAHKARAM and M. KERMANI. The effects of temperature and pH on the characteristics of corrosion product in CO_2 corrosion of grade X70 steel. 2010, 31(7), pp.3559-3563.

73. DE WAARD, C., U. LOTZ and D. MILLIAMS. Predictive model for CO_2 corrosion engineering in wet natural gas pipelines. 1991, 47(12), pp.976-985.

74. YIN, Z.F., Y. FENG, W. ZHAO, Z. BAI and G. LIN. APPLICATION OF TECHNIQUES FOR THE ANALYSIS OF SURFACES and T. FILMS. Effect of temperature on CO_2 corrosion of carbon steel. 2009, 41(6), pp.517-523.

75. DUGSTAD, A. Fundamental Aspects of CO_2 Metal Loss Corrosion - Part 1: Mechanism. *In: CORROSION 2006*, 2006/1/1/, San Diego, California. NACE International, 2006, p.18.

76. LIN, G., M. ZHENG, Z. BAI and X. ZHAO. Effect of Temperature and Pressure on the Morphology of Carbon Dioxide Corrosion Scales. 2006, 62(6), pp.501-507.

77. ZHANG, G. and Y. CHENG. Electrochemical characterization and computational fluid dynamics simulation of flow-accelerated corrosion of X65 steel in a CO_2-saturated oilfield formation water. 2010, 52(8), pp.2716-2724.

78. DENPO, K. and H. OGAWA. Fluid flow effects on CO_2 corrosion resistance of oil well materials. 1993, 49(6), pp.442-449.

79. TIU, B.D.B., and ADVINCULA. Polymeric corrosion inhibitors for the oil and gas industry: Design principles and mechanism. 2015, 95, pp.25-45.

80. HOBBS, J.J.H. Reliable corrosion inhibition in the oil and gas industry. 2014, p.28.

81. JENKINS, A. Performance of High-Temperature, Biodegradable Corrosion Inhibitors. *In: CORROSION 2011*: NACE International, 2011.

82. DARIVA, C.G. and A.F. GALIO. Corrosion inhibitors–principles, mechanisms and applications. *In: Developments in corrosion protection*. InTech, 2014.

83. BRZESZCZ, J. and A. TURKIEWICZ. Corrosion inhibitors–application in oil industry. 2015, 71(2), pp.67--75.

84. SUN, W., K. CHOKSHI and S. NESIC. Iron carbonate scale growth and the effect of inhibition in CO_2 corrosion of mild steel. *In: CORROSION 2005*: NACE International, 2005.

85. ESMAEELY, S.N., D. YOUNG, B. BROWN and S. NEŠIĆ. Effect of incorporation of calcium into iron carbonate protective layers in CO_2 corrosion of mild steel. 2016, 73(3), pp.238-246.

86. TAVARES, L.M., E.M. DA COSTA, J.J. DE OLIVEIRA ANDRADE, R. HUBLER and B. HUET. Effect of calcium carbonate on low carbon steel corrosion behavior in saline CO_2 high pressure environments. 2015, 359, pp.143-152.

87. GAO, M., X. PANG and K. GAO. The growth mechanism of CO_2 corrosion product films. 2011, 53(2), pp.557-568.

88. HAN, J., D. YOUNG, H. COLIJN, A. TRIPATHI and S. NEŠIĆ. Chemistry and structure of the passive film on mild steel in CO_2 corrosion environments. 2009, 48(13), pp.6296-6302.

89. SUN, W. and S. NESIC. Basics revisited: kinetics of iron carbonate scale precipitation in CO_2 corrosion. 2006.

90. LIN, G., M. ZHENG, Z. BAI and X. ZHAO. Effect of temperature and pressure on the morphology of carbon dioxide corrosion scales. 2006, 62(6), pp.501-507.

91. DUGSTAD, A. *Mechanism of protective film formation during CO_2 corrosion of carbon steel*. NACE International, Houston, TX (United States), 1998.

92. TANG, X., S. RICHTER and S. NESIC. Study of wettability of different mild steel surfaces. *In: 17th International Corrosion Congress*, 2008, p.1298.

93. HUA, Y., A. SHAMSA, R. BARKER and A. NEVILLE. Protectiveness, morphology and composition of corrosion products formed on carbon steel in the presence of Cl^-, Ca^{2+} and Mg^{2+} in high pressure CO_2 environments. 2018, 455, pp.667-682.

94. JIANG, X., Y. ZHENG. Effect of calcium ions on pitting corrosion and inhibition performance in CO_2 corrosion of N80 steel. 2006, 48(10), pp.3091-3108.

95. GAO, K., F. YU, X. PANG, G. ZHANG, L. QIAO. Mechanical properties of CO_2 corrosion product scales and their relationship to corrosion rates. 2008, 50(10), pp.2796-2803.

96. PALMER, J.W., J. MARSH and R.C. NEWMAN. Evaluation of inhibitor performance for protection against localized corrosion. *In: CORROSION 2002*: NACE International, 2002.

97. WANG, B., M. DU, J. ZHANG and C. GAO. Electrochemical and surface analysis studies on corrosion inhibition of Q235 steel by imidazoline derivative against CO_2 corrosion. 2011, 53(1), pp.353-361.

98. DING, Y., B. BROWN, D. YOUNG and M. SINGER. Effectiveness of an imidazoline-type inhibitor against CO_2 corrosion of mild steel at elevated temperatures (120ºC-150ºC). 2018.

99. LIU, Z. and T. JACKSON. Understanding Thermal Stability and Inhibition Effectiveness of Corrosion Inhibitors at High Temperatures. *In: NACE International Corrosion Conference Proceedings*: NACE International, 2016, p.1.

100. HONG, T. and W. JEPSON. Corrosion inhibitor studies in large flow loop at high temperature and high pressure. 2001, 43(10), pp.1839-1849.

101. RAMACHANDRAN, S., Y.S. AHN, M. GREAVES, V. JOVANCICEVIC and J. BASSETT. Development of high temperature, high pressure corrosion Inhibitor. *In: CORROSION 2006*: NACE International, 2006.

102. CHEN, H.J., W.P. JEPSON and T. HONG. High temperature corrosion inhibition performance of imidazoline and amide. 2000.

103. FOSS, M., E. GULBRANDSEN and J. SJOBLOM. Oil Wetting and Carbon Dioxide Corrosion Inhibition of Carbon Steel with Ferric Corrosion Products Deposits. 2010, 66(2), pp.025005-025005-11.

104. FOSS, M., E. GULBRANDSEN and J. SJÖBLOM. Adsorption of corrosion inhibitors onto iron carbonate ($FeCO_3$) studied by zeta potential measurements. 2010, 31(2), pp.200-208.

105. WONG, J.E. and N. PARK. Effect of corrosion inhibitor active components on the growth of iron carbonate scale under CO_2 conditions. *In: CORROSION 2008*: NACE International, 2008.

106. Further investigation on the effect of corrosion inhibitor actives on the formation of iron carbonate on carbon steel. *In: CORROSION 2009*: NACE International, 2009.

107. BOMMERSBACH, P., C. ALEMANY-DUMONT, J.P. MILLET and B. NORMAND. Formation and behaviour study of an environment-friendly corrosion inhibitor by electrochemical methods. 2005, 51(6), pp.1076-1084.

108. ASTM, G. G 1-03. *Standard Practice for Preparing, Cleaning, and Evaluating Corrosion Test Specimens," Philadelphia, Pennsylvania: American Society for Testing and Materials*, 2003.

109. TECHNOLOGIES, C. *Datasheet: 108* [online]. [Accessed]. Available from: https://thermal-detection.com/.

110. INSTRUMENTS, C. *Specifications/Instructions UltraDeg® High-Pressure and/or High-Temperature Ag/AgCl Reference Probes* [online]. [Accessed]. Available from: https://www.brsystems.jp/wordpress/wp-content/uploads/sites/2/2017/01/Spec_Instructions-for-High-Pressure-Ref-Probes_Q0408.pdf.

111. STANDARDS, A.G.-J.A.B.O.A. Standard reference test method for making potentiostatic and potentiodynamic anodic polarization measurements. 2004, 3, pp.48-58.

112. GOLDSTEIN, J.I., D.E. NEWBURY, J.R. MICHAEL, N.W. RITCHIE, J.H.J. SCOTT and D.C. JOY. *Scanning electron microscopy and X-ray microanalysis.* Springer, 2017.

113. KELLY, A. and K.M. KNOWLES. *Crystallography and crystal defects.* John Wiley & Sons, 2012.

114. DAVIDSON, P.M., G.H. SYMMES, B.A. COHEN, R.J. REEDER and D.H. LINDSLEY. Synthesis of the new compound $CaFe(CO_3)_2$ and experimental constraints on the $(Ca,Fe)CO_3$ join. *Geochimica et Cosmochimica Acta*, 1993, 57(23), pp.5105-5109.

115. ALSAIARI, H.A. *Iron (II)-calcium carbonate: Precipitation interaction* thesis, Rice University, 2008.

116. CUBILLAS, P., M.W.J.Z. ANDERSON, R. CATALYSIS: SYNTHESIS and APPLICATIONS. Synthesis mechanism: crystal growth and nucleation. 2010, pp.1-55.

117. MUNOZ, A., J. GENESCA, R. DURAN and J. MENDOZA. Mechanism of $FeCO_3$ formation on API X70 pipeline steel in brine solutions containing CO_2. 2005.

118. HERNANDEZ, J., A. MUÑOZ and J. GENESCA. Formation of iron-carbonate scale-layer and corrosion mechanism of API X70 pipeline steel in carbon dioxide-saturated 3% sodium chloride. 2012, 69(560).

119. ESMAEELY, S.N., D. YOUNG, B. BROWN and S. NEŠIĆ. Effect of Incorporation of Calcium into Iron Carbonate Protective Layers in CO_2 Corrosion of Mild Steel. *CORROSION*, 2017, 73(3), pp.238-246.

120. ABBASOV, V.M., T.A. MAMMADOVA, K.R. VELIYEV and K.H. KASAMANLI. Hydroxy-and Aminoethyl Imidazolines of Cottonseed Oil Fatty Acids as Additives for Diesel Fuels. 2015.

121. USMAN, B.J. and S. ALI. Carbon dioxide corrosion inhibitors: a review. 2018, 43(1), pp.1-22.

122. BONDAREVA, S., V. LISITSKII, N. YAKOVTSEVA and Y. MURINOV. Hydrolysis of 1, 2-disubstituted imidazolines in aqueous media. 2004, 53(4), pp.803-807.

123. WAHYUNINGRUM, D., S. ACHMAD, Y.M. SYAH, B. BUCHARI and B. ARIWAHJOEDI. The synthesis of imidazoline derivative compounds as corrosion inhibitor towards carbon steel in 1% NaCl solution. 2008, 40(1), pp.33-48.

124. CRADDOCK, H.A. *Oilfield chemistry and its environmental impact.* Wiley Online Library, 2018.